Dune emergence in multidirectional wind regimes

Cyril Gadal

UNIVERSITÉ DE PARIS

Thèse préparée à l'Institut de Physique du Globe de Paris
École doctorale STEP'UP - ED560
Équipe de Dynamique des Fluides Géologiques

Dune emergence in multidirectional wind regimes

par
Cyril Gadal

présentée et soutenue publiquement le 15 octobre 2020

Thèse de doctorat des Sciences de la Terre et de l'Environnement
Spécialité : Géophysique
dirigée par Clément Narteau & Philippe Claudin

Valérie Vidal	Chargée de recherche (CNRS-ENS Lyon)	Rapporteure
Bruno Castelle	Directeur de recherche (CNRS - Université de Bordeaux)	Rapporteur
Laurent Lacaze	Chargé de recherche (CNRS-IMFT)	Examinateur
Edouard Kaminski	Professeur (Université de Paris, IPGP)	Examinateur
Elisabeth Guazzelli	Directrice de recherche (CNRS - Université de Paris)	Invitée
Clément Narteau	Professeur (Université de Paris, IPGP)	Directeur de thèse
Philippe Claudin	Directeur de recherche (CNRS-PMMH, ESPCI)	Co-directeur de thèse

Résumé

Emergence des dunes sous des régimes de vents multidirectionnels

Les dunes éoliennes résultent de l'entraînement et du dépôt des grains de sable transportés par le vent. Cet écoulement s'adapte à son tour à la forme du lit sédimentaire. Ce couplage entre topographie, hydrodynamique et transport contrôle la taille, orientation et morphologie des dunes, et ce particulièrement durant la phase initiale de leur croissance. Dans cette thèse, nous mettons en évidence l'influence de certains paramètres environnementaux, tel que le régime de vents, la disponibilité en sable et les conditions aux limites du champ de dunes sur la formation des dunes. Pour cela, nous utilisons une approche théorique, couplée à des expériences de laboratoire, des simulations numériques et des études de terrain.

Tout d'abord, nous validons la description de l'émergence des dunes dans les zones de fortes disponibilités sédimentaire sous forme d'instabilité linéaire. Ces dunes prennent la forme d'ondes de surface, dont l'amplitude augmente temporellement ou spatialement, suivant si elles se forment au milieu du lit sédimentaire, ou sur sa bordure amont. Leur orientation, longueur d'onde et taux de croissance spatial/temporel sont alors principalement contrôlés par la distribution angulaire des flux de sables.

Sur un sol non-érodable, les dunes se développent à partir de diverses source de sédiments (autres dunes, dépôts fluviaux, lacustres, etc ..). Sous des régimes de vents spécifiques, elles s'allongent pour former de longues crêtes linéaires. Nous montrons que l'organisation spatiale de ces dunes est contrôlée par la répartition des sources sédimentaires, et non par une échelle de longueur intrinsèque au mécanisme d'élongation. Ainsi, elles forment des champs de dunes périodiques sur les bordures aval des lits de sédiments, ou des structures isolés dans des zones de dépôt plus localisées. Dans ce dernier cas, elles peuvent atteindre un état d'équilibre stable, dont la morphologie est contrôlée par la période de réorientation des vents.

Enfin, nous effectuons une analyse à grande échelle du désert du Namib en nous appuyant sur le cadre théorique du transport sédimentaire et de la morphodynamique dunaire, couplé à des données de vent issues de réanalyses climatiques. Nous comparons alors des observations de terrain à nos prédictions sur les flux de sable et sur les dunes (orientations, morphologies, taux de croissance). Ces résultats permettent ainsi de discuter la formation et l'évolution des mers de sable sur des échelles de temps couvrant plusieurs cycles climatiques. Plus généralement, cette méthodologie permet aussi d'inférer certaines informations sur les vents ou le matériel sédimentaire lorsque celles-ci ne sont pas directement mesurables, ainsi que d'avoir un aperçu de l'évolution et de la résilience des systèmes dunaires soumis à des changements climatiques ou anthropiques.

Mots-clés : dune, transport sédimentaire, instabilités, géomorphologie des zones arides

Abstract

Dune emergence in multidirectional wind regimes

Aeolian dunes result from the erosion and deposition of sand grains transported by the wind. In turn, the flow adapts to the shape of the sedimentary bed. This coupling between topography, hydrodynamics and transport controls the dune size, orientation and morphology, particularly during the early stage of their growth. In this thesis, we highlight the influence of certain environmental parameters, such as wind regime, sand availability, and dune field boundary conditions on dune emergence. For this, we use a theoretical approach, coupled with laboratory experiments, numerical simulations and field studies.

First, we validate the description of dune emergence in areas of high sediment availability as a linear instability. These dunes form as surface waves, whose amplitude increases temporally or spatially, depending on whether they form in the middle of the sedimentary bed, or on its upstream edge. Their orientation, wavelength and spatial/temporal growth rate are then mainly controlled by the angular distribution of sand fluxes.

On a non-erodible ground, dunes develop from various sources of sediments (other dunes, river and lakes deposits, etc.). Under specific wind regimes, they elongate to form linear ridges. We show that the spatial organization of these dunes is then controlled by the distribution of sedimentary sources, and not by a length scale intrinsic to the elongation mechanism. Thus, they form periodic dune fields at the downstream edge of sediment beds, or remain isolated structures in zones of localized deposition. In the latter case, they can reach a stable equilibrium state, whose morphology is controlled by the wind reorientation period.

Finally, we carry out a large-scale analysis of the Namib Sand Sea based on the theoretical framework of sediment transport and dune morphodynamics, coupled to wind data from climate reanalyses. We then compare field observations with our predictions on sand fluxes and dunes (orientations, morphologies, growth rates). These results allow us to discuss the formation and evolution of sand seas on time scales covering several climatic cycles. More generally, this methodology also makes it possible to infer information on winds or sedimentary material when these are not directly measurable, as well as to gain insight into the evolution and resilience of dune systems subject to climate or anthropogenic changes.

Keywords : dune, sediment transport, instabilities, arid zone geomorphology

Table des matières

Introduction générale

Les dunes sont des amas sédimentaires formés par l'écoulement d'un fluide, air ou eau, sur un lit composé de grains. Lorsqu'il est assez fort, il permet l'entraînement, le transport et la déposition de ces derniers, amenant à la formation d'une large variété de structures dont la diversité reflète les nombreux environnements dans lesquels elles peuvent se former (Andreotti *et al.* 2012b). Dans les rivières, les mers et les océans, le courant et les vagues génèrent des dunes sous-marines, en partie visibles sous l'eau au bord des plages. Dans les zones enneigées, des dunes de glace ou de neige sont formées par le vent transportant les flocons. Dans cette thèse, nous nous concentrons plutôt sur les dunes de sables issues de l'action du vent, dont la taille varie de quelques mètres à plusieurs kilomètres. Elles se trouvent en grande majorité sur les côtes et dans les déserts, tout en interagissant avec les espaces urbains.

L'évolution constante des dunes de sable, à travers leur croissance et leur migration, présente ainsi des enjeux de gestion du territoire, pouvant nécessiter une intervention humaine (Provoost *et al.* 2011). La dune du Pilat, et de manière plus générale toute la côte des Landes, située entre Biarritz et Arcachon, en sont de bons exemples. Au XIX$^{\text{me}}$ siècle, la forêt des Landes est envahie de marécages et de dunes côtières mobiles, dont l'avancement menace les villages environnements. Sous l'impulsion de Napoléon III, les marécages sont asséchés afin de permettre une exploitation efficace de la forêt de pins. Afin de protéger cette dernière, les dunes sont quant à elles stabilisées à l'aide de végétation ; une méthode efficace ... sauf à l'endroit où se situe la Dune du Pilat. Cette dernière, se déplaçant de 1 à 5 m par an, menace ainsi toujours l'intérieur des terres tout en constituant une des attractions touristiques principales de la région. L'utilisation de végétation dans le but de stabiliser les dunes reste une méthode fortement employée, par exemple par la Chine dans son combat contre la désertification (Durán & Herrmann 2006). Afin de savoir où, quand et comment gérer la naissance et l'évolution des dunes, il faut tout d'abord comprendre les mécanismes qui contrôlent la dynamique de ces dernières.

D'un point de vue géologique, les dunes agissent aussi comme marqueurs du passé. Les zones désertiques, sèches, sont de bonnes conservatrices de la matière organiques, et les vestiges archéologiques enfouis dans les dunes y sont alors souvent très bien préservés. À l'intérieur de ces dernières, l'organisation des couches sédimentaires permet de retracer

une partie de leur histoire, contraignant dans une certaine mesure les hypothèses sur les climats antérieurs à notre époque. De manière analogue, les images satellites des motifs dunaires permettent aussi d'obtenir des informations sur les propriétés des sédiments ou du vent dans les endroits où les mesures ne sont ni disponibles, ni faisables, comme sur Mars, Vénus, ou Titan, un des satellites de Saturne (Fenton *et al.* 2014a;b, Runyon *et al.* 2017, Fernandez-Cascales *et al.* 2018).

Les dunes et leur évolution, en tant que système naturel, sont régies par un grand nombre de paramètres extérieurs, tels que le climat et les précipitations, la végétation, la topographie et le contexte géologique, l'apport en sédiments, etc.. (Ewing *et al.* 2006). Obtenir des prédictions fiables nécessite alors l'étude et la quantification de l'impact de chacun de ces paramètres. Bien que difficile à mettre en place en conditions naturelles, ceci est alors réalisable grâce à l'utilisation de modèles théoriques, numériques ou d'expériences de laboratoire reproduisant l'évolution des champs de dunes, dans lesquels ces paramètres peuvent être variés indépendamment les uns des autres (Narteau *et al.* 2009, Reffet *et al.* 2010, Courrech du Pont *et al.* 2014). Dans cette thèse, nous employons cette approche mixte afin de comprendre certains des mécanismes contrôlant les différents motifs apparaissant lors des premiers stades de la croissance des dunes.

Dans le premier chapitre, nous présentons une synthèse des connaissances sur la morphodynamique dunaire. Nous commençons par détailler les mécanismes à l'origine du transport du sable par le vent, puis nous lions ces derniers à la sélection en taille des dunes naissantes. Finalement, nous présentons les différents motifs de dunes matures, et les lois qui les gouvernent.

Chapitre 1

État de l'art

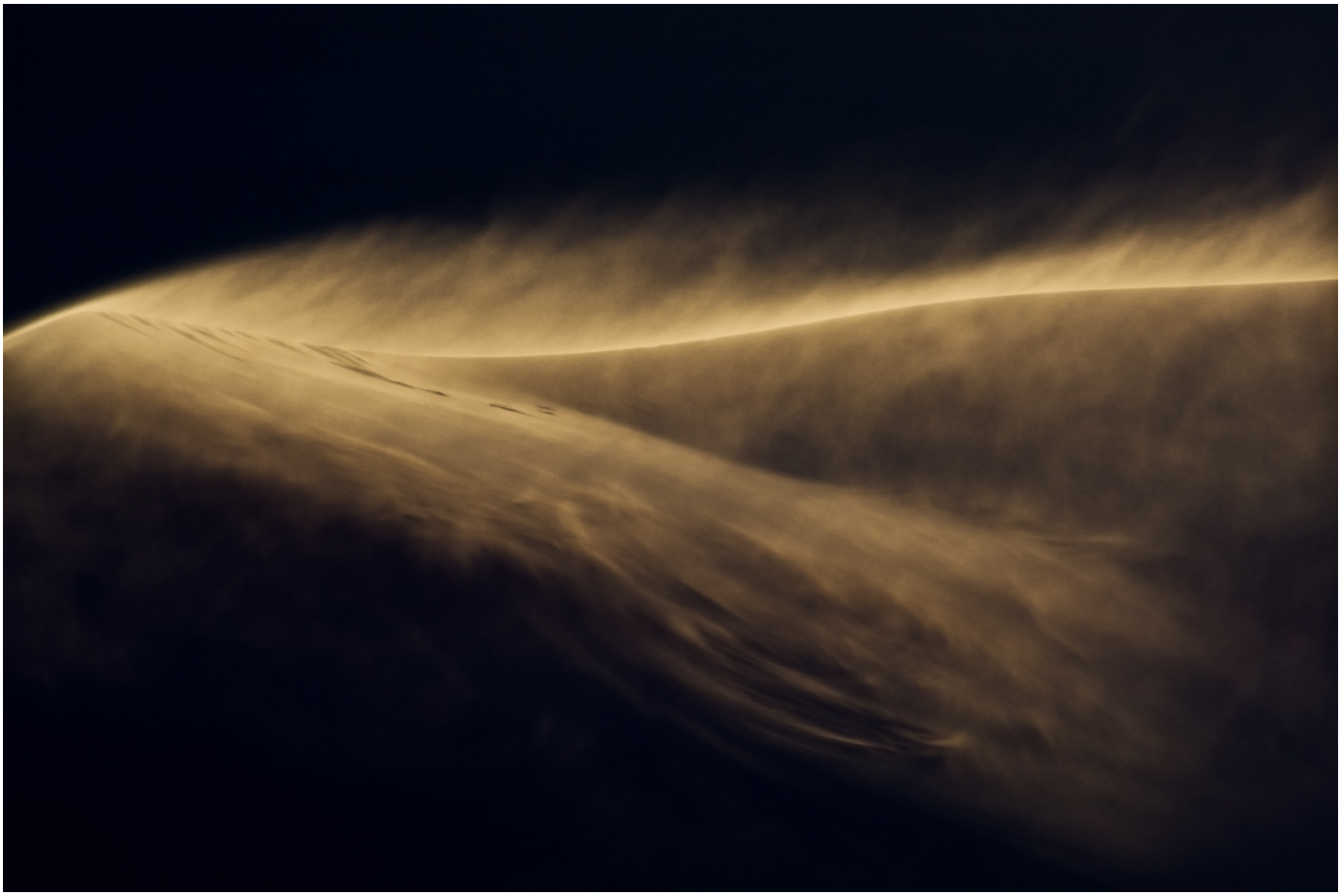

Sediment transport over a sand dune, Namibia - Paul van Schalkwyk

Contents

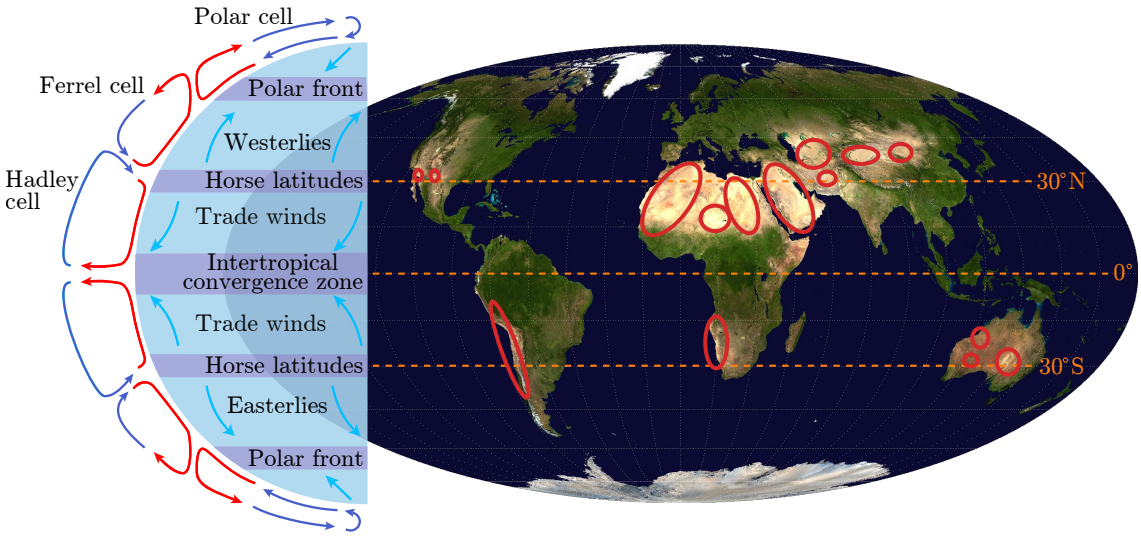

FIGURE 1.1 – Localisation des principales mers de sable (ellipses rouges) sur Terre (projection de Mollweide, planisphère provenant de Wikipédia). La plupart des dunes en Australie ne sont plus actives, stabilisées par la végétation. Le schéma de gauche représente la circulation atmosphérique dans la troposphère. Figure inspirée de Courrech du Pont (2015).

1.1 Introduction

En laissant de côté les dunes côtières, les dunes de sable se forment principalement dans des systèmes grandes échelles, appelées *mers de sable* ou encore *ergs*. Ces derniers couvrent près de 6% de la surface du globe terrestre, et se trouvent sur tous les continents à l'exception de l'Antarctique. La plupart d'entre eux se regroupent autour des latitudes dites *des chevaux*, aux alentours de 30° de part et d'autre de l'équateur (Figure 1.1). Les anticyclones semi-permanents qui y sont présents impliquent la présence de vents relativement faibles soufflant dans des directions très différentes. Se situant à la jonction des cellules de Ferrer et Hadley, le climat y est majoritairement contrôlé par l'air sec qui y descend en se réchauffant. À partir de ces deux ceintures subtropicales, les vents sont dirigés soit vers les pôles (vents d'est et d'ouest), soit vers l'équateur (alizés), tout en étant déviés par l'effet de Coriolis. Les chemins le long desquels le sable est transporté à travers les continents reflètent alors la répartition de ces vents, tout en étant localement influencés par la topographie.

Les dunes éoliennes sont formées de grains de sable composés principalement de quartz et de feldspath, bien que du gypse, du calcaire ou des cendres volcaniques puissent également être présents (Pye & Tsoar 1990). Lorsque ces grains sont mis en mouvement par le vent, des motifs apparaissent à différentes échelles. À l'échelle centimétrique, les rides éoliennes, issues du bombardement du sol par les grains en mouvement, génèrent un motif périodique de crêtes (Seppälä & Lindé 1978, Anderson 1987, Csahók *et al.* 2000, Andreotti *et al.* 2006; 2012b, Durán *et al.* 2014). À l'échelle du mètre, les dunes émergent à travers

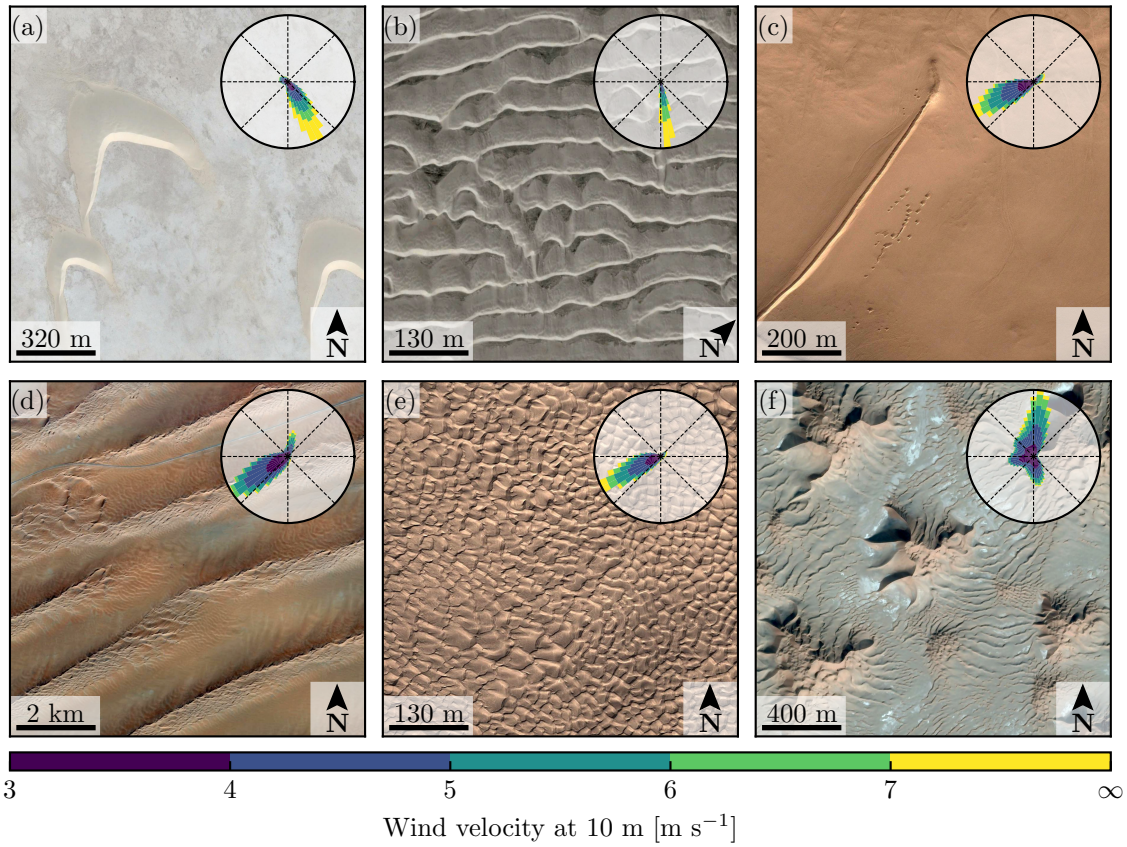

FIGURE 1.2 – Différents motifs dunaires, et régime de vents associés. (a) Barkhanes dans le désert du Rub' Al Khali, Qatar, 24°50′N, 51°18′E. (b) Dunes transverses sur la péninsule de Basse-California, Mexique, 27°58′N, 114°09′W. (c) Dune linéaire isolée dans le sud du désert du Taklamacan, Chine, 37°42′N, 82°33′E. (d) Dunes linéaires dans le désert du Rub' Al Khali, Arabie Saoudite, 17°27′N, 46°32′E. (e) Dunes en réseau dans le sud du désert du Taklamacan, Chine, 37°44′N, 82°37′E. (f) Dunes étoiles au sud du désert du Rub' Al Khali, Oman, 18°30′N, 53°10′E. En haut à droite de chaque image, la rose des vents (avec pour convention de direction celle où va le vent) montre les données de vents à 10 m issues du modèle de réanalyse climatique Era5 (Hersbach *et al.* 2020). Images satellites : Google^{TM}, Maxar Technologies, INEGI, CNES/Airbus.

les interactions entre le vent, les mécanismes du transport sédimentaire et la forme du lit de grains (Sauermann *et al.* 2001, Andreotti *et al.* 2002b). Enfin, à l'échelle kilométrique, les dunes géantes résultent de la coalescence des dunes de plus petites tailles (Coleman & Melville 1994; 1996, Kocurek *et al.* 2010, Gao *et al.* 2015a).

En plus de ces différentes tailles, un grande variété de formes est observée (voir figure 1.2). Sous un vent unidirectionnel, la surface d'un lit sable se déforme en une série de dunes linéaires appelées *dunes transverses*, dont les crêtes régulièrement espacées sont perpendiculaires à la direction du vent (Mainguet 1984, Livingstone & Warren 1996, Lancaster 2013). Dans des conditions de vent similaires, mais avec une faible disponibilité sédimen-

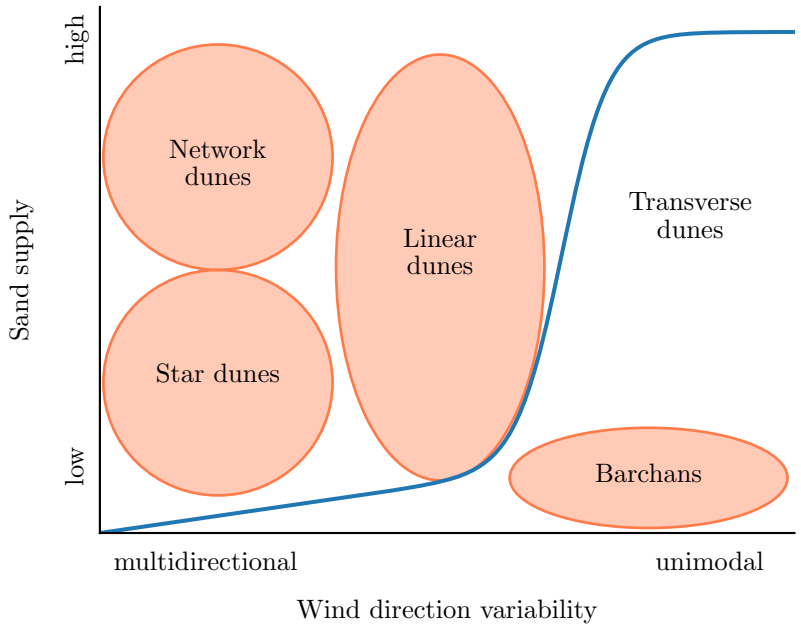

FIGURE 1.3 – Une classification spéculative des dunes venant de Livingstone & Warren (1996).

taire [1], une dune isolée migrant sur un sol non-érodable prend la forme caractéristique en croissant d'une *barkhane* (Andreotti *et al.* 2002a, Hersen 2004b). Ces deux types de dunes présentent un profil d'élévation asymétrique, avec une faible pente en amont, et une forte pente du côté aval. Dans les zones exposées à des régimes de vents de directions très variables au cours du temps, pour lesquels le transport de sable résultant est nul, on observe des *dunes étoiles*, possédant plusieurs crêtes d'orientations variables et dont les bras s'allongent dans différentes directions (Lancaster 1989, Zhang *et al.* 2012). Néanmoins, compte-tenu de la variabilité climatique issue du cycle saisonnier terrestre, la plupart des mers de sable sont modelées par un vent possédant deux directions dominantes. Cela donne lieu à des champs de *dunes linéaires* au profil symétrique, dont les longues crêtes parallèles définissent une orientation marquée (Lancaster 1982).

Ces motifs variés, de tailles et de formes différentes, paraissent de prime abord compliqués, reflétant le caractère erratique et variable des nombreux paramètres naturels qui les contrôlent (Kocurek & Ewing 2005, Ewing *et al.* 2006). Néanmoins, la volonté de comprendre l'origine de cette diversité a donné naissance à une classification des différents types de dunes basées sur deux paramètres dominants : la multidirectionnalité du vent, et la disponibilité sédimentaire [2] (Wasson & Hyde 1983, Mainguet 1984, Livingstone &

1. quantité de sable mobile, pouvant être transporté par le vent
2. La végétation est aussi un paramètre extrêmement important de la morphodynamique dunaire. Néanmoins, dans cette thèse, nous laissons de côté les dunes végétées pour nous concentrer sur les dunes entièrement actives, formées de sable meuble.

Warren 1996). Cette classification qualitative basée sur la forme, représentée en figure 1.3, permet une première approche des différents motifs, montrant que ces derniers reflètent les conditions extérieures dans lesquelles ils se forment. Les appréhender plus en profondeur nécessite alors une compréhension globale des mécanismes agissant dans la morphodynamique des dunes, depuis leur naissance jusqu'à leur forme géante. Ces mécanismes proviennent des processus élémentaires de l'hydrodynamique et du transport de sédiments, que nous allons détailler dans la section suivante.

1.2 Transport sédimentaire éolien

Afin de comprendre la dynamique à l'échelle des champs de dunes, il est tout d'abord nécessaire de se pencher sur les interactions à l'échelle des grains, et sur leur couplage avec le fluide ambiant. De manière très générale, les milieux granulaires forment une famille très diversifiée comprenant toute collection de particules de taille macroscopique (diamètre supérieur à 100 μm). Cette définition très vaste comprend ainsi des particules de toutes tailles, solides ou molles, dans des environments secs ou mouillés, que ce soit du sable, de la poudre, des brindilles transportées par un courant ou encore un éboulement rocheux. Ces milieux, à mi-chemin entre fluide et solide, possèdent des propriétés uniques donnant lieu à des comportements rhéologiques complexes (Forterre & Pouliquen 2008, Andreotti *et al.* 2012b).

Dans le cadre de cette étude, nous détaillerons seulement les propriétés des milieux granulaires liées à l'érosion et au transport sédimentaire dans le cadre des dunes éoliennes. Cela concerne alors des particules solides dont la taille est sélectionnée par le mode de transport dominant. Une fois mis en mouvement par l'écoulement, les grains sont transportés suivant différents modes de transport selon la nature des forces pouvant dominer ce processus.

Lorsque les forces hydrodynamiques dominent, par exemple pour les particules fines, les grains sont entraînés par l'écoulement sans contact avec le lit sédimentaire, retenus en suspension. Lorsque le poids des particules permet de confiner le transport dans une couche proche de la surface, les grains transportés suivent alors différents types de trajectoires. Les grains de taille moyenne effectuent une succession de sauts appelée saltation, tandis que les grains plus lourds roulent et ricochent sur la surface, dans un mode appelé charriage. Enfin, si, via les deux types de trajectoires décrites précédemment, les particules transportées au-dessus du lit sédimentaire transmettent à ce dernier assez d'énergie via leurs chocs avec la surface, les grains qui composent ce dernier se déplacent lentement dans un mouvement appelé reptation.

Le transport éolien est largement dominé par la saltation et le charriage (Andreotti 2004, Durán *et al.* 2011), ce qui correspond d'après les relevés de terrain à une taille

moyenne des grains d'environ 250 μm (Pye & Tsoar 1990). Cette valeur est cohérente avec les vitesses moyennes des vents des déserts terrestres (Durán 2007).

1.2.1 Écoulement proche de la surface

Nous commençons dans cette section par décrire l'écoulement à l'origine du transport sédimentaire éolien. Suivant le fluide, et les échelles de vitesse et de longueur associées au système, cet écoulement peut être dominé par les forces de dissipation visqueuse, son inertie ou encore par la turbulence générée au contact du lit. Le rapport entre les forces visqueuses et inertielles correspond au nombre sans dimension appelé le nombre de Reynolds :

$$R_e = \frac{\rho_f U L}{\eta}, \tag{1.1}$$

où η est la viscosité dynamique du fluide, ρ_f sa masse volumique et U et L les échelles de vitesse et longueur typiques de l'écoulement. L'écoulement est ainsi dit laminaire lorsque la viscosité domine ($R_e < 1$), et inertiel lorsque l'inertie prend le dessus ($R_e > 1$). Néanmoins, au fur et à mesure que l'inertie augmente, l'écoulement se déstabilise et voit apparaître aux petites échelles de multiple tourbillons, à l'aspect intermittent et aléatoire. Cette transition vers la turbulence s'effectue pour des nombres de Reynolds élevés ($R_e \sim 2000$ dans le cadre d'un écoulement dans une conduite cylindrique), et change les propriétés de l'écoulement.

Nature de l'écoulement à la surface de la Terre

Dans le cadre du transport éolien, les vents de surface soufflent dans la couche limite atmosphérique, la partie la plus basse de l'atmosphère. Ils y sont fortement influencés par les propriétés locales de la surface terrestre, que ce soit la température, l'humidité ou encore les frottements induits par la topographie ou la végétation. La taille de cette couche varie de quelques mètres à quelques kilomètres suivant les conditions locales de pression, température et humidité, et les vents y soufflent à une vitesse de l'ordre d'une dizaine de mètres par seconde. En tenant compte de la faible valeur de la viscosité cinématique de l'air ($\simeq 10^{-5}$ m^2 s^{-1}), le nombre de Reynolds caractéristique de la couche limite atmosphérique est aux alentours de 10^9. Les écoulements impliqués dans les processus éoliens sont alors dominés par la turbulence.

Loi du mur

La compréhension des écoulements impliqués nécessite une vision en terme de couches successives. Ainsi, dans la couche limite atmosphérique, l'écoulement est forcé à son sommet par les vents géostrophiques de la couche supérieure, et s'annule à son pied dans une couche visqueuse très proche de la surface.

Les fluctuations induites par la turbulence sont à l'origine de dissipation dans l'écoulement, induisant un cisaillement vertical τ. Ce dernier peut être lié de manière générale au gradient de vitesse vertical comme :

$$\tau = \eta_t \frac{\mathrm{d}u}{\mathrm{d}z}, \tag{1.2}$$

où η_t est la viscosité turbulente. La viscosité du fluide, quant à elle, est totalement inefficace à l'échelle de la couche limite turbulente, et n'agit que dans la couche proche de la surface. Dimensionnellement, les seules échelles de longueur et de temps proviennent alors de la distance au sol z et du gradient de vitesse. Il vient :

$$\eta_t = \kappa^2 \rho_f z^2 \frac{\mathrm{d}u}{\mathrm{d}z}, \tag{1.3}$$

où κ la constante de von Kármán (Von Kármán 1935, Prandtl 1925). En combinant les équations (1.2) et (1.3), et en intégrant, on obtient le profil de vent logarithmique :

$$u(z) = \frac{u_*}{\kappa} \ln\left(\frac{z}{z_0}\right), \tag{1.4}$$

où $u_* = \sqrt{\tau/\rho_f}$ est la vitesse de cisaillement, et z_0 la rugosité hydrodynamique (Stull 1988, Garratt 1994).

Rugosité hydrodynamique

Par définition, la rugosité hydrodynamique est la hauteur à partir de laquelle la vitesse du vent s'annule si l'on prolonge le profil logarithmique jusqu'au sol. L'expression dérivée précédemment ne s'applique ainsi pas lorsque $z \to 0$. Proche de la surface, la sous-couche visqueuse fait le lien entre la vitesse nulle sur les grains et le profil logarithmique au-dessus. Le cisaillement est continu à l'interface entre les deux couches, de telle sorte que :

$$\tau = \rho_f u_*^2 \simeq 5\eta u_* / l_\eta, \tag{1.5}$$

où $l_\eta = 5\nu/u_*$ est l'épaisseur de la couche limite visqueuse, de l'ordre de 100 μm pour l'air (Schlichting *et al.* 1955). Les trajectoires induites par la saltation prennent place bien au delà de cette couche visqueuse, bien qu'elle soit non-négligeable devant le diamètre d'un grain. Dans le cas d'une surface très lisse, l_η fixe néanmoins la valeur de la rugosité hydrodynamique.

Dans le cas d'un lit plat de grains immobiles, la rugosité effective est fixée par la rugosité géométrique de la surface, typiquement une fraction du diamètre des grains, de l'ordre de $d/10 - d/30$ (Bagnold 1941, Schlichting *et al.* 1955, Kamphuis 1974, Andreotti 2004). Lors du processus de saltation, la rétroaction du transport sur l'écoulement, que

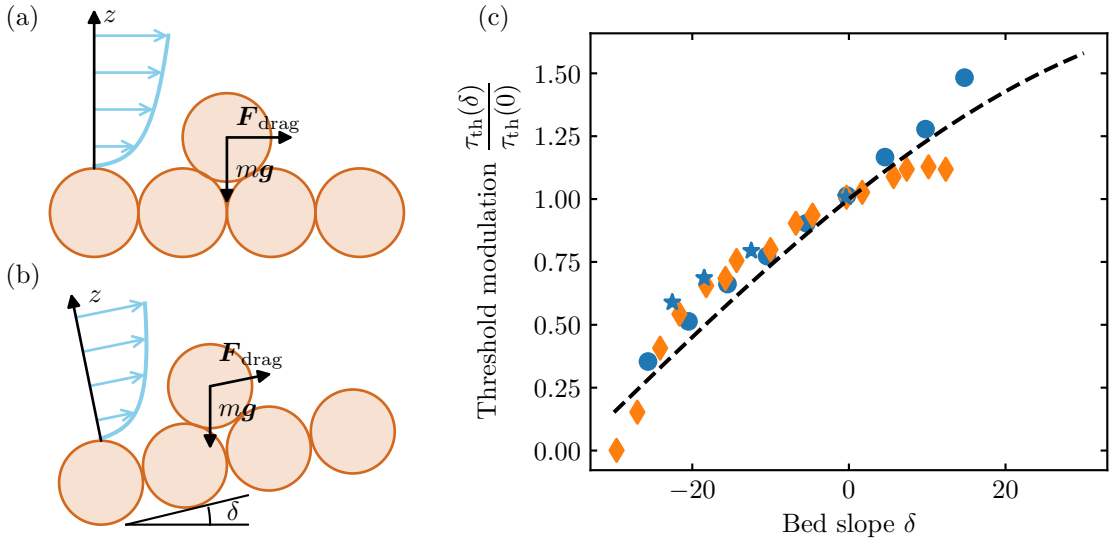

FIGURE 1.4 – (a) Schéma montrant l'origine du seuil de transport à l'échelle du grain. (b) Schéma montrant l'impact de la pente sur le seuil de transport. (c) Variation du seuil de transport en fonction de la pente longitudinale. Les symboles bleus correspondent au seuil de transport statique, obtenu via des mesures subaquatiques par Fernandez Luque & Van Beek (1976) (étoiles) et Dey (2003) (ronds). Les losanges oranges correspondent au seuil dynamique, obtenu via des mesures en soufflerie par Hardisty & Whitehouse (1988). La ligne noire correspond à $\cos\delta + \sin\delta/\mu$, avec $\mu = \tan(35°)$ (équation (1.15)). Figure inspirée de Durán *et al.* (2011).

nous détaillerons par la suite, conduit à une augmentation de la rugosité hydrodynamique jusqu'à une fraction de la hauteur de la couche de transport, de l'ordre du millimètre au lieu de la dizaine de micromètres.

Néanmoins, la rugosité géométrique pertinente dépend de l'échelle à laquelle le profil de l'écoulement est étudié. Ainsi, à l'échelle kilométrique de la couche limite atmosphérique, il est probable que la rugosité hydrodynamique soit fixée par les arbres, les bâtiments ou les dunes elles-mêmes. Dans cette thèse, nous aurons l'occasion de travailler avec des données de vents souvent mesurés à quelques mètres au-dessus du sol. À cette échelle, la rugosité est alors fixée par la taille des rides sableuses ou par la couche de transport, donnant typiquement $z_0 \sim 1$ mm.

1.2.2 Entraînement et seuil de transport

Lorsque l'on regarde les galets au fond d'une rivière, la plupart d'entre eux restent immobiles alors que la vitesse de l'écoulement est non-nulle. C'est donc qu'il existe un seuil, une vitesse critique dépendant du poids du grain au-dessus de laquelle l'érosion commence. Il en est de même pour le vent et le sable, et de manière plus générale pour tout fluide s'écoulant au-dessus d'un lit composé de grains. L'origine physique de ce seuil se trouve dans le piégeage des grains par gravité.

Seuil de transport statique

Une première vision du seuil de transport consiste ainsi à regarder les forces s'exerçant sur un grain (voir figure 1.4(a)). Lorsque le fluide s'écoule sur le lit granulaire, il y exerce une force de cisaillement, tangentielle à la surface :

$$f_t = \alpha d^2 \tau, \tag{1.6}$$

où α est un coefficient sans dimension dépendant de la nature de l'écoulement et de la forme du grain. Ce dernier est retenu par son poids, normal à la surface, qui s'exprime comme :

$$f_n = \beta(\rho_s - \rho_f) g d^3, \tag{1.7}$$

où β est une constante géométrique dépendant de la forme des grains ($\beta = \pi/6$ pour des sphères). Le rapport entre ces deux forces correspond au nombre de Shields (Shields 1936) :

$$\Theta = \frac{\beta}{\alpha}\frac{f_t}{f_n} = \frac{\tau}{(\rho_s - \rho_f) g d}. \tag{1.8}$$

En négligeant tout autre interaction de contact que la friction solide, la loi de Coulomb indique qu'au seuil d'entraînement,

$$f_t = \mu_s f_n, \tag{1.9}$$

où μ_s est le coefficient de friction statique entre deux grains. Le nombre de Shields prend alors sa valeur seuil :

$$\Theta_{\text{th}} = \frac{\beta}{\alpha}\mu_s. \tag{1.10}$$

Les mesures expérimentales du nombre de Shields seuil sont difficiles. Sa définition est liée à la fraction seuil des grains qui rentrent en mouvement, et peut donc changer d'une étude à l'autre (Yalin 1972, Buffington & Montgomery 1997, Shvidchenko *et al.* 2001).

Des modèles semi-empiriques permettent d'obtenir des expressions du nombre de Shields seuil selon les différents régimes, turbulent ou laminaire (Durán *et al.* 2011, Andreotti *et al.* 2012b). Dans le cas d'un écoulement turbulent, la force fluide s'exerçant sur le grain comporte, en plus de la composante tangentielle appelée traînée, une composante normale appelée portance, dirigée vers le haut. La combinaison des deux induit alors un mouvement de glissement/rotation autour du point de contact avec le grain situé directement en aval, aidant à la mise en mouvement. Pour un écoulement turbulent et un grain sphérique, la composante tangentielle s'écrit :

$$f_t = \frac{\pi}{16} C_\infty \rho_f d^2 U^2, \tag{1.11}$$

où C_∞ est le coefficient de traînée à grand nombre de Reynolds, respectivement de l'ordre

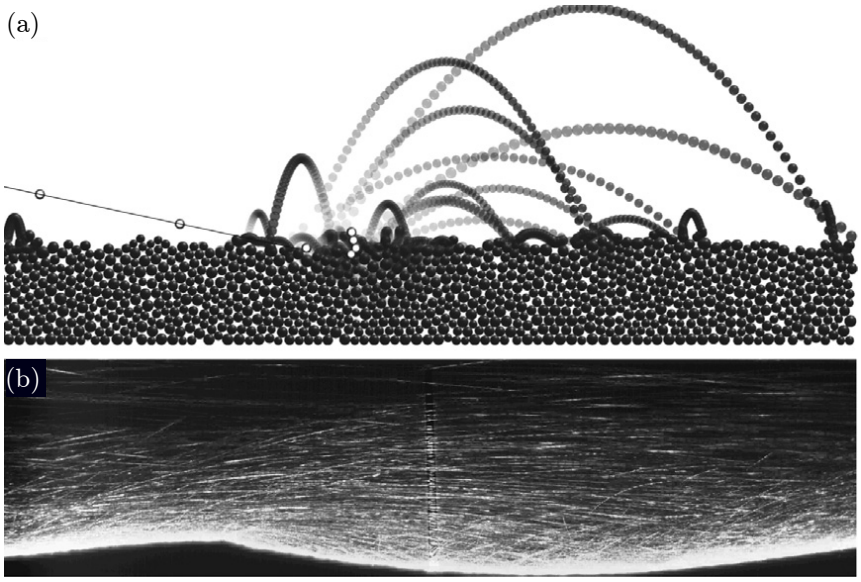

FIGURE 1.5 – (a) Éjection de grains suite à une collision très énergétique (simulation numérique) (b) Visualisation de trajectoires des grains transportés au-dessus de rides éoliennes. Figure provenant de Durán *et al.* (2011)

.

de 1/2 et 1 pour des sphères lisses et des grains réels. La vitesse du fluide U autour du grain peut être approximée en $z = d/2$ par le profil logarithmique caractéristique du régime turbulent (1.4). Ainsi, en ne prenant en compte que la composante tangentielle, le nombre de Shields seuil s'écrit (Durán *et al.* 2011) :

$$\Theta_{\text{th}} = \frac{8\mu_s\kappa^2}{3C_\infty \ln^2(d/(2z_0))}. \tag{1.12}$$

Le nombre de Shields est surtout utilisé en géomorphologie fluviale. Dans le cadre du transport éolien, la vitesse seuil correspondante est utilisée :

$$u_{\text{th}} = \sqrt{\frac{8\mu_s\kappa^2}{3C_\infty \ln^2\left(d/(2z_0)\right)} \frac{\rho_s - \rho_f}{\rho_f} gd}. \tag{1.13}$$

Ce modèle correspond bien aux résultats de diverses expériences sur le transport en milieu fluvial (Andreotti *et al.* 2012b). En revanche, les mesures de transport en conditions éoliennes montrent que la quantité de sable transportée par le vent tend vers zéro pour des vitesses inférieures à ce seuil statique.

Seuil de transport dynamique

Les expériences en soufflerie montrent qu'en conditions éoliennes, contrairement au transport en milieu aqueux, le charriage laisse rapidement place à la saltation [3] (Bagnold 1941, Iversen *et al.* 1987, Burr *et al.* 2015).

Une fois le grain délogé par le cisaillement fluide, il effectue alors une série de sauts dont la hauteur augmente au fur et à mesure. En effet, contrairement à des rebonds sur lit plat, la surface rugueuse permet de rediriger une partie de la quantité de mouvement horizontale vers le haut lors de chaque choc. À chaque impact avec la surface, d'autres grains sont délogés, et ainsi de suite (figure 1.5(a)). L'ensemble de ces grains en mouvement forme alors la couche de transport, dont l'épaisseur est contrôlée par la hauteur moyenne de leurs sauts (figure 1.5(b)).

Il résulte de ce mécanisme d'impact un seuil de transport dynamique, différent du seuil de transport statique décrit précédemment, plus faible. Une fois le processus de saltation enclenché, des vitesses de vent inférieures à la vitesse seuil (équation (1.13)) peuvent maintenir le transport. Ce seuil est modifié par la pente de la même manière que le seuil statique, comme le montre les symboles oranges sur la figure 1.4(c). Néanmoins, afin d'en obtenir une formulation analytique, il est nécessaire de connaître les propriétés des trajectoires des grains en saltation via l'intégration des équations du mouvement suivant le type de l'écoulement (Andreotti 2004, Claudin & Andreotti 2006, Lämmel *et al.* 2012, Pähtz & Durán 2018).

Le seuil dynamique étant toujours plus faible que le seuil statique dans le cas du transport éolien (Durán *et al.* 2011), il en devient la grandeur pertinente. Ceci reste néanmoins controversé dans certaines situations. Le seuil statique correspond au moment où le fluide peut commencer à déloger un grain, et ne prend pas en compte les chocs d'autres particules avec le lit, qui peuvent alors aider à la mise en mouvement. Ainsi, il reste pertinent lorsque ces collisions sont peu énergétiques devant l'écoulement, comme pour le démarrage de la saltation ou pour le charriage, typique du transport en milieu aqueux. Les mesures de terrain de Martin & Kok (2018) montrent que les flux issus d'épisodes intermittents de saltation peuvent être autant contrôlés par le seuil statique que le seuil dynamique. Ils précisent néanmoins que ce dernier suffit pour prédire des flux moyennés temporellement (~ 30 min), justifiant son utilisation dans l'étude de la dynamique des dunes.

Dans le cas où une mesure expérimentale est accessible, le seuil de transport pertinent peut alors être trouvé par extrapolation de la loi expérimentale liant le flux de sédiments au nombre de Shields/au cisaillement basal (Durán *et al.* 2011, Martin & Kok 2017, Abramian

3. Il faut néanmoins noter que les conditions sur le terrain, en particulier en terme de couche limite, sont différentes de celles en soufflerie. Cela pourrait donner lieu à des régimes de transport éolien par charriage (Pähtz *et al.* 2020).

et al. 2019a). Si cette mesure n'est pas accessible, le seuil de transport peut être calculé en utilisant l'expression empirique suivante :

$$u_{\mathrm{th}} \propto \sqrt{\frac{\rho_{\mathrm{s}}}{\rho_{\mathrm{f}}} g d}, \tag{1.14}$$

avec une constante de proportionnalité aux alentours de 0.1 (Iversen *et al.* 1976; 1987)

Pente longitudinale et cohésion

Lorsque le lit n'est plus plat mais pentu, le seuil de transport est modifié : il est plus difficile pour le vent de mettre en mouvement les grains s'il fait face à une pente positive, et inversement. Pour une pente δ, les forces tangentielles et normales agissant sur un grain sont respectivement modifiées comme $f_t - f_n \sin\delta$ et $f_n \cos\delta$ (voir figure 1.4(b)), donnant :

$$u_{\mathrm{th}}(\delta) = u_{\mathrm{th}}(0)\sqrt{\left(\cos\delta + \frac{\sin\delta}{\mu}\right)}. \tag{1.15}$$

Cette relation est bien vérifiée, pour le seuil statique comme pour le seuil dynamique, comme le montre la figure 1.4(c) (Fernandez Luque & Van Beek 1976, Iversen & Rasmussen 1994, Dey 2003, Durán *et al.* 2011).

Enfin, le seuil de transport peut être aussi modifié par la présence des forces de cohésion. Dues à de faibles tailles de grains, à la présence d'humidité, ou encore à la présence de liaisons chimiques (formation d'un ciment), elles sont responsables d'une augmentation du seuil de transport (Claudin & Andreotti 2006, Durán *et al.* 2011). La présence des forces de cohésion est contrôlée par le nombre sans dimension d_γ/d, où d_γ est une longueur capillaire correspondant à la taille du grain pour laquelle les forces de cohésion et de gravité s'équilibrent. Elle prend alors différentes expressions suivant l'origine physique de la cohésion (Andreotti *et al.* 2012b).

1.2.3 Transport par saltation et saturation du flux

Le processus d'amplification du nombre de grains en mouvement décrit précédemment, issu des chocs successifs avec le lit, finit par saturer. En effet, chaque grain éjecté par chaque collision à une chance de sauter assez haut pour se faire lui-même accélérer par le vent. L'augmentation de la densité de grains en mouvement dans la couche de transport, couplé à ce transfert de quantité de mouvement, induit alors une diminution conséquente de la vitesse du vent. Le transport atteint alors un état stationnaire lorsque chaque grain n'en éjecte en moyenne qu'un seul autre, tandis que la vitesse du vent est réduite à sa valeur seuil au sein de la couche de transport (Ungar & Haff 1987, Andreotti *et al.* 2002a, Durán *et al.* 2011).

À l'état stationnaire, la répartition des particules en mouvement dans la couche de

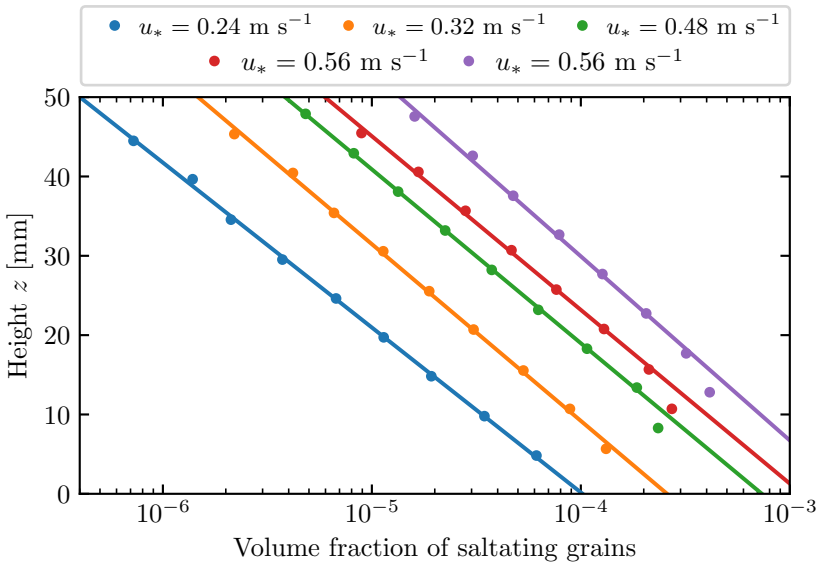

FIGURE 1.6 – Mesure en soufflerie de profils verticaux de fraction volumique de grains en saltation, pour différentes valeurs de vitesse de cisaillement (Creyssels *et al.* 2009).

transport n'est pas homogène. Des mesures en soufflerie (White 1982, Liu & Dong 2004, Rasmussen & Sørensen 2008, Creyssels *et al.* 2009) et sur le terrain (Namikas 2003, Rotnicka 2013) réalisées pour différentes vitesses de vents montrent que la densité de grains diminue exponentiellement avec la hauteur (voir figure 1.6). Ceci correspond alors à une distribution de Maxwell des vitesses d'éjection des particules.

De plus, la distance caractéristique sur laquelle décroît cette exponentielle est indépendante de la vitesse de cisaillement. Ainsi, la vitesse d'éjection la plus probable l'est aussi, ce qui est une manifestation directe de la rétroaction du transport sur l'écoulement (Ungar & Haff 1987, Andreotti *et al.* 2012b).

Flux saturé et loi de transport

En suivant l'approche de Bagnold (1941) et Ungar & Haff (1987), le flux de grains peut s'écrire comme le produit de deux quantités :

$$q_{\text{sat}} \propto n u_p, \tag{1.16}$$

où n est le nombre moyen de particules en mouvement et u_p leur vitesse moyenne.

Dans cet état stationnaire et homogène, la quantité de mouvement est conservée. Le cisaillement fluide non perturbé, s'appliquant au-dessus de la couche loin du lit, est égal à la somme de la contrainte basale et de la quantité de mouvement horizontale des grains $n\tau_p$ (Owen 1964, Sørensen 2004, Durán *et al.* 2011) :

$$\tau = \tau_{\text{th}} + n\tau_p. \tag{1.17}$$

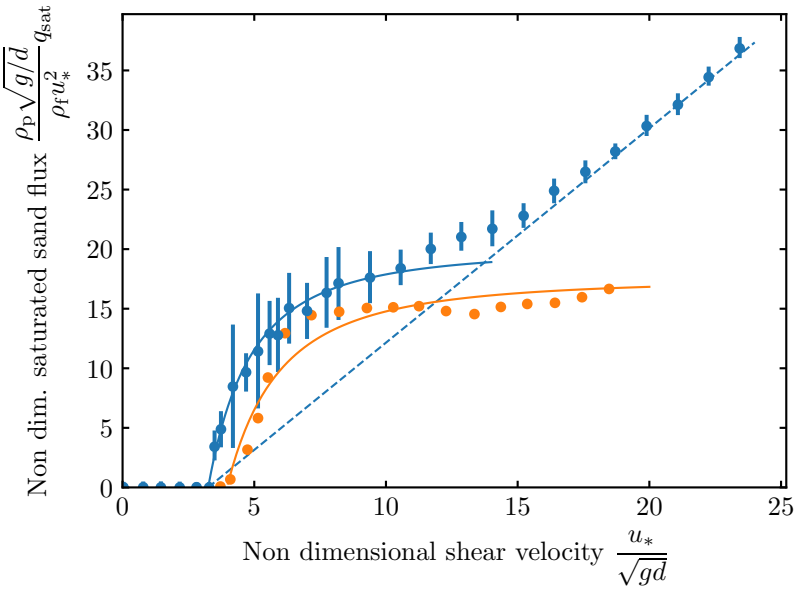

FIGURE 1.7 – Flux saturé en fonction de la vitesse de cisaillement provenant de mesures en soufflerie par Iversen & Rasmussen (1999) (orange) et de simulations numériques par Durán *et al.* (2011) (bleu). Le flux est normalisé par u_*^2 afin de montrer les comportements asymptotiques. Les courbes en traits pleins correspondent au comportement en $u_*^2 - u_{\text{th}}^2$, et celle en pointillés à celui en $u_* u_*^2 - u_{\text{th}}^2$. Figure adaptée de Durán *et al.* (2011)

À cause de la rétroaction du transport sur l'écoulement, les trajectoires des particules sont indépendantes de la vitesse du vent u_*, réduite à sa vitesse seuil dans la couche de transport : on obtient alors $u_p \propto u_{\text{th}}$, et $\tau_p \propto \tau_{\text{th}}$. Le nombre de particules en mouvement dépend alors seulement de l'écart au seuil de transport :

$$n \propto \tau - \tau_{\text{th}}, \tag{1.18}$$

de même que pour le flux saturé (Ungar & Haff 1987, Andreotti 2004) :

$$q_{\text{sat}} = \Omega\,(\tau - \tau_{\text{th}})\,, \tag{1.19}$$

où Ω est une constante dépendant des propriétés de grains et du fluide. Les mesures des expériences en soufflerie valident ce résultat (Iversen & Rasmussen 1999, Creyssels *et al.* 2009). De plus, de nombreuses simulations numériques permettent une calibration de cette loi (Werner 1990, Andreotti 2004, Almeida *et al.* 2008, Kok & Renno 2009, Creyssels *et al.* 2009, Durán *et al.* 2011) :

$$\Omega \simeq \frac{15}{\phi}\frac{\rho_f}{\rho_s}\sqrt{\frac{d}{g}}, \tag{1.20}$$

où $\phi \simeq 0.6$ est la fraction volumique de grains dans le lit sédimentaire.

Ces simulations montrent aussi que, lorsque la vitesse du vent augmente, typiquement

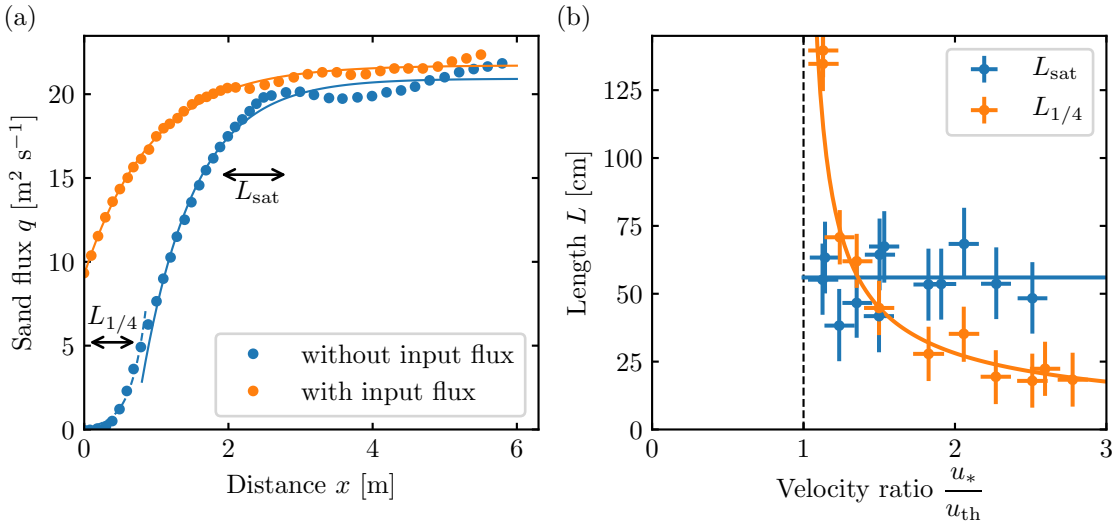

FIGURE 1.8 – (a) Flux le long d'un lit plat de sédiments avec (orange) et sans (bleu) flux en entrée, pour $d = 120$ μm et $u_*/u_{\mathrm{th}} \simeq 1.5$. Le lit commence en $x = 0$, précédé d'une zone non-érodable. Courbes en traits pleins : relaxation exponentielle proche de l'état saturé. Courbe pointillée : croissance exponentielle initiale. (b) Variation des deux longueurs caractéristiques en fonction de la distance au seuil de transport. Données provenant de Andreotti *et al.* (2010). Figure adaptée de Durán *et al.* (2011)

de l'ordre de 5 fois la vitesse seuil, le flux saturé commence à varier avec u_*^3 au lieu de u_*^2, ce qui correspond à l'approche initiale de Bagnold (1941) (voir figure 1.7). Pour de grandes vitesses de cisaillement, les trajectoires des grains les plus rapides dépassent la couche de transport. Leur vitesse dépend alors directement de la vitesse de cisaillement u_*, au lieu de la vitesse seuil u_{th}. Néanmoins, ce sont des conditions peu rencontrées sur Terre, où la vitesse du vent dépasse rarement 3 fois la vitesse seuil.

1.2.4 Longueur de saturation

Considérons maintenant une situation dans laquelle le cisaillement fluide n'est plus homogène, que ce soit en temps ou en espace. Le flux de sédiments ne s'adapte alors pas instantanément à un changement local de cisaillement, et nécessite un temps T_{sat} et/ou une longueur L_{sat} afin de relaxer vers sa valeur saturée (Bagnold 1941, Sauermann *et al.* 2001, Andreotti *et al.* 2002b, Charru 2006, Claudin & Andreotti 2006, Pähtz *et al.* 2013a). En pratique, le flux n'est néanmoins jamais loin de sa valeur saturée, et ce processus peut être modélisé par une équation de relaxation de premier ordre (Andreotti *et al.* 2002a;b) :

$$T_{\mathrm{sat}} \frac{\partial q}{\partial t} + L_{\mathrm{sat}} \frac{\partial q}{\partial x} = q_{\mathrm{sat}} - q. \tag{1.21}$$

Ce temps de saturation, de l'ordre de 1 s dans le cas éolien, est très faible devant les échelles de temps géomorphologiques d'évolution de la topographie ($\sim 10^5$ s). Il peut alors

être négligé, tandis que l'hydrodynamique et le transport de sédiments peuvent être étudiés en considérant la topographie comme fixe (Fourrière *et al.* 2010, Durán *et al.* 2011, Charru *et al.* 2013).

Mesure expérimentale

Ce phénomène de saturation est observé expérimentalement, ce qui permet une mesure directe la longueur associée. Considérons cette fois un lit plat de sédiments, précédé en amont d'un lit non-érodable, mais de rugosité géométrique similaire. Lorsque le vent souffle, le flux de sable associé est nul sur cette partie amont, et atteint sa valeur saturée un peu plus loin en aval.

Sur la figure 1.8(a), les profils de flux mesurés par Andreotti *et al.* (2010) montrent que, au voisinage de la saturation, le flux relaxe exponentiellement vers sa valeur saturée, en accord avec (1.21). Il s'agit néanmoins de distinguer la longueur de saturation de la longueur $L_{1/4}$, nécessaire à l'établissement de la saltation. Par conséquence, au tout début du lit érodable, le flux augmente exponentiellement avec la distance, alors qu'il se charge progressivement en particules, chaque grain en éjectant plusieurs autres par choc avec le lit. Cette augmentation exponentielle n'est plus présente sur le profil avec flux d'entrée, la saltation y étant déjà établie (figure 1.8(a)).

De plus, la longueur $L_{1/4}$ associée au début de la saltation diminue fortement avec u_*, traduisant l'augmentation de l'efficacité des chocs à éjecter un plus grand nombre de particules (voir figure 1.8(b)). En revanche, le voisinage de la relaxation vers la valeur saturée semble remarquablement indépendant de la vitesse du vent, bien qu'une dépendance en cette dernière soit prédite par Pähtz *et al.* (2013a).

La relaxation du flux est alors limitée dans un premier temps par l'érosion, puis rapidement par l'inertie des grains. En supposant que les grains sont accélérés à la vitesse du vent par une force de traînée turbulente, la longueur de saturation dépend alors de la longueur d'inertie correspondante :

$$L_{\mathrm{sat}} \sim \frac{\rho_s}{C_\infty \rho_f} d, \tag{1.22}$$

avec un préfacteur de l'ordre de 2 (Andreotti *et al.* 2002b, Andreotti 2004).

1.3 Instabilité et émergence des dunes

Les dunes, et de manière plus générale les motifs sédimentaires, sont omniprésents sur Terre dès lors que des sédiments sont transportés par un écoulement. Des ondulations typiques apparaissent alors à la surface du lit de sédiments, dont les crêtes transverses à l'écoulement définissent une longueur d'onde bien caractéristique (figure 1.9(a)). Forte-

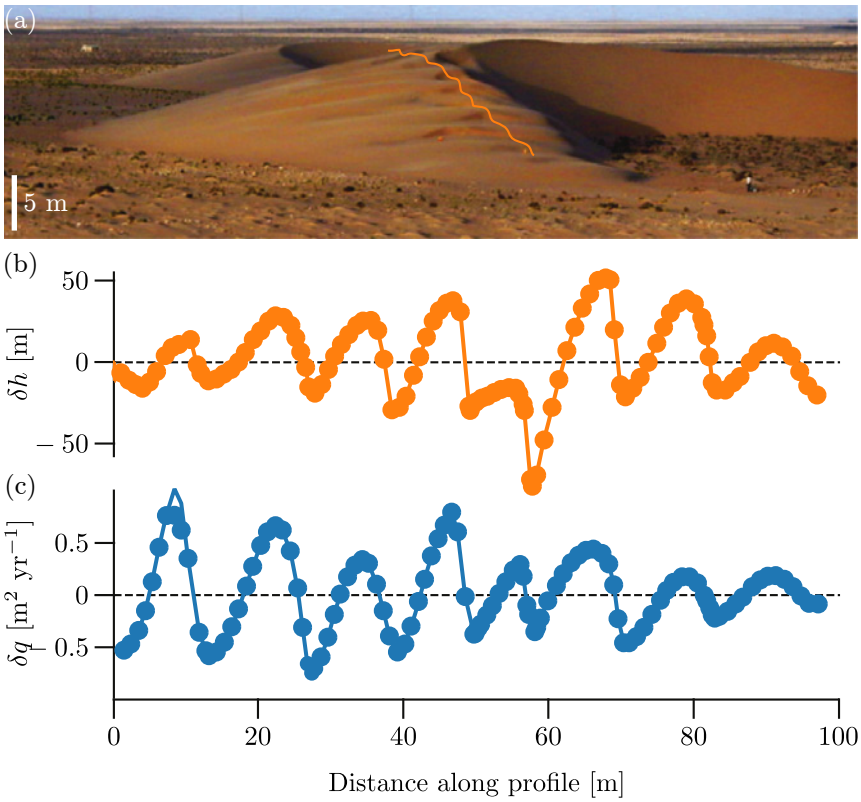

FIGURE 1.9 – (a) Oscillation de sable sur la corne d'une barkhane. La ligne orange correspond au profil des mesures de topographie (b) et de flux (c). La modulation du flux δq est calculée via le taux d'érosion en utilisant la conservation de la masse. Figure modifiée de Elbelrhiti *et al.* (2005).

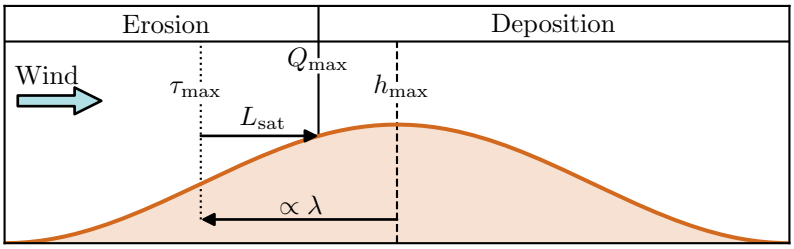

FIGURE 1.10 – Schéma résumant les mécanismes à l'origine de la naissance des dunes.

ment étudiées, ces ondes de surface sont maintenant interprétées comme provenant d'une instabilité linéaire, que ce soit en milieu aquatique laminaire (Charru & Hinch 2000, Lagrée 2003, Valance & Langlois 2005, Charru 2006, Devauchelle *et al.* 2010), turbulent (Kennedy 1963, Richards 1980, Colombini 2004, Fourrière *et al.* 2010, Colombini & Stocchino 2011, Andreotti *et al.* 2012a), ou en milieu éolien (Andreotti *et al.* 2002b, Elbelrhiti *et al.* 2005, Kouakou & Lagrée 2005, Claudin & Andreotti 2006, Durán *et al.* 2019).

Autour d'une bosse de sable de faible amplitude, le cisaillement ainsi que le flux de sable ne sont plus constants (figure 1.9(b)). Le fluide accélère le long du côté amont, le flux de sable augmentant en conséquence, et inversement en aval. La position du maximum du flux de sable, séparant la zone d'érosion en amont de la zone de dépôt en aval, permet alors de déterminer si cette bosse croît ou décroît (Kennedy 1963).

De manière générale, comme le montre le schéma en figure 1.10, le maximum de flux de sable n'est pas situé juste au niveau de la crête, mais légèrement en amont. Ce décalage est issu de deux contributions distinctes (Andreotti *et al.* 2002a, Kroy *et al.* 2002a, Fourrière *et al.* 2010, Claudin *et al.* 2013). Tout d'abord, un mécanisme hydrodynamique déstabilisant amène le maximum du cisaillement en amont de la crête, provenant du couplage entre inertie de l'écoulement et dissipation turbulente (Sykes 1980, Hunt *et al.* 1988b, Kroy *et al.* 2002b). Ensuite, la distance nécessaire au flux de sable pour s'adapter à un changement de cisaillement (voir section 1.2.4) implique un décalage stabilisant de son maximum, en aval de celui du cisaillement. L'équilibre entre ces deux mécanismes est alors à l'origine de la sélection en longueur d'onde des dunes naissantes.

Afin de pouvoir quantifier cet équilibre, il est tout d'abord nécessaire de caractériser plus en détail l'écoulement au-dessus d'une topographie de faible amplitude.

1.3.1 Écoulement au-dessus d'une faible topographie

Dans la section 1.2.1, nous avons détaillé les propriétés d'un écoulement turbulent sur un fond rugueux, plat et immobile. Dans des conditions naturelles, le fond n'est jamais parfaitement plat, ce qui donne lieu à d'importantes modifications (Pye & Tsoar 1990).

Dans les modélisations théoriques correspondantes, l'écoulement est alors divisé en plu-

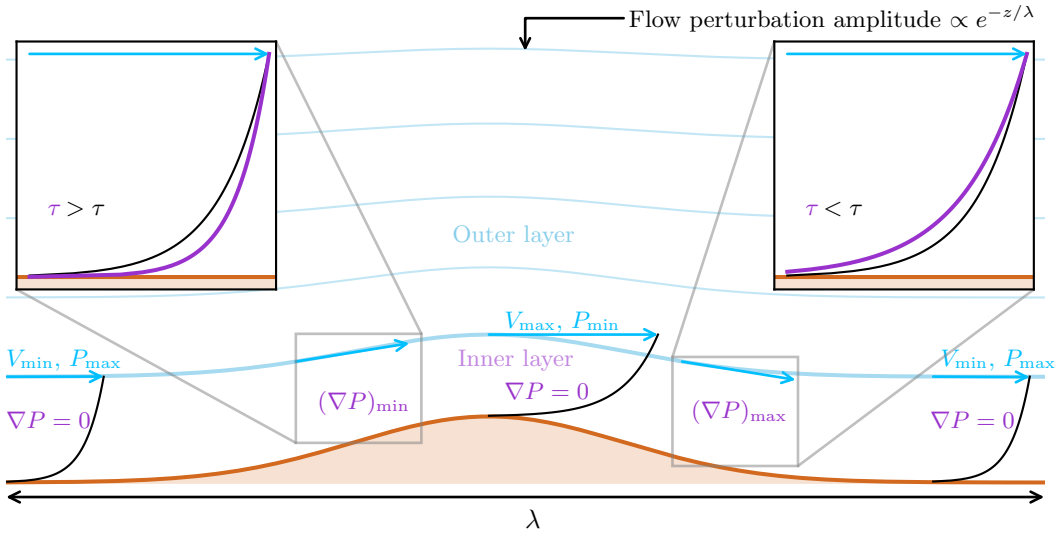

FIGURE 1.11 – Schéma représentant l'écoulement au-dessus d'une bosse de faible amplitude.

sieurs couches (Taylor & Gent 1974, Jackson & Hunt 1975, Hunt & Snyder 1980, Smedman & Bergström 1984, Zeman & Jensen 1987, Taylor *et al.* 1987, Hunt *et al.* 1988b;a). Comme sur un lit plat (section 1.2.1), il est forcé à son sommet par les vents géostrophiques de la couche supérieure, et s'annule à son pied dans une couche visqueuse très proche de la surface. Au milieu, il est perturbé par la présence de la topographie, et peut être divisé en deux : une couche externe, inertielle et contrebalancée par le gradient de pression, et une couche interne, dominée par la dissipation turbulente issue de sa proximité avec la surface rugueuse (figure 1.11).

Influence du gradient de pression sur le profil logarithmique

Dans la couche externe, suivant le théorème de Bernoulli, les lignes de courant se resserrent en haut de la bosse, traduisant une augmentation de la vitesse du fluide en phase avec la topographie (figure 1.11). Cette rétroaction de la topographie sur l'écoulement diminue ensuite verticalement comme l'exponentielle de la largeur de la bosse (voir aussi le calcul en appendice B.1).

Cette variation de vitesse et de pression le long de la bosse est transmise à la couche inférieure, dans laquelle le vent est alors contrôlé par deux mécanismes. Tout d'abord, la vitesse est contrainte de tendre vers 0 au voisinage de la surface, donnant lieu au profil logarithmique décrit en section 1.2.1. La variation de ce profil reste en phase avec la topographie, avec un cisaillement maximum au niveau du sommet de la bosse.

Ensuite, ce profil logarithmique est modifié par la présence du gradient longitudinal de pression hérité de la couche supérieure. Ce gradient, en quadrature de phase avec la topographie, est nul à la crête et maximum au milieu de la pente. Il déforme le profil

logarithmique en conséquence (figure 1.11), décalant ainsi le maximum du cisaillement légèrement en amont de la crête de la bosse [4] (voir figure 1.12(a)).

Cette théorie a été testée et validée par des simulations numériques, ainsi que des mesures de terrain (Sykes 1980, Britter *et al.* 1981, Mason & King 1985, Finnigan *et al.* 1990, Kim *et al.* 2000, Athanassiadou & Castro 2001, Cao *et al.* 2012, He *et al.* 2014). Elle a aussi été étendue pour des écoulements au-dessus de topographies en trois dimensions (Mason & Sykes 1979, Walmsley *et al.* 1982).

Mesures et modélisation

Dans la limite d'une topographie de faible amplitude, la cisaillement turbulent total peut alors s'écrire comme la somme du cisaillement constant sur lit plat τ_0, et d'une modulation issue de la topographie s'écrivant dans l'espace de Fourier :

$$\hat{\tau} = \tau_0 \left(\mathcal{A} + i\mathcal{B}\right) k\hat{h}, \tag{1.23}$$

où $\hat{\cdot}$ dénote la transformée de Fourier, k le nombre d'onde. Ici, $\mathcal{A}$ et $\mathcal{B}$ sont respectivement les composantes en phase et en quadrature de phase du cisaillement par rapport à la topographie.

La mesure et la modélisation des deux coefficients hydrodynamiques $\mathcal{A}$ et $\mathcal{B}$ ont fait l'objet de nombreuses études (Zilker *et al.* 1977, Frederick & Hanratty 1988, Finnigan *et al.* 1990, Poggi *et al.* 2007, Kroy *et al.* 2002b, Fourrière *et al.* 2010). Ils montrent notamment une dépendance de $\mathcal{A}$ et $\mathcal{B}$ dans la longueur d'onde du mode de Fourier correspondant (voir figure 1.12). Cette dépendance reste faible (logarithmique) dans le cas éolien, ce qui permet de les considérer comme constants. La seule mesure de terrain de ces coefficients, en présence de transport, a été réalisée par Claudin *et al.* (2013), et coïncide raisonnablement bien avec les mesures expérimentales et les prédictions issues des différents modèles théoriques, aboutissant à $\mathcal{A} \sim 3.5$ et $\mathcal{B} \sim 2$.

1.3.2 Analyse de stabilité linéaire

Ainsi, d'un côté, la position du maximum de cisaillement, situé en amont du maximum local de topographie ($\mathcal{B} > 0$ dans (1.23)), tend à faire croître les perturbations en déplaçant les zones de dépôt sur les crêtes. De l'autre, le processus de relaxation du flux vers sa valeur saturée agit de manière stabilisante en déplaçant la position de ces zones en aval, d'une distance égale à longueur de saturation L_{sat}.

4. Ce mécanisme est très semblable à celui du décollement d'une couche limite, visqueuse ou turbulente, amenant à la formation des boucles de recirculation.

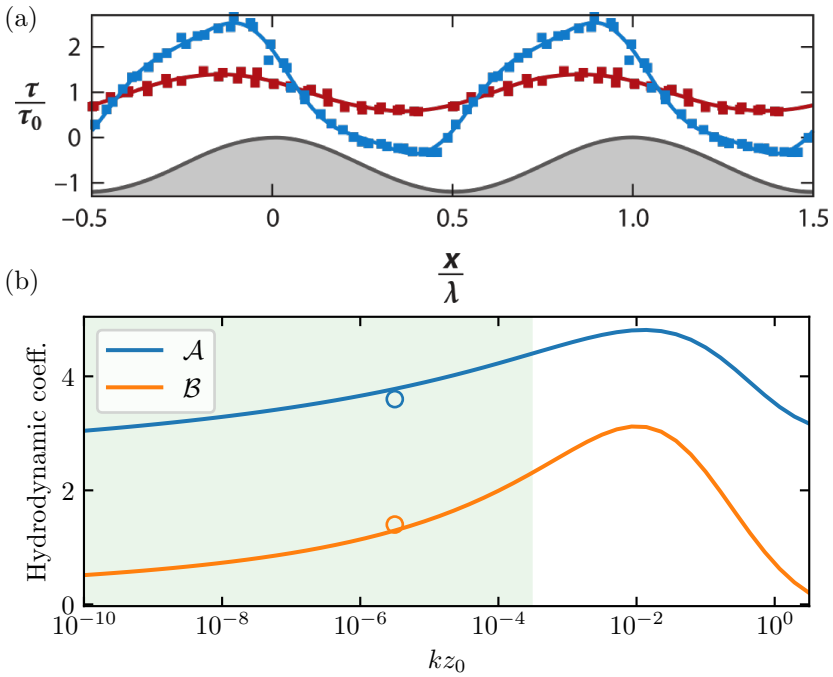

FIGURE 1.12 – (a) Mesure de cisaillement basal sur un lit ondulé lisse, pour $2h_0/\lambda = 0.0125$ (red squares) et 0.05 (blue squares), par Zilker *et al.* (1977). Adaptée de Charru *et al.* (2013). (b) Variation des coefficients hydrodynamiques $\mathcal{A}$ et $\mathcal{B}$ en fonction de kz_0. Lignes : calculs issus de Fourrière *et al.* (2010), avec une fermeture turbulente rugueuse. Ronds : mesures de Claudin *et al.* (2013) au-dessus d'une dune de faible amplitude et de 40 m de long. Zone verte : domaine concerné par les dunes éoliennes.

Relation de dispersion

Afin de formaliser cette discussion, nous réalisons dans un premier temps l'analyse de stabilité d'un lit plat infini de sédiments, à l'ordre linéaire. Le vent souffle au-dessus de manière homogène selon $\boldsymbol{e}_x$, induisant un cisaillement turbulent constant $\tau_0 = \rho_f u_*^2$ ainsi qu'un flux constant de sédiments.

Dans la réalité, le lit n'est jamais parfaitement plat, et la surface est composée d'une multitudes d'irrégularités de faibles amplitudes, conduisant à de faibles perturbations de l'écoulement et du flux. Le système sort alors de l'équilibre précédemment décrit, et son évolution est décrite par les équations liant :

- le cisaillement à la topographie (modulation du cisaillement (1.23)),
- le flux de sable saturé au cisaillement (loi de transport (1.19)),
- le flux de sable à sa valeur saturée (relaxation du flux (1.21)).

Ce système est clos par le lien entre l'évolution de la topographie et le flux de sable, donné par l'équation de conservation de la masse [5] :

$$\frac{\partial h}{\partial t} = -\frac{\partial q}{\partial x}. \tag{1.24}$$

Ces perturbations peuvent se décomposer en une multitude de sinusoïdes de longueurs d'ondes λ, se propageant chacune à une vitesse $c(\lambda)$ tout en croissant à un taux $\sigma(\lambda)$. À l'ordre linéaire, elles n'interagissent pas entre elles, et nous pouvons alors étudier séparément l'évolution de chaque mode :

$$h = h_0 e^{i(kx-\omega t)}, \tag{1.25}$$

où $k = 2\pi/\lambda$ est le nombre d'onde, et ω la pulsation telle que $c = \mathrm{Re}(\omega)$ et $\sigma = \mathrm{Im}(\omega)$. On en déduit la relation de dispersion suivante (Andreotti *et al.* 2002b, Elbelrhiti *et al.* 2005, Fourrière *et al.* 2010) :

$$\omega = \frac{Q}{L_{\mathrm{sat}}^2} \frac{(kL_{\mathrm{sat}})^2}{1 + i(kL_{\mathrm{sat}})^2} \left(\mathcal{A} + i\mathcal{B}_\mu\right), \tag{1.26}$$

où $Q = \Omega\tau_0$ est un flux de sable caractéristique, et

$$\mathcal{B}_\mu = \mathcal{B} - \frac{1}{\mu}\left(\frac{u_{th}}{u_*}\right)^2. \tag{1.27}$$

Apparaissent ainsi dans l'équation (1.26) un temps et une longueur caractéristique, respectivement L_{sat}^2/Q et L_{sat}, que nous utilisons dès maintenant pour rendre nos équations

5. Dans ce contexte, cette équation est aussi appelée équation d'Exner.

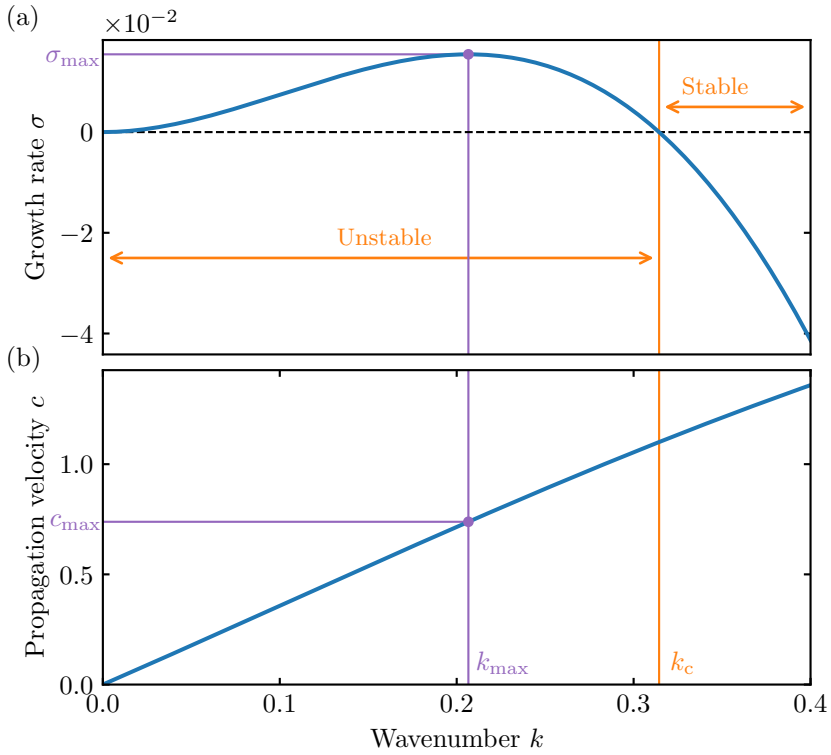

FIGURE 1.13 – Taux de croissance et vitesse de propagation sans dimension correspondant à l'équation (1.29), pour $\mathcal{A} = 3.5$, $\mathcal{B} = 2$ et $\mu = \tan(35°)$. Le mode le plus instable se trouve en $k_{\max} = 0.207$, ce qui correspond pour $L_{\text{sat}} \simeq 0.7$ m à $\lambda \simeq 20$ m.

sans dimension. Le taux de croissance et la vitesse du mode k s'écrivent alors :

$$\sigma = \text{Im}(\omega) = \frac{k^2}{1+k^2}\left(\mathcal{B}_\mu - \mathcal{A}k\right), \tag{1.28}$$

$$c = \text{Re}(\omega) = \frac{k}{1+k^2}\left(\mathcal{A} + \mathcal{B}_\mu k\right). \tag{1.29}$$

Mode émergent

Ces deux quantités sont tracées en figure 1.13. Les valeurs de k pour lesquelles le taux de croissance est négatif sont les modes stables du système ; les valeurs positives, quant à elles, sont les modes instables pouvant croître au cours du temps. Le mode marginal k_c, pour lequel $\sigma = 0$, délimite alors le domaine de stabilité. Il correspond à la taille minimale des dunes, en dessous de laquelle une bosse de sable est vouée à disparaître (Hersen *et al.* 2002, Parteli *et al.* 2007).

À l'intérieur de cette bande des modes instables, le taux de croissance possède un unique maximum correspondant au mode le plus instable $k_{\max}$. En négligeant la dépendance des coefficients $\mathcal{A}$ et $\mathcal{B}$ dans la longueur d'onde, on obtient dans la limite où $k \ll 1$ (toujours vérifiée dans le cas de l'émergence des dunes éoliennes) $k_{\max} \sim (2/3)k_c$, avec $k_c = \mathcal{B}_\mu/\mathcal{A}$. La

longueur d'onde la plus instable s'écrit alors sous forme dimensionnelle comme :

$$\lambda_{\max} \sim \frac{3\pi\mathcal{A}}{\mathcal{B} - \frac{1}{\mu}\left(\frac{u_{th}}{u_*}\right)^2} L_{\text{sat}}. \tag{1.30}$$

Elle correspond à celle des dunes émergentes, de l'ordre de 15 – 20 m pour des grains de diamètre $d \sim 200$ μm. Les coefficients $\mathcal{A}$ et $\mathcal{B}$ étant ici supposés constants, elle dépend principalement de la longueur de saturation, et donc des propriétés des grains et du fluide. Cette loi d'échelle est bien vérifiée à travers les différents environnements dans lesquels peut se développer cette instabilité, comme les dunes de neige, sous l'eau ou sur d'autres planètes (Claudin & Andreotti 2006). Enfin, cette longueur d'onde dépend aussi de la distance au seuil de transport, et augmente lorsque l'on se rapproche de celui-ci. Nous vérifierons expérimentalement cette propriété en section 3.4. De la même manière, le taux de croissance et la vitesse du mode le plus instable s'écrivent :

$$c(\lambda_{\max}) \sim \frac{Q_{\text{sat}}}{L_{\text{sat}}}\mathcal{A}\frac{2\pi L_{\text{sat}}}{\lambda_{\max}}, \tag{1.31}$$

$$\sigma(\lambda_{\max}) \sim \frac{Q_{\text{sat}}}{L_{\text{sat}}^2}\frac{\mathcal{A}}{2}\left(\frac{2\pi L_{\text{sat}}}{\lambda_{\max}}\right)^3. \tag{1.32}$$

La vérification directe de cette théorie reste difficile. La longueur de saturation comme les coefficients hydrodynamiques ont été mesurés de manière indépendante (Andreotti *et al.* 2010, Claudin *et al.* 2013, Selmani *et al.* 2018). En revanche, il est compliqué de suivre de manière continue l'évolution de topographies de faibles amplitudes sur le temps caractéristique du régime linéaire, de l'ordre de quelques mois. Ainsi, seule l'étude de Elbelrhiti *et al.* (2005) propose une validation en conditions éoliennes des prédictions de l'analyse de stabilité linaire, et seulement pour la longueur d'onde et la vitesse de migration.

1.3.3 Fin du régime linéaire

Le régime linéaire de la croissance dunaire, caractérisé par une croissance exponentielle à longueur d'onde constante, ne reste présent que tant que le rapport d'aspect reste assez faible ($k_{\max}h \ll 1$). Lorsque ce dernier atteint environ 1/13, l'hydrodynamique commence à répondre non-linéairement à la perturbation (carrés bleus sur la figure 1.12(a)), avec la formation d'une boucle de recirculation en aval de la crête (Fourrière *et al.* 2010). Le cisaillement y diminue drastiquement, devenant inférieur à la valeur seuil. Le transport s'arrête, alors qu'il continue en amont, conduisant progressivement à l'apparition d'un profil dunaire asymétrique. Le rapport d'aspect en aval de la dune augmente, jusqu'à l'apparition d'une face d'avalanche.

Parallèlement à la formation de la face d'avalanche, l'apparition de la boucle de recirculation impacte aussi directement la croissance de la dune. Elle entraîne une diminution

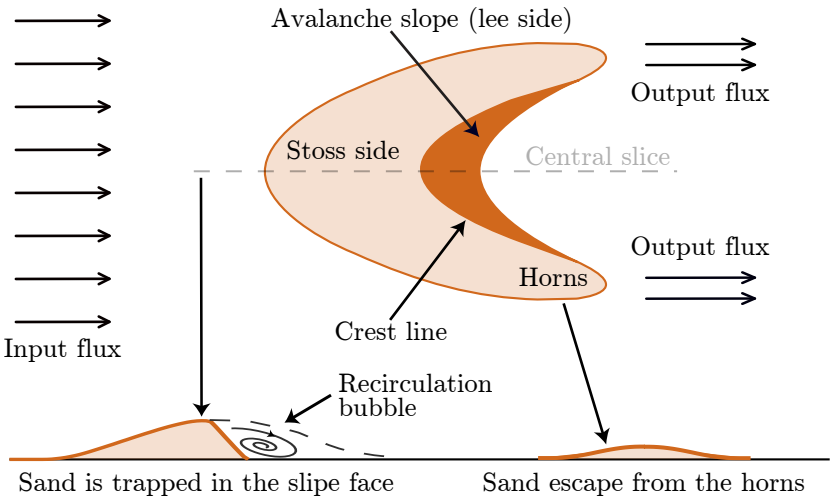

FIGURE 1.14 – Schéma d'une barkhane inspiré de Hersen (2004b) et Courrech du Pont (2015).

progressive du coefficient hydrodynamique $\mathcal{B}$, responsable du décalage en amont du maximum de cisaillement, impliquant une diminution du taux de croissance. L'amplitude croît alors linéairement en fonction du temps (Fourrière *et al.* 2010, Courrech du Pont *et al.* 2014, Ping *et al.* 2014). Elle finit néanmoins par saturer lorsque le déphasage entre la crête de la dune et le maximum du flux devient nul, tandis que la dune atteint sa forme d'équilibre caractérisée par un rapport d'aspect d'environ 1/12 (Baddock *et al.* 2007, Parteli *et al.* 2006).

1.4 Évolution sous un vent unidirectionnel

La description sous forme d'instabilité de la morphodynamique dunaire n'est valable que pour l'émergence des dunes à partir d'un lit de sable. Elle ne convient ainsi pas à la description de dunes matures, dont l'évolution repose sur de nombreux processus non-linéaires. Dans cette section, nous présentons les processus gouvernant la dynamique des deux motifs apparaissant sous un régime de vent unidirectionnel, les barkhanes et les dunes transverses.

1.4.1 Barkhanes

Les barkhanes sont les dunes les plus étudiées (Howard *et al.* 1978, Hersen *et al.* 2002, Andreotti *et al.* 2002a, Momiji *et al.* 2002, Sauermann *et al.* 2003, Hersen 2004b, Hersen & Douady 2005, Schwämmle & Herrmann 2005, Katsuki *et al.* 2005, Franklin & Charru 2011, Alvarez & Franklin 2019, Khosronejad & Sotiropoulos 2017). Se formant sous un vent unidirectionnel dans des conditions de faible disponibilité sédimentaire, elles migrent sur un sol non-érodable en prenant la forme caractéristique d'un croissant (Hersen 2004b).

Comme le montre la figure 1.14, vues de dessus, elles possèdent une face amont convexe de faible pente, suivie après la crête par une phase d'avalanche. De part et d'autre de cette dernière, deux cornes pointent vers l'aval. Leur section centrale est alors asymétrique. Elles sont issues de patchs de sable se trouvant sur un sol non-érodable, pourvu que ce dernier soit plus grand que la taille minimale des dunes, sans quoi il est voué à disparaître (Hersen *et al.* 2002, Andreotti *et al.* 2002b, Parteli *et al.* 2007). Ces patchs peuvent être issus de l'accumulation du sable à certains endroits (rugosité, végétation ...) (Baddock *et al.* 2018), ou venir d'une partie d'une dune plus grande ayant cassé (extrémité des cornes d'une barkhane plus grande ou d'une dune linéaire par exemple). Elles peuvent aussi venir de la déstabilisation de dunes transverses suivant un mécanisme décrit dans la section suivante (voir 1.4.2).

On trouve sur Terre des barkhanes de toutes tailles, dont les hauteurs varient de 1 m à 50 m pour des longueurs (du bas de la face amont jusqu'au bas de la face d'avalanche) et largeurs (distance entre les cornes) variant de 10 m à 500 m (Courrech du Pont 2015). Même si les barkhanes ne sont pas totalement des objets auto-similaires, leurs dimensions sont néanmoins linéairement corrélées lorsqu'elles sont assez grosses (Hesp & Hastings 1998, Elbelrhiti *et al.* 2008). La hauteur tend néanmoins vers 0 pour des longueurs non nulles approchant la taille minimale contrôlée par la longueur de saturation (voir section 1.3). Leur rapport d'aspect correspond à celui sélectionné par les non-linéarités de l'hydrodynamique (voir section 1.3.3), et varie typiquement entre 0.1 et 0.15, augmentant légèrement avec la taille de la barkhane (Hesp & Hastings 1998, Andreotti *et al.* 2002b), ainsi qu'avec la vitesse du vent (Groh *et al.* 2008, Zhang *et al.* 2010).

Stabilité

Presque tout le sable transporté le long de la face amont est capté par la phase d'avalanche, qui agit comme un piège à sédiments. Du sable est néanmoins perdu à l'extrémité des cornes, dont le faible rapport d'aspect les fait se comporter comme un lit plat et non comme un piège à sédiments (figure 1.14). Les barkhanes nécessitent alors un flux d'entrée arrivant sur la face amont afin de se propager tout en gardant la même taille (Tsoar 2001). Cette équilibre entre flux d'entrée et pertes par les cornes reste instable. En effet, comme le montre la figure 1.15, ces deux flux dépendent de la taille de la barkhane, mais le flux de sortie augmente moins vite que celui d'entrée en fonction de cette dernière (Hersen *et al.* 2004).

En partant d'un objet à l'équilibre, une légère augmentation du flux d'entrée entraîne alors une augmentation de la taille de la barkhane. Cette augmentation en taille entraîne à son tour une augmentation du flux d'entrée qui n'est pas assez compensée par l'augmentation du flux de sortie, et la barkhane continue de grossir. Le processus est inverse pour une diminution du flux d'entrée, et la taille d'équilibre de la barkhane est ainsi un état

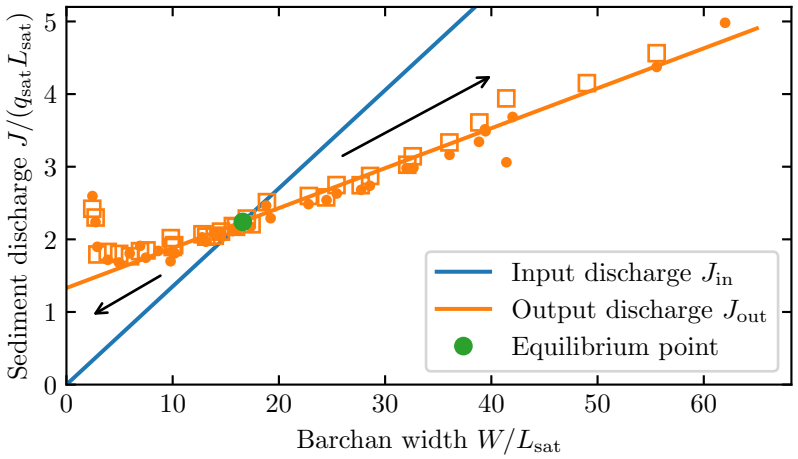

FIGURE 1.15 – Estimation numérique du débit de sédiments J_{out} perdu en sortie de la barkhane en fonction de sa largeur. Les points correspondent à des mesures en condition bouclées (le sable perdu est re-injecté en amont), et les carrés à des mesures faites pour un débit de sédiments J_{in} nul en entrée. Figure adaptée de Hersen (2004a).

instable (Hersen *et al.* 2004).

Par la suite, nous présentons les lois gouvernant leur migration et leur croissance à l'aide d'une approche dimensionnelle.

Flux de sable

Considérons une barkhane en deux dimensions (la tranche passant par le milieu de la crête), de hauteur H et de longueur L, possédant une pente d'avalanche sur son coté aval. Lorsque le vent arrive à l'encontre de la dune, il accélère jusqu'à la crête, transportant de plus de plus de sable, qu'il va ensuite déposer dans la phase d'avalanche. Cette accélération était déjà présente dans la phase linéaire de la croissance, à la fois dans la couche interne et externe, où elle diminue exponentiellement (voir figure 1.11). Elle dépend principalement de la forme de la dune, mais aussi d'autres paramètres tels que la rugosité, ou la hauteur de la couche convective atmosphérique (Jackson & Hunt 1975, Mason & Sykes 1979, Britter *et al.* 1981, Hunt *et al.* 1988b). Néanmoins, au premier ordre, l'accroissement relatif de la vitesse entre le bas et la crête de la dune est proportionnel au rapport d'aspect H/L de la dune. Dans le cas des barkhanes, qui ont un rapport d'aspect d'environ 1/10, il prend ainsi des valeurs comprises entre 1 et 2 (Britter *et al.* 1981, Wiggs *et al.* 1996, Lancaster *et al.* 1996, Neuman *et al.* 1997, Walker & Nickling 2003, Elbelrhiti *et al.* 2005, Baddock *et al.* 2007, Wu *et al.* 2011, Claudin *et al.* 2013).

Le flux de sable, dépendant directement du cisaillement en un point donné, varie en conséquence (voir figure 1.16). Au premier ordre en rapport d'aspect, le flux de sable

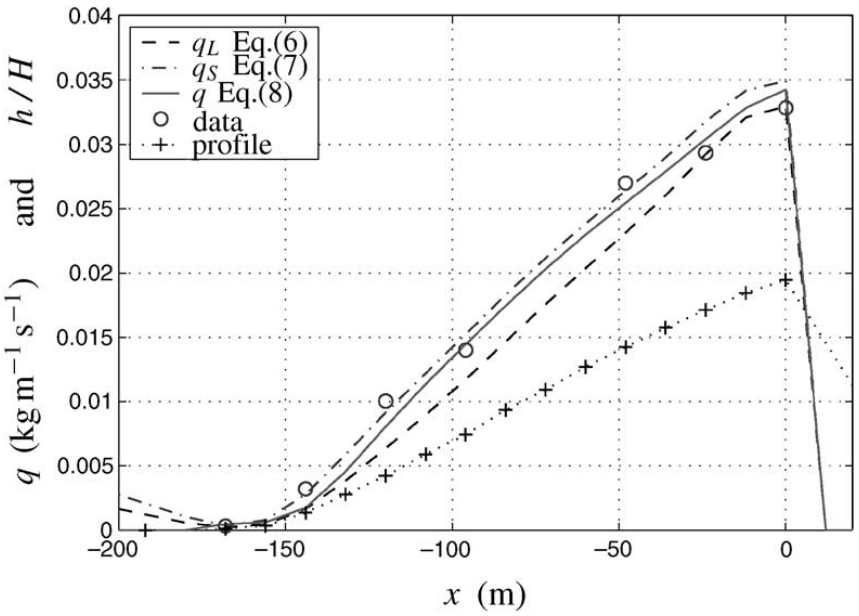

FIGURE 1.16 – Flux le long de la section centrale d'une barkhane. Les prédictions théoriques sont faites à partir de mesures de vitesse du vent en utilisant les formules de flux saturé de Lettau & Lettau (1978) (q_L) et Sørensen (1991) (q_S). La ligne pleine q prend en compte la relaxation spatiale du flux, avec la longueur de saturation. Figure provenant de Sauermann *et al.* (2003).

maximum s'écrit alors :

$$Q_{\text{crest}} = Q_0 \left(1 + \beta \frac{H}{L}\right), \tag{1.33}$$

où β est un coefficient prenant en compte la rétroaction de la topographie sur le flux (Courrech du Pont *et al.* 2014, Gao *et al.* 2015b, Courrech du Pont 2015).

Vitesse de propagation

Dimensionnellement, la vitesse de propagation de la dune peut s'écrire comme :

$$c = Q_{\text{crest}}/H. \tag{1.34}$$

En utilisant l'équation (1.33), cette relation peut aussi s'écrire :

$$c = (1 + \gamma)\, \frac{Q_0}{H}, \tag{1.35}$$

ce qui correspond à la loi de Bagnold (Bagnold 1941). En comparant cette loi à des données sur la migration de barkhanes, on trouve $\gamma = \beta H/L \simeq 1.7$ (voir figure 1.17). De plus, on s'attend à ce que cette vitesse corresponde, dans la limite des dunes de très faibles amplitudes, à la vitesse de propagation $c(\lambda_{\max})$ (1.31) des ondes de surface issues de l'instabilité décrite dans la section précédente. Cela conduit à modifier la loi de Bagnold

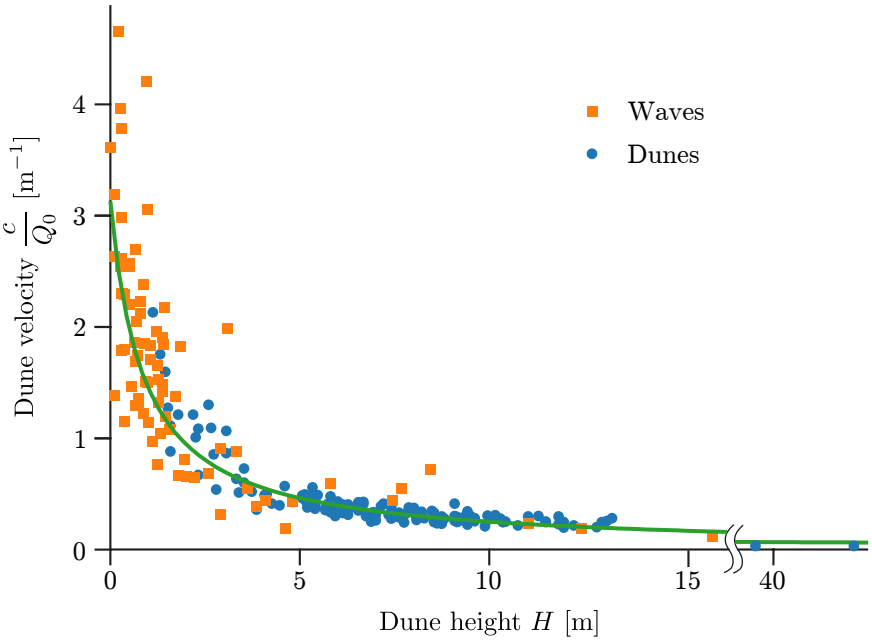

FIGURE 1.17 – Comparaison des vitesses de migration des dunes et des ondes de surface. La ligne verte correspond à l'équation (1.36) avec $\gamma = 1.7$ et $H_0 = 87$ cm. Figure modifiée de Elbelrhiti *et al.* (2008).

(Elbelrhiti *et al.* 2005; 2008) :

$$c = (1+\gamma)\,\frac{Q_0}{H+H_0}, \tag{1.36}$$

avec

$$H_0 = \frac{(1+\gamma)\,L_{\text{sat}}}{\mathcal{A}}\left(\frac{\lambda_{\max}}{2\pi L_{\text{sat}}}\right) \simeq 1.5 \text{ m}, \tag{1.37}$$

en accord avec les données de Elbelrhiti *et al.* (2008) présentées en figure 1.17. De plus, le rapport d'aspect $H_0/\lambda_{\max} \simeq 0.08$ concorde aussi avec celui correspondant à la sortie du régime linéaire des dunes naissantes (voir section 1.3.3).

Taux de croissance

Le taux de croissance s'écrit de manière dimensionnelle comme :

$$\sigma = \frac{1}{H}\frac{\Delta H}{\Delta T}, \tag{1.38}$$

où, le symbole Δ dénote une variation à l'échelle de la dune. La variation temporelle de la hauteur peut s'exprimer à l'aide de la conservation de la masse (Courrech du Pont *et al.* 2014) :

$$\frac{\Delta H}{\Delta T} = -\frac{\Delta Q}{\Delta x} \approx \frac{Q_{\text{crest}} - Q_{\text{bottom}}}{L}. \tag{1.39}$$

Le flux de sable étant presque entièrement capté par la phase d'avalanche, on considère ici qu'il est nul en bas de la dune (Courrech du Pont *et al.* 2014). Le taux de croissance

obtenu est alors :

$$\sigma = (1+\gamma)\,\frac{Q_0}{HL}. \tag{1.40}$$

De la même manière que pour la vitesse, il peut être modifié afin de retrouver le taux de croissance des ondes de surface $\sigma(\lambda_{\max})$ (équation (1.32)). On trouve ainsi :

$$\sigma = (1+\gamma)\,\frac{Q_0}{HL+S_0}, \tag{1.41}$$

où

$$S_0 = \frac{2\,(1+\gamma)\,L_{\text{sat}}^2}{\mathcal{A}}\left(\frac{\lambda_{\max}}{2\pi L_{\text{sat}}}\right)^3 \simeq 25\ \text{m}^2. \tag{1.42}$$

En utilisant un rapport d'aspect typique de 1/10, cette section de coupure correspond à une hauteur de 1.5 m, en accord avec la valeur trouvée à partir des mesures de vitesse. Néanmoins, contrairement à ces dernières, qui peuvent se faire par le biais d'images satellites, la mesure du taux de croissance nécessite un suivi de la topographie sur une longue période de temps (plusieurs années). Ainsi, cette relation n'a jamais été testée à notre connaissance, et la valeur de S_0 jamais mesurée à ce jour.

Dynamique des champs de barkhanes

L'existence même des barkhanes est contradictoire avec le fait qu'elles soient des objets instables. Néanmoins, on les trouve souvent regroupées en champs de dunes. On y observe notamment une sélection en taille, ainsi qu'une organisation typique en couloir, bien que les conditions aux limites ne diffèrent pas à travers le champ (Elbelrhiti *et al.* 2008).

Deux mécanismes basés sur les interactions entre dunes peuvent alors réguler la taille des barkhanes. Tout d'abord, la différence de vitesse induite par la différence en taille entre les dunes induit des collisions. Cela peut entraîner la fusion de ces dunes, ou leur division en plusieurs autres petites dunes, suivant leurs tailles relatives et leur chevauchement latéral lors de la collision (Endo *et al.* 2004, Hersen & Douady 2005, Durán *et al.* 2009, Vermeesch 2011). Ensuite, lorsque les cornes des barkhanes sont assez longues devant la longueur d'onde du mode le plus instable de l'instabilité de lit plat, cette dernière peut s'y développer en tant que motif superposé. Sa croissance fait alors casser les cornes en de petites dunes de taille similaire à $\lambda_{\max}$.

Ces processus ont été implémentés dans des modèles numériques considérant la barkhane comme cellule élémentaire, qui permettent alors d'étudier l'organisation spatiale de ces champs de dunes (Durán *et al.* 2009, Génois *et al.* 2013a, Worman *et al.* 2013). Ces modèles arrivent à reproduire la sélection statistique en taille des barkhanes. En revanche, l'organisation de ces dunes en couloirs apparaît seulement de manière dynamique et transitoire, et uniquement lorsque les collisions produisent statistiquement un nombre croissant de dunes. Autrement, le champ de dunes atteint un état d'équilibre caractérisé par une

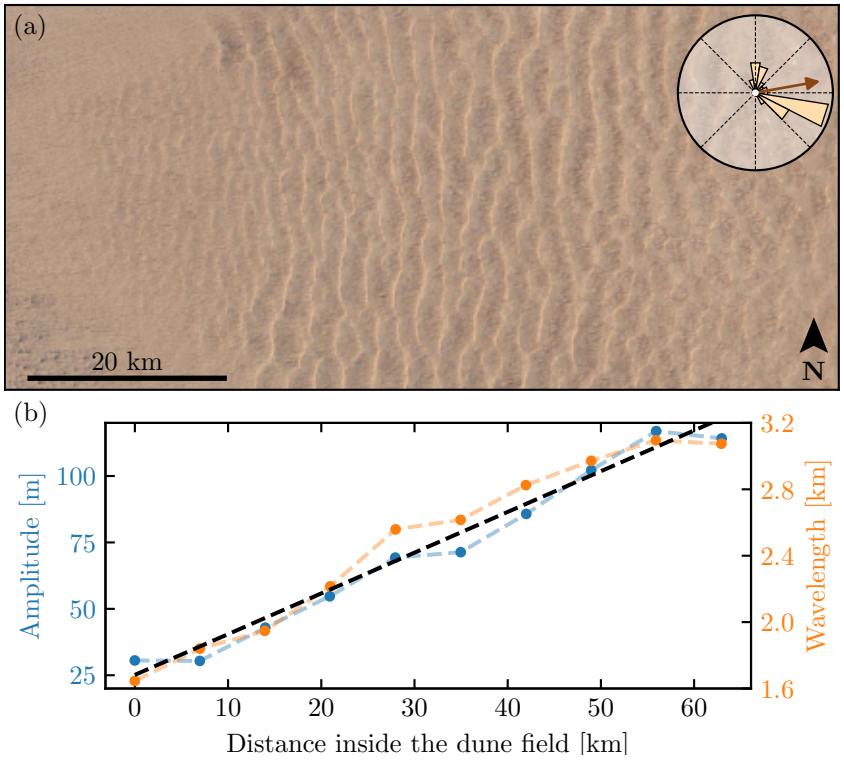

FIGURE 1.18 – (a) Champ de dunes transverses dans le désert du Rigestan, Afghanistan (30° 35′N, 65° 45′E). En haut à droite, la distribution angulaire des flux de sable sur lit plat est calculée à partir des données de vents à 10 m du modèle de réanalyse climatique Era5 (Hersbach *et al.* 2020), en supposant une taille de grain de 180 μm et une rugosité aérodynamique de 1 mm. La flèche marron donne la direction du flux résultant correspondant. Image satellite : Google^{TM}, CNES/Airbus. (b) Mesures de la longueur d'onde et de l'amplitude des dunes transverses dans le désert du Rigestan le long d'un profil allant d'est en ouest. Les deux semblent alors augmenter linéairement avec la distance (ligne noire pointillée). Données provenant de Gao *et al.* (2015a).

distribution stationnaire des tailles des dunes.

1.4.2 Dunes transverses

Contrairement aux barkhanes, les dunes transverses sont observées sous un vent unidirectionnel lorsque la disponibilité en sable est assez grande. Elles possèdent de longues crêtes, souvent sinueuses, qui sont perpendiculaires à la direction du vent. Comme les barkhanes, leur section est asymétrique, dotée d'une faible pente en amont terminée par une pente d'avalanche en aval. Elles ont aussi un rapport d'aspect similaire, augmentant avec la vitesse du vent (Gao *et al.* 2015a).

Maturation des motifs et augmentation de la longueur d'onde

Les crêtes, régulièrement espacées, forment un motif au caractère fortement périodique, résultant directement de l'évolution non-linéaire de l'instabilité décrite en section 1.3. Une

fois le rapport d'aspect d'équilibre atteint, on observe dans les expériences ou sur le terrain une augmentation de la longueur d'onde (Fourrière *et al.* 2010, Courrech du Pont *et al.* 2014, Gao *et al.* 2015a). En effet, au moment où l'amplitude sature à travers les non-linéarités hydrodynamiques (voir section 1.3.3), d'autres processus tels que les interactions entre dunes prennent le relais afin de faire mûrir le motif.

Dans les expériences subaquatiques, la longueur d'onde augmente logarithmiquement lorsque le nombre de Reynolds particulaire Re_p (dont l'échelle de longueur est la taille du grain) est faible, et linéairement lorsqu'il est grand, avec une transition autour de $Re_p \sim 4$ (Coleman & Melville 1994, Langlois & Valance 2007b, Fourrière *et al.* 2010, Courrech du Pont *et al.* 2014). Les dunes éoliennes se situent dans ce dernier cas (Durán *et al.* 2019), mais aucune expérience de terrain ne confirme à ce jour la linéarité de cette augmentation. Les simulations numériques de Gao *et al.* (2015a) montrent quant à elles une croissance en $t^{1/3}$. Comme le montre la figure 1.18, certaines études de terrain rapportent néanmoins une augmentation linéaire de la longueur d'onde à travers le champ de dunes (Ewing & Kocurek 2010, Gao *et al.* 2015a), comme le montre la figure 1.18. Évolutions spatiale et temporelle pouvant être équivalentes dans le cas d'une migration à vitesse constante, cela tend à confirmer les résultats des expériences subaquatiques.

La maturation des motifs dépend de nombreux facteurs non-linéaires et reste encore mal comprise. Sans autre contrainte, la longueur d'onde et l'amplitude peuvent continuer d'augmenter jusqu'à ce que des effets de surface libre interviennent (Zhang *et al.* 2010, Fourrière *et al.* 2010). Pour les dunes éoliennes, la taille géante est alors définie par la hauteur de la couche limite atmosphérique (Andreotti *et al.* 2009). Néanmoins, Gao *et al.* (2015a) ont montré que, pour des vents faibles, proches du seuil de transport, la croissance peut aussi s'arrêter avant la taille géante lorsque le cisaillement dans les creux tombe sous le seuil de transport. Enfin, ces deux mécanismes de saturation ne peuvent s'exprimer que si la disponibilité sédimentaire est assez grande.

Disponibilité en sable et instabilité transverse

Les dunes transverses possèdent rarement une crête parfaitement droite, mais souvent sinueuse. Cette propriété intrinsèque du système provient d'une instabilité secondaire se déclenchant lorsque la disponibilité en sable décroît (l'inter-dune commence à laisser apparaître le sol non-érodable). Les expériences de Reffet *et al.* (2010), suivies de simulations numériques (Parteli *et al.* 2011, Guignier *et al.* 2013) ont montré qu'une barre de sable migrant sur un sol non-érodable est instable. Elle devient de plus en plus sinueuse, jusqu'à casser en barkhanes (voir figure 1.19).

Cette instabilité repose sur deux mécanismes déstabilisants. D'une part, une perturbation en hauteur le long de la barre induit une différence de vitesse entre deux tranches adjacentes ($c \propto 1/H$, équation 1.36), modulant alors la barre en longueur. D'autre part,

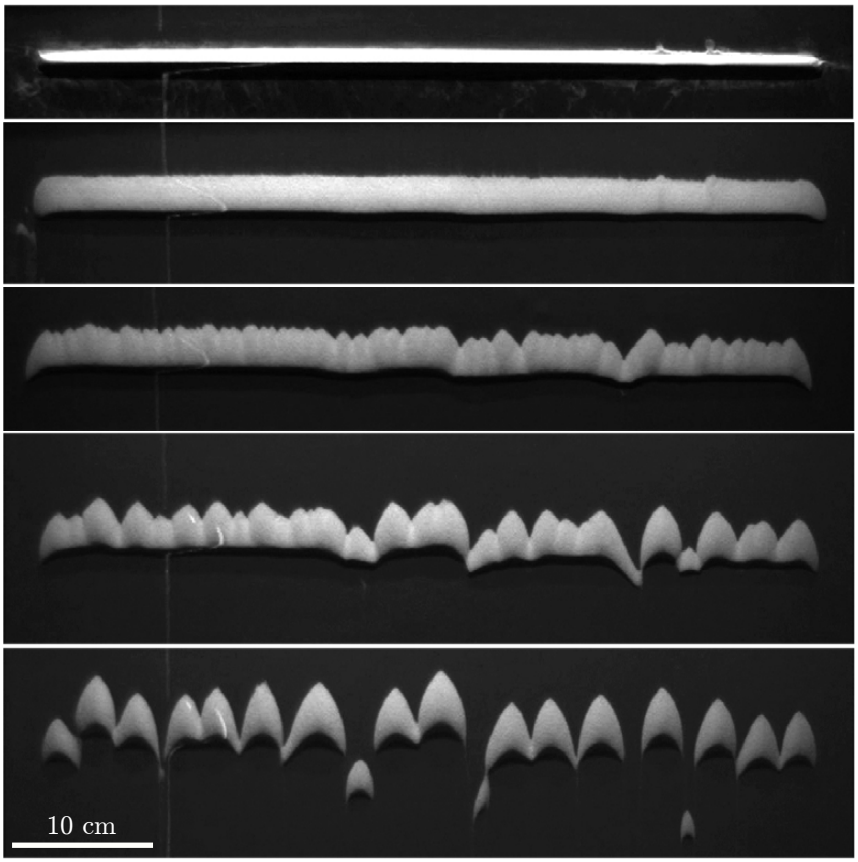

FIGURE 1.19 – Évolution d'une barre de sable sous un écoulement unidirectionnel (ici du haut vers le bas) dans une expérience subaquatique. Figure provenant de Courrech du Pont (2015).

dans la phase d'avalanche, le flux est redirigé vers le centre des zones concaves, soit depuis les tranches basses vers les tranches hautes (Melo *et al.* 2012). La perturbation initiale est alors amplifiée, jusqu'à ce que la barre casse en barkhanes, dont la taille est contrôlée par la hauteur initiale de la dune transverse (Reffet *et al.* 2010, Niiya & Nishimori 2010, Parteli *et al.* 2011, Guignier *et al.* 2013).

1.5 Régimes de vents multidirectionnels et orientation des dunes

1.5.1 Orientation des dunes

Sur Terre, les régimes de vents unidirectionnels (typiquement issus des vents alizés) ne concernent qu'une faible minorité des champs de dunes, souvent en bordure de mer où les variations climatiques restent faibles. Due au rythme des saisons, la majorité des mers de sable sont sujettes à des régimes bidirectionnels. De manière générale, différents régimes de vents peuvent produire différentes orientations de dunes. Traditionnellement, ces orientations sont mesurées par rapport à la direction du flux résultant (moyenne temporelle du *vecteur* flux de sable). Si l'écart entre les deux est plus que faible que 15°, l'orientation est dite longitudinale. Si au contraire, l'écart est supérieur à 75°, elle est transverse. Enfin, entre les deux, on parle de dunes obliques.

Sur un lit de sable meuble, les dunes croissent en hauteur, initiées par l'instabilité de lit plat décrite en section 1.3. Le motif reste alors périodique, avec des crêtes dont l'orientation et la longueur d'onde sont bien définies. Si cette dernière croît à travers de complexes mécanismes au cours du temps, l'orientation reste quant à elle relativement constante à travers toutes les échelles. Elle est de manière générale le plus perpendiculaire possible aux différentes directions que prend le transport au cours du temps (Rubin & Hunter 1987, Rubin & Ikeda 1990, Courrech du Pont *et al.* 2014). En revanche, si on laisse ces dunes croître jusqu'à ce que le socle apparaisse dans l'inter-dune, on observe deux procédés distincts suivant le régime de vent. Si le régime de vent est plutôt unidirectionnel, les crêtes vont se déstabiliser et casser en barkhanes comme décrit en section 1.4.2. Si le régime de vent est plutôt multidirectionnel, les crêtes se réorientent de manière à s'aligner un peu plus avec la direction du vent dominant (voir figure 1.20(a)). La différence entre l'orientation des dunes sur un lit non-érodable et sur un lit plat de sable est d'autant plus grande qu'une des directions du vent prévaut sur les autres en terme de transport (Courrech du Pont *et al.* 2014).

Une barre migrant sur un sol non-érodable sous un vent unidirectionnel est ainsi sujette à une instabilité la faisant casser une multitude de barkhanes. Néanmoins, de nombreuses observations de terrain rapportent l'existence de dunes linéaires s'étendant sur plusieurs

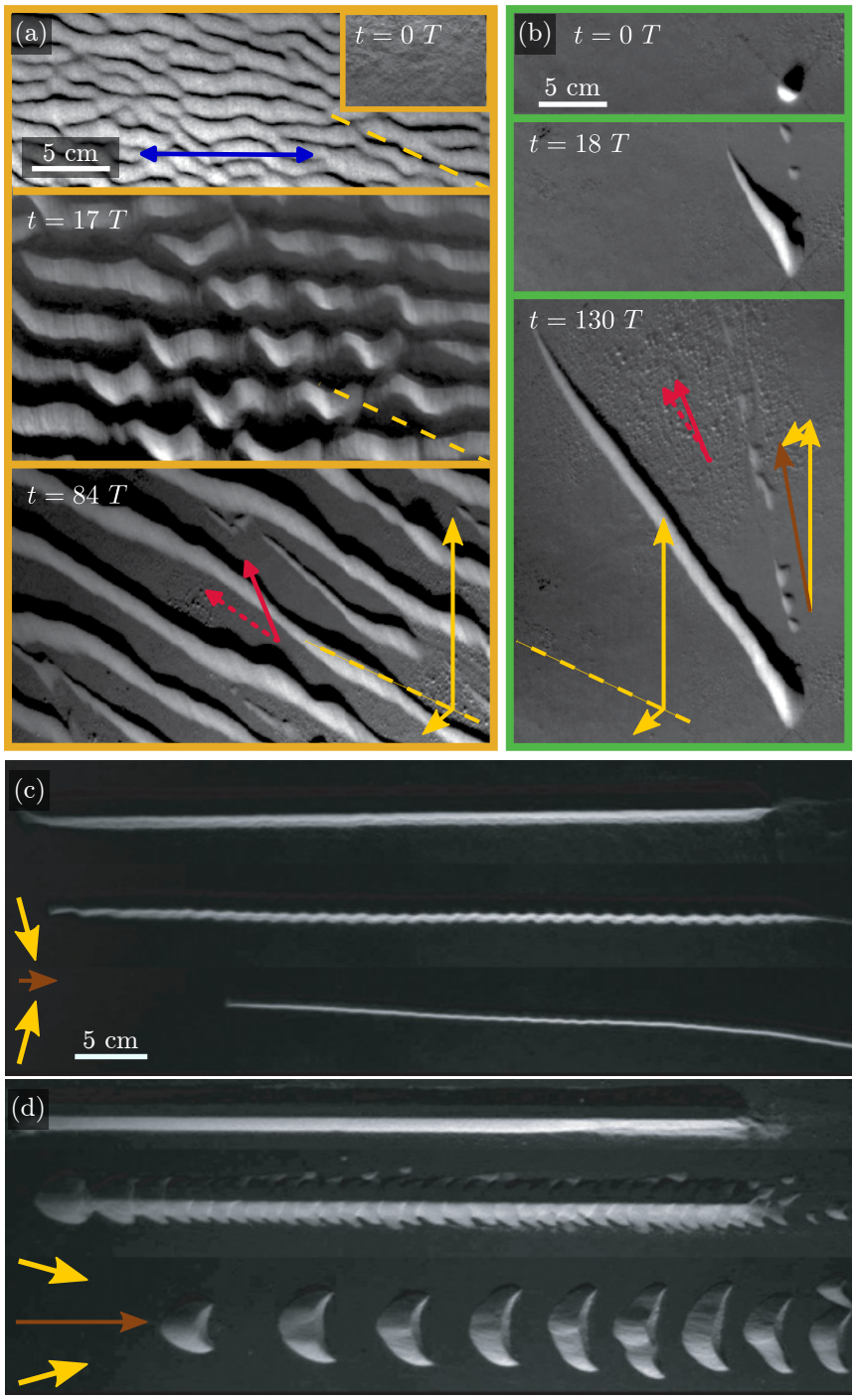

FIGURE 1.20 – Expériences subaquatiques sur l'orientation des dunes. (a) Croissance à partir d'un lit de sable de profondeur finie. Lorsque l'inter-dune touche le socle, l'orientation change. (b) Élongation à partir d'une source fixe de sable sur un socle non-érodable (figures issues de Courrech du Pont *et al.* (2014)). (c-d) Évolution d'une barre de sable sur un sol non-érodable dans un régime de vent bidirectionnel (figures issues de Reffet *et al.* (2010)). Le régime de vent est représenté par les flèches oranges. Dans (a-b), les directions sont séparées de 30°, et l'écoulement transporte en moyenne 5 fois plus dans la direction dominante que dans l'autre. Dans (c-d), les deux directions, séparées respectivement de 145° et 25°, transportent en moyenne autant l'une que l'autre. La ligne pointillée jaune donne la bissectrice, et la flèche marron le flux résultant sur lit plat. Les flèches rouges donnent les orientations prédites (lignes pleines) et mesurées (lignes pointillées) correspondant au mécanisme d'élongation. La bleue donne l'orientation correspondant à l'instabilité de lit plat (les orientations prédites et mesurées coïncident).

kilomètres sur un sol non-érodable (Lancaster 1982, Pye & Tsoar 1990, Lucas *et al.* 2014; 2015). Leur remarquable stabilité est alors due aux vents qui soufflent alternativement de part et d'autre de la crête (voir figure 1.20(c)).

Sous des régimes de vent similaires, des expériences et simulations numériques plus récentes ont alors montré qu'une dune pouvait s'allonger à partir d'une source fixe de sédiments dans la direction du flux résultant (voir figure 1.20(b)). Cette orientation peut aussi être interprétée comme la stabilisation de l'instabilité transverse décrite en section 1.4.2. Sous des vents multidirectionnels, il est possible de trouver une orientation telle que les flux perpendiculaires s'annulent, de sorte à empêcher la migration. Cette condition amène alors à la stabilisation de la barre de sable, et explique la transition en orientation entre les zones de croissance sur lit de sable et sur sol non-érodable (Reffet *et al.* 2010, Nakao-Kusune *et al.* 2020). Ceci a été confirmé par les expériences subaquatiques de Reffet *et al.* (2010), rajoutant que les directions des vents doivent être assez espacées (environ 90° ou plus).

La stabilité des dunes issues du mécanisme d'élongation reste un sujet ouvert. Les simulations numériques de Gao *et al.* (2015b) ont montré que deux transitions peuvent arriver. La première, liée à la disponibilité en sable, différencie les régimes où l'orientation est contrôlée par l'instabilité de lit des régimes dominés par l'élongation. La seconde, liée au régime de vent, est une transition morphologique entre dune linaire et barkhanes. Elle arrive lorsque les vents sont trop rapprochés, ou que l'un d'entre eux domine largement sur les autres. Dans ces cas-là, l'instabilité de lit plat se développe en tant que motif superposé à la dune linéaire, la faisant casser en une série de barkhanes (voir figure 1.20(d)) [6].

1.5.2 Un modèle pour l'orientation des dunes

Rubin & Hunter (1987), suivis de Courrech du Pont *et al.* (2014), ont développé un modèle pour prédire l'orientation des dunes sous des régimes de vents multidirectionnels, combinant le principe de l'analyse de stabilité linéaire avec une approche dimensionnelle.

Considérons une dune de longueur infinie, de largeur L et de longueur H fixées, dont la crête linéaire forme un angle α avec le vecteur unitaire $\boldsymbol{i}$ de la base orthonormée directe $(\boldsymbol{i}, \boldsymbol{j})$. Le vent souffle en alternant entre plusieurs directions, formant un cycle de durée totale T. La direction $\psi(t)$ et l'intensité du flux $Q_0(t)$ dépendent alors du temps.

En tenant compte du rapport d'aspect vu par le vent à un instant t, le flux à la crête peut être calculé de manière analogue à l'équation (1.33). Ainsi, la largeur de la dune vue par le vent étant $L(t) = L/|\sin(\psi(t) - \alpha)|$, le flux associé s'écrit :

$$\boldsymbol{Q}_{\text{crest}}(t) = Q_0(t)\left(1 + \beta\frac{H}{L}|\sin(\psi(t) - \alpha)|\right)(\cos\psi(t)\boldsymbol{i} + \sin\psi(t)\boldsymbol{j})\,. \tag{1.43}$$

6. Il ne faut pas confondre ce processus avec l'instabilité transverse, voir section 1.4.2.

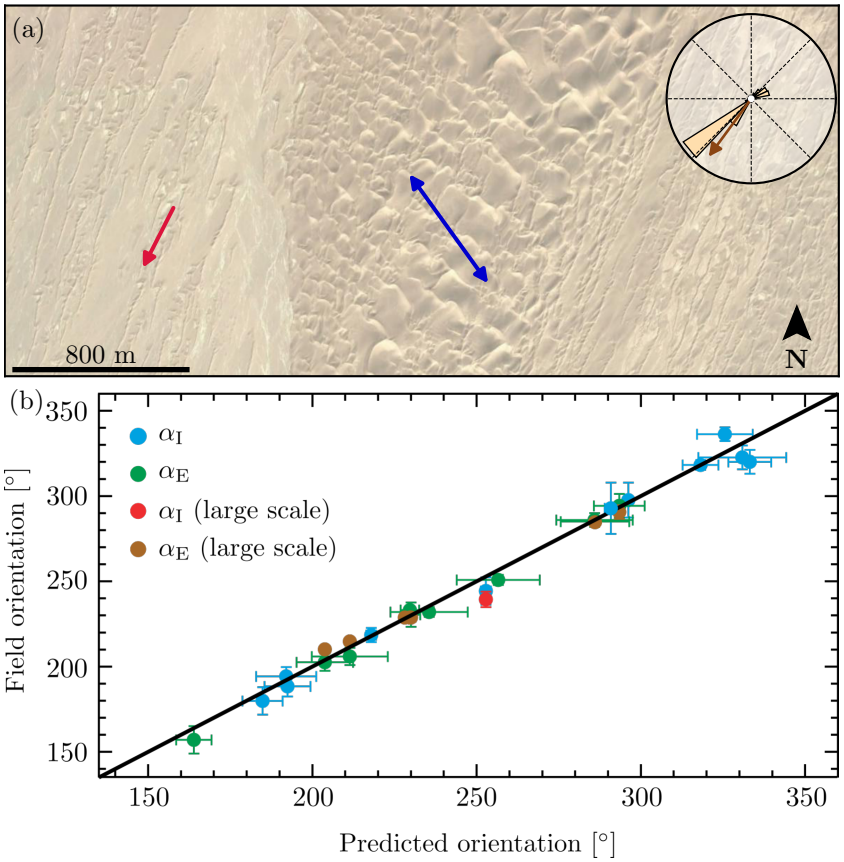

FIGURE 1.21 – (a) Coexistence de deux orientations distinctes dans le désert du Taklamacan en Chine (38.3°N, 86.7°E). Les orientations prédites par l'équation (1.46) pour le mécanisme d'élongation (rouge) et par l'équation (1.45) pour l'instabilité de lit (bleu) correspondent aux crêtes visibles sur l'image satellite (image satellite : Google^{TM}, Maxar technologies). En haut à droite, la distribution angulaire des flux de sable sur lit plat est calculée à partir des données de vents à 10 m du modèle de réanalyse climatique Era5 (Hersbach *et al.* 2020), en supposant une taille de grain de 180 μm et une rugosité aérodynamique de 1 mm. La flèche marron donne la direction du flux résultant correspondant. (b) Comparaison des orientations prédites par le modèle de Courrech du Pont *et al.* (2014) avec des mesures effectuées sur des images satellites de 11 régions dans les déserts du Sahara, Rub'Al Khali, Taklamacan et Mu Us. Les orientations sont mesurées dans le sens trigonométrique par rapport à l'est, à petite (~ 30 m) et grande (~ 1 km) échelles. Figure adaptée de Courrech du Pont *et al.* (2014).

Croissance sur un lit de sable

Sur un lit de sable, la croissance est initiée par l'instabilité décrite en section 1.3. Comme l'orientation ne change que très peu durant les différentes phases de la croissance, il reste raisonnable de penser que l'orientation vue dans le régime non-linéaire reste celle qui maximise le taux de croissance. Dans le cas d'un régime de vent multidirectionnel, les différents vents participent à la croissance. Si la durée du cycle de vent est assez faible devant le temps caractéristique de la dune ($T \ll HL/\langle\|\boldsymbol{Q}_{\text{crest}}\|\rangle$), l'orientation de la dune ne change pas et le taux de croissance peut être moyenné sur un cycle de vent T. En s'inspirant de l'équation 1.40, il vient :

$$\sigma \propto \frac{1}{THL}\int_T \|\boldsymbol{Q}_{\text{crest}}(t)\|\,|\sin\left(\psi(t)-\alpha\right)|\mathrm{d}t. \tag{1.44}$$

L'orientation sélectionnée est alors celle qui maximise le taux de croissance, soit :

$$\left.\frac{\mathrm{d}\sigma}{\mathrm{d}\alpha}\right|_{\alpha_I} = 0. \tag{1.45}$$

Elle correspond alors à celle qui maximise les flux perpendiculaires à la crête, une règle déjà proposée par Rubin & Hunter (1987), à laquelle Courrech du Pont *et al.* (2014) ont ajouté la rétroaction de la dune sur le flux de sable $\gamma = \beta H/L$.

Élongation sur un lit non-érodable

Sur un lit non-érodable, les dunes s'alignent avec le flux résultant à la crête $\langle\boldsymbol{Q}_{\text{crest}}\rangle$. Mathématiquement, cette orientation correspond aussi à celle qui permet d'annuler les flux perpendiculaires à la crête. On obtient alors :

$$\tan\alpha_E = \frac{\langle\boldsymbol{Q}_{\text{crest}}\rangle\cdot\boldsymbol{j}}{\langle\boldsymbol{Q}_{\text{crest}}\rangle\cdot\boldsymbol{i}}. \tag{1.46}$$

1.5.3 Coexistence des deux mécanismes

Ainsi, suivant le régime de vent et la disponibilité en sable, l'un ou l'autre des deux mécanismes prévaut. Lorsque la disponibilité en sable est grande, la naissance des dunes est contrôlée quel que soit le régime des vents par l'instabilité de plat, où les dunes croissent en hauteur. Lorsqu'elle est plus faible, les dunes peuvent soit prendre la forme de barkhanes si le régime de vent est plutôt unidirectionnel, soit s'allonger dans la direction du flux résultant suivant le mécanisme d'élongation.

Les orientations prédites par le modèle dimensionnel de Courrech du Pont *et al.* (2014) pour ces deux mécanismes de croissance correspondent remarquablement bien aux observations de terrain (voir figure 1.21(a)), mais aussi aux expériences subaquatiques (Courrech

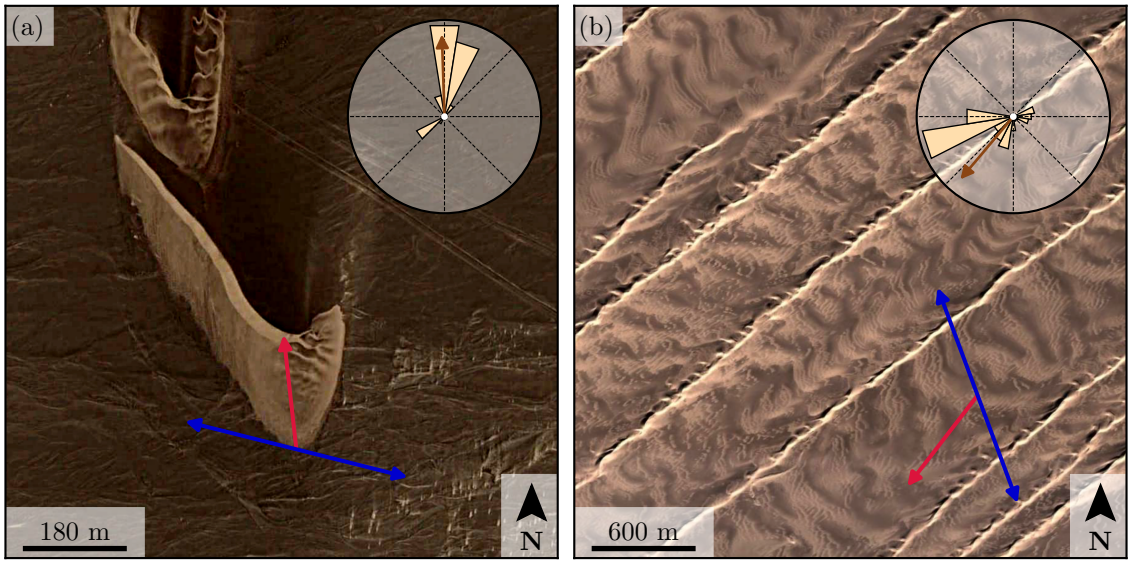

FIGURE 1.22 – (a) Barkhane asymétrique au sud de la Skeleton Coast, Namibie (20°21″S, 13° 19″E). (b) Dunes râteaux au nord du désert du Kumtagh, Chine (40°10″N, 92° 11″E). Les distributions angulaires des flux de sable sont calculées à partir des données de vents à 10 m du modèle de réanalyse climatique Era5 (Hersbach *et al.* 2020), en supposant une taille de grain de 180 μm et une rugosité aérodynamique de 1 mm. Les orientations prédites par l'équation (1.46) pour le mécanisme d'élongation (rouge) et par l'équation (1.45) pour l'instabilité de lit (bleu) en utilisant ces distributions correspondent aux crêtes visibles sur l'image satellite (images satellites : Google^{TM}, CNES/Airbus, TerraMetrics, Maxar Technologies).

du Pont *et al.* 2014) et aux simulations numériques (Gao *et al.* 2015b). Le meilleur accord est trouvé pour $\gamma \approx 1.6$, en accord avec la valeur trouvée à partir de migration des barkhanes (voir section 1.4.1), reflétant la quasi-universalité du rapport d'aspect des dunes matures.

Dans des conditions naturelles, il arrive très souvent que ces deux mécanismes coexistent. Un même endroit, avec un même régime de vent, peut à la fois présenter des zones où la disponibilité en sable est forte et des zones de socle non-érodable, et donc deux orientations distinctes (voir figure 1.21(b)). Lorsque seules des images satellites sont disponibles, l'utilisation de ces deux orientations permet de contraindre de manière forte les régimes de vents possiblement à l'origine de ces motifs, comme sur Mars ou Titan (Fenton *et al.* 2014a;b, Runyon *et al.* 2017, Fernandez-Cascales *et al.* 2018).

Des motifs issus de la coexistence des deux mécanismes

Enfin, certaines morphologies de dunes sont intrinsèquement formées par la coexistence de ces deux mécanismes. La transition entre barkhane (vent plutôt unidirectionnel) et dune linéaire (vent plutôt bidirectionnel) n'est pas abrupte (Lü *et al.* 2018). Lorsqu'une direction de vent domine sur les autres, on rencontre souvent des barkhanes asymétriques dont l'une

des cornes s'allonge suivant le mécanisme d'élongation (Bourke *et al.* 2010, Lü *et al.* 2016). Bien que les barkhanes se forment lorsque la disponibilité sédimentaire est faible, leur crête est, quant à elle, considérée dans la littérature comme possédant l'orientation du mécanisme de l'instabilité, définie au niveau de la section centrale (voir figure 1.22(a)).

Les dunes râteaux sont composées d'une crête linéaire, orientée suivant le mécanisme d'élongation, à laquelle sont attachées, sur un côté, de semi-barkhanes périodiquement espacées (Dong *et al.* 2010). Ces dernières sont dues à l'instabilité se développant de manière superposée sur un des côtés de la crête principale (Lü *et al.* 2017). Leur morphologie peut être vue comme l'assemblage d'une série de barkhanes asymétriques, liées entre elles par leur bras le plus long (voir figure 1.22(b)).

Enfin, sous des régimes de vents multidirectionnels dont le flux résultant est faible, des dunes étoiles se forment : leurs bras s'allongent contre chaque vent, mus par les vents opposés à ce dernier via le mécanisme d'élongation. Ils sont alors connectés entre eux au centre, où la disponibilité sédimentaire est plus forte, par différentes crêtes dont l'orientation provient de l'instabilité liée à chaque vent (Zhang *et al.* 2012). Leur morphologie peut alors être vue comme l'assemblage circulaire d'un ensemble barkhanes asymétriques, fusionnées par la tête et dont le bras le plus long pointe vers l'extérieur.

1.6 Conclusion et organisation du manuscrit

Dans ce chapitre, nous avons dressé un bref état des connaissances actuelles sur la morphodynamique dunaire. Cette dernière semble alors être contrôlée par deux paramètres principaux, le régime de vents et la disponibilité en sédiments.

D'une part, sur un lit de sable (forte disponibilité en sédiments), la croissance dunaire est initiée via une instabilité couplant le transport sédimentaire, l'écoulement et la forme du lit. Cette instabilité est bien caractérisée sous des régimes de vents unidirectionnels, où l'analyse de stabilité linéaire permet de prédire la longueur d'onde, la vitesse de migration et le taux de croissance des dunes naissantes. Néanmoins, alors que ce modèle est basé sur de nombreux paramètres, il a seulement été testé vis-à-vis de la longueur d'onde et de la vitesse de migration, et ce sans mesure indépendante de tous ces paramètres. Il manque alors une validation de ces trois quantités à la fois pour un seul et même champ de dunes. C'est l'objet du second chapitre de ce manuscrit, où nous étudions le développement spatial et temporel de l'instabilité dunaire dans le désert des White Sands, Mexico.

De plus, cette méthode d'analyse n'a jamais été étendue à des régimes de vents quelconques, sous lesquels seule l'orientation des dunes peut être prédite, à l'aide de l'analyse dimensionnelle de Courrech du Pont *et al.* (2014). Dans le troisième chapitre, nous étendons alors l'analyse de stabilité linéaire à des régimes des vents bidirectionnels, puis multidirectionnels.

D'autre part, sur un sol non-érodable, les dunes peuvent s'allonger à partir d'une source de sédiments dans le sens du flux résultant lorsqu'elles se trouvent sous des régimes de vents au moins bidirectionnels. Elles sont donc plutôt alignées avec le vent dominant, ce qui les distingue clairement des dunes issues de l'instabilité de lit, plutôt perpendiculaires à ce dernier. De manière analogue à ces dernières, les dunes issues du mécanisme d'élongation peuvent néanmoins former des motifs périodiques clairement définis, bien qu'elles peuvent aussi former des motifs apériodiques ou rester isolées. La question de cette périodicité est alors traitée numériquement dans la première partie du quatrième chapitre de cette thèse. Tandis que la direction d'allongement est bien comprise, les propriétés du mécanisme d'élongation, et des dunes qui y sont associées, restent à étudier. C'est l'objet de la seconde partie du quatrième chapitre, où nous étudions numériquement les propriétés de la dune isolée.

Ce cadre théorique englobant le transport de sédiments et la croissance des dunes permet alors de lier ces derniers aux propriétés locales des vents et des grains. Dans le cinquième et dernier chapitre, nous effectuons une analyse grande échelle du désert du Namib, et déduisons des données de vents issues de réanalyses climatiques les flux de sédiments et les caractéristiques des dunes à travers toute la mer de sable.

Chapter 2

Spatial and temporal development of incipient dunes

Balloon rally at the White Sands dune field, New Mexico, USA - Ybratcher

Contents

2.1 Abstract

In zones of loose sand, wind-blown sand dunes emerge due the linear instability of a flat sedimentary bed. This instability has been studied in experiments and numerical models but rarely in the field, due to the large time and length scales involved. We examine dune formation at the upwind margin of the White Sands Dune Field in New Mexico (USA), using 4 years of lidar topographic data to follow the spatial and temporal development of incipient dunes. Data quantify dune wavelength, growth rate and propagation velocity, but also the characteristic length scale associated with the growth process. We show that all these measurements are in quantitative agreement with predictions from linear stability analysis. This validation makes it possible to use the theory to reliably interpret dune-pattern characteristics, and provide quantitative constraints on associated wind regimes and sediment properties, where direct local measurements are not available or feasible.

2.2 Introduction

The development of sand dunes, from incipient to mature bedforms, and their evolution, through interaction and coarsening processes, involve characteristic time and length scales that relate to elementary mechanisms of hydrodynamics and sediment transport (Wiggs 2013, Courrech du Pont 2015). Over loose granular beds, bedform emergence is driven by a hydrodynamic instability induced by the interaction between the sand bed, flow and sediment transport (Charru *et al.* 2013). The stream-wise offset between topography and sediment flux has two contributions (Andreotti *et al.* 2002b, Kroy *et al.* 2002a, Fourrière *et al.* 2010, Claudin *et al.* 2013). First, a hydrodynamic destabilization originates from the coupling between flow inertia and dissipation, which results in a maximum basal fluid shear stress located upstream of the crest (Sykes 1980, Hunt *et al.* 1988b, Kroy *et al.* 2002b). Second, the sand flux needs a characteristic length, called the saturation length, to adapt to a spatial change in shear stress (Sauermann *et al.* 2001, Andreotti *et al.* 2010, Durán *et al.* 2011, Pähtz *et al.* 2013b). This results in a stabilizing downstream lag of the maximum sand flux with respect to the maximum of the shear stress. These balancing processes give rise to the development and propagation of sand waves at a specific wavelength and propagation speed, associated with the most unstable mode of the pattern, with crests perpendicular to the dominant wind direction.

The early stage of growth and development of sedimentary ripples and dunes has been theoretically studied with linear stability analyses of coupled transport and hydrodynamic equations (Kennedy 1963, Richards 1980, Andreotti *et al.* 2002b, Lagrée 2003, Colombini 2004, Claudin & Andreotti 2006, Fourrière *et al.* 2010, Devauchelle *et al.* 2010, Andreotti *et al.* 2012a, Durán *et al.* 2019). These analyses predict the incipient pattern wavelength,

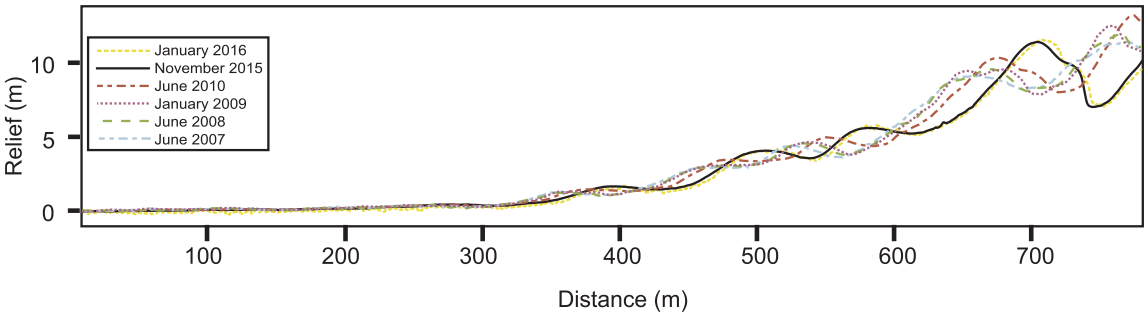

Figure 2.1 – Topographic profile on the upwind margin of the White Sands Dune field, Mexico. Figure taken from Phillips *et al.* (2019).

propagation velocity and growth rate as functions of model parameters, which encode the wind and grain characteristics. For the aeolian case in particular, the dune wavelength has been shown to be proportional to the saturation length. However, measuring the bed elevation together with sediment and fluid transport is difficult, thereby making the direct comparison between theory and field or experimental data rather challenging.

In aeolian conditions, the hydrodynamic and sediment transport responses have been investigated independently of each other, and separate measurements of the saturation length as well as the upwind shift of the shear stress have been carried out, in the field and in wind tunnel expreriments (Andreotti *et al.* 2010, Claudin *et al.* 2013, Selmani *et al.* 2018). In contrast, few field studies addressing the early stage of aeolian dune growth are available in the literature (Cooper 1958, Fryberger & Dean 1979, Kocurek *et al.* 1992, Elbelrhiti *et al.* 2005, Ping *et al.* 2014, Baddock *et al.* 2018). First, in situ monitoring of the evolution of small amplitude bedforms is difficult due to the involved length and time scales (tens to hundreds of meters, days to months). Second, inherent wind variability — even in overall unidirectional dune fields — makes application of the theory challenging. Emergence of subaqueous sand ripples has also been experimentally investigated (Coleman & Melville 1996, Baas 1999, Langlois & Valance 2007a, Fourrière *et al.* 2010), and more generally the quantification of sedimentary bedforms in different environmental – including extraterrestrial – conditions in relation to hydrodynamics and sediment transport remains an active current subject of research (Lapôtre & et al. 2016, Jia *et al.* 2017, Lapôtre *et al.* 2018, Durán *et al.* 2019).

Previous studies have focused on spatially homogeneous conditions where the bedforms develop and grow everywhere simultaneously. However, non-homogeneous situations are very common in natural conditions, for example where boundary conditions introduce spatial discontinuities. In this case, as shown by figure 2.1, the dune instability can be triggered at a specific point, resulting in a sequence of spatially amplifying sand waves developing downstream (Ewing & Kocurek 2010, Phillips *et al.* 2019). This configuration is typically found at the upwind border of large sandy areas where the sediment starts

to accumulate, but has not been studied in the framework of the spatial linear stability analysis.

Here, we study the upwind margin of the White Sands Dune Field, where the spatial development of dunes can be observed (Phillips *et al.* 2019). We follow the spatio-temporal evolution of incipient dunes and extract their wavelength and propagation velocity, as well as their temporal and spatial growth rates. We then show that these four quantities all quantitatively compare to the predictions of the spatial linear stability analysis.

This chapter is adapted from an article submitted to *Geophysical Research Letters*.

2.3 White Sands Dune Field

White Sands Dune Field is located in southern New Mexico, USA. The sand covers an area of about 400 km^2, resulting in the largest gypsum dune field on Earth. Dominant winds are mainly towards the northeast, and shape the sedimentary bed into transverse and barchan dunes, progressively turning into parabolic dunes as the vegetation cover increases (Figures 2.2 and 2.3a) (McKee 1966, Jerolmack *et al.* 2012, Baitis *et al.* 2014). Dunes emerge on the upwind margin (figure 2.3b). There, the sediment is made of coarse, elongate, and angular grains (see figure A.2), with a measured diameter $d = 670 \pm 120$ μm and a bulk density $\rho_\mathrm{p} = 2300 \pm 100$ kg m^{-3}. The saturation length, relevant in the process of dune emergence (see section 2.4), directly depends on these grain properties (Andreotti *et al.* 2010):

$$L_\mathrm{sat} \simeq 2.2 \frac{\rho_\mathrm{p}}{\rho_\mathrm{f}} d = 2.8 \pm 0.5 \text{ m}, \tag{2.1}$$

where $\rho_\mathrm{f} \simeq 1.2$ kg m^{-3} is the air mass density in ambient conditions. Grains are also rough, and we measured an avalanche slope $\mu = 0.8 \pm 0.05$ (see appendix A.1). However, the grains are non-homogeneous in size and shape across the dune field. As one moves further into the dune field, the grain diameter and angularity both decrease, due to abrasion and sorting (Jerolmack *et al.* 2011, Phillips *et al.* 2019). Because we restrict our analysis of the dune development to the first kilometer along the margin, we can ignore this spatial evolution of the grain characteristics.

The sand flux is calculated from the hourly wind data of the weather station at Holloman Air Base (KHMN, 32°51′N, 106°06′W), using the method described in Courrech du Pont *et al.* (2014) (see also appendix A.2). The wind is characterized by its shear velocity u_*, representative of the logarithmic profile inside the turbulent boundary layer. Its threshold value u_th below which saltation cannot sustain steady transport is estimated with $u_\mathrm{th} = a\sqrt{(\rho_\mathrm{p}/\rho_\mathrm{f})\, gd} = 0.35$ m s^{-1}, and $a \simeq 0.1$ (Iversen & Rasmussen 1999). The corresponding typical velocity ratio u_*/u_th is then about 1.26 ± 0.05 (all these values are then gathered in table 2.2). As shown in figure 2.2 and documented by Pedersen *et al.* (2015), the wind regime is multimodal. Southwesterly winds dominate the transport as noted by

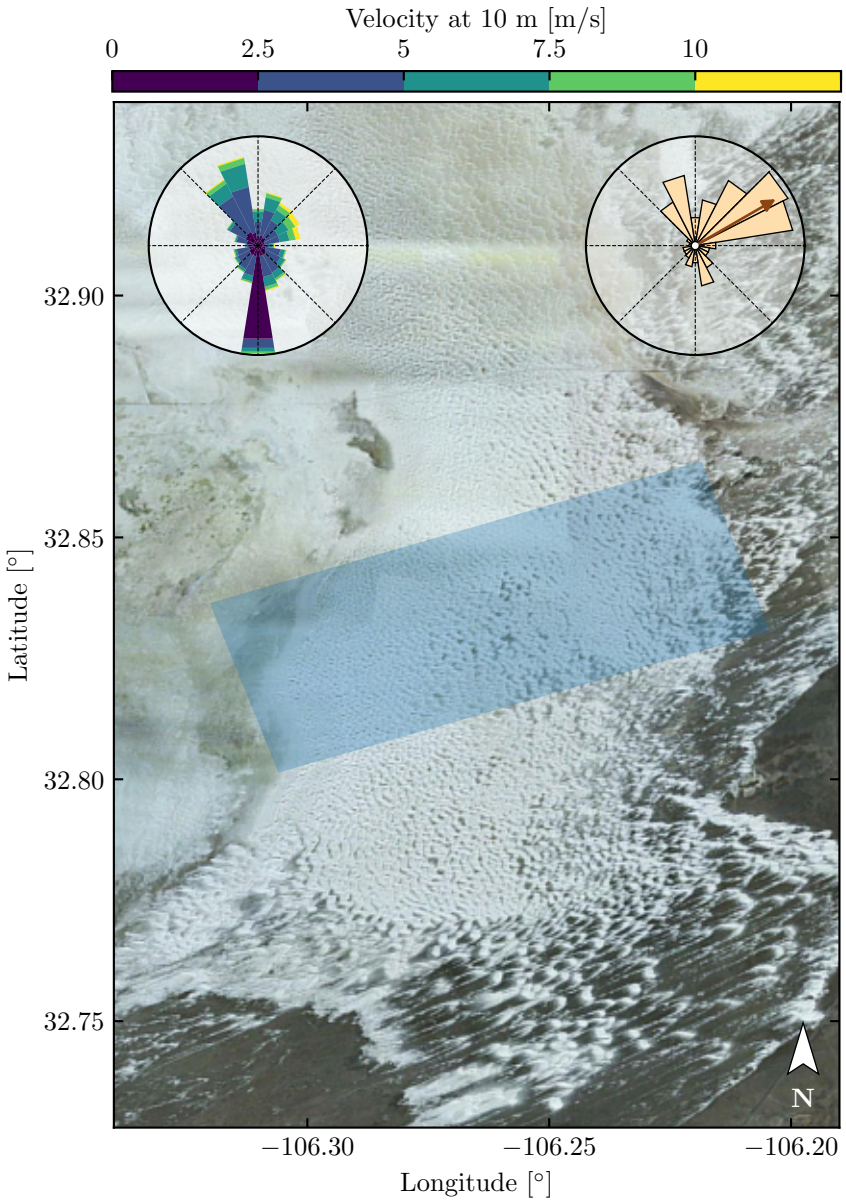

Figure 2.2 – Satellite image of the White Sands Dune Field (Google™, Landsat-Copernicus). The left rose shows the wind data from 2007 to 2017 (direction toward which the wind is blowing). The right rose shows the corresponding distribution of sand flux orientations and the resultant flux direction (brown arrow). Both agree well with that reported by Ewing *et al.* (2015) and Pedersen *et al.* (2015). The blue area corresponds to the location of the digital elevation measurements shown in figure 2.3.

the nearly unimodal sand flux distribution toward the northeast. The other modes from the north and southeast moderately impact the dune shape and migration (Swanson *et al.* 2016).

Elevation data of the blue area in figure 2.3 have been obtained using lidar-derived topography at five different times (June 2007, June 2008, January 2009, June 2010 and August 2015). Along the upwind margin, we extracted 75 dune profiles from the surface elevation data, spaced 50-m apart and aligned with the direction of the resulting sand flux (figure 2.3a). The average topography is removed using a Butterworth high-pass filter (order = 5, cutoff frequency = 0.005 m^{-1}). We limit our analysis to the first dunes of the filtered profile, i.e. typically the first kilometer, to ensure that we stay as much as possible in the early stage of dune growth (red area in figure 2.3b). As shown by figure 2.3c, these incipient dunes have very low aspect ratios and do not exhibit any slipfaces (Phillips *et al.* 2019). The detrended bed elevation exhibits a spatially amplified oscillating behaviour (figure 2.4a and 2.4b). We now interpret these profiles using the theoretical framework provided by the linear stability analysis developed in the next section.

2.4 Dune linear stability analysis

The linear stability analysis of a flat sedimentary bed sheared by a constant fluid flow has been derived in section 1.3.2, and allows the prediction of incipient dunes properties, i.e. their wavelength, growth rate and celerity. More specifically, introducing a sinusoidal perturbation of the bed elevation:

$$h(x,t) = \zeta e^{i(kx-\omega t)}, \tag{2.2}$$

of wavenumber k and pulsation ω, at a small amplitude ζ ($k\zeta \ll 1$), leads to the dune dispersion relation:

$$\omega = \frac{Q}{L_{\mathrm{sat}}^2}\frac{(kL_{\mathrm{sat}})^2}{1+ikL_{\mathrm{sat}}}\left(\mathcal{A}+i\mathcal{B}_\mu\right), \tag{2.3}$$

where

$$\mathcal{B}_\mu = \mathcal{B} - \frac{1}{\mu}\left(\frac{u_{\mathrm{th}}}{u_*}\right)^2 \tag{2.4}$$

accounts for the dependence of the threshold on the bed slope $\partial_x h$. In this calculation, the bed is assumed to be spatially homogeneous at the beginning, and only temporal growth is considered.

However, as all unstable modes are found to be propagating downwind, the instability is said to be *convective*: perturbations grow while propagating. Then, only for an artificial situation with periodic boundary conditions, for example in numerical simulations, the instability can simultaneous grow in time, everywhere. Likewise, if one could flatten the

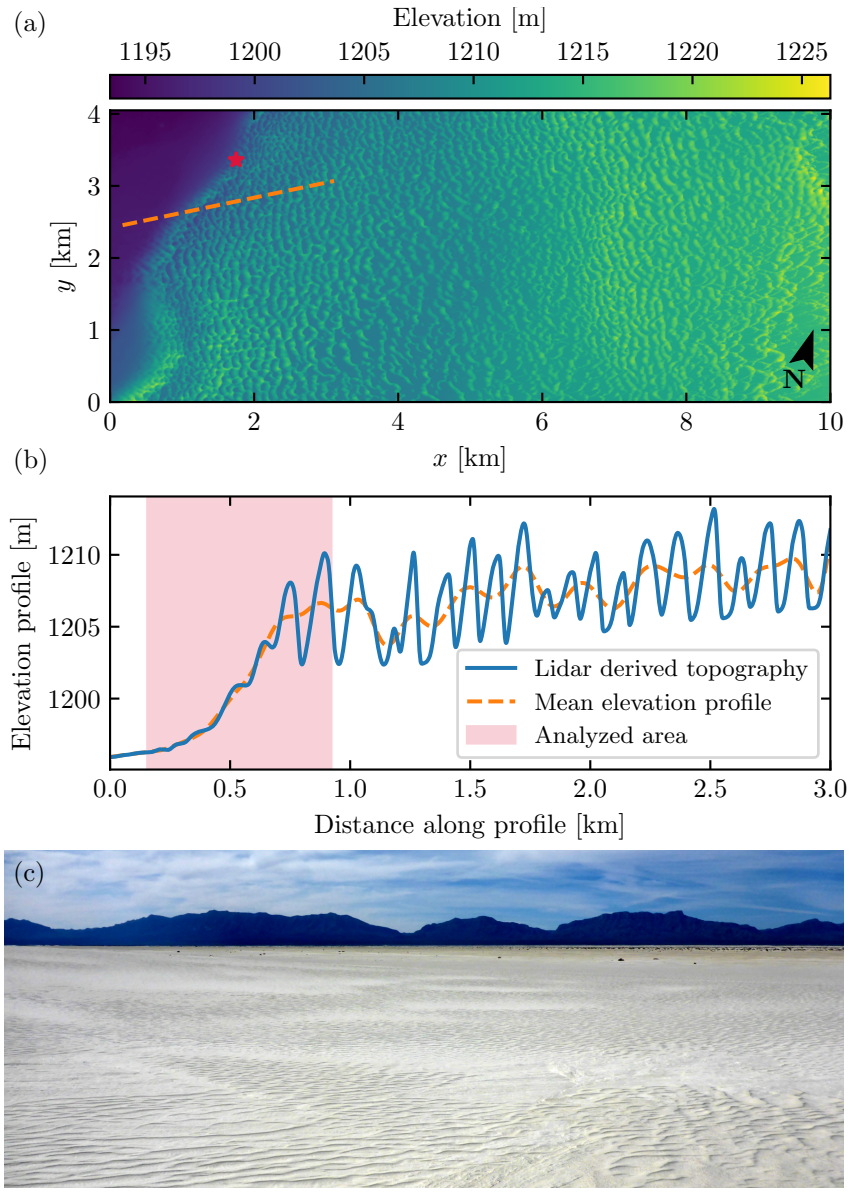

Figure 2.3 – Digital elevation data taken in June 2007. The dashed orange line is the location of the transect shown in (b), taken along the direction of the resultant flux. The red star is the location of the photo shown in (c), which is a view to the southwest of the dune field upwind margin.

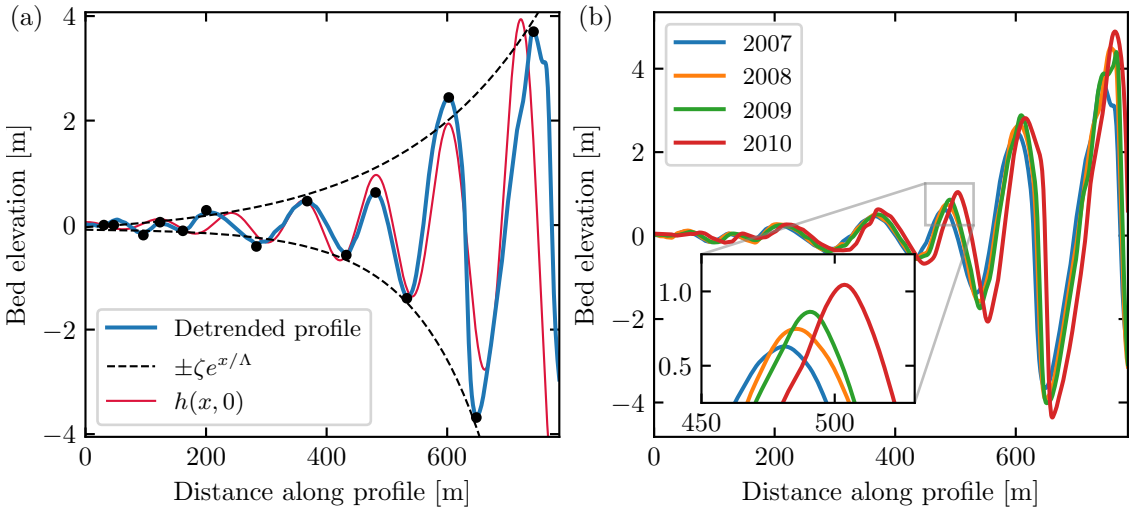

Figure 2.4 – The spatial exponential dune growth. (a) Detrended profile corresponding to that of figures 2.3a and 2.3b. The black dashed lines are exponential fits to the dune crests (black dots), giving $\Lambda = 225$ m (top) and $\Lambda = 135$ m (bottom). The theoretical red profile parameters, defined in equation (2.16), are $\zeta = 0.06$ m, $\lambda = 120$ m, and $\Lambda = 170$ m. (b) Temporal evolution of the detrended elevation profile, with a close-up on one crest.

sand bed at a kilometer scale, one would see the spatially-homogeneous emergence of the instability in time. Nevertheless, the dunes generated from noise at the upstream boundary condition would eventually invade, by propagation, a larger and larger domain.

Since both temporal and spatial growths are possible, either k, or ω, or both can be complex numbers in (2.3), depending on the studied situation:

$$k = k_r + ik_i, \tag{2.5}$$

$$\omega = \omega_r + i\omega_i, \tag{2.6}$$

whose real parts (k_r, ω_r) represent spatial and temporal oscillations, and whose imaginary parts (k_i, ω_i) represent growth or decay of the amplitude of the perturbation. Setting k to be real and allowing ω to be a complex number is called a *temporal stability analysis*; it corresponds to previous works on the dune instability. On the contrary, setting ω to be real and allowing k to be a complex number is used to investigate spatial growth; it is called a *spatial stability analysis* (Charru 2011, Gallaire & Brun 2017).

For sake of clarity, the pulsation and wavenumber will thereby only refer to their real parts, while one defines the temporal and spatial growth rates from their imaginary parts.

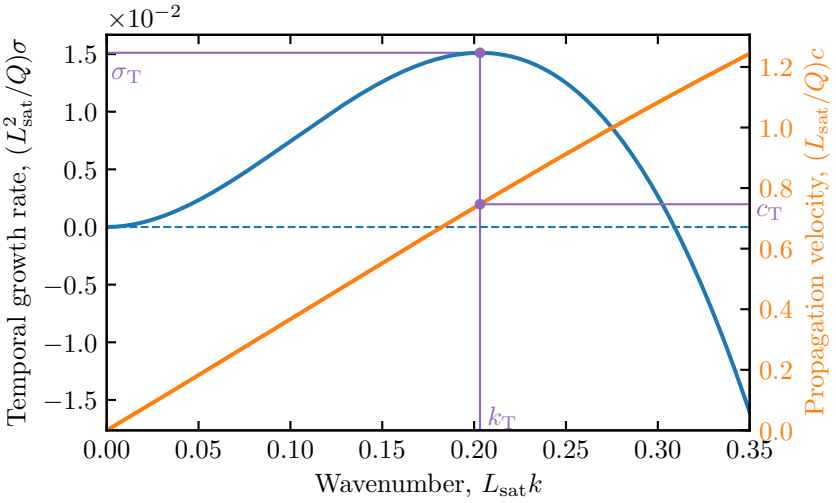

Figure 2.5 – Temporal growth rate and propagation speed corresponding to the temporal linear stability analysis. Purple lines and dots indicates the most unstable mode. Here, we take $\mathcal{A} = 3.6$, $\mathcal{B} = 1.9$, $\mu = 0.8$ and $u_*/u_{\mathrm{th}} = 1.26$.

From now on, the notations will then be the following:

$$k_r \equiv k, \tag{2.7}$$

$$\omega_r \equiv \omega, \tag{2.8}$$

$$\omega_i \equiv \sigma, \tag{2.9}$$

$$-k_i \equiv 1/\Lambda, \tag{2.10}$$

where Λ is the characteristic growth length. The propagation velocity of the pattern is then defined as $c = \omega/k$. In the following, we derive and compare both temporal and spatial linear stability analyses. Note that we neglect the weak (logarithmic) dependence of the hydrodynamic coefficient $\mathcal{A}$ and $\mathcal{B}$ in the wavenumber (see section 1.3).

2.4.1 Temporal linear stability analysis

We first consider a spatial sinusoidal perturbation over the whole sedimentary bed, of given wavelength $\lambda = 2\pi/k$ and initial amplitude ζ. In response to the wind shift and the flux lag, it can grow or decay in time, and does so at a rate σ. This occurs everywhere simultaneously, which implies $1/\Lambda = 0$: there is neither spatial growth not decay. There is however propagation of the perturbation at velocity c, and the bed elevation can be written along the direction x of the wind as:

$$h(x,t) = \zeta\, e^{\sigma t} \cos\left[\frac{2\pi}{\lambda}\,(x - ct)\right]. \tag{2.11}$$

As shown by figure 2.5, both temporal growth rate and propagation speed can be computed as functions of λ from the dispersion relation (2.3) (see section 1.3.2). Positive values of the growth rate are associated with unstable perturbations, and these are typically for large values of λ. Conversely, small wavelengths are stable, with $\sigma < 0$. The cut-off wavelength λ_c, associated with a neutral growth rate $\sigma(\lambda_c) = 0$, relates to the model parameters as:

$$\lambda_c = \frac{2\pi\mathcal{A}}{\mathcal{B} - \frac{1}{\mu}\left(\frac{u_{\mathrm{th}}}{u_*}\right)^2} L_{\mathrm{sat}}, \tag{2.12}$$

and separates growing ($\lambda > \lambda_c$) to decaying ($\lambda < \lambda_c$) perturbations. It can thus be interpreted as a minimal dune size. Furthermore, in the limit $L_{\mathrm{sat}}/\lambda_c \ll 1$, the characteristics of the fastest growing perturbation read:

$$\lambda_{\mathrm{T}} \sim \frac{3}{2}\lambda_c, \tag{2.13}$$

$$\sigma_{\mathrm{T}} \sim \frac{Q}{L_{\mathrm{sat}}^2}\frac{\mathcal{A}}{2}\left(\frac{2\pi L_{\mathrm{sat}}}{\lambda_{\mathrm{T}}}\right)^3, \tag{2.14}$$

$$c_{\mathrm{T}} \sim \frac{Q}{L_{\mathrm{sat}}}\mathcal{A}\frac{2\pi L_{\mathrm{sat}}}{\lambda_{\mathrm{T}}}, \tag{2.15}$$

where $Q = \Omega u_*^2$ gives the characteristic scale of the sediment flux associated with the wind regime (Fourrière *et al.* 2010). Here, X_{T} denotes the quantity X derived from the temporal linear stability analysis, to be distinguished below from X_{S}, derived from the spatial analysis.

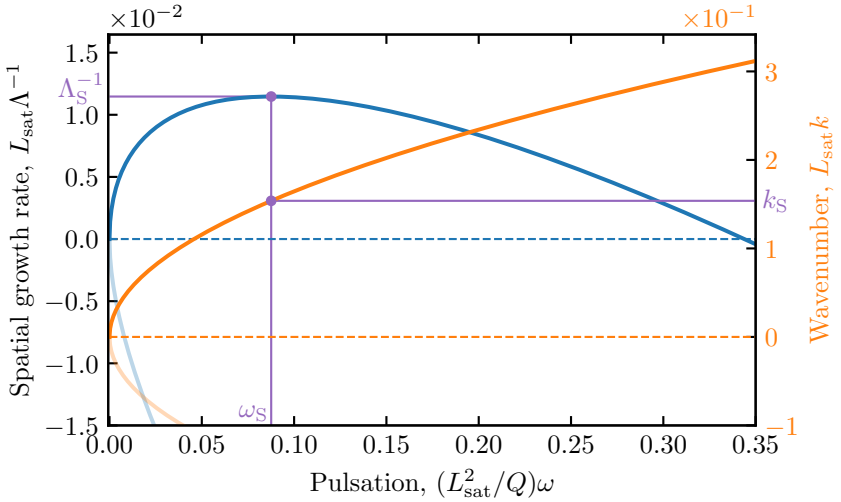

Figure 2.6 – Spatial growth rate and wavenumber corresponding to the spatial linear stability analysis. Purple lines and dots indicates the most unstable mode. Opaque and transparent curves correspond to the positive and negative branches k_+ and k_-, relating to upstream and downstream propagating waves, respectively. Here, we take $\mathcal{A} = 3.6$, $\mathcal{B} = 1.9$, $\mu = 0.8$ and $u_*/u_{\mathrm{th}} = 1.26$.

2.4.2 Spatial linear stability analysis

We consider now a temporal perturbation of the bed at a specific position in space ($x = 0$), taking the form of a sinusoid of amplitude ζ and with an angular frequency ω. From this point, successive dunes emerge and propagate downwind, resulting in a spatial development of the pattern. Here there is no temporal growth: at a given location, the amplitude of the bed oscillation is the same at any time ($\sigma = 0$). The bed elevation along the x direction can this time be written as:

$$h(x,t) = \zeta\, e^{x/\Lambda} \cos\left[\frac{2\pi}{\lambda}\,(x - ct)\right], \tag{2.16}$$

where $1/\Lambda$ is the spatial dune growth rate. This is equivalent to rewrite the dispersion relation (2.3) as:

$$(\mathcal{A} + i\mathcal{B}_\mu)\, L_{\mathrm{sat}}^2 \left(k - i\Lambda^{-1}\right)^2 - i\frac{L_{\mathrm{sat}}^2}{Q}\omega L_{\mathrm{sat}}\left(k - i\Lambda^{-1}\right) - \frac{L_{\mathrm{sat}}^2}{Q}\omega = 0, \tag{2.17}$$

which solves into:

$$L_{\mathrm{sat}}\left(k - i\Lambda^{-1}\right) = \frac{1}{2\,(\mathcal{A} + i\mathcal{B}_\mu)}\left[i\frac{L_{\mathrm{sat}}^2}{Q}\omega \pm \sqrt{\frac{L_{\mathrm{sat}}^2}{Q}\omega\left[4\,(\mathcal{A} + i\mathcal{B}_\mu) - \frac{L_{\mathrm{sat}}^2}{Q}\omega\right]}\right]. \tag{2.18}$$

The two roots k_+ and k_- relate to waves propagating downstream and upstream, respectively. Splitting the above expression into real and imaginary part, we obtain:

$$L_{\mathrm{sat}} k(\omega) = \frac{1}{2\left(\mathcal{A}^2 + \mathcal{B}_\mu^2\right)}\left(\mathcal{B}_\mu \frac{L_{\mathrm{sat}}^2}{Q}\omega \pm \mathcal{F}(\omega)\left[\mathcal{A}\mathcal{G}(\omega) + \mathcal{B}_\mu \mathcal{H}(\omega)\right]\right), \tag{2.19}$$

$$L_{\mathrm{sat}} \Lambda^{-1}(\omega) = \frac{1}{2\left(\mathcal{A}^2 + \mathcal{B}_\mu^2\right)}\left(-\mathcal{A}\frac{L_{\mathrm{sat}}^2}{Q}\omega \pm \mathcal{F}(\omega)\left[\mathcal{B}_\mu \mathcal{G}(\omega) - \mathcal{A}\mathcal{H}(\omega)\right]\right), \tag{2.20}$$

where

$$\mathcal{F}(\omega) = \sqrt{\frac{1}{2}\frac{L_{\mathrm{sat}}^2}{Q}\omega\left(4\mathcal{A} - \frac{L_{\mathrm{sat}}^2}{Q}\omega\right)}, \tag{2.21}$$

$$\mathcal{G}(\omega) = \sqrt{1 + \sqrt{1 + \left(\frac{4\mathcal{B}_\mu}{4\mathcal{A} - \frac{L_{\mathrm{sat}}^2}{Q}\omega}\right)^2}}, \tag{2.22}$$

$$\mathcal{H}(\omega) = \sqrt{\sqrt{1 + \left(\frac{4\mathcal{B}_\mu}{4\mathcal{A} - \frac{L_{\mathrm{sat}}^2}{Q}\omega}\right)^2} - 1}. \tag{2.23}$$

The spatial growth rate $1/\Lambda$ is plotted for both branches in figure 2.6 as a function of the pulsation ω. Only the positive branch k_+ corresponding to waves propagating downstream exhibits positive values, and can grow. It also shows a single maximum, corresponding to the most unstable pulsation ω_S. The corresponding wavelength, propagation velocity and growth length are:

$$\lambda_S = \frac{2\pi}{k\left(\omega_S\right)}, \tag{2.24}$$

$$c_S = \frac{\omega_S}{k\left(\omega_S\right)}, \tag{2.25}$$

$$\Lambda_S = \Lambda\left(\omega_S\right). \tag{2.26}$$

Unfortunately, no simple analytical and accurate formulae like (2.13-2.15) can be derived for these quantities in this case. However, temporal and spatial analyses are consistent, and we typically find $\lambda_S \simeq 1.3\lambda_T$ and $c_S \simeq 0.77 c_T$. Those numerical factors do not vary by more than a few percent upon changing the parameters $\mathcal{A}$ and $\mathcal{B}$ within a reasonable range of values.

2.4.3 Lagrangian quantities

In both spatial an temporal development of the instability, an individual bump grows in height while propagating downwind at a constant velocity. Its amplitude therefore varies exponentially with respect to time and position. As a result, one can define in temporal linear stability analysis a Lagrangian spatial growth rate σ_T/c_T, in the reference frame of the bump. This rate is consistent with the spatial analysis, and we typically find

$$\Lambda_S \simeq 1.8\frac{c_T}{\sigma_T}. \tag{2.27}$$

Likewise, in the spatial analysis, the Lagrangian temporal growth rate $\varsigma_S \equiv c_S/\Lambda_S$ (inset of figure 2.7) is found to be close to σ_T, within a factor of $\simeq 0.43$, again with variations on the order of a few percent.

The dunes on the upwind margin of the White Sands dune field develop from the upstream boundary condition, where the sand bed starts. In the following, we thus use the exact results of the spatial analysis to interpret the field data.

2.5 Field data analysis

After removing the average topography (figure 2.3b), the detrended bed elevation profile exhibits an exponentially amplifying sinusoidal shape, as predicted by the spatial linear theory for dune emergence (figure 2.4a). Using these profiles and their temporal evolution (figure 2.4b), we have extracted the three independent characteristics of the pattern (λ,

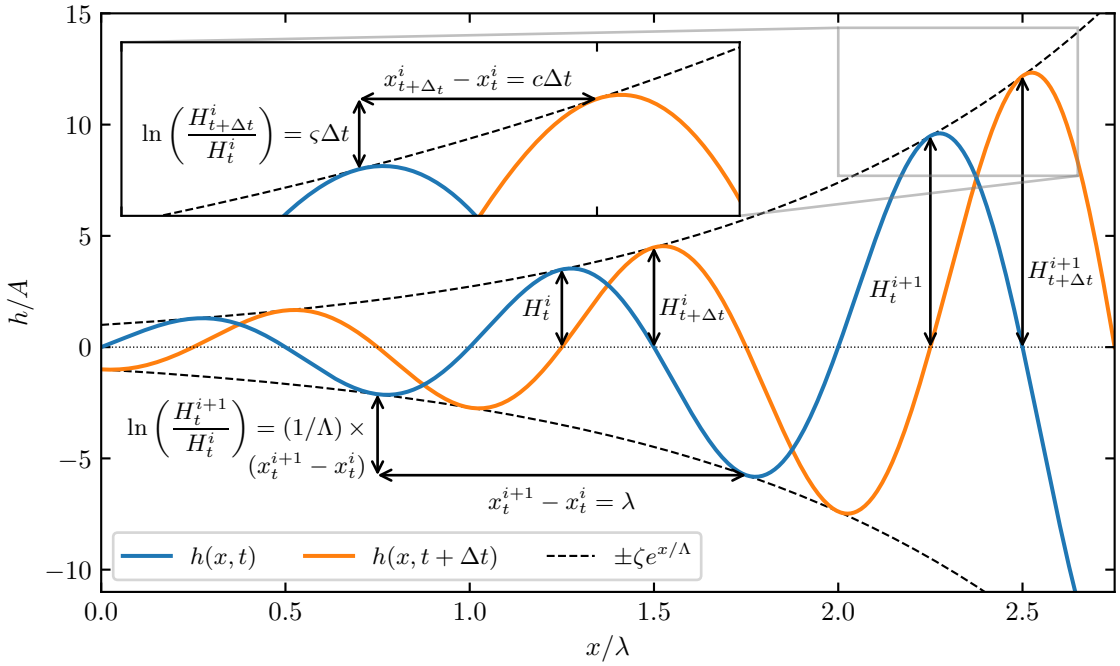

Figure 2.7 – Schematics of the spatial dune development. The theoretical profile h is defined in equation (2.16)

c and Λ or ς) using two different methods. For each profile, we either look at each peak separately (peak-to-peak method), or extract quantities averaged over the whole profile (global approach).

Wavelength and growth length

The wavelength λ is computed by autocorrelation of the bed elevation profile (global method), and from the spacing between two adjacent peaks (peak-to-peak method). The fit of an exponential to the peaks of each profile gives the spatial growth length Λ (global method, see dashed line in figure 2.4a). The spatial growth length is alternatively computed from the difference in height between two adjacent peaks (peak-to-peak method, see figure 2.7).

Lagrangian growth rate and propagation velocity

The Lagrangian growth rate ς and the propagation velocity c are obtained by fitting exponential and linear functions to the temporal variation of the dune height and position, respectively. However, both are also time-dependent through the characteristic sand flux Q and the slope effect $(1/\mu)(u_{\mathrm{th}}/u_*)^2$. In the fitting procedure to extract ς and c, we neglect this second contribution, but take into account the temporal variations of Q. Following (2.14) and (2.15), the Lagrangian growth rate and propagation velocity are proportional

to the characteristic sand flux, such that we can write at each time step:

$$\varsigma_t = \frac{Q_t}{L_{\text{sat}}^2}\bar{\varsigma}, \tag{2.28}$$

$$c_t = \frac{Q_t}{L_{\text{sat}}}\bar{c}, \tag{2.29}$$

where $\bar{\varsigma}$ and $\bar{c}$ are non dimensional, and assumed to be independent of time.

From the exponential growth and the linear propagation of a bump in the linear regime of the instability, the peak height H and position x at a time step t can be expressed as:

$$H_t = H_0 \exp\left(\Sigma_t \varsigma_t \delta t\right), \tag{2.30}$$

$$x_t = x_0 + \Sigma_t c_t \delta t, \tag{2.31}$$

which can be rewrittten as:

$$\ln\left(\frac{H_t}{H_0}\right) = \frac{\langle Q_t\rangle}{L_{\text{sat}}^2}\bar{\varsigma}\,\Sigma_t \frac{Q_t}{\langle Q_t\rangle}\delta t = \langle\varsigma\rangle t^*, \tag{2.32}$$

$$x_t - x_0 = \frac{\langle Q_t\rangle}{L_{\text{sat}}}\bar{c}\,\Sigma_t \frac{Q_t}{\langle Q_t\rangle}\delta t = \langle c\rangle t^*, \tag{2.33}$$

where $\langle\cdot\rangle$ denotes the time average. We then see that an effective time t^* arises:

$$t^* = \Sigma_t \frac{Q_t}{\langle Q_t\rangle}\delta t_t. \tag{2.34}$$

It allows the extraction of the time average growth rate and propagation velocity (see figure 2.8), in which the average characteristic sand flux should be used for comparison with the theoretical predictions,

Here, the peak-to-peak method looks at the height and position of each peak separately (see inset of figure 2.7). For a global measurement, the average propagation speed can be determined from the cross-correlation curve between the same profiles at different times, and the average Lagrangian growth rate from the temporal evolution of the bed elevation standard deviation.

2.6 Time and length scales of the incipient dunes

2.6.1 Field results

The output of the analysis of the 75 transects is shown in figure 2.9. Both peak-to-peak and global methods exhibit similar distributions for the wavelength λ, the propagation velocity c, the Lagrangian growth rate ς and the growth length Λ, with clear dominant (most probable) values. The incipient dune wavelength and growth length are both on the

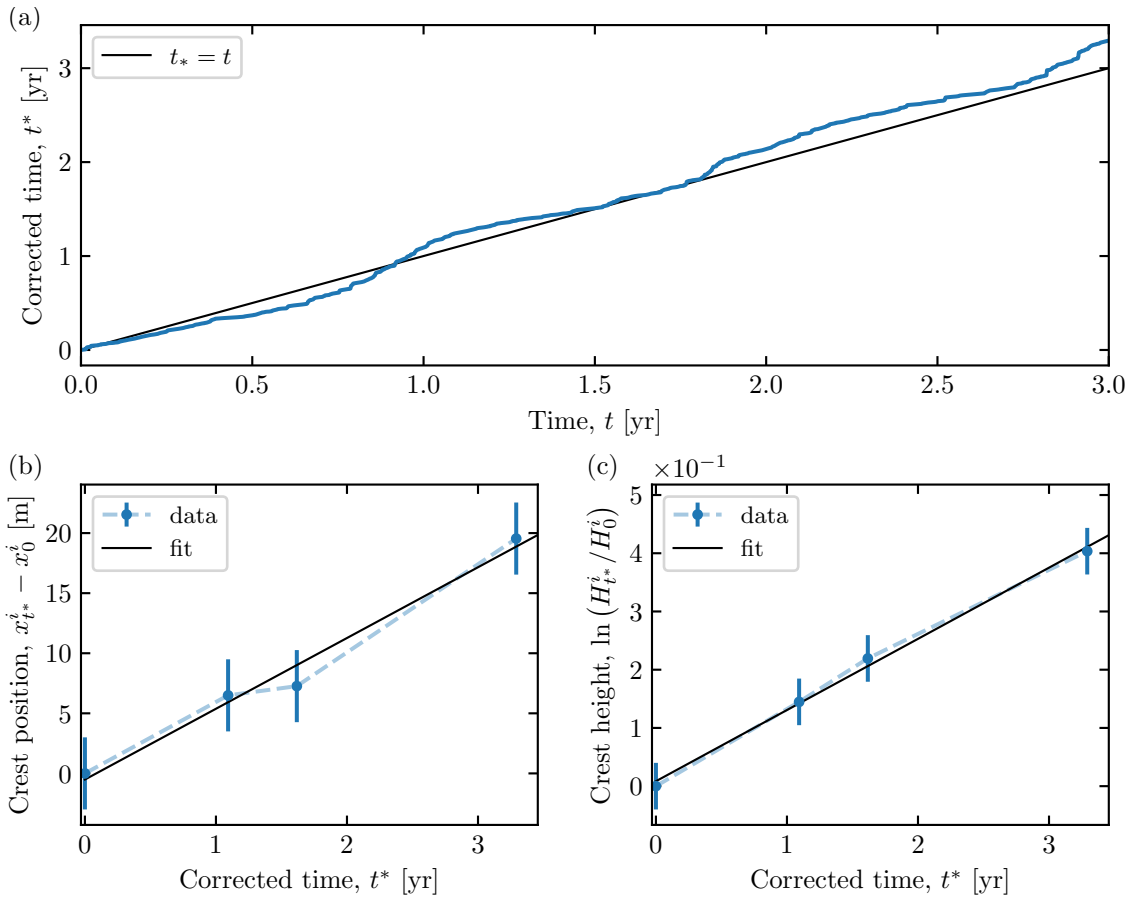

Figure 2.8 – (a) Corrected time as a function of real time. (b) Position of a bump crest with respect to time. The dashed line is a linear fit giving $c = 5.9$ m yr^{-1}. (c) Height log-ratio of a bump crest with respect to time. The dashed line is a linear fit giving $\varsigma = 0.012$ yr^{-1}. Errorbars come from the uncertainty due to the procedure for peak detection.

order of a hundred meters; their propagation velocity is around 5 m yr^{-1} and their growth rate is about 0.015 yr^{-1}. These values, as well as the typical dispersion around them (i.e. the width of these distributions), are more precisely reported in table 2.1. For λ and c, our results are consistent with the measurements of Phillips *et al.* (2019), made on a single elevation profile. Their dispersion is on the order of 20%, because these quantities can be measured with a good accuracy, especially with the global method using correlation. As the measurement of Λ and ς is more delicate, the corresponding distributions are more dispersed. The peak-to-peak method is actually sensitive to the behaviour of individual peaks, that can respond to various types of local disturbances. For example, they may induce irregularities in the spacing between the peaks, or asymmetry between positive and negative detrended topography (figure 2.4(a)). As a result, a few negative values of the velocity, growth rate and characteristic growth length are reported. Nevertheless, these data provide reliable and meaningful statistics to test the theory, which must be able to account for those four quantities concomitantly.

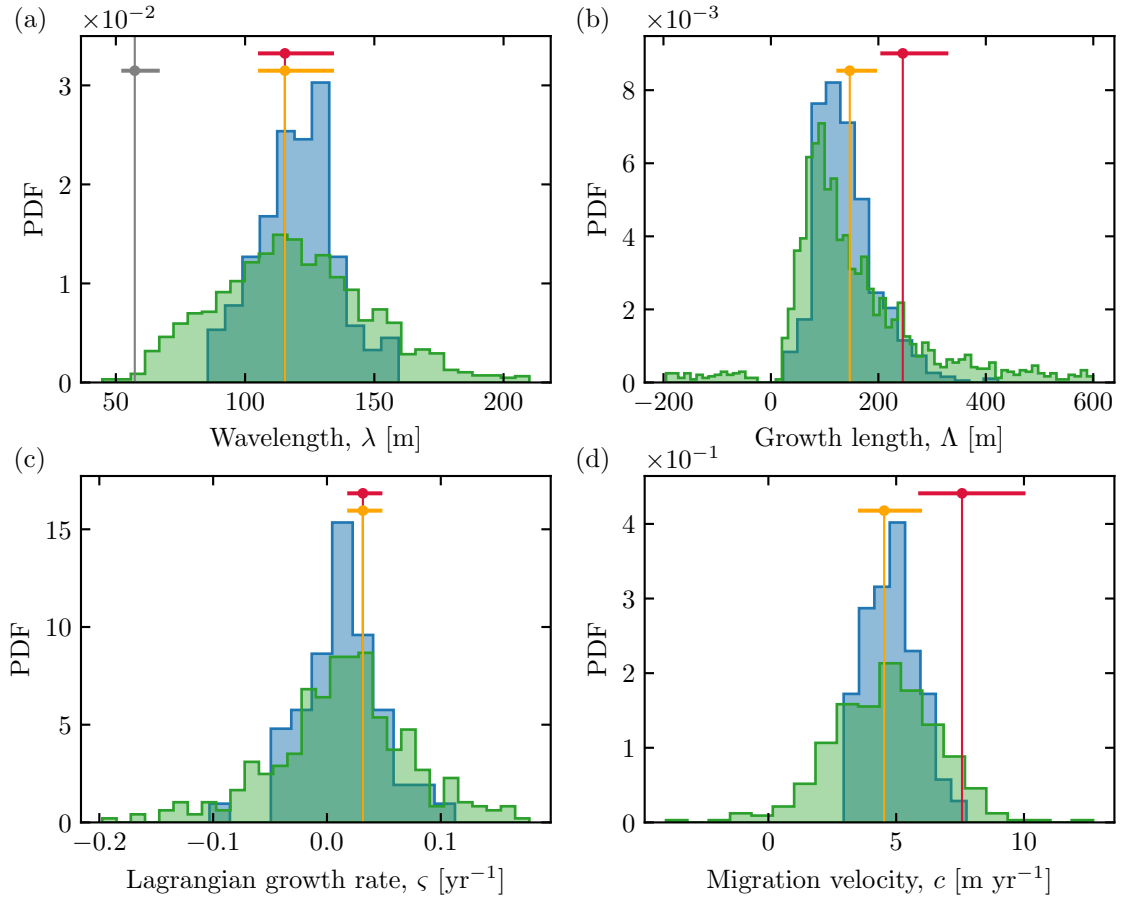

Figure 2.9 – Distributions of incipient dune time and length scales. Blue and green distributions shows the results of the global and peak-to-peak methods, respectively. Errorbars gives the range of values obtained from the spatial linear stability analysis with $\mathcal{A} = 3.6 \pm 0.6$ and $\mathcal{B} = 1.9 \pm 0.3$, and dots shows the average. Raw predictions based on a unidirectional wind are in red, and predictions taking into account the correction due to reversing winds are in orange (see table 2.1). The cut-off wavelength λ_c is in grey.

2.6.2 Comparison with theoretical data

The incipient dune wavelength peaks around 120 m, and is therefore significantly larger than the usually reported value ($\simeq$ 20 m, for sand particles of size 180 μm) (Elbelrhiti *et al.* 2005). How can the theory reproduce such a large value? First, as the wavelength is proportional to the saturation length, and thus to the grain size (equations 2.1, 2.12 and 2.13), the presence here of much coarser grains provides a factor $670/180 \simeq 3.7$ corresponding to the ratio between grains diameters. Second, the most unstable wavelength is predicted to increase when sediment transport occurs close to the threshold, in relation to the denominator of equation 2.12 (Andreotti *et al.* 2010, Charru *et al.* 2013). Here, with $u_*/u_{\rm th} \simeq 1.3$, we can expect an additional factor of 2 with respect to a situation far above threshold.

	Wavelength λ, (m)	Growth length Λ, (m)	Lagrangian growth rate ς, (yr^{-1})	Propagation velocity c , (m yr^{-1})
Data from global method				
Peak value	122	112	0.013	4.4
Peak width	19	70	0.036	1.5
Data from 'peak-to-peak' method				
Peak value	116	86	0.015	4.6
Peak width	80	125	0.06	3.2
Predictions under a unidirectional wind (red line in figure 2.9)				
Mean	115	245	0.032	7.6
Minimum	105	204	0.018	5.9
Maximum	134	330	0.049	10.1
Predictions with correction due to reversing winds (orange line in figure 2.9)				
Mean	115	147	0.032	4.5
Minimum	105	122	0.018	3.5
Maximum	134	197	0.049	6

Table 2.1 – Measured and predicted values of the characteristics of the emerging dune pattern. The peak value corresponds to the maximum of the smoothed distribution. The peak width is estimated at 3/4 of its height.

Inversion of the hydrodynamic coefficients

In order to compare the predictions of the spatial linear stability analysis to the field data, we need to set the hydrodynamic coefficients $\mathcal{A}$ and $\mathcal{B}$, as the others are set independently using the wind and sediment properties (see table 2.2). The field data are distributed around central values (see figure 2.9), due to the intrinsic variability in dune fields. It is important to note that linear stability analysis predicts such a variability: the initial noise is selectively amplified in a range of wavelengths around the maximum growth rate. Here, we perform an inversion analysis and we determine the most probable values of $\mathcal{A}$ and $\mathcal{B}$, given the observations, using a simple method. We consider values of wavelength, growth length, Lagrangian temporal growth rate and propagation velocity inside the following intervals, which are representative of the peaks of the distributions:

$$\lambda \in [100, 130] \text{ m}, \tag{2.35}$$

$$\Lambda \in [90, 250] \text{ m}, \tag{2.36}$$

$$\varsigma \in [0.0005, 1] \text{ yr}^{-1}, \tag{2.37}$$

$$c \in [3.5, 6.1] \text{ m yr}^{-1}. \tag{2.38}$$

From a quadruple $\{\lambda, \Lambda, \varsigma, c\}$, we compute the best tuple $\{\mathcal{A}, \mathcal{B}\}$, taking the optimum prediction from the equations developed in section 2.4.2. This method results in a distribution for the hydrodynamic coefficients $\mathcal{A}$ and $\mathcal{B}$, determined from the statistical variability of the dune field. It exhibits clear dominant values, slightly different from the average ones

Parameter	Notation	Value	Unit
Grain diameter*	d	670 ± 120	μm
Grain bulk density*	ρ_p	2300 ± 100	kg/m^3
Avalanche slope*	μ	0.8 ± 0.05	
Air density	ρ_f	1.2 ± 0.1	kg/m^3
Saturation length	L_sat	2.8 ± 0.5	m
Shear velocity ratio	u_*/u_th	1.26 ± 0.05	
Characteristic flux	Q	38 ± 5	m^2/yr

Table 2.2 – Parameters used for the linear stability analysis at the White Sands dune field. The star denotes direct measurements, while the others quantities are derived from measurements using calibrated laws. The air density is the value at 20°C, and the corresponding error includes corrections for elevation as well as for temporal variations in humidity and temperature.

due to the distribution shape. By taking the number of independent measurements into account, the error bars on $\mathcal{A}$ and $\mathcal{B}$ can be graphically represented by the ellipse of figure 2.10(a). The tilt of the ellipse shows that the hydrodynamic coefficients covary, which indicates a better precision on the ratio $\mathcal{B}/\mathcal{A}$ than on the individual values of $\mathcal{A}$ and $\mathcal{B}$.

Average and most probable values also depend on the fixed parameters Q, L_sat, μ and u_*/u_th, whose uncertainties are given in table 2.2. Taking those uncertainties into account results in multiple different distributions (see for example figure 2.10b). Note that all the corresponding ellipses have roughly the same sizes, fixed by the dispersion of the measured quantities. The ratio $\mathcal{B}_\mu/\mathcal{A}$ is robustly determined as it is in principle related to both λ/L_sat and Λ/L_sat. The stability analysis predicts that it should be constant, and independent of any other parameter:

$$\frac{\lambda_\mathrm{S}}{\Lambda_\mathrm{S}} \propto \frac{\lambda_\mathrm{T}\sigma_\mathrm{T}}{c_\mathrm{T}} \propto \frac{\mathcal{B}_\mu}{\mathcal{A}}, \tag{2.39}$$

Likewise, the theory also predicts that:

$$\frac{\lambda_\mathrm{S} c_\mathrm{S}}{Q} \propto \frac{\lambda_\mathrm{T} c_\mathrm{T}}{Q} \propto \mathcal{A}. \tag{2.40}$$

As a consequence, any uncertainty on $\langle Q_t \rangle$ results into an uncertainty on $\mathcal{A}$.

We therefore have two different sources of uncertainty; one resulting from the dispersion of the measured quantities, and one from the uncertainty on the fixed parameters. The value of L_sat is required to calculate λ and Λ, and directly affects the estimate of $\mathcal{B}/\mathcal{A}$. Likewise, the value of Q is required to calculate c, and mostly affects $\mathcal{A}$. Finally, the amplitude of the slope effect, $(1/\mu)(u_\mathrm{th}/u_*)^2$ directly affects $\mathcal{B}$, as $\mathcal{B}_\mu$ remains the same. The resulting uncertainty on hydrodynamic coefficients results from all contributions, leading to the final result: $\mathcal{A} = 3.6 \pm 0.6$ and $\mathcal{B} = 1.9 \pm 0.3$.

The simultaneous fit of the four quantities predicted by the spatial linear stability analysis to the data allows us to reproduce quantitatively the dominant wavelength and growth

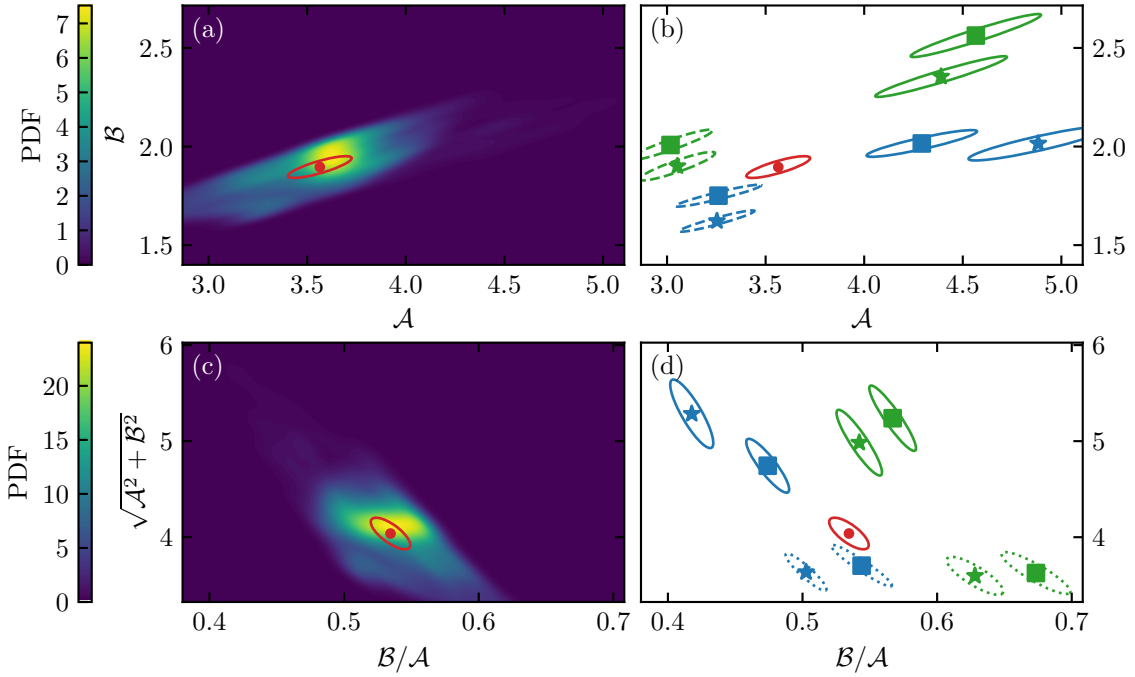

Figure 2.10 – Distributions of the hydrodynamic parameters resulting from the inversion process. (a) Contour lines of the distribution when the parameters Q, L_{sat}, μ and u_*/u_{th} are fixed to their mean value (Table 2.2). The markers represent the mean value, and the ellipse the confidence interval at 95%. (b) Variation of this ellipse when taking into account the uncertainty of the parameters given in table 2.2. Blue and green ellipses are for minimum and maximum plausible values of L_{sat}, respectively. Plain and dashed ellipses are for minimum and maximum plausible values of flux Q. Squares and stars are the mean values of the distributions for minimum and maximum plausible values of the slope effect $(1/\mu)(u_{\text{th}}/u_*)^2$. (c) and (d) are the same than (a) and (b), but represented in the space spanned by the modulus $\sqrt{\mathcal{A}^2+\mathcal{B}^2}$ and the ratio $\mathcal{B}/\mathcal{A}$.

rate. The predicted values fall in the peak of the distributions (red lines in figures 2.9(a) and 2.9(c)). This adjustment however overestimates the growth length and the propagation velocity, whose predictions exceed the dominant values by an amount comparable to the peaks' width (red lines in figures 2.9(b) and 2.9(d)).

Correction due to reversing winds

This discrepancy can be understood by questioning our approximation of a unidirectional wind. A finer analysis of the flux rose shows in fact secondary winds, with non-zero components perpendicular to the crest toward the southwest. Reversing winds have cumulative effects on the growth rate and the selected wavelength. They however partially cancel each other out, impeding the propagation, and thus the spatial development of the dune pattern (equation (2.27)). Such a process is supported by observations of reactivation surfaces formed by reversing winds in the stratigraphy at White Sands (Phillips *et al.* 2019, Kocurek *et al.* 2007). The value of the characteristic sand flux Q (given in table 2.2)

is a time average that does not account for changes in wind orientation. The ratio between the scalar and vector averages of Q, taking into account the variations in orientation of the sand fluxes over time, is about 0.6 (see appendix A.2). Once corrected by this ratio, the predicted migration velocity and growth length come into quantitative agreement with the corresponding dominant values of the distributions (orange lines in figure 2.9).

2.7 Discussion

The exponentially amplified sinusoidal behaviour of the White Sands bed elevation profiles is field evidence for the spatial development of the dune instability. The linear analysis is able to quantitatively reproduce the three characteristics of the emergent pattern: dune wavelength, propagation velocity, growth length (or equivalently Lagrangian growth rate). To obtain this agreement, the two hydrodynamic coefficients were adjusted, resulting in $\mathcal{A} = 3.6 \pm 0.6$ and $\mathcal{B} = 1.9 \pm 0.3$. All the other parameters of the theory were fixed independently from sediment and wind data, either by direct measurement (grain diameter and density, avalanche slope) or using well calibrated relationships (saturation length, sediment flux). Note that the uncertainty on the hydrodynamic coefficients is dominated by those of these parameters, rather than the dispersion in the measurements of λ, c, Λ and ς.

Importantlty, concomitant agreement of all four quantities is a stringent test of the theory. This study is therefore a step forward in the general 'dune inverse problem', trying to infer, for example, grain or wind properties from dune characteristics (Fenton *et al.* 2014a;b, Ewing *et al.* 2015, Runyon *et al.* 2017, Fernandez-Cascales *et al.* 2018). It is remarkable that the resulting values determined from our field data are very close to those directly measured by Claudin *et al.* (2013) on a single 40 m long dune ($\mathcal{A} \simeq 3.4$ and $\mathcal{B} \simeq 1.6$), as well as to the predictions of hydrodynamic models (Fourrière *et al.* 2010, Charru *et al.* 2013). Through the inversion process, these values depend on the theoretical framework used in this study. It thus supports the reliability of the linear analysis in the interpretation of field, experimental or numerical data relating to the emergence of incipient dunes (Elbelrhiti *et al.* 2005, Narteau *et al.* 2009, Fourrière *et al.* 2010).

A limitation of the linear theory is of course the presence of non-linear effects. They occur when the aspect ratio of the sand waves becomes too large or when the dunes interact with each other, so that each bed perturbation cannot be considered as independent of the others. Bumps with aspect ratios above $\simeq 1/13$ are expected to start to develop flow recirculation on their downwind side, usually associated with the formation of an avalanche slip face (Fourrière *et al.* 2010). In the region we have studied, the waves furthest inside the dune field could reach aspect ratios of about 1/10, but no slip faces were observed. Similar to Phillips *et al.* (2019), we also recognize the coexistence of multiple wavelengths at the upwind side of the profiles (associated with different celerities and growth rates or

lengths), and these are partly the cause of the distribution widths in figure 2.9. We could not, however, infer from these data signs of interactions, such as collisions, coalescence or ejection (Hersen & Douady 2005, Katsuki *et al.* 2005, Gao *et al.* 2015a, Bacik *et al.* 2020).

Although studied here at the boundary of a dune field, the spatial development of the dune instability is also present on pre-existing large dunes, providing a similar upwind boundary condition in terms of sand availability. As a matter of fact, the emergence of bed oscillations on the flanks of barchans has been proposed as a key mechanism to understand their stability, as these superimposed waves eventually grow until they can break from the horns, causing large sand losses (Elbelrhiti *et al.* 2005, Zhang *et al.* 2010, Lee *et al.* 2019). Likewise, in narrow bidirectional wind regimes, the growth of the instability over elongating linear dunes breaks them into trains of barchans (Gao *et al.* 2015b). This work therefore provides a reliable base to study the stability of large dunes and thus the formation of large-scale structures inside dune fields (Worman *et al.* 2013).

Chapter 3

Incipient dune growth under multidirectional winds

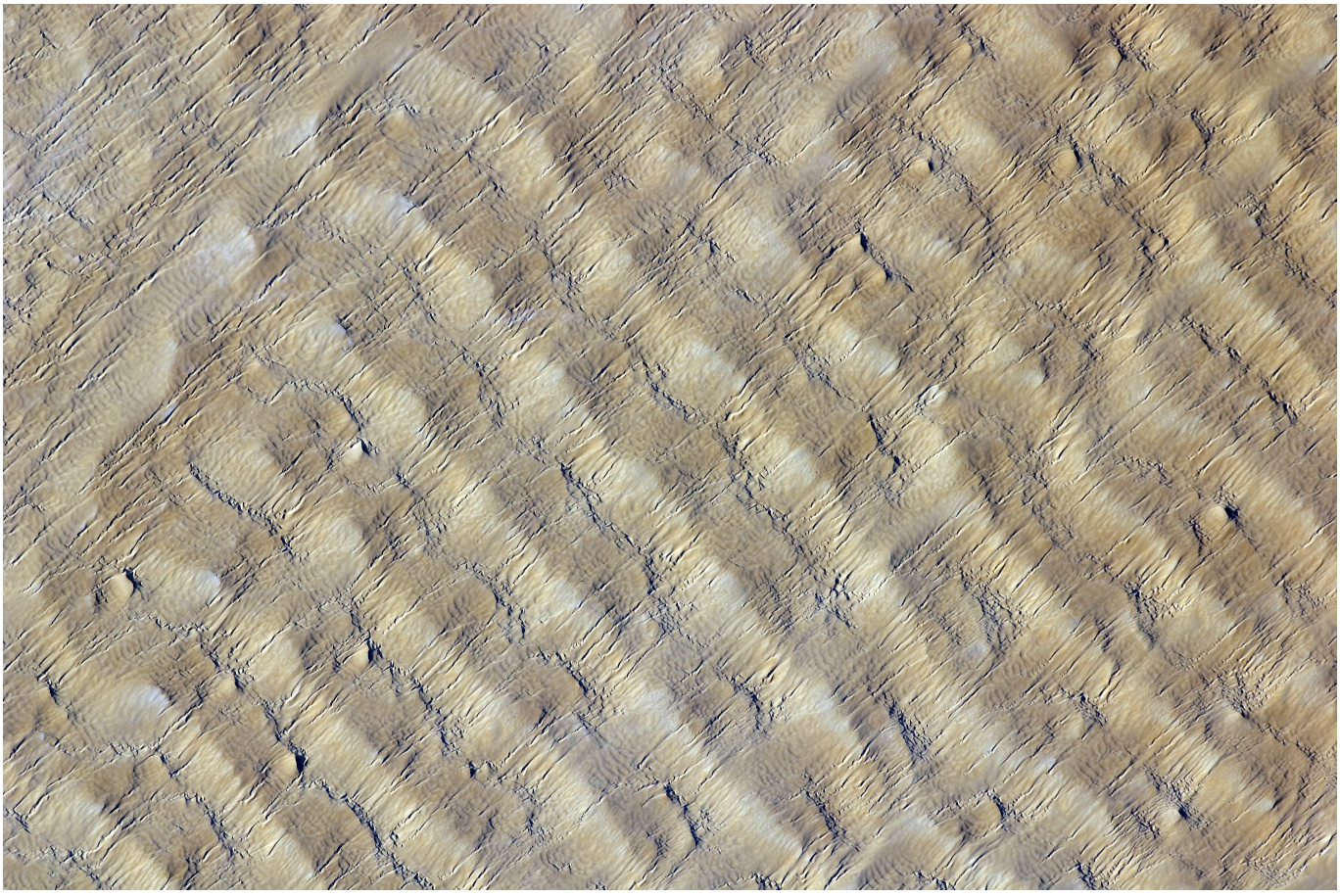

Astronaut photograph of a dune pattern, Tenere Desert, Niger - NASA's Earth Observatory

Contents

3.1 Abstract

Most terrestrial sand seas form at 'horse' latitudes, where the wind direction exhibits seasonal variation. Here, we extend the two-dimensional linear stability analysis of a flat sand bed associated with a unidirectional wind to the three-dimensional case in order to account for multidirectional wind regimes. Focusing on the simplest case of bidirectional flow regimes, we show that the transition from transverse to oblique or longitudinal patterns is controlled by the transport ratio and the divergence angle between the two flows. Our predictions agree with previous results for dune orientation, and also provide a wider range of possible alignments depending on flow strength, especially when the two winds are perpendicular, at which the transition occurs. This analysis also predicts the selected pattern wavelength, which either decreases close to the transition angle for strong winds, due to a geometric effect, or increases at low winds, when the bed slope affects the transport. This theoretical analysis is complemented by analogous subaqueous experiments and numerical simulations, where bedforms are submitted to alternate water flows. For transverse bedforms, the experimental data validate the model at strong flows, providing evidence for the predicted geometric effect, but also for the increase of the wavelength close to the transport threshold. For longitudinal bedforms, a discrepancy is observed, which we interpret as the sign of enhanced nonlinearities induced by the development of slip faces when the flow alternately blows on both sides of the dune.

3.2 Introduction

In chapters 1 and 2, we described dune emergence under a unidirectional wind regime. The early stage of the growth is now understood as resulting from a linear convective instability coupling topography, flow and sediment transport.

However, the variability in wind velocity and direction has been recognized as a key variable in understanding the diversity of observed dune patterns. While this variability is ubiquitous on Earth, dune morphodynamics in multidirectional wind regimes has been the subject of few quantitative studies, partly due to the difficulties in implementing experimental and numerical methods. Their main contribution relate to the dependence of the crest orientation of mature objects in sediment availability. In zones of loose sand, the orientation is the one that maximizes dune growth, following the *gross bedform normal transport rule*. In zones of limited sediment supply, the elongation mechanism dominates, and crests align with the resultant sand flux direction.

In the following, we present an extension of the linear stability analysis to bidirectional, and then multidirectional wind regimes. We compare its predictions to the model of Courrech du Pont *et al.* (2014), based on the *gross bedform normal transport rule*, and

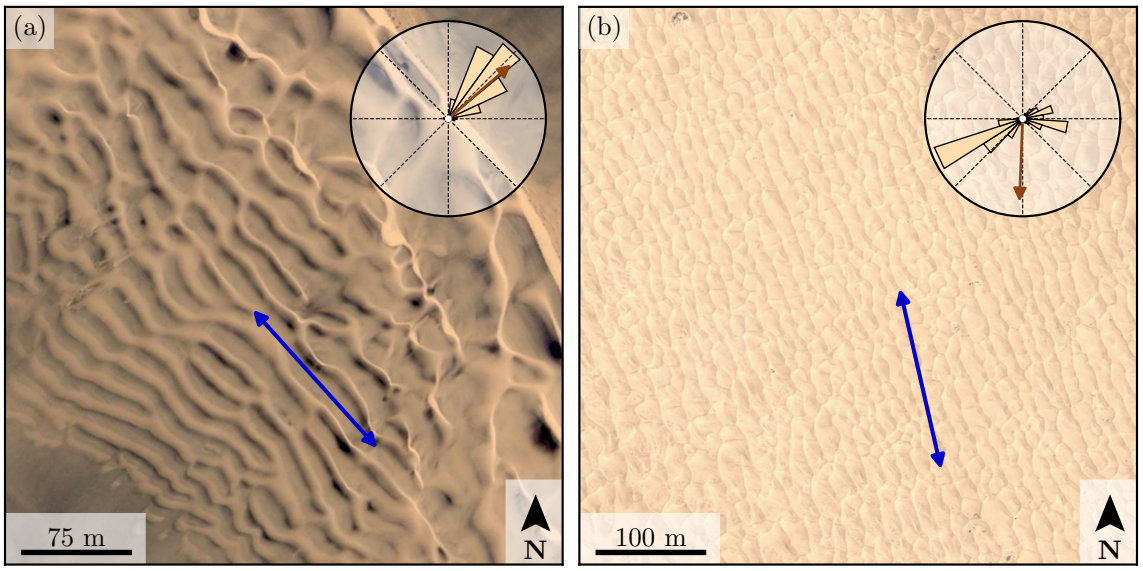

Figure 3.1 – Dune pattern for two different multidirectional wind regimes in (*a*) Angola, Namib desert (16°27′S 11°58′E), and (*b*) in China, Taklamakan desert (37°25′N 81°50′E). Sand flux roses are computed from the wind data of the ERA-Interim project, the latest global atmospheric reanalysis produced by the European Center for Medium-Range Weather Forecasts (Uppala & et al. 2005, Dee *et al.* 2011). Brown arrow: corresponding resultant sand flux direction. Blue arrow: corresponding prediction of the pattern orientation maximizing the growth rate (3.61). Satellite images: Google^{TM}, Maxar Technologies.

then test it with respect to underwater experiments and numerical simulations. Most of the work presented in this section has already been published in *Journal of fluid mechanics* (Gadal *et al.* 2019).

3.3 Extension of the linear stability analysis to bidirectional wind regimes

3.3.1 Brief summary of the growth under a unidirectional wind

Before extending the linear stability analysis to multidirectional flows, we first consider the interaction of a unidirectional wind with a sinusoidal bed whose crests make an arbitrary angle with respect to the wind direction, i.e without invariance of the problem in the cross stream direction. Fortunately, this has already been investigated in the study of underwater ripple, chevrons and antidunes (Devauchelle *et al.* 2010, Andreotti *et al.* 2012a). Note that in our case, the problem is much simpler. Incipient aeolian dunes do not interact the convective atmospheric boundary layer when emerging, and aeolian flows are typically subcritical ($Fr \ll 1$), such that the influence of the free surface can be neglected.

We consider a unidirectional wind blowing in the x-direction above a flat sand bed. The y-direction is the transverse coordinate in the horizontal plane and the z-direction is

vertical. To investigate the linear stability analysis of the flat bed, we aim to compute the temporal evolution of a sinusoidal perturbation of the surface, whose elevation profile is of the form

$$Z = \zeta e^{ik(\cos\alpha x + \sin\alpha y - ct) + \sigma t}, \tag{3.1}$$

where α is the angle between the wavevector $\boldsymbol{k} = (k\cos\alpha, k\sin\alpha)$ and the flow direction, as sketched in figure 3.2(a). We then compute the dispersion relations $\sigma(\alpha, k)$ and $c(\alpha, k)$ following Andreotti *et al.* (2012a).

Turbulent flow over a sinusoidal bottom

Denoting by a hat $\hat{\cdot}$ the Fourier transform of the variables, the x- and y- components of the bed shear stress perturbation induced by the undulated bed (3.1) can be written as:

$$\hat{\tau}_x = \tau\,(\mathcal{A}_x + i\mathcal{B}_x)\,k\hat{Z} \qquad \text{and} \qquad \hat{\tau}_y = \tau\,(\mathcal{A}_y + i\mathcal{B}_y)\,k\hat{Z}, \tag{3.2}$$

where $\{\mathcal{A}_x, \mathcal{A}_y\}$ and $\{\mathcal{B}_x, \mathcal{B}_y\}$ are the in-phase and in-quadrature components of the stress perturbation with respect to the topography, respectively. These coefficients are functions of the wavenumber, and can be numerically derived from the linearisation of a turbulent model based on the Navier-Stokes equations on a steady sinusoidal bed (see the supplementary material of Andreotti *et al.* (2012a)). However, this dependence can be neglected for small wavenumbers ($kL_{\text{sat}} \ll 1$), which is is typically the case for aeolian dunes where $kL_{\text{sat}} \simeq 10^{-4}$ (see section 1.3.1). For the sake of simplicity, we then use the approximate but analytical expressions:

$$\mathcal{A}_x = \mathcal{A}_0 \cos^2\alpha, \tag{3.3}$$

$$\mathcal{B}_x = \mathcal{B}_0 \cos^2\alpha, \tag{3.4}$$

$$\mathcal{A}_y = \frac{1}{2}\mathcal{A}_0 \cos\alpha \sin\alpha, \tag{3.5}$$

$$\mathcal{B}_y = \frac{1}{2}\mathcal{B}_0 \cos\alpha \sin\alpha, \tag{3.6}$$

where $\{\mathcal{A}_0, \mathcal{B}_0\}$ are the coefficients when the dune crests are perpendicular to the flow ($\alpha = 0°$). The dependence of these coefficients on α corresponds to the scaling of the velocity for a potential flow over a sinusoidal topography (B.18), i.e. in the outer layer where the fluid inertia is balanced by the pressure gradient (Andreotti *et al.* 2012a). The factor 1/2 in the transverse direction is due to the variation of the shear stress as the square of the velocity, which is a common approximation for turbulent flows. Here we use $\mathcal{A}_0 = 3.5$ and $\mathcal{B}_0 = 2$, as measured in the field on a flat transverse dune (Claudin *et al.* 2013).

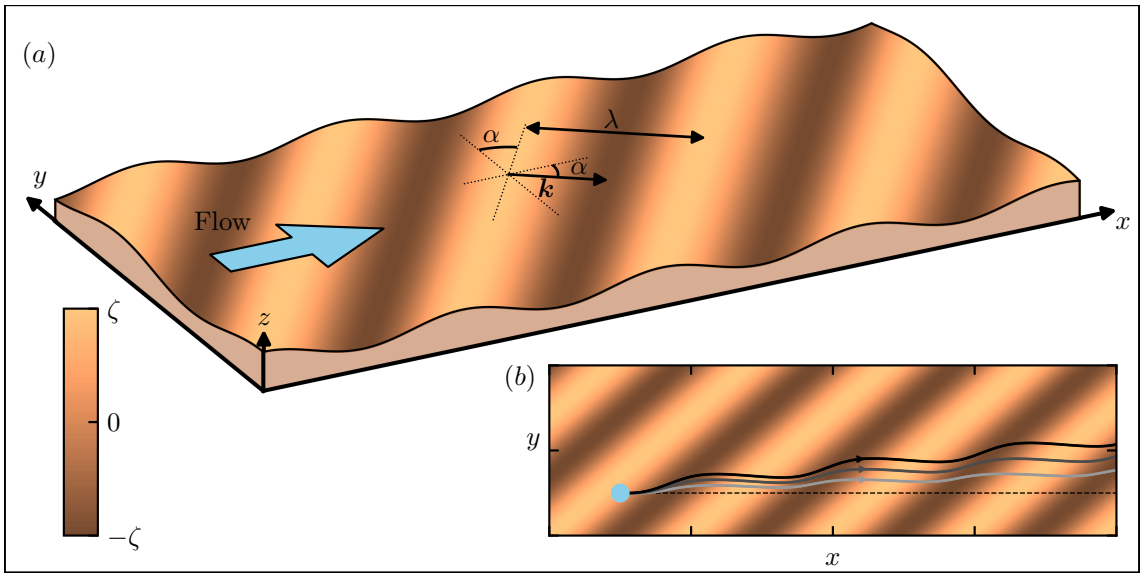

Figure 3.2 – Sinusoidal sand bed. (*a*) Sketch in a perspective view. The base flow is in the direction of the x-axis. The crest lines make an angle α with respect to the transverse y-axis. The colour bar indicates the bed elevation. (*b*) Top view. Solid lines are lines tangent to the transport direction $\boldsymbol{t}$ (here for $k\zeta = 0.25$). Lines from light to dark greys encode increasing values of the velocity ratio $u_*/u_{\rm th} \in \{1.6, 2.5, 5\}$. For reference, the dashed line shows the direction of transport over transverse bedforms ($\alpha = 0°$).

Sediment transport

Sediment transport can be described almost as developed in chapter 1. The equations relating the sand flux to the basal shear stress still write, in a vectorial form to account for both x- and y- components of the flux,

$$\boldsymbol{q}_{\rm sat} = \Omega\,(\tau - \tau_{\rm th})\,\boldsymbol{t}, \tag{3.7}$$

and

$$L_{\rm sat}\,(\boldsymbol{t}\cdot\nabla)\,\boldsymbol{q} = \boldsymbol{q}_{sat} - \boldsymbol{q}. \tag{3.8}$$

Here Ω is a dimensional constant, and $\boldsymbol{t}$ is the saturated flux direction (corresponding to the direction of the flow $\boldsymbol{e}_x$ for a flat sand bed). In subaqueous environments where bedload is the dominant mode of transport, the sediment flux varies with the bed shear stress with an exponent 3/2 as $q_{\rm sat} \propto \sqrt{\tau/\tau_{\rm th}}\,(\tau - \tau_{\rm th})$ (Bagnold 1956, Meyer-Peter & Müller 1948, Durán *et al.* 2012). However, the results of the linear stability analysis do not qualitatively depend on the exponent of the transport law.

The transport threshold, which can be expressed in terms of a shear stress τ_{th} or a velocity u_{th}, is defined as $\tau_{th} \equiv \rho_f u_{th}^2$. For a flat bed with a longitudinal slope $\partial_x Z$, this threshold is modified at the linear order in $k\zeta$ as $\tau_{th}(1 + \partial_x Z/\mu)$, where μ is an effective friction coefficient corresponding to the avalanche slope $\mu \simeq \tan(35°) = 0.7$. This slope

effect has been calibrated for both saltation (Hardisty & Whitehouse 1988, Iversen & Rasmussen 1999) and bedload transport (Dey 2003, Fernandez Luque & Van Beek 1976, Loiseleux *et al.* 2005).

At the linear order, the transverse slope $\partial_y Z$ has no impact on the threshold value but affects the transport direction. Following Andreotti *et al.* (2012b), in analogy with a sliding frictional disc on an inclined surface, particles are driven by the flow but also attracted downwards in the direction of the steepest slope by gravity. This results in a transport direction that reads

$$\boldsymbol{t} = \boldsymbol{e}_x + \left(\frac{\tau_y}{\tau} - \frac{1}{\mu_y} \frac{u_{\mathrm{th}}}{u_*} \partial_y Z \right) \boldsymbol{e}_y. \tag{3.9}$$

This behaviour has been tested for bedload transport by Sekine & Parker (1992), showing that the coefficient μ_y is also equal to the avalanche slope μ. However, saltating grains may have a different dynamics because they are not in permanent contact with the bed. In contrast with the case of longitudinal slope, there are no available experimental data to calibrate (3.9). This expression accounts, however, for the correct symmetry and trend with respect to $\partial_y Z$. For the sake of simplicity, we then also take $\mu_y = \mu = \tan(35°)$, but we keep in mind that this may overestimate the impact of the bed transverse slope on the direction of the saltation flux.

The flux deviates from the direction of the base flow $\boldsymbol{e}_x$, due to the y-component of the shear stress induced by the oblique perturbation. This deflection is maximum at large flow velocity, but it is reduced close to the transport threshold by the slope effect. We thus show lines following the transport direction for different velocity ratios u_*/u_{th} in figure 3.2(b). At wind velocities far from the threshold, the lines directly follow the shear stress direction. Just like the upwind shift of the maximum shear stress, this deviation results from the combination of inertia and dissipation. Above such a topography, an inertial flow is deflected symmetrically due to the pressure differences between the crests and the troughs (see figure B.1). However, due to the coupling with turbulent dissipation, the shear stress is higher just upstream of the crest (see section 1.3.1). This shortens the upwind path and lengthens the downwind path. Then, the time spent in the downwind side is longer, and the associated deviation prevails, leading to larger deviations on the lee side of the ridges. Close to the transport threshold, the slope affects the transport direction, reducing the drift in the lee zones. The corresponding lines are therefore closer to the base line.

Growth rate and most unstable mode

Following Andreotti *et al.* (2012a), we couple the equations for the flow and sediment transport with the evolution of the bed elevation profile, governed by the sediment mass

conservation equation (see section 1.3). To deal with dimensionless quantities, we rescale lengths by L_{sat} and times by L_{sat}^2/Q, where Q is the reference flux $Q = \rho_f \Omega u_*^2$. The dispersion relations can then be expressed in a dimensionless form as

$$\sigma = \frac{k^2}{1+(k\cos\alpha)^2}\left[b_x\cos\alpha + b_y\sin\alpha - k\cos\alpha\left(a_x\cos\alpha + a_y\sin\alpha\right)\right], \tag{3.10}$$

$$c = \frac{k}{1+(k\cos\alpha)^2}\left[a_x\cos\alpha + a_y\sin\alpha + k\cos\alpha\left(b_x\cos\alpha + b_y\sin\alpha\right)\right], \tag{3.11}$$

where the coefficients are

$$a_x = \mathcal{A}_x, \tag{3.12}$$

$$b_x = \mathcal{B}_x - \cos\alpha\frac{1}{\mu}\frac{u_{\mathrm{th}}^2}{u_*^2}, \tag{3.13}$$

$$a_y = \left(1 - \frac{u_{\mathrm{th}}^2}{u_*^2}\right)\mathcal{A}_y, \tag{3.14}$$

$$b_y = \left(1 - \frac{u_{\mathrm{th}}^2}{u_*^2}\right)\left(\mathcal{B}_y - \sin\alpha\frac{1}{\mu}\frac{u_{\mathrm{th}}}{u_*}\right). \tag{3.15}$$

Plugging the stress coefficients ((3.3)-(3.6)) into the expression for the growth rate, we obtain

$$\sigma = \frac{(k\cos\alpha)^2}{1+(k\cos\alpha)^2}\left[\mathcal{B}_0\cos\alpha\left(1+\frac{r\tan^2\alpha}{2}\right) - \frac{1}{\mu}\frac{u_{\mathrm{th}}}{u_*}\left(\frac{u_{\mathrm{th}}}{u_*} + r\tan^2\alpha\right)\right. \tag{3.16}$$

$$\left. - k\cos\alpha\mathcal{A}_0\cos\alpha\left(1+\frac{r\tan^2\alpha}{2}\right)\right], \tag{3.17}$$

where $r \equiv 1 - (u_{\mathrm{th}}/u_*)^2$ quantifies the transport in the direction transverse to the flow (equations (3.9), (3.14) and (3.15)). This function σ is shown in figure 3.3 in the plane (α, k) for the velocity ratios $u_*/u_{\mathrm{th}} = 1.6$ and $u_*/u_{\mathrm{th}} = 2.5$. The growth rate is positive (unstable modes) for small wavenumbers (large wavelengths) and transverse flows ($\alpha \to 0$). Large wavenumbers are stabilised by the flux relaxation process; longitudinal modes are stabilised by the slope effect on the transport direction. The marginal mode ($\sigma = 0$) corresponds to the cutoff wavenumber

$$k_{\mathrm{c}}(\alpha) = \frac{1}{\cos\alpha\mathcal{A}_0}\left[\mathcal{B}_0 - \frac{\frac{u_{\mathrm{th}}}{u_*}\left(\frac{u_{\mathrm{th}}}{u_*} + r\tan^2\alpha\right)}{\mu\left(1+\frac{r}{2}\tan^2\alpha\right)}\right]. \tag{3.18}$$

The selected pattern is the one that maximises the growth rate, and we denote its wavenumber by $k_{\max}$ and its orientation by $\alpha_{\max}$. Taking the derivative of the growth rate (3.10) with respect to k at constant α, the most unstable wavenumber k_α for a given dune orien-

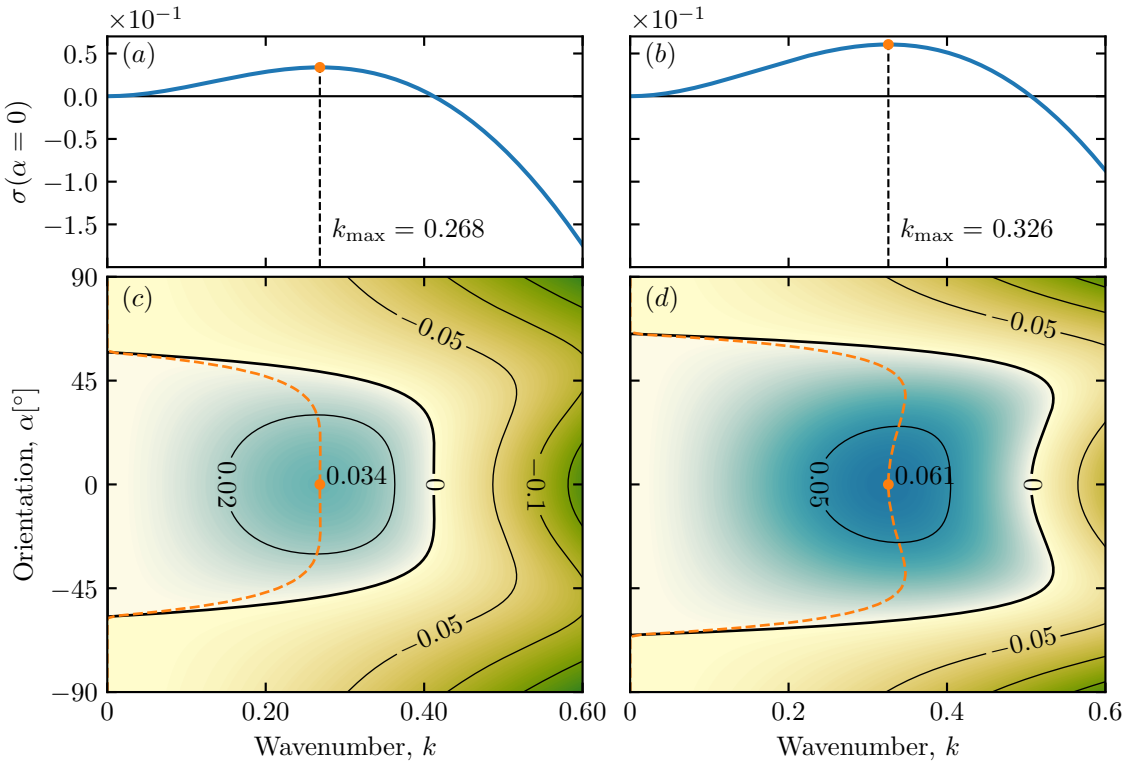

Figure 3.3 – Growth rate σ as a function of the wavenumber k and the orientation angle α of the bed perturbation, for $u_*/u_{\text{th}} = 1.6$ (a, c) and $u_*/u_{\text{th}} = 2.5$ (b, d). (a, b): reference transverse case $\alpha = 0°$. (c, d): growth rate in the plane (α, k) with contour lines as indicated. Orange dashed line: location of the maximum growth rate for each α. Orange dot: global maximum growth rate, corresponding to the most unstable mode $(\alpha_{\text{max}}, k_{\text{max}})$. Here, for a unidirectional wind regime, $\alpha_{\text{max}} = 0°$, independently of u_*/u_{th}.

tation satisfies

$$k_\alpha = \frac{1}{\cos\alpha}\left(X^{1/3} - X^{-1/3}\right), \tag{3.19}$$

where:

$$X = \sqrt{1 + [\cos\alpha k_c(\alpha)]^2} + \cos\alpha k_c(\alpha). \tag{3.20}$$

As the saturation length is significantly smaller than the dune wavelength, we can expand the above expressions in the limit $k_c(\alpha) \ll 1$, and we obtain:

$$k_\alpha \sim \frac{2}{3} k_c(\alpha). \tag{3.21}$$

The overall unstable mode is then $k_{\max} = k_{\alpha_{\max}}$. Under a unidirectional flow, the selected orientation is perpendicular to the flow, i.e $\alpha_{\max} = 0°$, which gives

$$k_{\max} \sim \frac{2}{3} k_c(0) = \frac{2}{3\mathcal{A}_0}\left(\mathcal{B}_0 - \frac{1}{\mu}\frac{u_{\text{th}}^2}{u_*^2}\right), \tag{3.22}$$

in agreement with the results of the two-dimensional linear stability analysis (Andreotti *et al.* 2002a, Fourrière *et al.* 2010, Charru *et al.* 2013).

Importantly, we see that the unstable mode exists only if the velocity ratio u_*/u_{th} is larger than $1/(\sqrt{\mathcal{B}_0\mu})$. This condition is always satisfied with the above values of $\mathcal{B}_0$ and μ because $1/(\sqrt{\mathcal{B}_0\mu}) \simeq 0.8 < 1 \leq u_*/u_{\text{th}}$. Another related effect is that the selected wavelength $\lambda_{\max} = 2\pi/k_{\max}$ tends to increase close to the threshold $u_*/u_{\text{th}} \to 1$.

For infinitely large values of this velocity ratio, the slope effect on the transport direction vanishes and suppresses the stabilisation of longitudinal modes, so that σ diverges in the double limit $k \to +\infty$ and $\alpha \to \pm 90°$. Numerically, for the adopted values of $\mathcal{A}_0$, $\mathcal{B}_0$ and μ, the regular shape of the growth rate, with a well-defined global maximum, is lost above $u_*/u_{\text{th}} \gtrsim 15$ (an unrealistic regime in practice). However, the coherence of the model is recovered by taking into account cross-stream diffusion, as discussed later in section 3.5.1.

3.3.2 Linear contribution to the growth rate

We consider two wind directions making an angle θ, called the divergence angle, whose bisector defines the x-axis (figure 3.4). The wind blows alternately in directions of the unitary vectors $\boldsymbol{e}_1$ and $\boldsymbol{e}_2$ over durations t_1 and t_2, and with reference fluxes Q_1 and Q_2. In this bidirectional flow regime, we define the resultant flux $\boldsymbol{Q}_\Sigma$ as

$$\boldsymbol{Q}_\Sigma = \frac{t_1}{t_1 + t_2} Q_1 \boldsymbol{e}_1 + \frac{t_2}{t_1 + t_2} Q_2 \boldsymbol{e}_2. \tag{3.23}$$

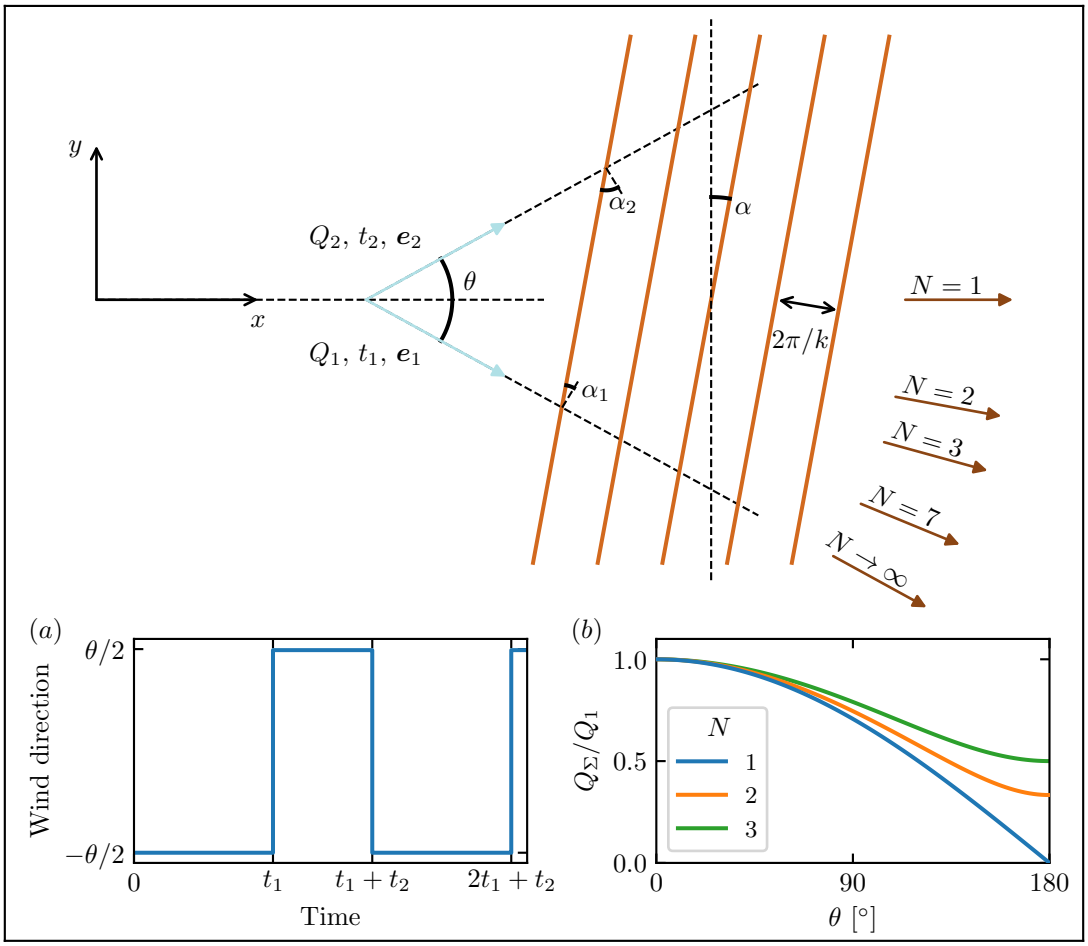

Figure 3.4 – Characteristics of a bidirectional flow regime. The sketch shows the geometry of the system. The x-axis is defined as the bisector of the divergence angle θ between the two wind directions (black arrows, unit vectors $\boldsymbol{e}_{1,2}$). For the linear stability analysis, we consider a sinusoidal mode characterised by a wavenumber k and an angle α with respect to the transverse direction (y-axis). The brown arrows are the directions of the resultant sand flux $\boldsymbol{Q}_\Sigma$ (3.23) corresponding to different values of the transport ratio $N = (Q_1 t_1)/(Q_2 t_2)$. Inset (a): alternation between the two wind directions with respect to time. Inset (b): variation of the amplitude of the resultant flux Q_Σ for $Q_1 = Q_2$ as a function of θ.

The intensity of this flux decreases with θ as the two winds compensate each other (figure 3.4(b)). We also define a time-averaged reference flux as

$$Q = \frac{t_1}{t_1 + t_2} Q_1 + \frac{t_2}{t_1 + t_2} Q_2. \tag{3.24}$$

The period of wind reorientation $t_1 + t_2$ is assumed to be small in comparison to the characteristic growth time of the bed perturbation of the order of $(1/\sigma_{\max}) L_{\text{sat}}^2/Q$ (Rubin & Ikeda 1990). Thus, the flow changes direction many times while the dune is still in its linear growth regime, during which its orientation and wavelength remain constant. The growth rate σ_Σ of a mode characterised by (α, k) can then be expressed as the sum of the contributions of each wind:

$$\sigma_\Sigma = \frac{1}{N+1}\Big[N\sigma(Q_1, \alpha_1, k) + \sigma(Q_2, \alpha_2, k)\Big], \tag{3.25}$$

where $N = (Q_1 t_1)/(Q_2 t_2)$ is the transport ratio between the two winds (Rubin & Hunter 1987, Rubin & Ikeda 1990, Reffet *et al.* 2010, Courrech du Pont *et al.* 2014). The growth rates $\sigma(Q_{1,2}, \alpha_{1,2}, k)$ are computed from that derived under a unidirectional flow (3.17) using

$$\alpha_{1,2} = \Big[(\alpha \pm \frac{\theta}{2} + 90^\circ) \mod 180^\circ\Big] - 90^\circ, \tag{3.26}$$

which are the angles between the pattern and the perpendicular to each flow direction (figures 3.2 and 3.4). For simplicity, we further assume that the winds blow with the same shear velocity u_*, so that $Q_1 = Q_2 = Q$. As a consequence, different values of N correspond to different blowing times.

The growth rate σ_Σ and the location of its maximum $(\alpha_{\max}, k_{\max})$ are shown in figure 3.5 for some values of N and θ. This maximum integrates the effect of the two winds and gives the orientation and wavenumber of the emerging dune pattern. These selected dune orientations and wavelengths are the main output of the analysis. A third output is the propagation velocity of the selected mode. In the next subsections, we quantitatively discuss the behaviour of these selected quantities with respect to N, θ and u_*/u_{th}.

3.3.3 Selection of the pattern orientation

As shown in figure 3.6, the orientation of the most unstable mode changes from transverse ($\alpha_{\max} \approx 0^\circ$) when the divergence angle θ is small, to longitudinal ($\alpha_{\max} \approx -90^\circ$) when the winds tends to be opposite (large divergence angle). This transition is the signature of a change in the normal to the crest fluxes (Rubin & Hunter 1987, Courrech du Pont *et al.* 2014). When the divergence angle is smaller than 90°, the crests are more likely to be perpendicular to the resulting flux, as the sand is mainly transported along the x-direction. By contrast, when the divergence angle is larger than 90°, the crests are more likely to be

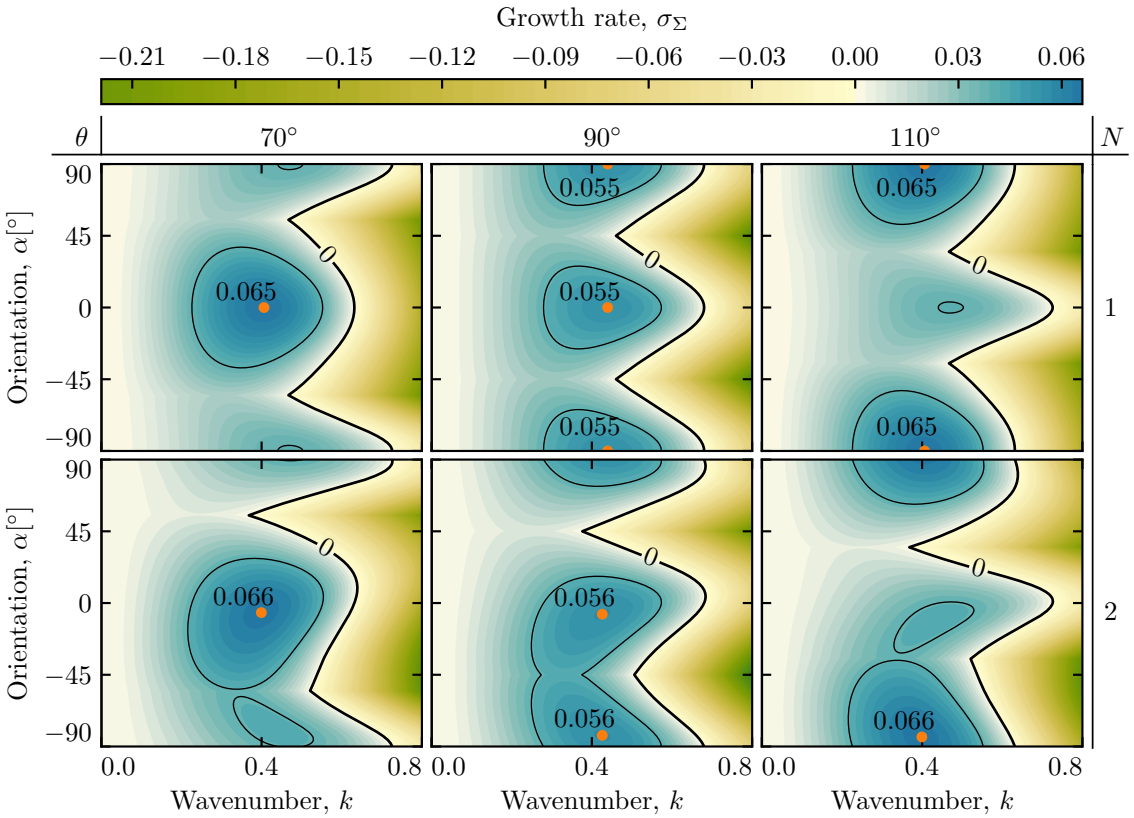

Figure 3.5 – Growth rate σ_Σ as a function of the wavenumber k and the orientation α of the bed perturbation for $u_*/u_{\text{th}} = 5$ and different values of the divergence angle θ (columns) and the transport ratio N (rows). Orange dots: most unstable mode $(\alpha_{\max}, k_{\max})$. The contour line corresponds to $\sigma_\Sigma = 0.039$.

aligned with the resulting flow as the sand is mostly transported along the y-direction. As discussed below, this transition depends on the transport ratio N and the velocity ratio u_*/u_{th}.

Let us first consider a fixed wind strength ($u_*/u_{\mathrm{th}} = 1.6$ in figure 3.6(a)) and discuss the effect of N. For winds of the same transport capacity ($N = 1$), the switch occurs at the transition angle $\theta = 90°$, with a discontinuous jump from a pattern perpendicular to the resultant flux direction ($\alpha_{\mathrm{max}} = 0°$) to a pattern aligned with the resultant flux direction ($\alpha_{\mathrm{max}} = -90°$). This transition from a purely transverse to a purely longitudinal dune orientation is specific to the case $N = 1$. When one of the two winds transports more than the other ($N > 1$), intermediate orientations (oblique patterns) more perpendicular to the prevailing wind are permitted. There is still a discontinuous transition at the transition angle, but the jump decreases in amplitude as N increases. This discontinuity is associated with two distinct maxima of equal growth rates (figure 3.5, central column). In the limit of unidirectional flows ($N \to +\infty$), the variation of α_{max} tends to a continuous linear function, which simply corresponds to the orientation perpendicular to the dominant wind.

The effect of the velocity ratio u_*/u_{th}, displayed in figure 3.6 with light grey regions, can be summarised as follows. Strong winds tend to enhance the orientation discontinuity at $\theta = 90°$, keeping α_{max} either closer to 0° ($\theta < 90°$) or to −90° ($\theta > 90°$). This corresponds to a selected orientation less perpendicular to the prevailing wind. By contrast, winds close to the threshold reduce this discontinuity, with orientations closer to the perpendicular to the prevailing wind. When $u_*/u_{\mathrm{th}} \gg 1$, slope effects become negligible and oblique modes stabilised by transverse transport are less damped for large velocity ratios u_*/u_{th} (figure 3.3 in the case of a unidirectional wind). When the growth rates associated with the two winds are combined, the 'cost' to remain away from the perpendicular to the prevailing wind is not so strong, and the selected orientation reflects this trend. When $u_*/u_{\mathrm{th}} \to 1$, slope effects are strong, and mainly affect longitudinal transport, i.e. the coefficient b_x (3.13), where two terms compete. The first one, of hydrodynamic origin, scales with $\cos^2 \alpha_{1,2}$, as deduced from the properties of the potential flow. The second one is related to the variation of the threshold with the slope, i.e. proportional to $-\cos \alpha_{1,2}$. This difference in the dependence with $\alpha_{1,2}$ favours a crest orientation perpendicular to the prevailing wind, for which the destabilizing hydrodynamics is the strongest.

3.3.4 Comparison with the dimensional analysis of Courrech du Pont *et al.* (2014)

The prediction of the dune orientation by this linear stability analysis can be directly compared to that of Courrech du Pont *et al.* (2014). Based on an estimation of the sand flux at the dune crest, these authors computed by dimensional analysis the dune growth rate accounting for the wind speed-up by the topography (see section 1.5.2).

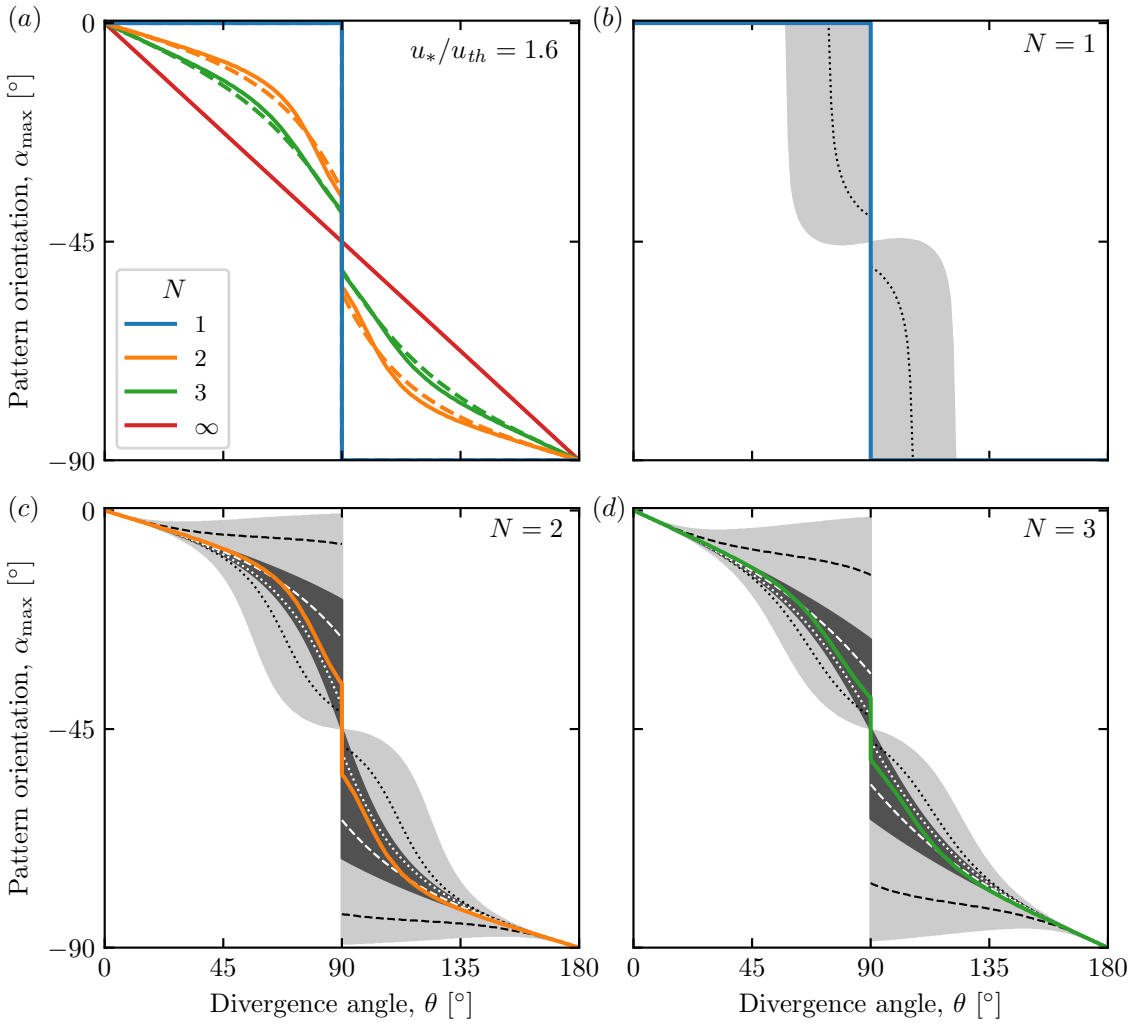

Figure 3.6 – Pattern orientation $\alpha_{\max}$ as a function of the divergence angle θ for various transport N and velocity u_*/u_{th} ratios. (*a*) Solid lines: predictions of the linear stability analysis for $u_*/u_{\text{th}} = 1.6$. Dashed lines: predictions of Courrech du Pont *et al.* (2014) for $\gamma = 1.7$. (*b-d*) Solid lines: reference curves shown in (*a*) for $u_*/u_{\text{th}} = 1.6$. Dashed and dotted black lines: predictions of the linear stability analysis for $u_*/u_{\text{th}} = 5$ and $u_*/u_{\text{th}} = 1.2$, respectively. Dashed and dotted white lines: predictions of Courrech du Pont *et al.* (2014) for $\gamma = 0.5$ and $\gamma = 5$, respectively. Light grey region: all possible orientations predicted by this analysis when u_*/u_{th} is increased from 1.005 to 15. Dark grey region: all possible orientations predicted by Courrech du Pont *et al.* (2014) when γ is varied from 0 to $+\infty$ (3.31). Note that, in the strict case of $N = 1$, the growth rate has an equal maximum for $(-\alpha_{\max}, k_{\max})$.

The model of Courrech du Pont *et al.* (2014) in our notations

Following what we presented in section 1.5.2, we derive here the dune growth rate following the dimensional analysis of Courrech du Pont *et al.* (2014), expressed with our notation and conventions. Considering an infinitely long linear dune of height Z and width W, the fluxes associated with each of the two winds can be expressed as

$$\boldsymbol{Q}_1 = Q_0\left(1+\beta\frac{Z}{W_1}\right)\boldsymbol{e}_1 = Q_0\left(1+\gamma\cos\alpha_1\right)\boldsymbol{e}_1, \tag{3.27}$$

$$\boldsymbol{Q}_2 = Q_0\left(1+\beta\frac{Z}{W_2}\right)\boldsymbol{e}_2 = Q_0\left(1+\gamma\cos\alpha_2\right)\boldsymbol{e}_2, \tag{3.28}$$

where $W_{1,2} = W/\cos\alpha_{1,2}$ are the widths of the dune in the direction of each of the winds. The flux-up ratio γ linearly depends on the dune aspect ratio Z/W with a prefactor β and accounts for the wind increase at the dune crest. Following the mass conservation equation, the dune growth rates associated with each of the two winds are related to the divergence of those fluxes,

$$\sigma_1 = -\frac{1}{Z}\nabla\cdot\boldsymbol{Q}_1 \approx \frac{1}{Z}\frac{Q_1}{W_1}, \tag{3.29}$$

$$\sigma_2 = -\frac{1}{Z}\nabla\cdot\boldsymbol{Q}_2 \approx \frac{1}{Z}\frac{Q_2}{W_2}, \tag{3.30}$$

so that the growth rate σ can be expressed as the weighted sum of these contributions:

$$\sigma_\Sigma = \frac{1}{N+1}\left(N\sigma_1+\sigma_2\right) \tag{3.31}$$

$$\approx \frac{Q_0}{ZW(N+1)}\left(N\cos\alpha_1 + N\gamma\cos^2\alpha_1 + \cos\alpha_2 + \gamma\cos^2\alpha_2\right). \tag{3.32}$$

Comparison with the linear stability analysis

For $\gamma = 1.7$ (a value also derived from field observations and numerical models by Gao *et al.* (2015b)), the results of that model are found to quantitatively match our predictions for $u_*/u_{\mathrm{th}} = 1.6$ (see figure 3.6). When γ is varied, the curve $\alpha_{\max}(\theta)$ changes, and the dark grey area in figure 3.6$(b-d)$ displays the whole range of possible orientations, showing an overall similar behaviour.

The present linear analysis corresponds to the limit $k\zeta \ll 1$, whereas the computation of Courrech du Pont *et al.* (2014) considers a dune with a finite aspect ratio, for which nonlinearities are expected. In a similar fashion to Courrech du Pont (2015) and Gao *et al.* (2015b) (in Supplementary Material), the parameter γ can be related to the parameters of the present model as

$$\gamma = \frac{|\hat{q}_{\mathrm{sat}}|}{q_{\mathrm{sat}}} = \frac{k\zeta}{r}\sqrt{\mathcal{A}_0^2+\mathcal{B}_0^2}, \tag{3.33}$$

where $\hat{q}_{sat}$ is the Fourier transform of the perturbation of the saturated flux. With the

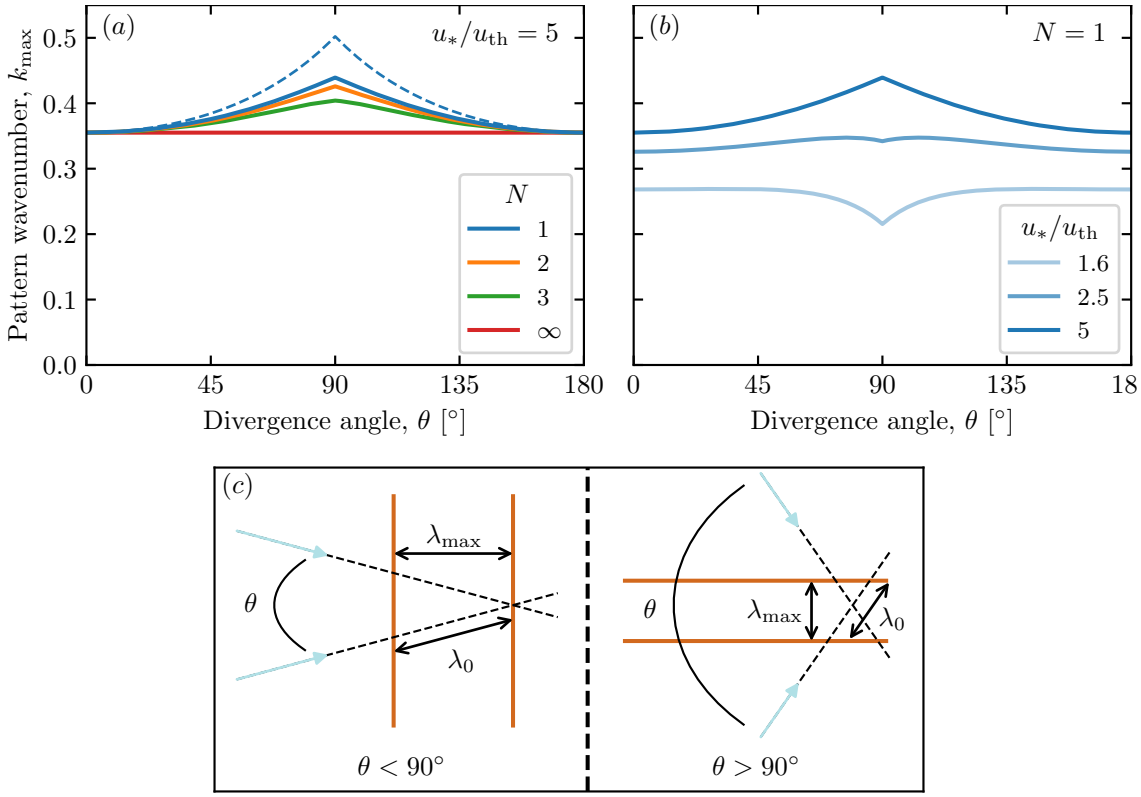

Figure 3.7 – Pattern wavenumber k_{max} as a function of the divergence angle θ for various transport N and velocity u_*/u_{th} ratios. (*a*) Solid lines: prediction of the linear stability analysis for $u_*/u_{th} = 5$. Dashed line: prediction using the geometric scaling (3.37) and (3.39), sketched in (c) for $N = 1$. (*b*) Prediction of the linear stability analysis for $N = 1$. Note that for comparison with figure 3.15 the increasing/decreasing trends are opposite as $\lambda_{max} = 2\pi/k_{max}$,

values $\mathcal{A}_0 = 3.5$, $\mathcal{B}_0 = 2$ and $u_*/u_{th} = 1.6$ (or equivalently $r \simeq 0.7$, see (3.17)), the parameter $\gamma = 1.7$ corresponds to a bed perturbation of aspect ratio of $2\zeta/\lambda = 1/12$. This value is consistent with the typical aspect ratio of fully developed dunes (Parteli *et al.* 2006, Baddock *et al.* 2007, Elbelrhiti *et al.* 2008). This general consistency between the two approaches emphasises the role played by the normal-to-the-crest components of transport in the selection of dune orientation during the linear but also nonlinear phase of dune growth.

3.3.5 Selection of the pattern wavenumber

The second key output of the linear stability analysis is the selected pattern wavenumber k_{max}. Remember that k is here made dimensionless by L_{sat}, the relevant characteristic length scale of the problem. The shape of k_{max} as a function of the divergence angle θ is displayed in figure 3.7, for different values of the transport N and velocity u_*/u_{th} ratios. We can see a non-monotonic behaviour, with variations that can reach $\simeq 30\%$ close to the transition angle $\theta = 90°$. Interestingly, these variations can be positive or negative,

depending on whether the wind strength is far from or close to the transport threshold.

For symmetric winds ($N = 1$) and in the limit of large shear velocities, a geometric argument sketched in figure 3.7(c) can explain the dependence of the wavelength on the divergence angle (solid curves in that figure). Let us call λ_0 the selected wavelength in the unidirectional regime, and $k_0 = 2\pi/\lambda_0$ the corresponding wavenumber. Far from the transport threshold, and thus without any slope effect, the balance between stabilizing and destabilizing processes occurs along the wind direction. In a bidirectional wind regime, the selected orientation is oblique to each flow direction, and we can infer that the growth rate is maximum when the wavelength λ_0 is selected in the direction of each wind.

This argument can be made more precise as follows. Far from the transport threshold, the second term in (3.18) associated with the slope effects vanishes asymptotically as $u_{\rm th}/u_* \to 0$, and this leads to

$$k_\alpha \sim \frac{2}{3} k_c(\alpha) \sim \frac{2}{3} \frac{1}{\cos\alpha} \frac{\mathcal{A}_0}{\mathcal{B}_0} = \frac{1}{\cos\alpha} k_0. \tag{3.34}$$

Assuming that the most unstable mode maximises the growth rate associated with each of the two winds, we obtain

$$k_{\max} = k_{\alpha_1(\alpha_{\max})} = k_{\alpha_2(\alpha_{\max})}, \tag{3.35}$$

implying that

$$\cos\alpha_1(\alpha_{\max}) = \cos\alpha_2(\alpha_{\max}). \tag{3.36}$$

The corresponding wavelength then writes:

$$\lambda_{\max} = \cos\alpha_{1,2}(\alpha_{\max})\lambda_0. \tag{3.37}$$

The equality (3.36) can be verified only if $\alpha_{\max} = 0°$, or $\alpha_{\max} = -90°$, i.e for a symmetrical wind regime ($N = 1$). Using (3.26), we then have

$$\cos\alpha_{1,2}(\alpha_{\max}) = \begin{cases} \cos\frac{\theta}{2} & \text{for} \quad \theta \le 90°, \\ \sin\frac{\theta}{2} & \text{for} \quad \theta \ge 90°, \end{cases} \tag{3.38}$$

which gives

$$\lambda_{\max} = \begin{cases} \lambda_0 \cos\frac{\theta}{2} & \text{or} \quad k_{\max} = k_0/\cos\frac{\theta}{2} \quad \text{for}\, \theta \le 90°, \\ \lambda_0 \sin\frac{\theta}{2} & \text{or} \quad k_{\max} = k_0/\sin\frac{\theta}{2} \quad \text{for}\, \theta \ge 90°. \end{cases} \tag{3.39}$$

For $N > 1$, we detailed previously that the selected mode integrates the two winds instead of maximizing the growth rate associated with each of the two. As the transport ratio N increases, the orientation becomes more aligned with the dominant wind direction such that

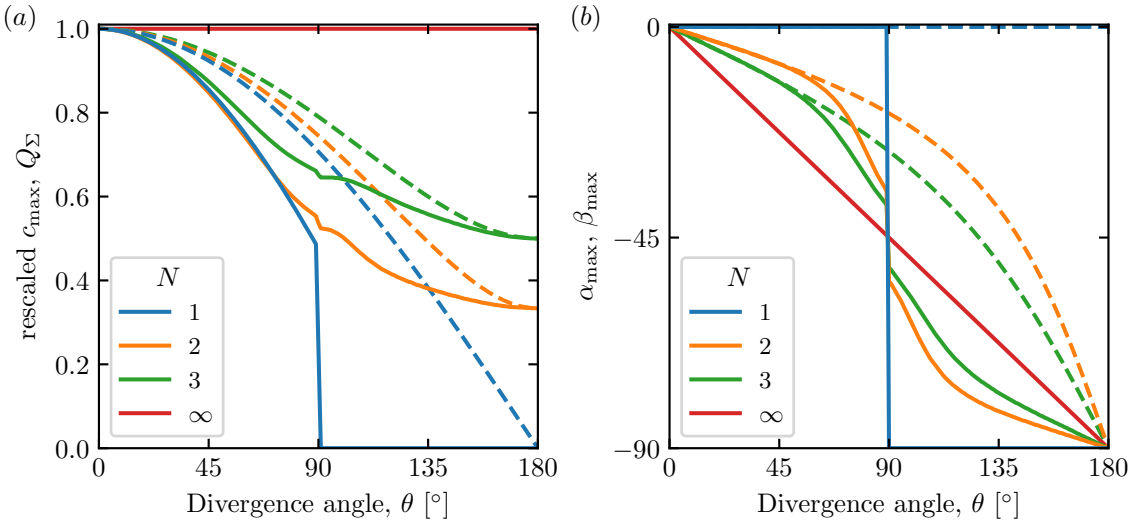

Figure 3.8 – Propagation velocity of the most unstable mode $\boldsymbol{c}_\Sigma(\alpha_{\max}, k_{\max})$ and resultant flux $\boldsymbol{Q}_\Sigma$ as functions of the divergence angle θ for $u_*/u_{\text{th}} = 1.6$ and various transport ratio N. (a) Solid lines: propagation velocity $c_{\max}$ of the most unstable mode. Dashed lines: resultant flux Q_Σ. Both are rescaled by their value in $\theta = 0°$. (b) Solid lines: Direction of the resultant flux $\beta_{\max}$ measured with respect to the x-axis. For comparison, the pattern orientation $\alpha_{\max}$ (see figure 3.6(a)) is also plotted (dashed lines).

$\alpha_1(\alpha_{\max})$ increases while $\alpha_2(\alpha_{\max})$ decreases. The equality 3.36 can thus not be verified; using equation 3.37 with either $\alpha_1(\alpha_{\max})$ or $\alpha_2(\alpha_{\max})$ thus leads to different variation of the wavelength with respect to θ.

This asymptotic prediction of the wavenumber is shown in figure 3.7(a) by the dotted line. We recover with this geometric argument the trends predicted by the linear stability analysis at finite u_*/u_{th}. We notice, however, a slight overestimation of the peak at $\theta = 90°$, because the slope effects are still present.

The role of the velocity ratio u_*/u_{th} on the selected wavenumber is shown in figure 3.7(b) for $N = 1$. When the wind strength decreases, the threshold and direction of transport are changed as the slope effects are increasingly important (3.9). First, because the amplitude of the hydrodynamic shift is reduced (the '$\mathcal{B}$ effect'), the selected wavenumber is smaller, as in the unidirectional case (3.22). Moreover, for a bidirectional flow regime, $k_{\max}$ is even smaller near the transition angle $\theta = 90°$. This is a consequence of the stabilizing action of the transverse component of sediment transport, as discussed in section 3.3.1. This effect is the strongest at the transition angle, as it depends on the component of the slope perpendicular to the flow direction. As a result, the curves close to and far from the transport threshold show opposite behaviours. For intermediate wind strengths, the curve $k_{\max}(\theta)$ is almost flat, as the geometric and slope mechanisms compensate each other.

3.3.6 Propagation velocity of the most unstable mode

Similarly to the growth rate (3.25), the propagation velocity of the emerging pattern can be expressed as the sum of the contribution of each wind:

$$\boldsymbol{c}_\Sigma = \frac{1}{N+1}\left[Nc(Q_1,\alpha_1,k) + \mathrm{sgn}(\theta-90)c(Q_2,\alpha_2,k)\right]\frac{\boldsymbol{k}}{k}. \tag{3.40}$$

When the divergence angle is larger than 90°, the displacements of the pattern induced by each of the winds are opposite, resulting in the prefactor $\mathrm{sgn}(\theta-90)$ accounting for changes in propagation direction. From the propagation velocity can be computed that of the most unstable mode $c_{\max} = \|\boldsymbol{c}_\Sigma(\alpha_{\max}, k_{\max})\|$. This quantity, as well as the resultant flux Q_Σ on a flat bed (3.23) and its direction quantified by $\beta_{\mathrm{sat}} = \measuredangle(\boldsymbol{Q}_\Sigma, \boldsymbol{e}_x)$, are shown in figure 3.8 as functions of the divergence angle θ for a velocity ratio $u_*/u_{\mathrm{th}} = 1.6$ and different values of the transport ratio N.

The propagation velocity is controlled by the component of Q_Σ perpendicular to the crest and by the pattern wavelength. For $\theta < 70°$, the overall behaviour is simple: $c_{\max}$ and Q_Σ vary in the same way. Their directions are almost the same, as the flux direction is not significantly modified by the pattern. As shown in figure 3.8(a) by the dashed lines, the resultant flux and thus the propagation velocity decrease for wider divergence angles, because the winds increasingly compensate each other. This compensation is weaker when one wind is stronger than the other ($N > 1$). For $\theta > 110°$, the resultant sand flux is mostly aligned with the dune crest leading to a slower propagation. The velocity even vanishes for $N = 1$. Finally, around the transition angle $\theta = 90°$, the resultant flux direction is strongly modified by the pattern orientation. In addition, the wavelength is also affected by the slope effects. Both effects lead to a complex behaviour of the propagation velocity, which depends on the velocity ratio u_*/u_{th}.

3.4 Underwater laboratory experiments

Subaqueous experiments are another test of the proposed linear stability analysis, especially with regard to the selected pattern wavelength. In laboratory experiments, an initial flat sand bed is subjected to a bidirectional flow regime leading to the formation of ripples. Although subaqueous bedload differs from aeolian saltation in several aspects, these ripples originate from the same physical mechanism as dunes, i.e. a destabilizing role of the hydrodynamics balanced by a stabilizing role of transport relaxation (Charru *et al.* 2013). One can then take these ripples as analogous to aeolian dunes, with downscaled size and time scales (Rubin & Ikeda 1990, Hersen *et al.* 2002, Reffet *et al.* 2010, Taniguchi *et al.* 2012, Courrech du Pont *et al.* 2014). For that reason, and to be consistent with the aeolian context of this work, we shall use the term *dunes* for these subaqueous bedforms

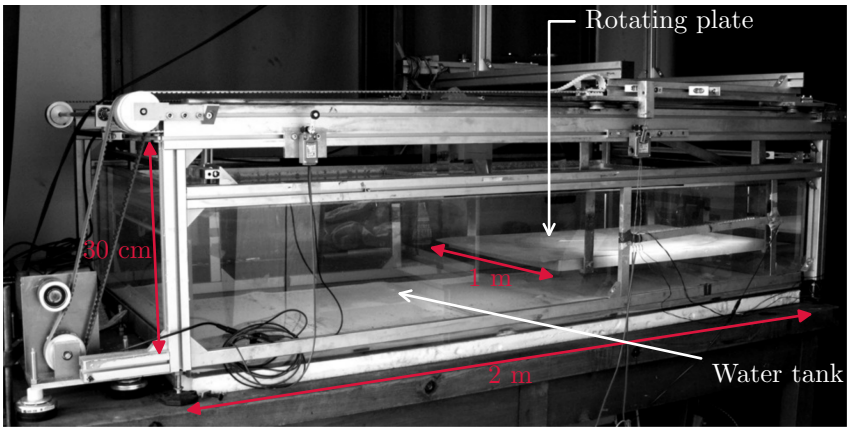

Figure 3.9 – Experimental setup used in this section. Photograph taken from the supplementary material of Courrech du Pont *et al.* (2014).

in the rest of this section.

3.4.1 The experimental setup

The setup is the one used by Reffet *et al.* (2010) and Courrech du Pont *et al.* (2014), which we briefly recall here (see figure 3.9). The granular material (ceramic beads of diameter $d = 90$ μm and density $\rho = 3800$ kg m^{-3}) lies on a 80 cm wide square plate, which can move from one side to the other of a 2 m long and 1 m wide water tank. The tank is filled to a water height of 30 cm and the plate stands at mid-height. The plate first quickly moves in one direction at a velocity that generates sediment transport, and slowly translates in the opposite way at 2 cm s^{-1} to prevent grain motion. This sequence, which we call a blow, simulates a unidirectional flow over the bed. At the centre of the plate, a 70 cm diameter disc can rotate to change the relative direction of the flow with respect to the bed. A camera set above the plate allows us to follow the evolution of the bed after each blow.

The quick motion of the plate is decomposed into two steps. The plate accelerates from rest to the final velocity in 250 ms and then gently decelerates in few seconds to prevent a backflow (see figure 3.10(a)). Depending on the final velocity, different plate trajectory are then possible, with different associated blow duration. For simplicity, we choose the mean plate speed V as the parameter representing the plate movement (see figure 3.10(b)). Because the translation of the plate puts the fluid into motion inside a boundary layer that grows over time, the shear stress on the bed is maximum during the acceleration stage and most of the transport takes place during this first phase. The time needed for the boundary layer to reach the water surface is much larger than the translation time, so that the flow can be considered as unbounded.

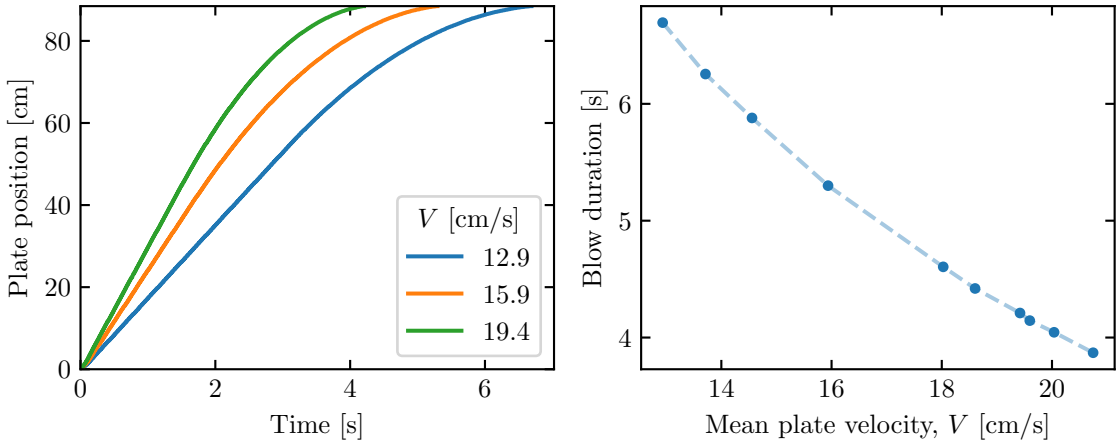

Figure 3.10 – (a) Different plate trajectory as a function of time. (b) Blow duration as a function of the mean plate velocity. Hence, each point corresponds to a different plate trajetory.

3.4.2 Calibration of the unsteady transport

The transport threshold was not quantitatively determined for this experimental setup in previous studies. Because our predictions depend on the velocity ratio u_*/u_{th}, it is important to know how far from the threshold experiments are run. We can provide a first estimation with the observation that no pattern is visible after 2020 blows for a mean plate velocity $V = 13.7$ cm s^{-1}. However, since growth rates are much smaller close to the transport threshold, this estimation is made more precise by using the migration velocity C of barchan dunes of different sizes submitted to a unidirectional flow regime. We vary the mean plate translation velocity V while keeping the plate acceleration time constant. Figure 3.11(a) shows the velocity of barchans as a function of their width for a fixed translation motion ($V = 20.8$ cm s^{-1}). The barchan velocity is smaller for larger barchans, and is well fitted by the Bagnold-like law (Bagnold 1941)

$$C = \frac{Q_{\mathrm{exp}}}{W + W_0}. \tag{3.41}$$

This propagation law, usually expressed in terms of the dune height H, derives from the conservation of mass assuming a constant aspect ratio for the dunes. Under this assumption, the height, the spanwise width W and the streamwise length of barchans are proportional to each other, and W is a more convenient observable on the photos. In (3.41) W_0 accounts for a correction of Bagnold's law at small sizes (Elbelrhiti *et al.* 2008). As illustrated in figure 3.11(a), this law agrees well with the velocity measurements, and its fit allows us to extract an effective flux Q_{exp} from the different datasets corresponding to various values of V. In this fitting procedure, the adjustable parameter W_0 has been constrained to be the same for all the data.

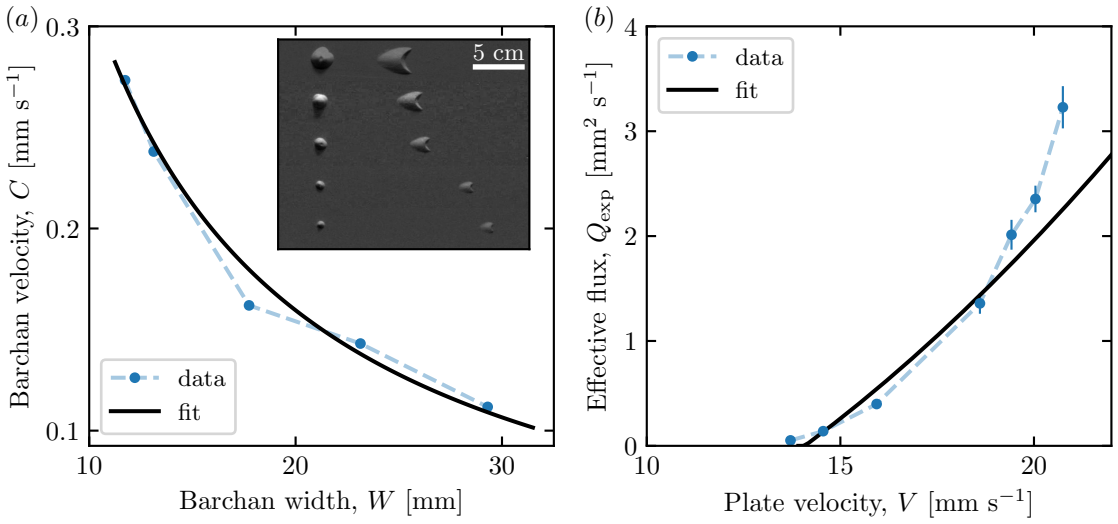

Figure 3.11 – Estimation of the transport threshold in the experimental setup. (*a*) Velocity C of the barchans as a function of their widths W for a plate velocity $V = 20.8$ cm s^{-1}. The dots are the experimental data, and the solid line is the fit of the Bagnold-like law (3.41) with $W_0 = 0.1 \pm 0.2$ mm and $Q_{\text{exp}} = 3.3 \pm 0.2$ mm^2 s^{-1}. The inset is a photomontage showing the corresponding initial sand piles and subsequent dunes after 169 blows. (*b*) Transport law with the effective flux Q_{exp} extracted from the barchan velocities for different values of V. Error bars correspond to 95%-confidence intervals in the fitting process. The solid line shows the fit of $Q_{\text{exp}} \propto (V^2 - V_{\text{th}}^2)$, which gives $V_{\text{th}} = 14.2 \pm 0.1$ cm s^{-1}.

Plotting the effective flux Q_{exp} as a function of the plate velocity (figure 3.11(*b*)), we see as expected an increasing behaviour with a threshold below which the barchans do not move. Although the sediment transport is intermittent in this experiment, we fit the data with the usual transport law $Q_{\text{exp}} \propto (V^2 - V_{\text{th}}^2)$. This gives a threshold plate velocity $V_{\text{th}} = 14.2 \pm 0.1$ cm s^{-1}. Note that this value does not depend much on the precise choice of the fitting function.

3.4.3 Comparison with theoretical predictions

The general mechanism at the origin of dunes holds in many different environments (Claudin & Andreotti 2006). However, differences remain, and in order to make comparisons between these experiments and the linear stability analysis developed for aeolian dunes, the model should be adapted to the subaqueous case (Durán *et al.* 2019).

Choice of the transport law

The transport law for bedload is different from that of saltation, with a power 3/2 rather than the linear relationship (3.7) between the saturated sediment flux and the basal shear stress. However, the details of this transport law affect the linear stability analysis by changing the expression of the characteristic flux Q, i.e. by modifying the prefactors in the expression of the growth rate (3.10) and celerity (3.11) only (Fourrière *et al.* 2010,

Andreotti *et al.* 2012a). It therefore just impacts the timescales associated to the linear regime, and we have checked that all the discussed results (e.g., increase of wavelength close to transport threshold, decrease of wavelength close to $\theta = 90°$) are qualitatively robust with respect to any choice of transport law. Also, the transient nature of the flow and grain transport in the experiment prevents us from considering this configuration as a standard bedload situation, where we could quantitatively rely on well-calibrated transport laws. For these reasons, we opted for simplicity and chose to keep the linear transport law (3.7).

Choice of the hydrodynamic coefficients

Even if we do not necessarily aim at a quantitative matching of the model with the experimental data, the values for the basal shear stress coefficients can nevertheless be more consistent with the experimental case. In fact, the coefficients $\mathcal{A}_0 = 3.5$ and $\mathcal{B}_0 = 2$ are typical values measured in the field for aeolian dunes of 10 m wavelength (Claudin *et al.* 2013). These coefficients are weak (logarithmic) functions of the pattern wavenumber at small kz_0, but show stronger variations in the range $10^{-4} < kz_0 < 10^{-2}$ due to an anomalous hydrodynamic response of the flow to the bed perturbation, as first experimentally evidenced by Zilker *et al.* (1977) and Frederick & Hanratty (1988).

Furthermore, the hydrodynamic response represented by these coefficients actually depends on both the wavelength-based Reynolds number Re_λ (laminar, inertial, turbulent), and on the grain-based Reynolds number Re_d (smooth or rough). Here, typical plate velocities and pattern wavelength are around 0.15 m s^{-1} and 10 mm respectively, leading to $Re_\lambda \simeq 1.5 \times 10^3$ and $Re_d \simeq 15$. According to the results of Durán *et al.* (2019), the experiment is thus at the limit of the rough/turbulent regime characteristic of the aeolian condition. For simplicity, we do not push this discussion further, and stay with the functions for the turbulent/rough regime presented in section 1.3.1.

The hydrodynamic roughness z_0 is more difficult to estimate under these transient water flow and sediment transport conditions. Typically a fraction of the grain diameter, we take $z_0 \simeq 0.1d$ (Fourrière *et al.* 2010), and obtain $kz_0 \simeq 5 \times 10^{-3}$, i.e. almost two orders of magnitude larger than in the aeolian case. For such a value, the coefficients become $\mathcal{A}_0 = 4.5$ and $\mathcal{B}_0 = 3$ (Fourrière *et al.* 2010, Charru *et al.* 2013), and we take these values to be fixed for all theoretical computations in this section. Note that increasing these coefficients corresponds to a larger relative weight of hydrodynamic effects compared to slope effects. Interestingly, with these slightly larger values of $\mathcal{A}_0$ and $\mathcal{B}_0$ compared to the aeolian case, the slope effects are no longer strong enough to induce an increase of the wavelength at $\theta = 90°$ close to the transport threshold (figure 3.7(b)). Only the geometric variation leading to the decrease of the wavelength at the transition angle remains. This is consistent with the experimental observations.

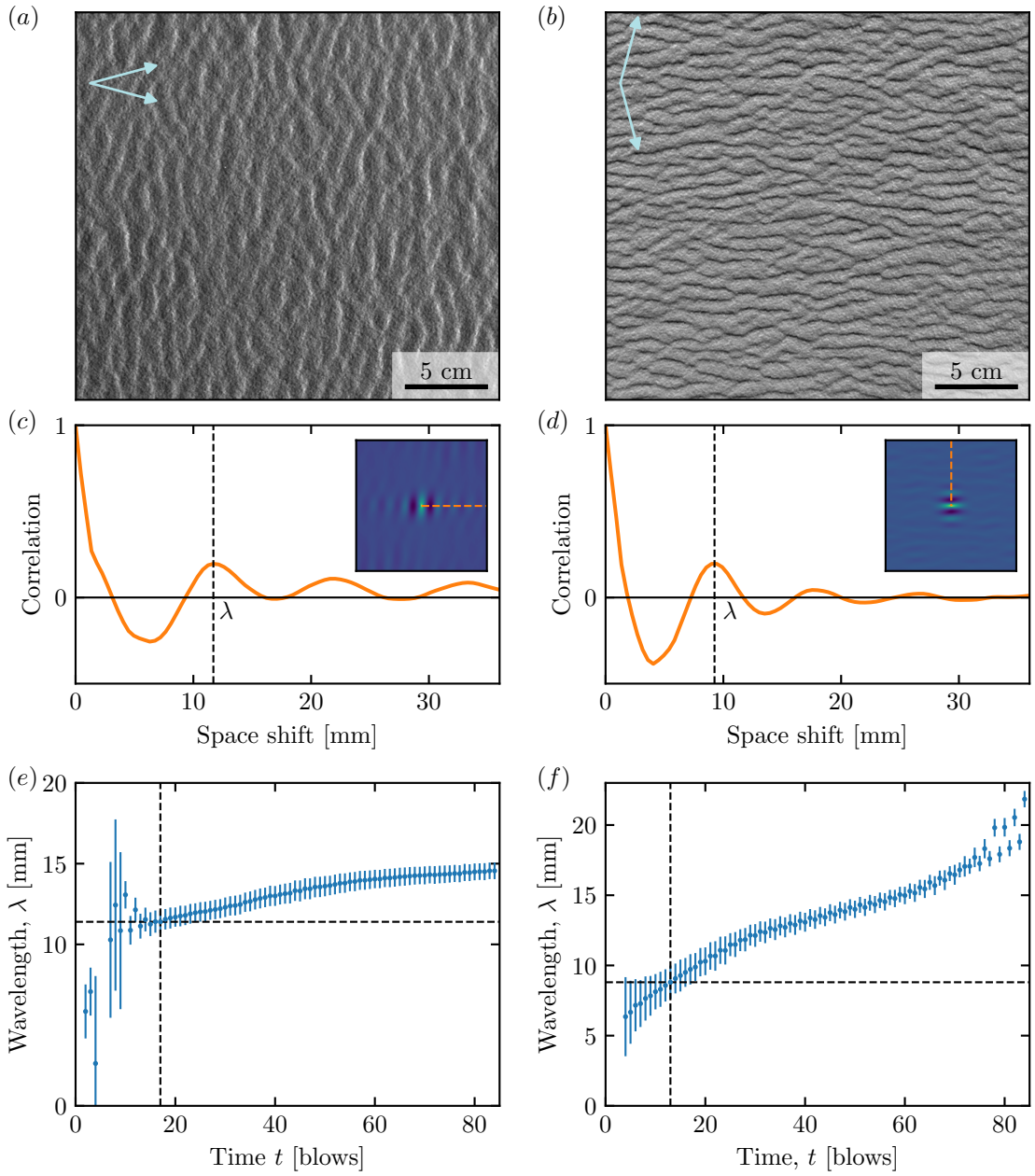

Figure 3.12 – Pattern formation from a flat bed in a bidirectional flow regime for $\theta = 30°$ (left) and $\theta = 150°$ (right), for $V/V_{\text{th}} = 1.4$. (a, b) Pictures after 17 and 13 blows respectively, starting from a flat bed. (c, d) Autocorrelation of the above pictures. Insets: central zone of the autocorrelation matrix, which gives the pattern orientation and wavelength. The curves are the autocorrelation signal along the red dashed lines, i.e. perpendicular to the dune orientation. The measured wavelength λ corresponds to the position of the first maximum of the autocorrelation curve. (e, f) Wavelength as a function of time. Dotted lines: initial wavelength and corresponding time at which the spatial coherence of the autocorrelation signal extends over one wavelength. Error bars encode the quality of this signal.

From the plate velocity ratio to the flow velocity ratio

The most unstable wavelength $\lambda_{\max}$ selected by the linear stability analysis depends on the velocity ratio u_*/u_{th}. This ratio is not directly equal to the plate velocity ratio V/V_{th} in the experiment because of the transient nature of the flow. Here, we assume that they are linearly related to each other:

$$\left(\frac{V}{V_{\text{th}}} - 1\right) = C_v \left(\frac{u_*}{u_{\text{th}}} - 1\right), \tag{3.42}$$

where C_v is an adjustable constant. In the fitting procedure, the most unstable wavelength is thus a function of V/V_{th} (and N and θ in bidirectional flow regimes), with two free parameters C_v and L_{sat}.

3.4.4 Experimental results

We present here results in the case of symmetric winds ($N = 1$): the central disc of the plate is rotated by θ and $-\theta$ alternately after every blow. Starting from an initial flat bed, dunes rapidly form after a few blows with a characteristic wavelength and orientation, which are measured by picture autocorrelation (see figure 3.12). We mainly focus below on the dependence of the wavelength with the divergence angle θ and the velocity ratio u_*/u_{th}. The behaviour of the pattern orientation in this experimental setup has already been discussed in Courrech du Pont *et al.* (2014), showing agreement with their approach (see section 3.3.4), and thus the present analysis (figure 3.6).

Figure 3.12 displays results of two well-contrasted cases with a small and a large divergence angle ($\theta = 30°$ and $\theta = 150°$, respectively), both at the same plate velocity ratio $V/V_{\text{th}} = 1.4$. When $\theta = 30°$, transverse dunes form perpendicular to the resultant transport direction with an initial wavelength of 11.8 ± 0.7 mm (figure 3.12(e)). When $\theta = 150°$, longitudinal dunes form parallel to the resultant transport direction with an initial wavelength of 8.8 ± 0.5 mm (figure 3.12(f)). After the emergence of the pattern, some coarsening is observed, with an increase of the wavelength with time.

At the transition between the two dune orientations, close to $\theta = 90°$, the two perpendicular modes are observed simultaneously in the building dune pattern, as shown in figure 3.13. The longitudinal orientation seems to overcome the transverse one at the transition. This asymmetry appears to be specific to incipient dunes, as the transition is sharper once dunes are more mature (Reffet *et al.* 2010).

Variation of the wavelength with the velocity ratio

We start by investigating the impact of the plate velocity ratio on the incipient wavelength. Under a unidirectional flow ($\theta = 0°$), the wavelength λ_0 is found to decrease with

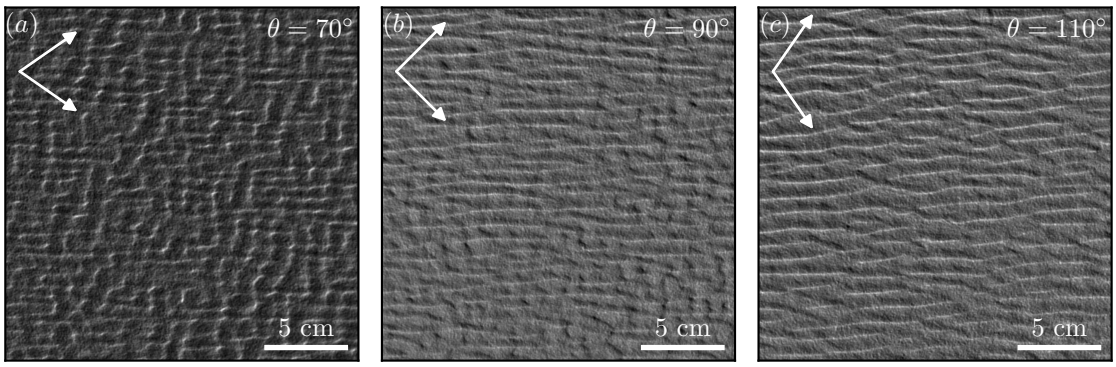

Figure 3.13 – Photographs of the dune pattern in the experiment across the transition from transverse to longitudinal orientations, starting from a flat bed, for V/V_{th} = 1.4. Flow directions are shown with arrows. From left to right, the pictures have been taken after 30, 32, and 30 blows, respectively

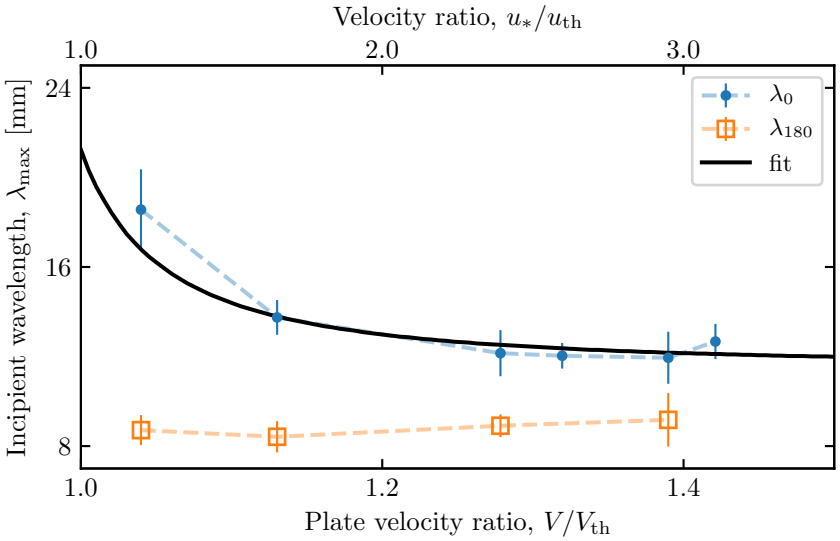

Figure 3.14 – Initial wavelength as a function of the plate velocity ratio for $\theta = 0°$ (λ_0, blue bullets) and $\theta = 180°$ (λ_{180}, orange squares). Solid line: fit of the linear stability analysis under a unidirectional flow, giving $L_{\mathrm{sat}} = 0.8 \pm 0.1$ mm and $C_v = 5 \pm 2$

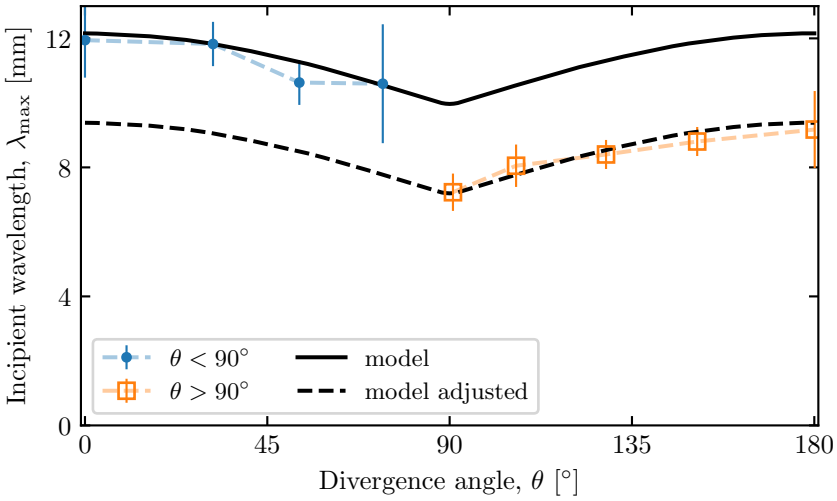

Figure 3.15 – Initial wavelength as a function of the divergence angle θ (symmetric winds $N = 1$). Symbols: experimental data for $V/V_{th} = 1.4$. Solid line: model prediction for $u_*/u_{th} = 3$ and $L_{sat} = 0.8$ mm. Dashed line: solid line shifted below and adjusted in $\theta = 180°$ (we subtracted $(\lambda_0 - \lambda_{180})$).

V/V_{th}. As shown by figure 3.14, it is significantly larger close to the transport threshold, in comparison to the asymptotic value of approximately 12 mm corresponding to large V/V_{th}.

This variation of the wavelength with the velocity ratio is due to the sensitivity of the threshold to the bed slope. This is a result predicted by the linear stability analysis (Fourrière *et al.* 2010), which have been observed in field measurements (Charru *et al.* 2013) or numerical simulation (Narteau *et al.* 2009). We provide here the first quantification of this effect using laboratory experiments. The comparison between data and theory is shown by the black line in figure 3.14. The observed increase of the wavelength close to the transport threshold is quantitatively reproduced by the model. The fit gives $L_{sat} = 0.8 \pm 0.1$ mm (i.e. $\simeq 9$ grain diameters) and $C_v = 5 \pm 2$. These values are now fixed and used for the subsequent computation of theoretical curves at all divergence angles, without any further adjustment.

By contrast, the wavelength λ_{180}, defined under two opposed flows ($\theta = 180°$), is approximately 9 mm and does not show any clear dependence on the plate velocity. This is surprising in the light of the results of the linear stability analysis, that predicts identical variations of the wavelengths λ_0 and λ_{180} (see section 3.3.5).

Variation of the wavelength with the divergence angle

From now, we run all experiments at $V = 19.6$ m s^{-1}, i.e. $V/V_{th} = 1.4$, which corresponds to a velocity ratio $u_*/u_{th} = 3$, from (3.42).

Figure 3.15 shows the behaviour of the wavelength when the divergence angle θ is

varied over the whole range. When $\theta < 90°$, transverse dunes form. Their wavelength is maximum for $\theta = 0°$ and decreases when θ increases. When $\theta > 90°$, longitudinal dunes form and exhibit opposite behaviour: their wavelength increases with θ and is maximum for $\theta = 180°$. Again, this variation of the dune wavelength with the divergence angle is not symmetric with respect to $\theta = 90°$, and longitudinal dunes systematically form at smaller wavelengths than transverse ones. This is true for all values of the plate velocity ratio V/V_{th} that we have tested (see previous section and figure 3.14).

As shown by figure 3.15, the linear stability analysis captures well the variation of the wavelength for divergence angles smaller than 90° (solid line). Note that here, we do not *fit* the theory to the data, as all parameters have been previously fixed. For divergence angles larger than 90°, the experimental data are significantly smaller than predicted whereas the model predicts a symmetric variation of the wavelength with respect to the transition angle $\theta = 90°$. Nevertheless, the decrease of the wavelength close to $\theta = 90°$ is recovered relative to the wavelength at $\theta = 180°$ (dashed line).

Variation of the associated characteristic time

We can also estimate the characteristic time needed to observe incipient dunes in the experiment. This time is a proxy for the inverse of the instability growth rate. It is displayed in figure 3.16 as a function of the divergence angle θ. Both transverse and longitudinal dunes emerge typically after a dozen blows, but systematically more rapidly in the case of longitudinal ones. The pattern coarsening is also quicker for longitudinal dunes than for transverse dunes (figure 3.12(e, f)), an observation already reported by Reffet *et al.* (2010).

The variation of the characteristic time for pattern formation close to the transition angle is also recovered by the predicted variation of $1/\sigma_{\text{max}}$ for divergence angles smaller than 90° (figure 3.16). As the angle between the dune crest and the flow direction decreases (i.e when $\theta°$ approaches 90°), the perpendicular-to-the crest component of the sand flux also decreases, leading to smaller growth rates. However, this is not the case for $\theta > 90°$, where the characteristic time seems rather independent of $\theta°$.

Linear regime in the experiment

Finally, we can provide estimations of time scales in the experiment, taking as a typical example the case $V/V_{\text{th}} = 1.4$. Each blow takes $\simeq 4$ s. Because most of the grain motion occurs during the acceleration phase of the plate, the time during which the dune pattern is active is a fraction of the blow duration. The effective wind period $t_1 + t_2$ is thus of the order of a few seconds. For $V/V_{\text{th}} = 1.4$, we have $Q_{\text{exp}} = 2$ mm^2 s^{-1} (figure 3.11 (b)). Importantly, this is the flux at the crest of barchan dunes, larger than the flux at the bottom (see section 1.4.1). Taking $\gamma = 1.7$, we then obtain a reference flux $Q \simeq 0.74$ mm^2 s^{-1}.

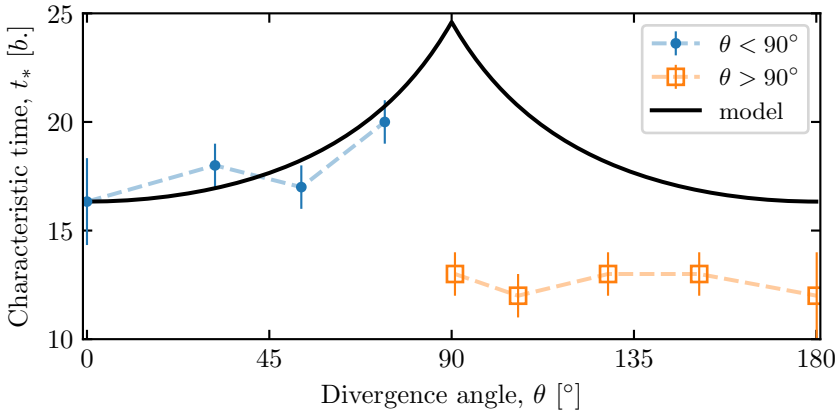

Figure 3.16 – Characteristic time (in blows) of pattern emergence as a function of θ. Symbols: experimental data for $V/V_{\text{th}} = 1.4$. Solid line: model prediction for $u_*/u_{\text{th}} = 3$, adjusted in $\theta = 0°$.

With a saturation length $L_{\text{sat}} = 0.8$ mm, we have a characteristic pattern growth time $(1/\sigma_{\max})L_{\text{sat}}^2/Q \simeq 6$ s, where $\sigma_{\max} \simeq 0.14$ is the dimensionless growth rate given by the linear stability analysis corresponding to the experimental conditions ($\mathcal{A}_0 = 4.5$, $\mathcal{B}_0 = 3$ and $u_*/u_{\text{th}} = 3$).

Despite both time scales being comparable in the experiment, the emerging dunes still develop by integrating the two flow directions. While the experimental conditions are at the limit of validity of the linear stability analysis, some of the characteristics of the linear regime remain, such as the variations of the dune orientation or wavelength with respect to the divergence angle.

These results question the ability to observe the linear regime in the experiment, especially when $\theta > 90°$. Such a regime is theoretically associated with bedforms whose wavelength remains constant while their amplitude grows at a rate σ. Clearly, as soon as a pattern wavelength is detected by autocorrelation of the experimental pictures, it keeps increasing with time, especially for longitudinal dunes (figure 3.12(e, f)). Enhanced nonlinear effects when $\theta > 90°$ can be understood as follows. In a bidirectional flow regime, transverse dunes are blown from the same side by the two winds. On the contrary, each wind blows from a different side of the longitudinal dunes. As a consequence, the sand flux is all the more affected if the incipient dunes develop an avalanche face. A larger dune aspect ratio is a stronger perturbation for the flow, leading to larger sediment flux variations, and thus an enhanced dune growth rate. These nonlinearities may explain the shortcomings of the linear analysis in reproducing the experimental wavelengths for $\theta > 90°$. These effects also support the shorter characteristic time for dune formation in the longitudinal mode and the prevalence of longitudinal dunes over transverse ones at the transition, when the divergence angle is close to 90°.

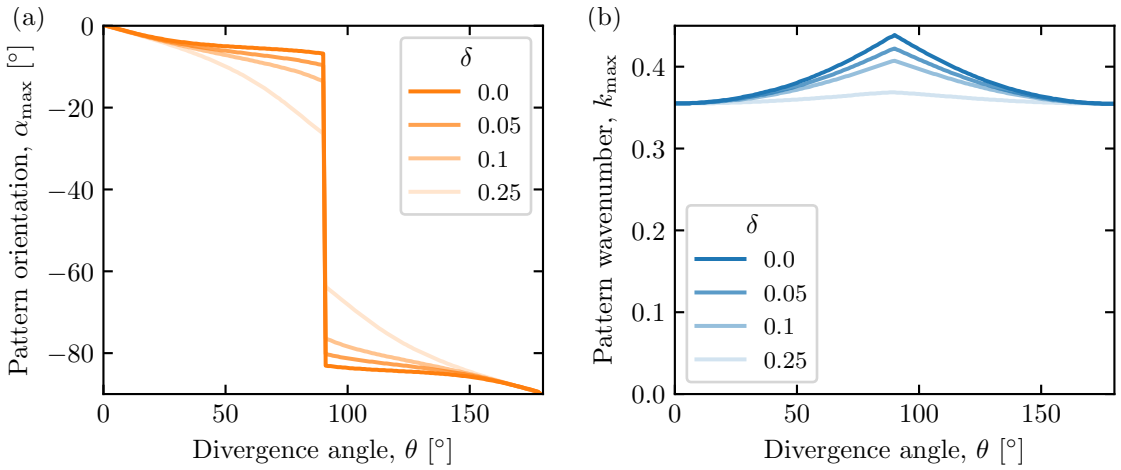

Figure 3.17 – (a) Pattern orientation as a function of the divergence angle for $N = 2$ and $u_*/u_{\text{th}} = 5$. (b) Pattern wavenumber as a function of the divergence angle for $N = 1$ and $u_*/u_{\text{th}} = 5$. The curves for $\delta = 0$ correspond to figure 3.6(c) and figure 3.7, respectively.

3.5 Impact of other processes

The linear stability analysis presented previously has been developed under some approximations concerning the description of the flow and sediment transport. In this section, we present some additional processes and discuss their impact on our results.

3.5.1 Impact of cross-stream diffusion

When transported, sediment grains bounce on a rough bed, which naturally induces random deviation of their trajectories. Combined to the turbulent fluctuations of the flow, it eventually induces cross-stream diffusion. In average, saltating grains are deviated of an angle $\beta \simeq 20°$ between two chocs with the sediment bed (Zhang *et al.* 2007, Yang *et al.* 2009, Andreotti *et al.* 2012b). In the direction transverse to the winds, it results in a random walk of mean free path $l_d \sim \beta l_s$, where l_s is the average grain hop length.

As a consequence, the sediment flux is modified by the apparition of a diffusive component transverse to the flow. Under a unidirectional wind, it reads in the notations of section 3.3.1:

$$\boldsymbol{q}_d = -\beta l_s \frac{\partial q_x}{\partial y} \boldsymbol{e}_y \tag{3.43}$$

By adding the previous equation to our model, the coefficients (3.12-3.15) become:

$$a_x = \mathcal{A}_x, \tag{3.44}$$

$$b_x = \mathcal{B}_x - \cos\alpha \frac{1}{\mu}\frac{u_{\mathrm{th}}^2}{u_*^2}, \tag{3.45}$$

$$a_y = r\mathcal{A}_y - \delta k \sin\alpha b_x, \tag{3.46}$$

$$b_y = r\left(\mathcal{B}_y - \sin\alpha \frac{1}{\mu}\frac{u_{\mathrm{th}}}{u_*}\right) - \delta k \sin\alpha a_x, \tag{3.47}$$

where $\delta = \beta l_{\mathrm{s}}/L_{\mathrm{sat}}$ is a new non-dimensional parameter accounting for the importance of cross-stream diffusion. In aeolian saltation, the mean hop length of the grains is around 200 d for a grain diameter $d \simeq 200\mu$m (Ho *et al.* 2011). With a saturation length $L_{\mathrm{sat}} \simeq 0.7$ m, it leads to $\delta \simeq 0.02$.

Plugging these coefficients into the general expression of the growth rate (3.10) gives:

$$\sigma = \frac{(k\cos\alpha)^2}{1+(k\cos\alpha)^2}\Bigg[\mathcal{B}_0\cos\alpha\left(1+\frac{r\tan^2\alpha}{2}\right) - \frac{1}{\mu}\frac{u_{\mathrm{th}}}{u_*}\left(\frac{u_{\mathrm{th}}}{u_*}+r\tan^2\alpha\right) \tag{3.48}$$

$$- k\cos\alpha\mathcal{A}_0\cos\alpha\left(1+\left[\frac{r}{2}+\delta\right]\tan^2\alpha\right) \tag{3.49}$$

$$- (k\cos\alpha)^2\delta\tan^2\alpha\left(\mathcal{B}_0\cos\alpha - \frac{1}{\mu}\frac{u_{\mathrm{th}}^2}{u_*^2}\right)\Bigg]. \tag{3.50}$$

The diffusion therefore adds two new terms in this expression compared to the growth rate (3.17) derived previously. Both are negative, reflecting that cross-stream diffusion is here a classical stabilizing mechanism, stronger for orientations aligned with the flow direction. In particular, it suppresses the divergence of the growth rate of longitudinal modes for very large values of the velocity ratio (see section 3.3.1).

Figure 3.17 shows the impact of the diffusion parameter δ on the most unstable mode. The more the orientations are aligned with the flow, the more cross-stream diffusion reduces their growth rate. As a result, larger values of δ induce selected orientations more perpendicular to the dominant flow direction (figure 3.17(a)). Note that this effect is stronger for large velocity ratios, as orientations are in these conditions closer to the wind bisector, and thus more aligned with the two winds (see section 3.3.3). Diffusion also decreases the growth rate of small wavelengths (large wavenumber). Likewise, it is stronger close to $\theta = 90°$ where bedforms are the most aligned with the two flow directions. As a result, figure 3.17(b) shows that increasing diffusion tends to flatten the geometric variation of the wavelength with respect to the divergence angle (see 3.3.5).

For typical aeolian conditions ($\delta \simeq 0.02$), diffusion has a negligible effect from both most unstable orientations and wavelengths, and this up to δ-values almost an ordre of magnitude larger, which are unrealistic in practice. Under water, the grain hop length

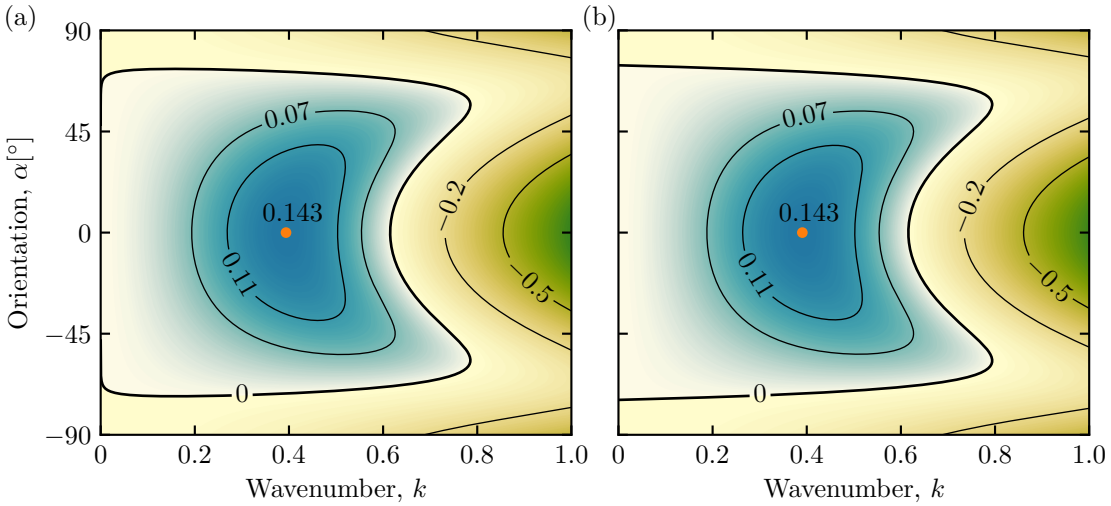

Figure 3.18 – Growth rates under a unidirectional wind. (a) Taking into account the dependence of the hydrodynamic coefficients in the wavenumber, for $z_L = 2 \times 10^{-2}$. (b) With constant $\mathcal{A}_0 = 4.8$ and $\mathcal{B}_0 = 3.1$, calculated using (3.51) with the same z_L and $k = k_{max}$, the most unstable wavenumber of (a). Both are computed for $u_*/u_{th} = 3$.

is only a few grain diameter, which suggests that diffusion is even more negligible in the problem of dune emergence [1].

3.5.2 Using non-constant hydrodynamic coefficients

In the case of a wind blowing over transverse bedforms, the dependence of the hydrodynamic coefficients $\mathcal{A}_0$ and $\mathcal{B}_0$ in the wavenumber is well known (section 1.3.1). More specifically, they are functions of the dimensionless variable kz_0, involving the *dimensional* wavenumber and the hydrodynamic roughness. Their variation is weak (logarithmic), such that they have been considered as constant in previous studies on the dune instability (Andreotti *et al.* 2002b, Elbelrhiti *et al.* 2005, Fourrière *et al.* 2010).

When bedforms are inclined with respect to the flow, the hydrodynamic coefficients then depend on both kz_0 and the pattern orientation α. They must be computed by integration of the Navier-Stokes equations, choosing a turbulent closure (Andreotti *et al.* 2012a). However, for asymptotically small values of kz_0, Andreotti *et al.* (2012a) show that the two variables can be separated. The α-dependence can then still be represented by the approximate expressions (3.3 - 3.6) we used in the previous sections (see in particular section 3.3.1), up to $kz_0 \simeq 10$, way beyond all possible aeolian conditions.

For the kz_0-dependence, we thus use in (3.3 - 3.6) the expressions of $\mathcal{A}_0$ and $\mathcal{B}_0$ calculated by Fourrière *et al.* (2010) for the rough/turbulent case (and represented in fig-

1. Note that some studies suggest that diffusion could be a driving mechanism for the emergence of another type of longitudinal bedforms (Abramian *et al.* 2019b).

ure 1.12). Both can be analytically represented by the following function:

$$\mathcal{F}(R,\boldsymbol{p}) = p_0 + \frac{p_1 + p_2 R + p_3 R^2 + p_4 R^4}{1 + p_5 R^2 + p_6 R^4}, \tag{3.51}$$

where $R = \ln(2\pi/(kz_0))$. We then have $\mathcal{A}_0(k,z_0) = \mathcal{F}(R,\boldsymbol{a})$ and $\mathcal{B}_0(k,z_0) = \mathcal{F}(R,\boldsymbol{b})$ with:

$$\boldsymbol{a} = (2, 1.0702, 0.093069, 0.10838, 0.024835, 0.041603, 0.0010625), \tag{3.52}$$

$$\boldsymbol{b} = (0, 0.036989, 0.15765, 0.11518, 0.0020249, 0.0028725, 0.00053483). \tag{3.53}$$

Two length scales are now involved in the growth rate: the saturation length L_{sat} and the hydrodynamic roughness z_0. In our previous notations, the wavenumber k is made non-dimensional using the saturation length L_{sat}. To remain consistent, we introduce the non-dimensional number $z_{\text{L}} = z_0/L_{\text{sat}}$ such that now, $R = \ln(2\pi/(kz_{\text{L}}))$. In aeolian and subaqueous conditions, we typically have $z_{\text{L}} \simeq 1.5\times10^{-3}$ and $z_{\text{L}} \simeq 2\times10^{-2}$, respectively (see section 3.4.3).

Figure 3.18 compare the growth rate computed using the hydrodynamic coefficients derived in this section to the growth rate (3.17) with constant $\mathcal{A}_0$ and $\mathcal{B}_0$. Both are quantitatively similar, and only differ for asymptotically small wavenumbers. This supports the approximation using hydrodynamic coefficients independent of the wavenumber, providing that they are chosen according to the values of $k_{\max}$ and z_{L} in the studied situation.

3.5.3 Impact of the slope on the sand flux

In section 1.2.2, we discussed the impact of the transverse slope on the transport threshold. The sand flux is expected to be modified accordingly: smaller on positive slopes where the threshold velocity is higher, and vice versa. However, wind tunnel experiments shows that the full variation of the sand flux cannot be captured by simply changing the threshold (Iversen & Rasmussen 1999). Then, the gravity g in the prefactor of the transport law needs to be modified for a slope ϕ as $g\,(\cos\phi + \sin\phi/\mu)$. Following Durán *et al.* (2011), the corresponding transport law can be written as:

$$\boldsymbol{q}_{\text{sat}} = \Omega' u_{\text{th}}^{-1}\left(u_*^2 - u_{\text{th}}^2\right)\boldsymbol{t}, \tag{3.54}$$

where Ω' is dimensional constant, and u_{th} is modified at the first order by $\sqrt{(1+\partial_x Z/\mu)}$ (see section 3.3.1). When using this new transport law in our model, only the coefficient (3.13) changes to:

$$b_x = \mathcal{B}_x - \frac{1}{2\mu}\left(1 + \frac{u_{\text{th}}^2}{u_*^2}\right)\cos\alpha. \tag{3.55}$$

Note that the slope effect on the transport threshold does not vanish anymore for large velocity ratios. After changing the characteristic flux to $Q = \Omega' u_*^2/u_{\text{th}}$, the non-dimensional

growth rate reads:

$$\sigma = \frac{(k\cos\alpha)^2}{1+(k\cos\alpha)^2}\left[\mathcal{B}_0\cos\alpha\left(1+\frac{r\tan^2\alpha}{2}\right)-\frac{1}{\mu}\frac{u_{\rm th}}{u_*}\left(\frac{1}{2}\left[\frac{u_*}{u_{\rm th}}+\frac{u_{\rm th}}{u_*}\right]+r\tan^2\alpha\right)\right. \tag{3.56}$$

$$\left.-k\cos\alpha\mathcal{A}_0\cos\alpha\left(1+\frac{r\tan^2\alpha}{2}\right)\right], \tag{3.57}$$

The most unstable wavenumber under a unidirectional flow, for which $\alpha_{\rm max} = 0°$, is slightly different:

$$k_{\rm max} \sim \frac{2}{3}k_{\rm c}(0) = \frac{2}{3\mathcal{A}_0}\left(\mathcal{B}_0-\frac{1}{2\mu}\left[1+\frac{u_{\rm th}^2}{u_*^2}\right]\right), \tag{3.58}$$

Close to the transport threshold ($u_*/u_{\rm th} \to 1$), the selected wavelength is the same, but it is smaller for large velocity ratios.

Under bidirectional wind regimes, results are qualitatively the same as the ones presented in section 3.3. The only change relates to the slope effect on the transport threshold, stronger here. As a consequence, everything happens as if we were closer to the threshold compared to the equations developed in section 3.3: for a given velocity ratio, growth rates are smaller, orientations are closer to the perpendicular to the dominant wind direction, and the geometric variation of the wavelength is weaker.

It is unclear why the friction coefficient μ introduced for the velocity threshold is relevant here, as the two mechanisms are fundamentally different. The physical origin of the impact of the slope on the sand flux remains also unclear. One possible explication could relate to the presence of two types of moving grains: besides saltons (saltating grains), more sensible to the wind, the reptons, which spend more time in contact with the bed (similarly to bedload transport), would be more sensible to the bed slope and to the same friction coefficient μ (Howard 1977, Hersen 2004b, Andreotti 2004).

3.6 Numerical study using the ReSCAL cellular automaton model

Due to the different time and spatial scales involved, the study of aeolian dunes cannot only rely on the few possible field studies. Underwater laboratory experiments are a useful alternative, but it is now clear that the analogy cannot be taken further than general processes due to differences in hydrodynamical regimes (Durán *et al.* 2019). The use of numerical models then allows greater flexibility in terms of space parameter exploration, or number of configurations that can be tested. Three different types of numerical models are used to study dunes. First, direct simulations of grain dynamics solve the associated equation of motions. This type of models is mostly used to investigate sediment transport processes, and stops at the scale of impact ripples or subaqueous dunes (a few centimeters)

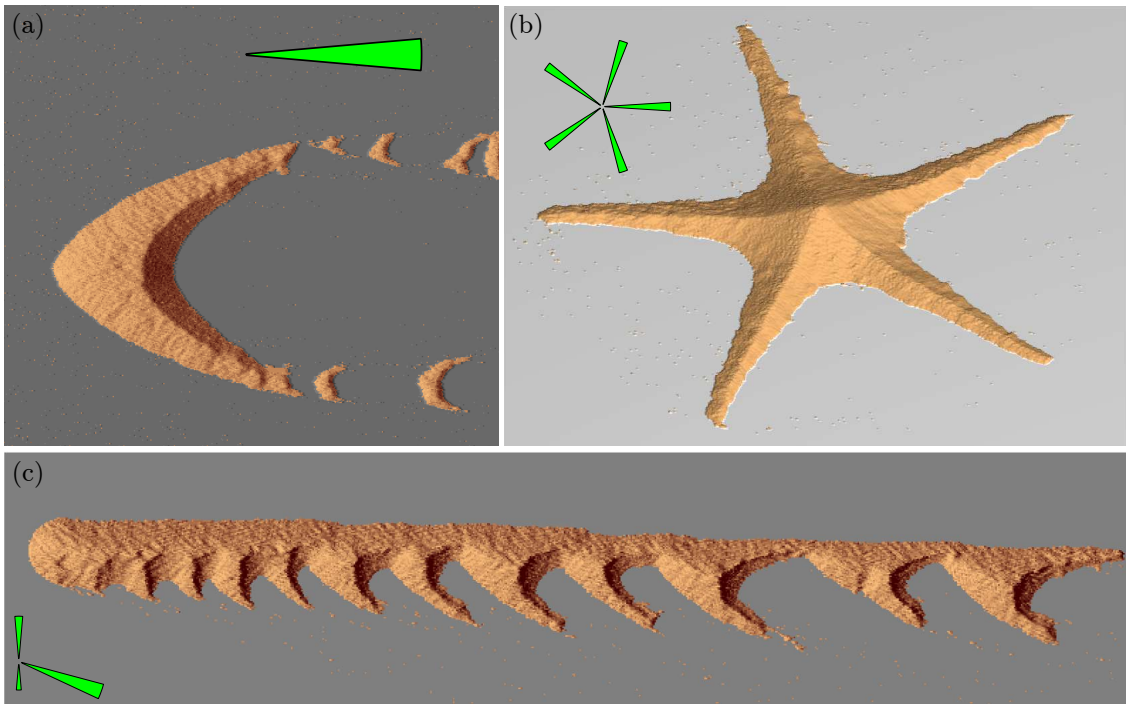

Figure 3.19 – Dune patterns reproduced by the cellular automaton model ReSCAL. (a) Barchan dune from Gao *et al.* (2018). (b) Star dune from Zhang *et al.* (2012). (c) Raked linear dune from Lü *et al.* (2017). Angular sand fluxe distributions are indicated in green.

due to their high computational cost (Anderson & Hallet 1986, Anderson & Haff 1988, Durán *et al.* 2012; 2014, Pähtz *et al.* 2015, Schmeeckle 2014, Sun & Xiao 2016, Clark *et al.* 2017, Mazzuoli *et al.* 2019). Then, simulations solving the coupled continuous equations of hydrodynamics and sediment transport allow the investigation of larger scales problems (Sauermann *et al.* 2001, Kroy *et al.* 2002a, Andreotti *et al.* 2002a, Hersen 2004b, Parteli *et al.* 2007, Baas & Nield 2007, Parteli *et al.* 2009, Zheng *et al.* 2009, Parteli *et al.* 2011, Durán & Moore 2013, Lima *et al.* 2017, Khosronejad & Sotiropoulos 2017, Giudice & Preziosi 2020). While these simulations reproduce well the dynamics of isolated dunes, they would require a better description of the recirculation bubble in order to simulate interacting dunes or superimposed patterns. (Parteli *et al.* 2007, Durán *et al.* 2010, Courrech du Pont 2015).

Along with continuous models, cellular automaton models have been used in dune field modelling, mainly because of their low computational time, more suited to the study of landscape-scale problems. (Nishimori & Ouchi 1993, Werner 1995, Nishimori *et al.* 1998, Momiji *et al.* 2000, Bishop *et al.* 2002, Baas 2002, Nield & Baas 2008, Narteau *et al.* 2009, Eastwood *et al.* 2011, Zhang *et al.* 2012, Gao *et al.* 2016; 2018). Cellular automata are based on a stochastic approach. In these models, the three-dimensional space is made up of elementary cells that can take on different states, depending on the studied system (e.g.

air, sediment or vegetation in the case of dune cellular automaton models). These cells can switch from one state to another according to arbitrary transitions with associated probabilities, chosen to represent specific processes (erosion, deposition, diffusion, etc.).

In the case of dune studies, cellular automaton models have successfully reproduced the wide variety of existing dune patterns by playing on sediment supply and wind regime variability (see figure 3.19). However, the time and length scales of these models directly depend on the transitions and associated probabilities, making them difficult to use for quantitative approaches. Narteau *et al.* (2009) overcame this problem, setting the scales of the ReSCAL dune model[2] by comparing incipient dune growth inside the model to field data. By coupling a lattice-gas cellular automaton for high Reynolds-flow simulation (Frisch *et al.* 1986, d'Humieres *et al.* 1986, Chopard & Droz 1998) to a cellular automaton model for sediment transport, this model also achieved to reproduce interacting dunes and superimposed bedforms (Narteau *et al.* 2009, Gao *et al.* 2015a).

In this section, we present the ReSCAL numerical model, and then discuss its relevance to the study of incipient bedforms in multidirectional wind regimes.

3.6.1 The ReSCAL dune model

Principle

One can find a full and detailed description of the ReSCAL dune model in Narteau *et al.* (2009). In this cellular automaton model, cell states (air, non-erodible soil, erodible soil and moving grains) and transitions (erosion, transport, deposition and diffusion) are chosen to represent the dynamic of sediment transport (see figure 3.20). In this model, an important point is that each doublet transition is associated to a transition rate Λ_i, such that the whole process can be described as a generalized Poisson process. The probability of each transition can therefore be calculated from these transition rates (Narteau *et al.* 2001; 2009, Rozier & Narteau 2014). In addition, other key mechanisms are present. First, an angle of repose is imposed for the granular material in order to include avalanching processes.

Then, fluid flow is represented using a lattice gaz. In the model, only 2D flows are considered in order to highly reduce the computation time. Fluid particles are confined on a set of uniformly spaced vertical planes parallel to the flow direction, in which they can fly from air cells to air cells. The no-slip condition at the bottom spontaneously generates a vertical logarithmic profile, whose aerodynamic roughness is given by the elementary length scale of the cells l_0. This also produces a direct feedback of the topography on the

2. ReSCAL is actually a base-model able to generate a lot of different cellular automaton models (Rozier & Narteau 2014). Aside dunes, it has for example been used to study general landscape evolution (Rozier & Narteau 2014), snow dynamics (Kochanski *et al.* 2019, Sharma *et al.* 2019), or dissolution at the core-mantle boundary (Mandea *et al.* 2015).

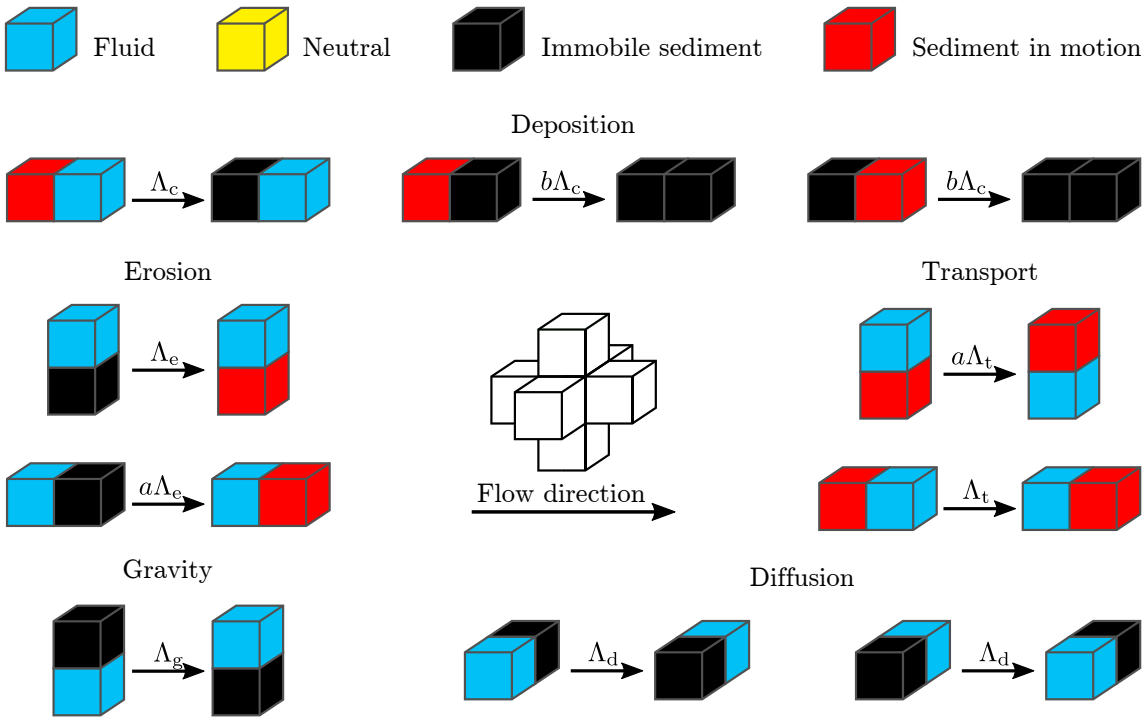

Figure 3.20 – Active transitions in the ReSCAL dune model. The parameters Λ_i are transition rates in units of t_0^{-1}. They are constant, except for Λ_e that depends on the basal shear stress according to equation (3.59). Here, a and b are positive constants. The central inset shows the direction of the unidirectional flow and the orientation of the nearest neighbors in a regular cubic lattice. Figure from Gao *et al.* (2015a).

Table 3.1 – ReSCAL model parameters used in our simulations.

Parameter	Λ_{e0}	Λ_c	Λ_t	Λ_d	Λ_g	τ_1	τ_2
Value	4	2	6	0.02	1000	0	1100

flow at the origin of recirculation zones in the lee side of dunes (Narteau *et al.* 2009, Zhang *et al.* 2010).

Finally, the transport law and the existence of a threshold are incorporated in the model by linking the erosion rate Λ_e to the basal shear stress τ_b, calculated from the dynamics of the lattice gaz. The corresponding law is then:

$$\Lambda_e = \begin{cases} 0 & \text{if } \tau_b \leq \tau_1, \\ \Lambda_{e0} \dfrac{\tau_b - \tau_1}{\tau_2 - \tau_1} & \text{else if } \tau_1 \leq \tau_b \leq \tau_2, \\ \Lambda_{e0} & \text{else,} \end{cases} \tag{3.59}$$

where Λ_{e0} is a constant rate, and τ_2 a slope parameter.

In this manuscrit, except when explicitly mentioned, we keep all ReSCAL parameters constant, equal to those given in table 3.1, used in previous calibrations and studies using this model (Narteau *et al.* 2009, Zhang *et al.* 2010; 2012; 2014, Gao *et al.* 2014; 2015a;b; 2016, Lü *et al.* 2016; 2017; 2018, Gao *et al.* 2018).

Saturation properties

Narteau *et al.* (2009) and Zhang *et al.* (2007) give a complete an detailed scaling of the model, with the derivation of all transport quantities. Here, we leave aside theoretical calculations and present direct 'measurements' on the model.

Figure 3.21(a) shows the measurement of saturation length and saturated flux in the model, similar to the wind tunnel experiment shown in figure 1.8. On the erodible bed, the sediment flux exponentially relaxes towards a constant saturated value $Q_{sat} = 0.26\ l_0^2\ t_0^{-1}$ over a characteristic length $L_{sat} = 1.6 \pm 0.1\ l_0$, in agreement with Narteau *et al.* (2009) and Zhang *et al.* (2007). The value of the saturated flux then decreases with time and tends to $\sim 0.1\ l_0^2\ t_0^{-1}$, as the cells cluster together and change the characteristic roughness of the bed (figure 3.21(b)). This is consistent with the value inferred from measurements of barchan and sand wave velocities in the model, similar to figure 1.17, resulting in $Q_{sat} \sim 0.13\ l_0^2\ t_0^{-1}$ (Zhang *et al.* 2010).

Dune emergence

In the model, the bed is not destabilized by the hydrodynamics. As shown in figure 3.22, the modulation of the basal velocity is in phase with the topography, which is equivalent

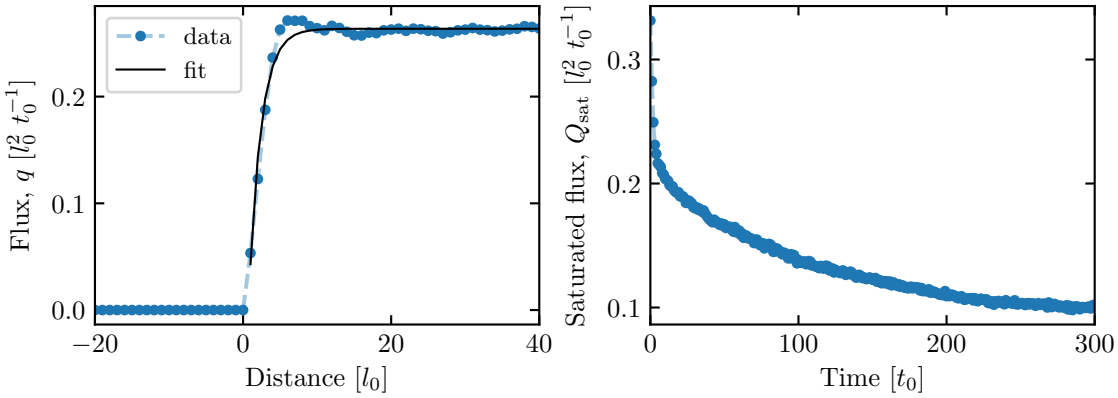

Figure 3.21 – (a) Sediment flux over a flat bed in the ReSCAL dune model, averaged of the first 5 t_0, and along the cross stream direction (10000 l_0). The erodible bed starts in $x = 0$, preceded by neutral non-erodible cells. The fit of the exponential relaxation (1.21) gives $Q_{\mathrm{sat}} = 0.26 \pm 0.001\ l_0^2\ t_0^{-1}$ and $L_{\mathrm{sat}} = 1.6 \pm 0.1\ l_0$. (b) Saturated flux as a function of time.

to $\mathcal{B} = 0$. Although the advance of the shear stress with respect to the topography is essential for the emergence of dunes in physical situations, it is here replaced by an inherent asymmetry to the model, induced by the choice of the transitions. Indeed, there is no transition allowing erosion in the lee side of a pile of elementary cells (figure 3.20), which is equivalent to the shadow zone introduced in other cellular automaton models (Werner 1995, Baas 2002).

Whereas the mechanism at the origin of dune emergence is different in the model, the overall behaviour remains the same. Indeed, Narteau *et al.* (2009) performed a numerical linear stability analysis by looking at the evolution of a set of transverse sinusoidal topographies of different wavelengths. The numerically obtained growth rate exhibits a maximum for $\lambda \simeq 40\ l_0$. By identifying this value to the incipient dune wavelength in natural conditions, around 20 m, the authors set the intrinsic length scale of the model to $l_0 \simeq 0.5$ m. Likewise, using typical values of saturated sand flux on earth leads to an intrinsic time scale of $t_0 \simeq 8 \times 10^{-4}$ yr.

3.6.2 Methods

In order to quantify bedforms emergence inside the model, following Narteau *et al.* (2009), a numerical linear stability analysis of a flat sediment bed is performed in the model under bidirectional wind regimes. We modulate the sand layer by a sinusoidal topography of wavenumber k and angle α, with a very small initial amplitude of $\zeta = 4\ l_0$. After stabilizing the flow above this elevation profile, we start the sediment transport model and compute at regular time intervals the amplitude, the wavelength and the orientation using two-dimensional autocorrelation. The growth rate is then inferred from the exponential increase of the amplitude over the first 60 t_0, during which we checked that the wavelength

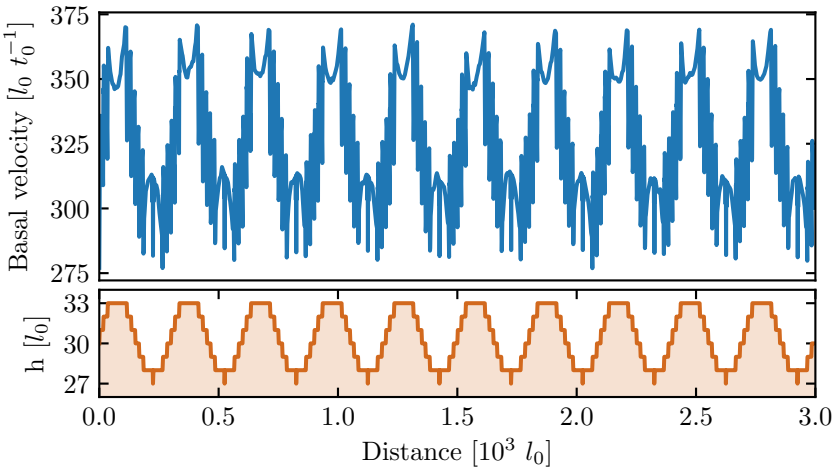

Figure 3.22 – Basal velocity above a fixed sinusoidal topography of wavelength $\lambda = 200\ l_0$ in the ReSCAL dune model, averaged over $10^5\ t_0$.

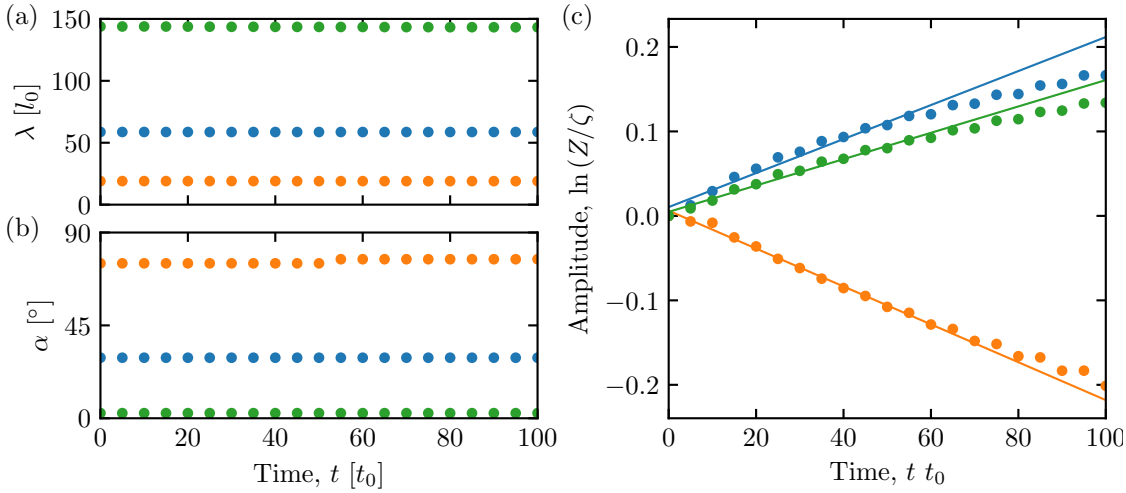

Figure 3.23 – Incipient evolution of a sinusoidal sediment layer in the ReSCAL dune model, for $\theta = 30°$ and $N = 1$ (a) Pattern wavelength as a function of time. (b) Pattern orientation as a function of time. (c) Logarithm of the pattern amplitude as a function of time. Points are the numerical data, and plain lines are linear fits for the first 60 t_0.

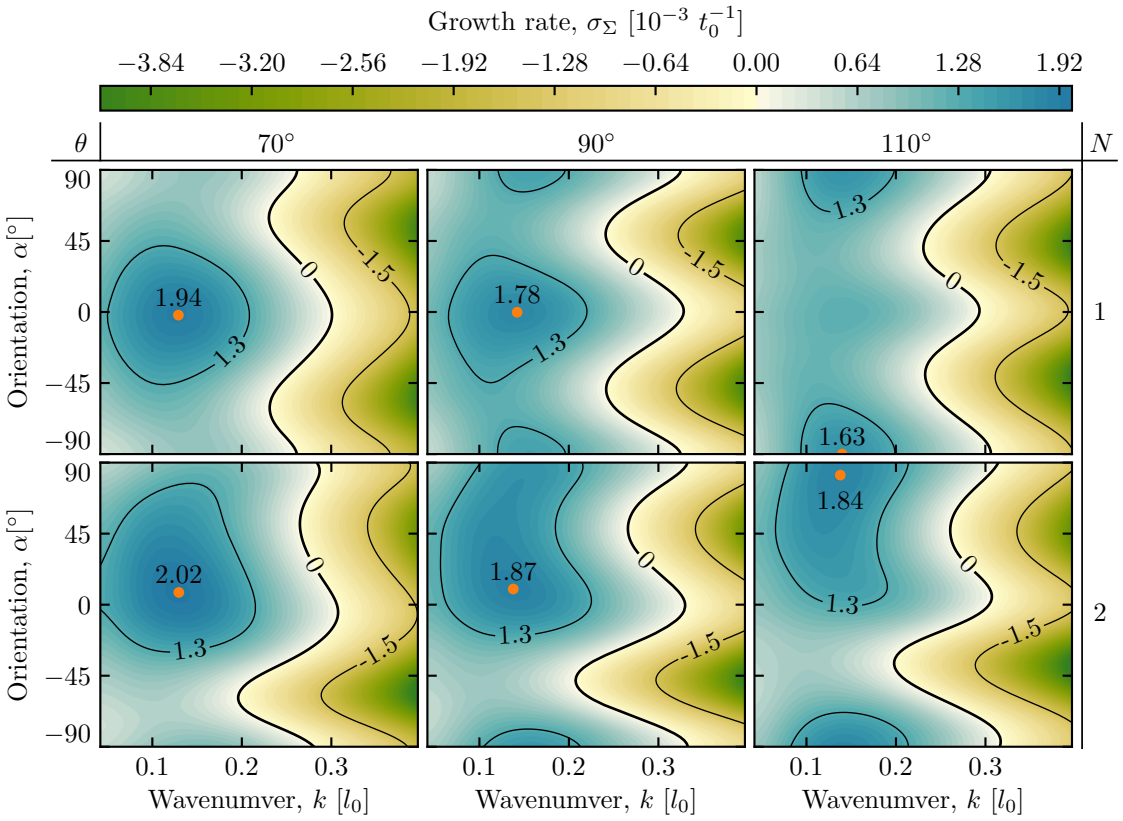

Figure 3.24 – Growth rate σ_Σ in the ReSCAL dune model as a function of the wavenumber k and the orientation α of the bed perturbation for different values of the divergence angle θ (columns) and the transport ratio N (rows). Orange dots: most unstable mode $(\alpha_{\max}, k_{\max})$ (the corresponding value of σ_Σ has been multiplied by 10^3 for clarity). The signal has been smoothed using a gaussian filter.

and the orientation remain constant (see figure 3.23).

By varying the initial wavelength from 10 l_0 to 160 l_0 and the angle from −90° to 90°, we compute stability maps analogous to the theoretical ones presented in figures 3.5. Figure 3.24, shows that their aspect, and their variation with respect to N and θ are highly similar to those obtained by the theory (see figure 3.5). They all exhibit a well-defined maximum from which we can extract the most unstable mode $(\alpha_{\max}, k_{\max})$, and the associated maximum growth rate $\sigma_{\max}$.

3.6.3 Numerical results

Most unstable orientation

Figure 3.25 shows the most unstable orientation obtained form the numerical stability analysis as a function of the angle between the two winds θ, for different values of the transport ratio N. For $N = 1$, we recover the predicted orientations, either transverse ($\alpha_{\max} = 0°$) when $\theta \leq 90°$ or longitudinal ($\alpha_{\max} = 0°$) when $\theta \geq 90°$. As N increases, the

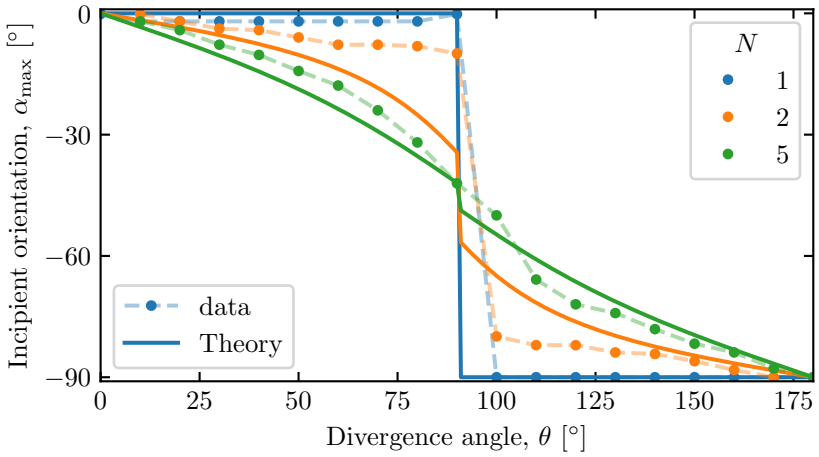

Figure 3.25 – Most unstable orientation as a function of the wind regime in the ReSCAL dune model, computed using a numerical linear stability analysis. Points are the data, and plain lines are the prediction of the model of Courrech du Pont *et al.* (2014) for $\gamma = 1.7$, presented in section 3.3.4. The uncertainty on the measurement of the most unstable orientation is estimated to ±2°.

orientation becomes closer to the perpendicular to the dominant wind direction.

Note that a first difference with respect to the results of previous sections relates to the divergence angle θ for which the transition occurs. In the theoretical linear stability analysis, the transition is predicted for $\theta = 90°$. However, we saw in the experiments that the longitudinal orientation already seems to prevail for this value. In contradiction, in the ReSCAL dune model, the pattern is dominated around $\theta = 90°$ by the transverse orientation, as shown by figure 3.25.

Because of all the differences between the model and physical conditions in terms of transport, flow and avalanching processes, comparing quantitatively the obtained orientations with the predictions of the theoretical linear stability analysis is difficult. They can however be compared with the dimensional model of Courrech du Pont *et al.* (2014) presented in section 3.3.4. As already found by Gao (2013), Courrech du Pont *et al.* (2014) and Gao *et al.* (2015b), the orientation of the flat bed instability in the ReSCAL dune model is closer to the wind bisector than the predicted ones.

Note that, in these previous works, the authors managed to recover to predicted orientation by increasing the transition rate associated to the diffusion Λ_d by two orders of magnitudes, increasing equivalently the associated diffusion length (see appendix B.2). This is consistent with the theoretical results presented in section 3.5.1, where increasing the non-dimensional diffusion length δ by two order of magnitudes gives orientations much closer to predictions of Courrech du Pont *et al.* (2014) (see figure 3.17).

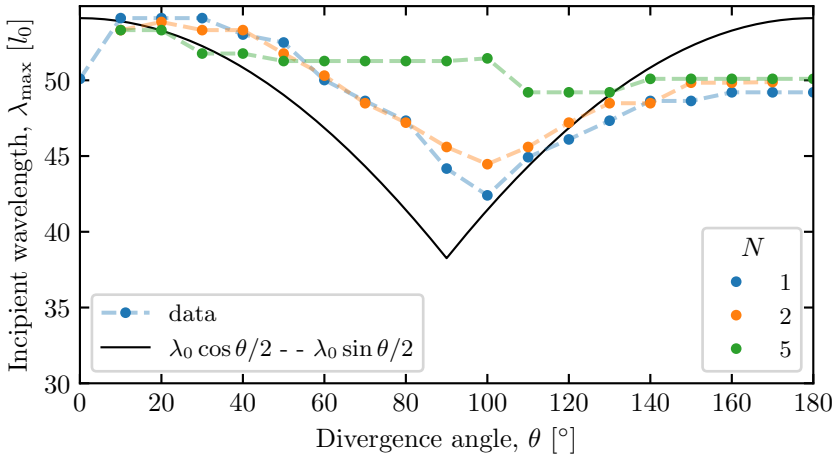

Figure 3.26 – Most unstable wavelength as a function of the wind regime in the ReSCAL dune model, computed using a numerical linear stability analysis. The black line corresponds to the geometrical model presented in section 3.3.5, adjusted in $\theta = 0°$ at 54 l_0. The measurement uncertainty on the wavelength is estimated to ±1 l_0.

Most unstable wavelength

Figure 3.26 shows the most unstable wavelength obtained form the numerical stability analysis as a function of the divergence angle θ, for different values of the transport ratio N. In agreement with the results of previous sections, the wavelength is smaller for divergence angles close to 90°. This effect is also weaker for larger values of N, when one wind prevails over the other. Note the first point at $\theta = 0°$, slightly out of trend. This discrepancy may result from numerical errors induced by rotations of the bed elevation, used to simulate multidirectional wind regimes, and thus not present for $\theta = 0°$. Furthermore, this point also differs from the results of Narteau *et al.* (2009) by about 10 l_0, probably because of the difference in the sampling points between the two studies coupled to the flatness of the growth rate around its maximum.

The magnitude of the variation of the wavelength is in agreement with the geometrical model presented in section 3.3.5, shown by the black line in figure 3.26. However, the minima of the two curves are separated of about 10°, in agreement with the fact that 'non-reversing dunes' [3] dominate the pattern around $\theta = 90°$.

Note that, similarly to the underwater experiments, this variation is not symmetric with respect to $\theta = 90°$, and 'reversing dunes' [4] form systematically at smaller wavelengths. The relative variation between λ_0 and λ_{180} is however smaller in the ReSCAL dune model (10%) than in the underwater experiments (25%).

3. When $N > 1$, bedform orientation is not necessarily transverse or longitudinal, but it can also be oblique. We will use here the term of 'non-reversing dunes' for dunes emerging under winds blowing on only one of its sides ($\theta < 90°$), in contrast to dunes built under winds blowing on both of its sides ($\theta > 90°$), named 'reversing dunes'.

4. See footnote 3.

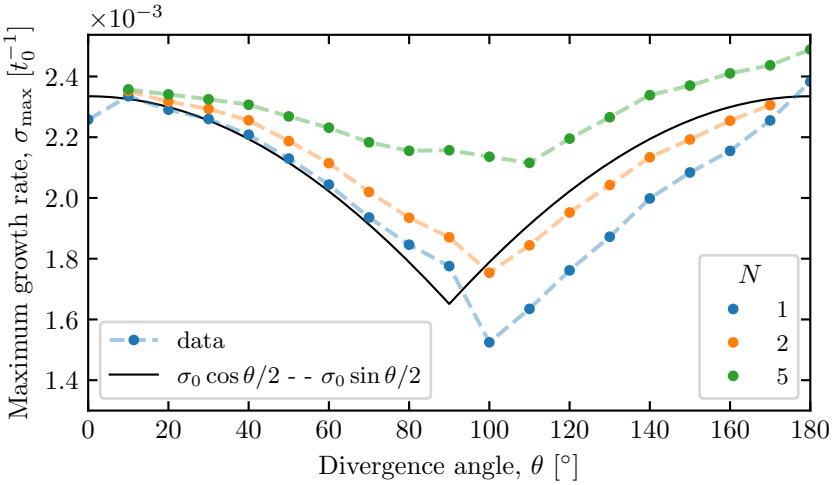

Figure 3.27 – Maximum growth rate as a function of the wind regime in the ReSCAL dune model, computed using a numerical linear stability analysis. The black line corresponds to the geometrical model, adjusted in $\theta = 0°$ at 2.3×10^{-3} t_0^{-1}. The measurement uncertainty on the growth rate is estimated to $\pm 2 \times 10^{-4}$ t_0^{-1}.

Maximum growth rate

Figure 3.27 shows the maximum growth rate obtained form the numerical stability analysis as a function of the angle between the two winds θ, for different values of the transport ratio N. In agreement with the results of previous sections, the growth rate decreases as the divergence angle approaches 90°. This effect is also weaker for larger values of N, when one wind prevails over the other.

Just like for the wavelength, an analogous geometric model can be written for the growth rate. For small wavenumbers, the growth rate is proportional to $k^2 \cos\alpha^3$ (see equation 3.3.1). Including the geometric variation of the wavelength (3.39) in this scaling leads to:

$$\sigma_{max} = \begin{cases} \sigma_0 \cos\frac{\theta}{2}, & \text{for } \theta \leq 90°, \\ \sigma_0 \sin\frac{\theta}{2}, & \text{for } \theta \geq 90°. \end{cases} \tag{3.60}$$

As shown by the black line in figure 3.25, this geometric model recovers the magnitude of the variation of the growth rate with respect to the divergence angle in the numerical simulations. Again, minima of the data and the geometric model are separated of about 10°. However, unlike the wavelength and what is observed in the experiments, the growth rate does not exhibit any clear asymmetry with respect to $\theta = 90°$, between reversing and non-reversing dunes.

3.7 Concluding remarks

This work addresses the emergence of a dune pattern from a flat bed submitted to a bidirectional wind regime. It generalises the dimensional approach of Rubin & Hunter (1987) and Courrech du Pont *et al.* (2014) with a more fundamental linear stability analysis where hydrodynamics over a modulated bed as well as transient sediment transport are described. Our predictions essentially agree with previous results for dune orientation with a transition from transverse to longitudinal dunes, but provide a wider range of possible alignments, especially when the two winds have a divergence angle close to the transition value 90°, depending on flow strength. This analysis also allows us to predict a preferred pattern wavelength, and we show that it either decreases close to the transition for strong winds, due to a geometric effect, or increases at low winds, when the bed slope affects the transport threshold.

In addition, analogous subaqueous experiments and numerical simulations where incipient dunes are submitted to alternate forcing in different directions validate part of the model. The geometric effect responsible for the variation of the wavelength close to the transition angle is recovered as well as the increase of the wavelength close to the transport threshold for transverse bedforms. However, longitudinal patterns deviate from the model as they systematically form at smaller wavelengths than expected, and also do not show any variation of their wavelength with the distance to the threshold. Finally, these laboratory experiments show the coexistence of the two pattern orientations predicted by the linear stability analysis close to the transition angle $\theta = 90°$. This coexistence continues beyond the linear regime in the experiments but also at much larger scale in deserts on Earth.

To describe the formation of dune patterns under natural multidirectional flow conditions, the analysis can be generalised to any wind rose by adding all the sediment flux contributions. Following (3.25), the dimensional overall growth rate σ_Σ of a mode (α, k) can be written as

$$\sigma_\Sigma(\alpha, k) = \frac{1}{L_{\mathrm{sat}}^2} \frac{\sum_i t_i Q_i \sigma\left(\frac{u_{*,i}}{u_{\mathrm{th}}}, \alpha, k\right)}{\sum_i t_i}, \tag{3.61}$$

where t_i, Q_i and $u_{*,i}/u_{\mathrm{th}}$ are the duration, the flux and the velocity ratio associated with each wind, that can be derived from field measurements or atmospheric models. Additional data, such as the typical grain size of the sand bed in order to estimate the velocity threshold u_{th} and the saturation length L_{sat}, are also necessary to compute σ_Σ. Its maximum then gives the most unstable mode $(\alpha_{\max}, k_{\max})$, predicting the incipient dune orientation and wavenumber for the considered region. As typical sand fluxes in terrestrial deserts are of the order of $Q \simeq 10$ m^2 yr^{-1}, the corresponding characteristic dune growth time $(1/\sigma_{\max})L_{\mathrm{sat}}^2/Q$ (with $\sigma_{\max} \simeq 0.07$, see figure 3.5) is about 8 months, not much

larger than but rather comparable to the seasonal period of wind reorientation (as for our subaqueous experiment). This estimation seems, however, to agree with field observations, as illustrated in figure 3.1, which emphasizes the robustness of the orientation prediction. Despite the difficulties in documenting the linear regime in natural environments, more sites should be systematically tested. This is the object of recent studies, that uses the theoretical framework described in this chapter to quantitatively interpret field data (Lucas *et al.* 2019, Iacono *et al.* 2020, Delorme *et al.* 2020).

The comparison of the dune orientation predictions with those of Courrech du Pont *et al.* (2014) suggests that these predictions are still valid in a nonlinear regime as long as dunes develop in areas of high sediment availability. As for the dune wavelength, however, pattern coarsening usually occurs soon after dune emergence and the wavelength grows by means of collisions and coalescence. Driven by the defects in the pattern (Gao *et al.* 2015b, Day & Kocurek 2018), this coarsening is likely to depend on the wind regime. Further studies are needed to investigate this process in order to fully understand the observed complexity of dune fields in nature.

Chapter 4

Numerical study of linear dunes

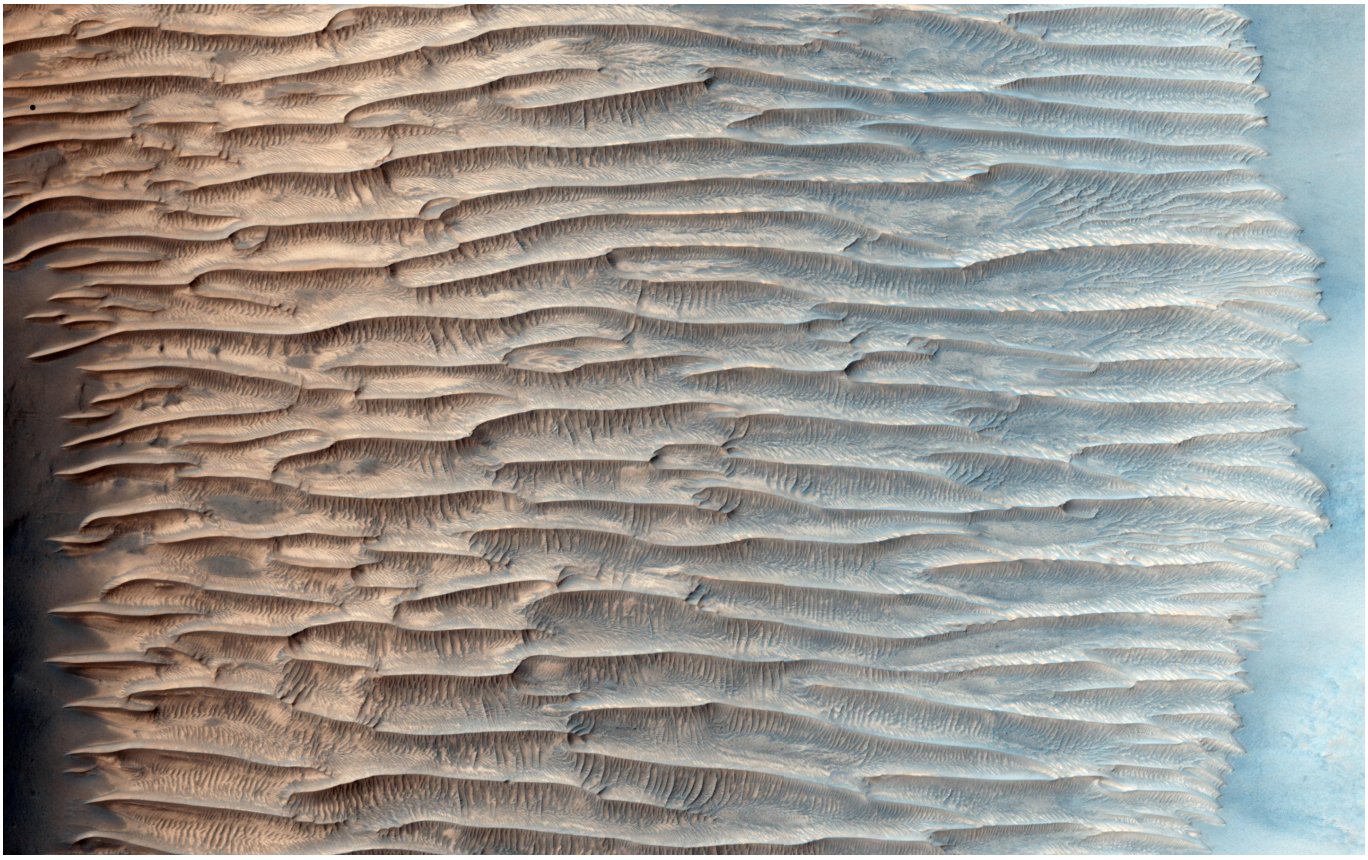

"Feathery Ridges", linear dunes on Mars - NASA/JPL-Caltech/Univ. of Arizona

Contents

In the previous chapters, we investigated the linear dynamics of emerging bedforms. The maturation of these patterns then leads to the appearance of objects with non-linear dynamics. Under a constant unidirectional wind, incipient dunes turn into mature transverse dunes and barchans, whose morphodynamics have been extensively studied. However, the presence of multidirectional wind regimes on Earth and other planetary bodies leads to a wide diversity of patterns, that have been described in chapter 1. In particular, elongating linear dunes are individual sand ridges aligned with the resultant transport direction. Also referred to as seif dunes (Lancaster 1982, Tsoar 1982) or silks (Mainguet & Callot 1978) when they are sinuous, these finger-like structures are widespread on Earth and other planetary bodies. They elongate under multidirectional wind regimes on non-erodible beds thanks to the deposition at the dune tips of the sediment transported along the crests.

This elongation mechanism has been reported in the field as well as in numerical simulations and underwater laboratory experiments, but still, not much is known about it. Dune elongation occurs only where the wind blows in at least two directions separated by a minimum angle of 90°. Then, the dune orientation is selected as the one that cancels the fluxes perpendicular to the crest, preventing any crest destabilization induced by migration (Reffet *et al.* 2010). When the wind regime is too unidirectional, only barchan dunes are reported. However, Gao *et al.* (2015b) suggest a complex dependence of dune morphology on the wind regime and sand availability. This implies that the existence and stability of elongating dunes seem to rely on more than just the angular distribution of the sand fluxes and the sand availability.

- Why is the elongation mechanism not visible in areas of high sediment supply? What do *low* and *high* mean in terms of sediment supply, and when does the transition from the bed instability to this mechanism occur ?
- Does the elongation mechanism control the periodicity of elongating dunes (when there is) in zones of low sediment supply, as it controls the orientation ?
- What is the impact of the wind reorientation period on the stability and morphology on elongating dunes ?
- More generally, what are the conditions of existence and stability of elongating dunes in terms of wind regime and sediment influx ?

In this chapter, we will give pieces of answers to these questions using the cellular automaton dune model ReSCAL, described in subsection 3.6.1. The first section is the retranscription of a letter published in *Geology*, and adresses the question of the periodicity (Gadal *et al.* 2020). In the next one, we sum up some important results about the elongation of isolated linear dunes from a work published in *Geophysical Research Letters*, which I could participate in during my thesis (Rozier *et al.* 2020).

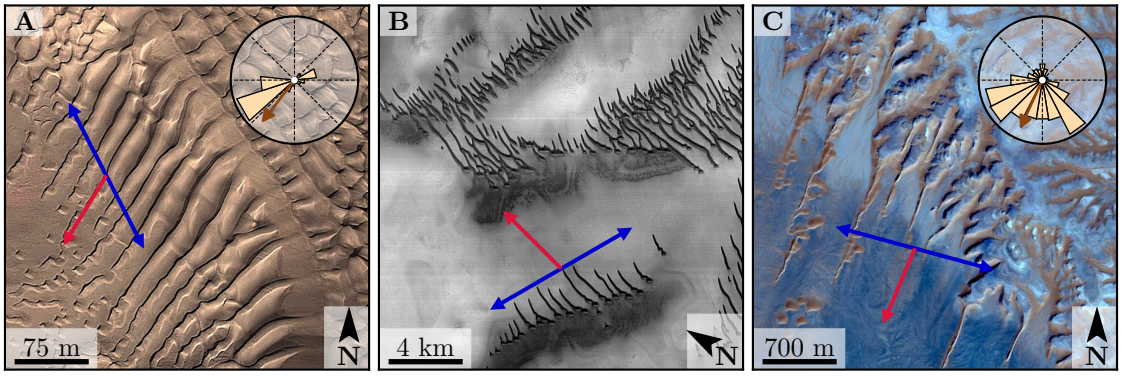

Figure 4.1 – **Periodic dune patterns.** **A**: Elongating dunes at the bottom of an avalanche slope, Taklamakan desert, China (37°45′ N, 82°36′ E). **B**: Elongating dunes on Mars, Scandia Cavi (78°04′ N, 151°10′ W). **C**: Elongating dunes at the bottom of an erosion pattern, Rub' Al Khali Desert, Saudi Arabia, (10°00′ N, 45°40′ E). Arrows show the dune orientations predicted from the wind data on a non-erodible bed (red) and a sand layer (blue) following Courrech du Pont *et al.* (2014), except for Mars (**B**) where dune orientations are inferred from the dune crests on the satellite image. Insets show sand flux roses. Satellite images: Google™, Maxar Technologies, NASA/JPL/University of Arizona.

4.1 Periodicity in fields of elongating dunes

4.1.1 Abstract

Dune fields are commonly associated with periodic patterns that are among the most recognizable landscapes on Earth and other planetary bodies. However, in zones of limited sediment supply, where periodic dunes elongate and align in the direction of the resultant sand flux, there has been no attempt to explain the emergence of such a regular pattern. Here we show, by means of numerical simulations, that the elongation growth mechanism does not produce a pattern with a specific wavelength. Periodic elongating dunes appear to be a juxtaposition of individual structures whose arrangement is due to regular landforms at the border of the field, acting as boundary conditions. This includes, among others, dune patterns resulting from the bed instability, or the crestline reorganization induced by dune migration. The wavelength selection in fields of elongating dunes therefore reflects the interdependence of dune patterns over the course of their evolution.

4.1.2 Introduction

Systematically highlighted by aerial photographs and satellite images, periodic geomorphological features have revealed the presence of dunes and atmospheric flows on planetary bodies, including Earth, Mars, Titan, Pluto and comets (McKee 1979, Cutts & Smith 1973, Ward *et al.* 1985, Lorenz *et al.* 2006, Bourke *et al.* 2010, Lorenz & Zimbelman 2014, Lucas *et al.* 2014, Jia *et al.* 2017, Diniega *et al.* 2017, Telfer *et al.* 2018). The origin of

these periodic patterns is a central issue in dune physics and planetary sciences, alongside with the diversity of dune shapes, sizes and orientations (Wasson & Hyde 1983, Rubin & Hunter 1987, Andreotti *et al.* 2009).

Under multidirectional flows, many dune fields with low sand availability exhibit linear dunes that extend for kilometers on non-erodible beds. These dunes result from an elongation growth mechanism leading to deposition at the dune tip of sediment transported along the crest under the action of reversing winds (Courrech du Pont *et al.* 2014, Gao *et al.* 2015b). While these elongating dunes can exist as isolated objects (Lucas *et al.* 2015), most of fields of elongating dunes display a periodicity (Fig. 4.1). The origin of this periodicity has not yet been investigated or compared to pattern formation in zones where dunes can grow in height with full sediment availability. A related point is thus how populations of dunes in transport and sediment-limited conditions are independent based on current understanding of the emergence of dune wavelengths.

Periodic dune patterns are typically linked to the development of incipient bedforms due to an instability mechanism, which select a characteristic length scale from the competition between destabilizing and stabilizing processes. The flat bed instability occurs in transport-limited conditions where dunes arise from the interaction between turbulent flow, sediment transport and topography at a wavelength $\lambda_{\max}$, for which the growth rate is maximal (Charru *et al.* 2013). Another instability occurs on transverse dunes migrating on a non-erodible bed. They break into a set of periodic barchan dunes with a size proportional to the height of the initial transverse dune (Reffet *et al.* 2010, Niiya & Nishimori 2010, Parteli *et al.* 2011, Guignier *et al.* 2013). The collective dynamics of individual bedforms can also govern the development of patterns. In sediment-limited environments, these individual structures take the shape of barchans, domes or star dunes according to the wind regime (Hersen 2004b, Zhang *et al.* 2012, Baddock *et al.* 2018, Gao *et al.* 2018). Whatever their shapes, as soon as they form populations, dunes interact by mass exchange induced either by collisions or sand flux. These interactions generate a higher level of organization, with a characteristic size, frequently observed along the sand flow paths in dune corridors, chains and clusters (Elbelrhiti *et al.* 2008, Worman *et al.* 2013, Génois *et al.* 2013a;b). In all dune fields, independently of the origin of the pattern, non-linear interactions also lead to an increase in dune amplitude and wavelength in space and time (Ewing & Kocurek 2010, Valance 2011, Gao *et al.* 2015a). While the smallest wavelengths are intrinsically associated with incipient bedforms, the coarsening process is restricted by boundary conditions that can ultimately set the maximum length scales of the dune pattern.

By means of numerical simulations, we study two independent configurations that produce periodic elongating dunes. We show that the spatial organization of these dunes is controlled by the geomorphological patterns from which they develop. The elongation

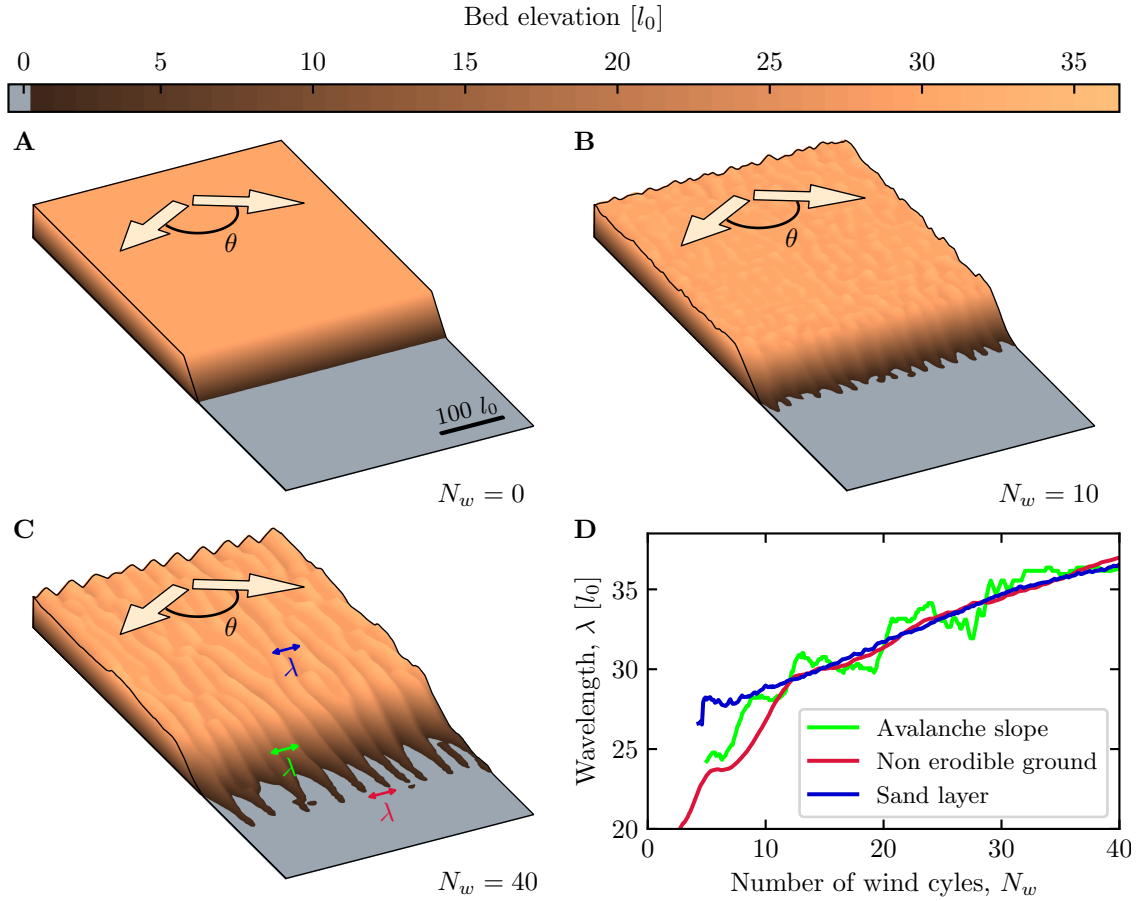

Figure 4.2 – **Dunes elongating at the border of a sediment layer**. **A-C**: Evolution of the sediment bed in the model. The non-erodible bed is shown in gray. **D**: Wavelengths of the pattern on the sediment layer (blue), on the avalanche slope (green) and the non-erodible bed (red) as a function of time.

growth mechanism does not itself select a characteristic wavelength but can express from pre-existing structures while retaining some of their properties. The periodic pattern is therefore inherited from past environments or specific boundary conditions upstream of the sand flow paths.

The first situation represent the border of a sand layer, where we relate the wavelength of the dunes elongating at the bottom of the avalanche slope to the pattern over the sediment layer. The second one show the migration of a sand bar subjected to a bidirectional wind. Here, we relate the wavelength of the elongating dunes to the initial bar height, and therefore to the crest destabilization process.

4.1.3 Methods

We use here a cellular automaton dune model that accounts for feedback mechanisms between the flow and the evolving bed topography (Rozier & Narteau 2014). This approach has been shown to be efficient in modeling dunes in multidirectional wind regimes and is

able to reproduce and quantify superimposed bedforms in dune fields (Zhang *et al.* 2012, Lü *et al.* 2017). The model parameters are the same as in Narteau *et al.* (2009), so that the model length and time units l_0 and t_0 are about 0.5 m and 10^{-3} yr, respectively. Based on field observations, we implement two specific configurations to generate periodic elongating dunes. In both cases, we consider a bidirectional wind regime with a divergence angle $\theta = 120°$ and a constant wind strength (the saturated flux over a flat sand bed is about 0.23 $l_0^2\ t_0^{-1}$). However, the duration of the winds can differ and the transport ratio N is the ratio between the time spent in the primary and secondary winds over a wind cycle T_w (Rubin & Hunter 1987). Autocorrelation of the bed elevation is used to measure the elongation rate and the wavelength of the dune patterns.

In the first configuration, we focus on the development of dune patterns at the interface between a sediment layer of height 30 l_0 and a non-erodible bed. An avalanche slope makes the transition between the two (Figs 4.2 and 4.3). We use the simplest case of winds of equal duration ($N = 1$, $T_\mathrm{w} = 100\ t_0$) with a resultant sand transport perpendicular to the avalanche slope. All dune orientations are aligned with the transport direction and there is no lateral dune migration. Along this direction, the output sand flux is lost (i.e open conditions). Perpendicularly, the cellular space is made periodic to mimic an infinitely wide system.

In the second configuration, a sand bar of height H is placed over a non-erodible bed. We study its migration when subjected to an asymmetric regime ($N = 3$, $T_\mathrm{w} = 40\ t_0$) for which the dominant wind is perpendicular to the bar orientation (Fig. 4.4A). Along this direction, we keep open the output sand flux condition, preserving the periodicity in the perpendicular direction. As in a unidirectional wind regime, the bar migrates and can destabilize due to the lateral mass redistribution. Furthermore, in the presence of a secondary wind, elongating dunes can develop.

Finally, we interpret field examples using the method described in Courrech du Pont *et al.* (2014). The predicted dune orientations are calculated from wind data provided by the ERA-Interim project or by local wind towers (Fig. 4.1A and C). For the martian example, they are measured from the dune crests on the satellite images (Fig. 4.1B).

4.1.4 Results

Elongation from a flat sediment layer

Figure 4.2A-C shows the evolution of the bedforms at the border of the sediment layer. Incipient dunes develop from the flat bed instability on the sediment layer and the avalanche slope, and also elongate at the bottom of this lee face. Both dune types exhibit a regular pattern with well defined wavelengths that connect with each other, as well as the same orientation due to the specific wind regime $N = 1$ (Fig. 4.2C). On the

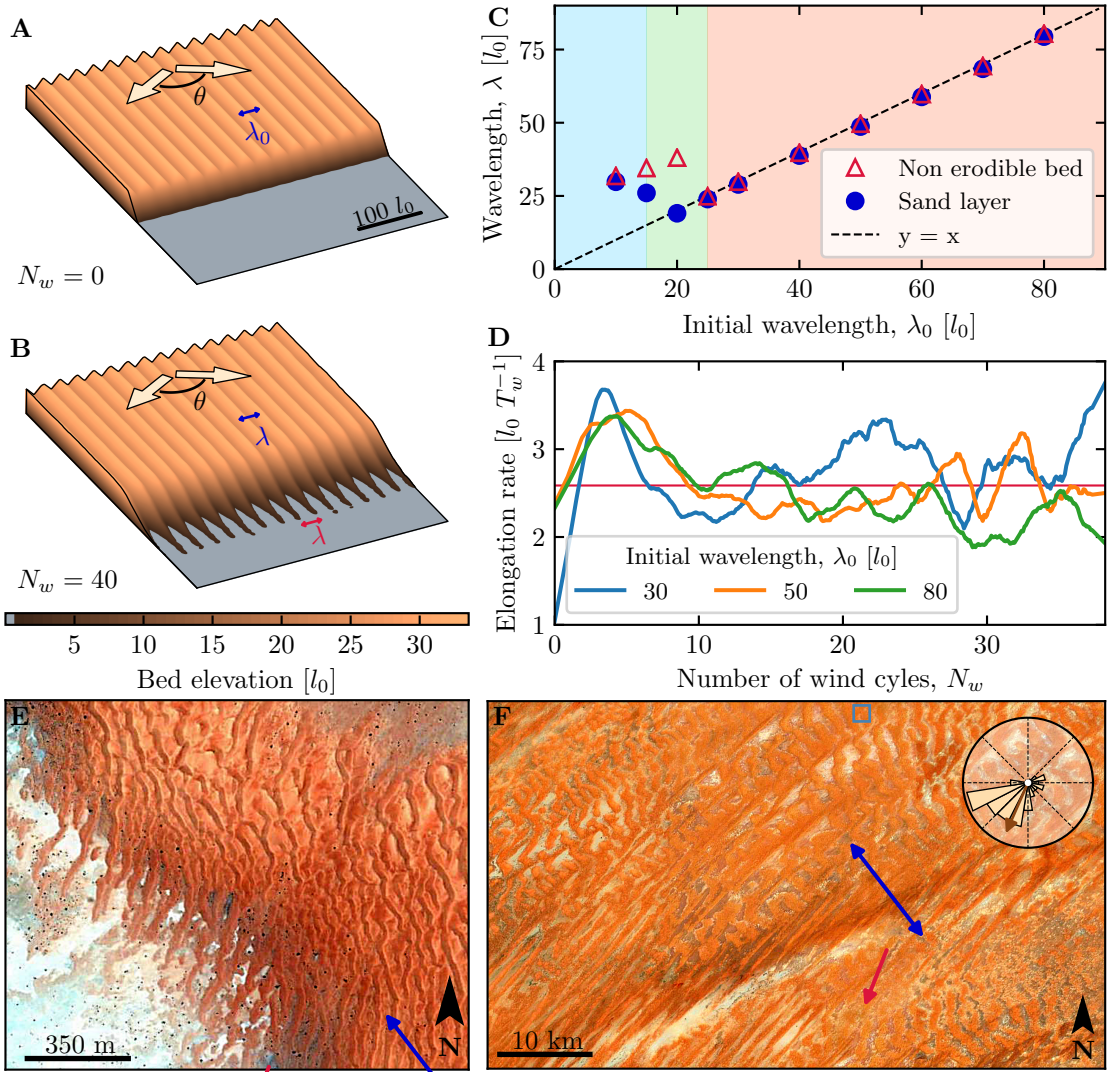

Figure 4.3 – **Dunes elongating at the border of a sinusoidal sediment layer**. **A-B**: Evolution of the sediment bed in the model for an initial wavelength λ_0 = 30 l_0. **C**: Wavelengths of the pattern on the sediment bed (blue) and on the non erodible bed (red) after 40 wind cycles as a function of the imposed wavelength λ_0. Shaded areas are arbitrarily defined to help describe the figure in the text. **D**: Elongation rate of the dunes as a function of time for different imposed wavelengths. The red line shows the average value. **E**/**F**: Field examples at small (**E**) and large (**F**) scales in the western Sahara, Mauritania (18°11′ N, 14°30′ W). Blue square is the location of **E** on **F**. Arrows show the dune orientations predicted from the wind data on a non-erodible bed (red) and a sand layer (blue) following Courrech du Pont *et al.* (2014). Insets show sand flux roses. Satellite images: Google™, Maxar Technologies, Landsat/Copernicus.

sediment layer, the dune wavelength starts from that of the most unstable mode associated with the bidirectional wind regime (Gadal *et al.* 2019). On the avalanche slope, the pattern wavelength starts at a slightly lower value, as well as the one on the non erodible ground. After a few wind cycles, both patterns connect through the avalanche slope, as the wavelengths become identical and then increase due to coarsening (Fig. 4.2D). The periodicity of the elongating dunes then appears to be controlled by that of the dunes on the sand layer. In addition, we observe that the pattern of the elongating dunes is directly impacted by the defects of the sediment layer pattern when the dunes reach the avalanche slope.

Elongation from a perturbed sediment layer

To test this control mechanism, we started simulations from a sediment layer with a sinusoidal elevation profile perpendicular to the resultant sand flux (Fig. 4.3A-B). Figure 4.3C shows the wavelength of the dune patterns on both side of the avalanche slope after 40 wind cycles with respect to the initial wavelength. For λ_0-values larger than $\lambda_{\max}$, there is perfect agreement between all these wavelengths (red part of Fig. 4.3C). As these large wavelengths are unstable with respect to the flat bed instability, the initial pattern persists throughout the simulation enforcing its periodicity to the elongating dunes. For λ_0-values smaller than $\lambda_{\max}$, however, the initial bed undulations are quickly replaced by those of the most unstable mode of the flat bed instability (blue part of Fig. 4.3C). As coarsening occurs along the resultant flux direction, the wavelength of the elongating dunes is a bit larger than the one measured on the sediment layer.

Figure 4.3D shows the elongation rate of the dunes developing at the bottom of the avalanche slope as a function of time. These measurements have been done for three large wavelengths (red part in Fig. 4.3C). After a short transient time period of 5 to 10 wind cycles, all three elongation rates fluctuate around the same constant value. This duration corresponds to the time needed for the dunes at the base of the avalanche slope to reach the minimal size integrating the two winds. In the next phase, during which they elongate at a constant average rate, the dune tip periodically breaks, migrates and disperses, explaining the observed variability. As no wavelength emerges faster than the others, the elongation mechanism does not select any length scale.

Elongation from the break-up of a sand bar

Using the second configuration, Figure 4.4A shows a migrating sandbar that becomes sinuous and ultimately breaks up into a periodic set of dunes. As in unidirectional wind regimes, the resulting wavelength of these dunes is determined by the height of the sandbar (Fig. 4.4). In bidirectional wind regimes, the crestline reorganization is not only related to the lateral redistribution of mass associated with the primary wind but also to the

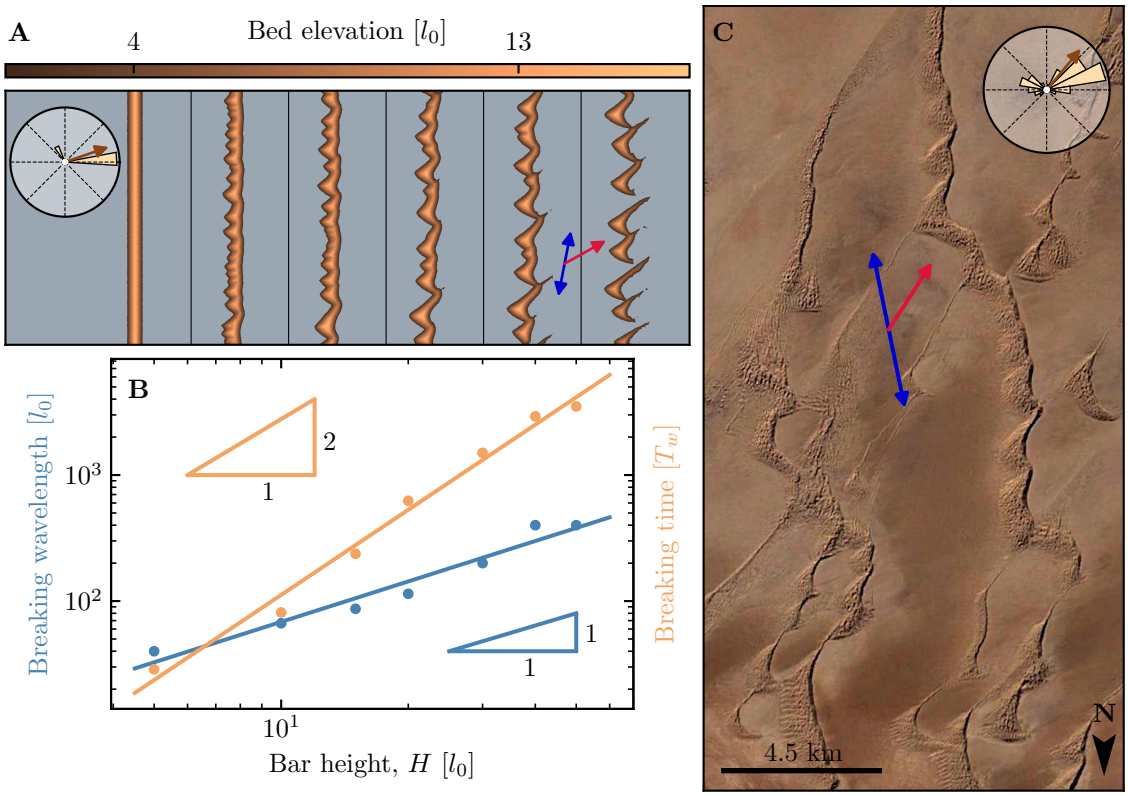

Figure 4.4 – **Break-up of a sand bar in a bidirectional wind regime**. **A**: Evolution of a sand bar during its migration (corresponding number of wind cyles: N_w = [0, 150, 225, 335, 400, 580]). **B**: Wavelength of the dune pattern and migration time as a function of the initial height of the bar, measured at breaking. Points are the numerical results and lines the best linear fits. **C**: Field example in the Kavir desert, Iran (34°06′ N, 53°40′ E). Arrows show the dune orientations predicted from the wind data on a non-erodible bed (red) and a sand layer (blue) following Courrech du Pont *et al.* (2014). Insets show sand flux roses. Satellite image: Google^{TM}, Maxar Technologies.

superimposed bedforms that develop and migrate in an oblique direction with respect to the orientation of the sandbar (Courrech du Pont 2015, Lü *et al.* 2017). Ultimately, the resulting periodic dunes also elongate under the action of the reversing winds, as in the experiments of Courrech du Pont *et al.* (2014) (Fig. 4.4C). In multidirectional flows, the break-up of pre-existing dunes is therefore another source of periodicity in fields of elongating dunes (Fig. 4.1B).

4.1.5 Discussion

We identify two relevant length scales for dune growth in bidirectional wind regimes, which are potential candidates for wavelength control in fields of elongating dunes. The first is the saturation length, associated with the spatial relaxation of transport in response to a bed perturbation (Andreotti *et al.* 2010). The second is proportional to $\sqrt{QT_w}$, where Q is the characteristic sand flux and T_w the duration of the wind cycle. As shown by

Rozier *et al.* (2020), these two length scales control the minimal size and the morphology of isolated elongating dunes. Nevertheless, our numerical simulations suggest that the periodicity in fields of elongating dunes comes from boundary and initial conditions rather than from length scales inherent to the elongation mechanism. This is supported by the fact that the elongation rate is independent of the initial wavelength (Fig. 4.3D).

We then recognize in this process the importance of the migration of dunes from areas of high to low sediment availability. When these dunes eventually fall into an avalanche slope in the transition zone, they impose a periodic modulation at its base, from which elongating dunes can develop (Fig. 4.1A). Interestingly, avalanche processes, and especially sand spreading during granular flow, can also add a level of complexity. In our numerical simulations, high slip faces can act as a filter and prevent transmission of upstream dune patterns of too short amplitude or wavelength down to the base of the avalanche slope. As a result, there is a range of wavelengths for which information is lost in the avalanche slope (green part of Fig. 4.3C).

In addition, superimposed bedforms also appear and develop directly on avalanche slopes, which are areas of loose sand similar to a flat bed for oblique winds. In doing so, they also allow the elongation of periodic dunes at the base. Finally, multidirectional wind regimes more complex than the simplest symmetric bidirectional case studied in Figures 4.2-4.3 would induce an upstream dune orientation oblique to the avalanche slope. As a consequence, under natural conditions, we expect additional geometric factors to be involved in the relation between the wavelength of the upstream bedforms and that of the elongating dunes.

Although the periodicity of many fields of elongating dunes appears to be governed by upstream dune patterns along the sand flow path, it can also be attributed to other spatially periodic landscapes. For example, channel formation and river erosion can lead to evenly spaced ridges and valleys (Fig. 4.1C). This could naturally give rise to a new type of interaction between aeolian and fluvial system in dryland environments (Bullard & Livingstone 2002).

In modern sand seas, a large number of extremely regular fields of elongating dunes have giant sizes, with a kilometer-scale spacing (Andreotti *et al.* 2009). Although we have mainly addressed small and medium sized dunes in our numerical simulations, our conclusions are valid at all length scales. When the dunes at the border have reached their giant size, the wavelength of the elongating dunes must adapt accordingly, preserving the periodicity along the sand flow paths (see Figure 4.3E-F). However, long-term interactions between elongating linear dunes and the resulting auto-organization requires more investigation. In particular, dunes exchange sand by means of lateral fluxes, which make them expand longer (Rozier *et al.* 2020). Whether this process acts as a stabilizing or a destabilizing mechanism for the pattern is an open question.

More generally, our results illustrate how the transmission of the pattern at the border of dune fields exerts a spatio-temporal control on the geomorphology of the landscape along the sand flow path. As any change at the border could be traced farther downwind over time, the observed dune morphodynamics provide information about upstream dune patterns or past environments. They introduces a long-term memory into the migrating dune system. The propagative aspect of the pattern dynamics is also apparent in the presence of an obstacle or in the elimination of defects present in the spatial arrangement of the dune crests. As the density of defects is lower in elongating dune fields than in transverse dune fields (Day & Kocurek 2018), periodicity may appear more easily there, even if it develops only under specific boundary conditions. On Earth, but also on other planetary bodies, these dynamic aspects can now be treated more carefully at the scale of major sand seas to learn more about the long-term evolution of arid landscapes and the variety of dune field patterns.

4.2 Elongation and stability of an isolated linear dune

In the previous section, we have shown that the spatial organisation of elongating linear dunes is deeply controlled by initial and boundary conditions. These dune fields thus appear to be a juxtaposition of individual structures, whose properties remain to be investigated. Sometimes, the upstream source of sediment is fixed, like for lee dunes elongating behind a topographic obstacle, as shown in figure 4.5(a) (Tsoar 1989). In such a situation, there is no lateral migration of the dune body, which can preserve its shape over tens of kilometers (Lucas *et al.* 2014, Lü *et al.* 2017). Understanding the sediment budget along these linear dunes and the conditions leading to their stability is key to assess time and length scales associated with the mechanism of elongation.

By means of numerical simulations, we study in this section the elongation properties of an isolated linear dune.

4.2.1 Methods

Numerical simulations are here again performed with the ReSCAL cellular automaton dune model, described in section 3.6.1. In all simulations, we set an asymmetric bidirectional wind regime of period T_w. Over a wind cycle, two winds of the same strength blow alternatively with a divergence angle $\theta = 120°$. The duration of the primary wind is twice that of the secondary wind, resulting in a mass transport ratio $N = 2$ on a flat bed. The two winds are oriented such that the dune elongates along the main axis of the cellular space of the model (see figure 4.5(b)).

We consider two different setups to investigate the elongation and stability of linear dunes. In the first setup, hereafter the 'injection setup', the simulated field is a corridor

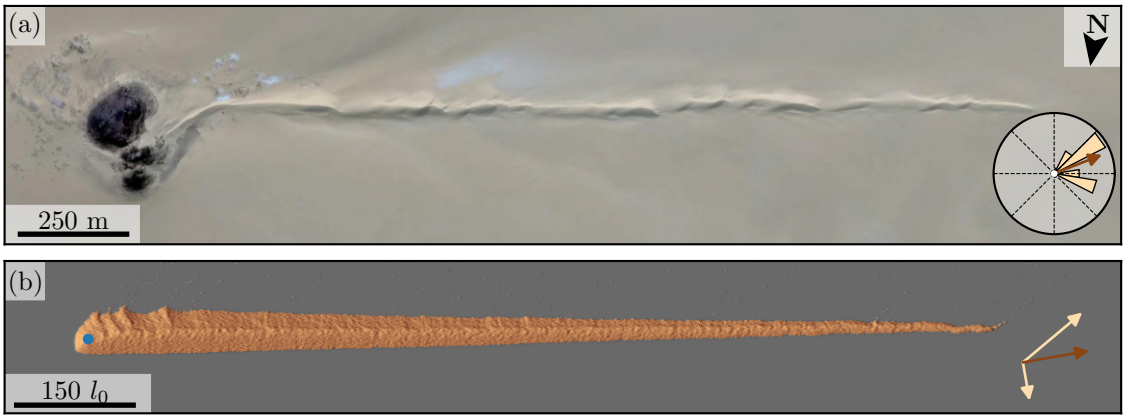

Figure 4.5 – Isolated elongating linear dunes. (a) Linear dune elongating behind a topographic obstacle in the Ténéré desert, Niger (18°31′N, 12°59′E) The sand flux distribution is computed from the wind data of the ERA-5 project (Hersbach *et al.* 2020) using the method described in appendix A.2. Satellite image: Google^{TM}, Maxar Technologies. (b) Linear dune elongating from a sediment source in the ReSCAL dune model, for $\theta = 120°$ and $N = 2$. Flux directions are indicated by the beige arrows. The blue dot indicates the position of the sediment feeder, placed above the dune. In both figures, brown arrows show the corresponding resultant sand flux direction.

with open boundary conditions. Sediment is injected locally from a fixed circular source near the upstream end of the field at a constant discharge J_{in} (see figure 4.5(b)). Using the injection setup, the model becomes computationally too expensive when simulating huge linear dunes. To analyze transverse sections over a wider range of dune sizes and wind conditions, we also simulate longitudinal sand bar with periodic boundary conditions. We refer to this setup as the 'infinite setup'. Starting from a uniform square cross section at $t = 0$, the sand bar then reaches the characteristic shape of a reversing dune in a few wind cycles. After an elapsed time of $\sim 104\ t_0$, we examine the shape properties.

4.2.2 Main results

Elongation and stability

We first start by using the injection setup. As soon as the sediment accumulates at the place of injection, the dune elongates under the action of the two winds. During the simulation, sediment is constantly lost at the dune tip, similarly to barchan horns, but also along the dune. As elongating dunes align with the resultant flux, wind directions are oblique to the crest; they thus experience a smaller dune aspect ratio. As a result, the corresponding recirculation zones are less developed in the lee side, and thus make a less efficient trap. This is especially true for the primary wind, more aligned with the dune (see left side of the dune on figure 4.5(a)). The evolution of the dune volume V is then

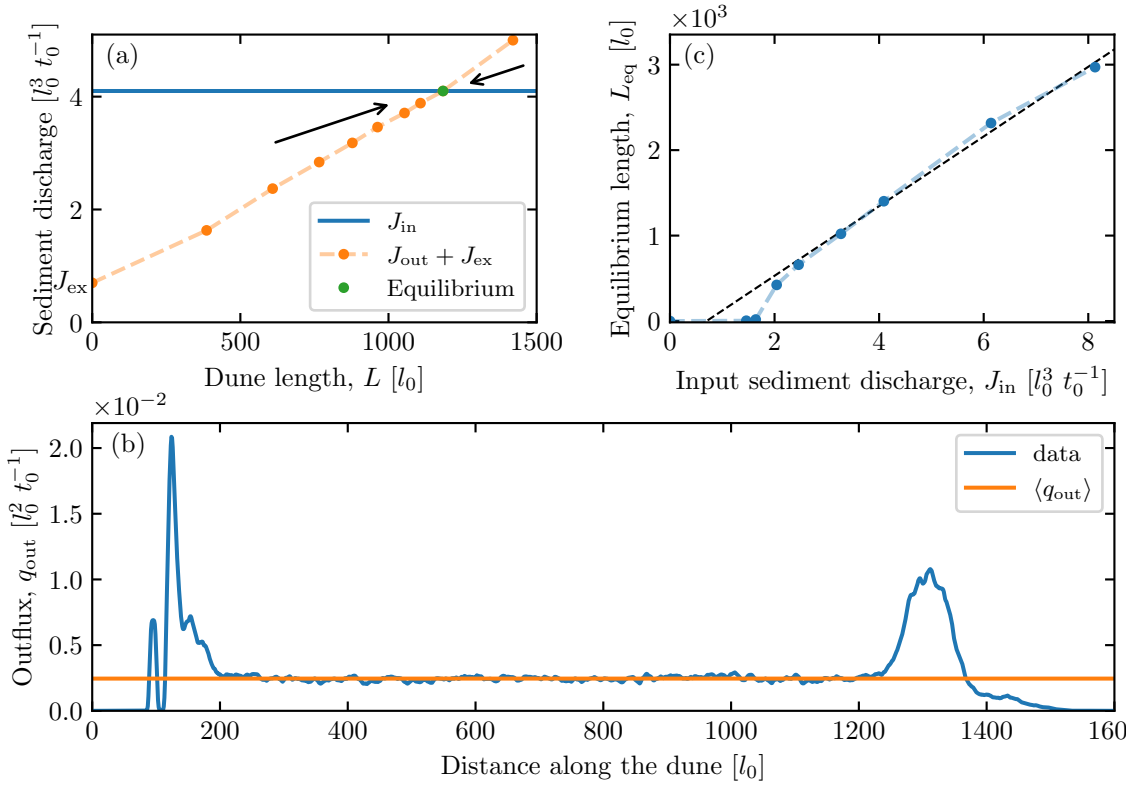

Figure 4.6 – Steady equilibrium state of an elongating linear dune (a) Input and output sediment discharges for different dune lengths, for $T_w = 300\ t_0$ and $J_{in} = 4.1\ l_0^3\ t_0^{-1}$. (b) Outflux along the corresponding equilibrium linear dune. (c) Equilibrium length as a function of the input sediment discharge for $T_w = 300\ t_0$. The dotted black line is the equation (4.2) with $J_{ex} = 0.7\ l_0^3\ t_0^{-1}$ and $\langle q_{out} \rangle = 2.5 \times 10^{-3}\ l_0^2\ t_0^{-1}$, measured in (a) and (b), respectively.

controlled by the balance between the input discharge and the losses:

$$\frac{\partial V}{\partial t} = J_{in} - J_{ex} - J_{out}, \tag{4.1}$$

where J_{ex} and J_{out} are the sediment discharges lost at the tip and along the dune, respectively.

During the elongation, the sediment discharge lost along the dune increases with the dune length, until the total losses balance the input discharge (figure 4.6(a)). As a result, the elongating dune reaches an equilibrium state, characterized by a steady triangular shape of length L and mean width W. Furthermore, unlike barchan dunes (see figure 1.15 and Hersen (2004a;b)), this equilibrium is stable. As shown by figure 4.6(a), decreasing the dune length from the equilibrium will decrease the lost sediment discharge accordingly. Consequently, the dune elongates back towards its equilibrium length.

As shown by figure 4.6(b), at equilibrium, the sediment outflux q_{out} is constant along the dune body, aside the large losses at the head and the tip. As these are encompassed into

the constant discharge J_{ex}, the lost sediment discharge J_{out} can be written $J_{out} = \langle q_{out} \rangle L$. At equilibrium, the dune length thus reads:

$$L_{eq} = \frac{J_{in} - J_{ex}}{\langle q_{out} \rangle}. \tag{4.2}$$

As shown by figure 4.6(b), the equilibrium length indeed increases roughly linearly with the input discharge J_{in}, in agreement with (4.2). Note that the presence of a threshold in terms of input discharge, because it first needs to overcome the constant sediment discharge $J_{ex} = 0.7\ l_0^3\ t_0^{-1}$ before the dune can elongate. Importantly, this threshold is not sharp, and the equilibrium length L_{eq} increases slowly at the beginning before reaching its linear asymptote.

Stable dune profile

In this section, we study the shape of a stable infinite linear dune using the 'infinite setup'. As shown by figure 4.7(a), despite the asymmetry of the wind regime, sections have a rather symmetric shape with slip faces in the lower part of both sides. These parts are barely reworked by the two winds, contrary to the neighbourhood of the crest, which moves back and forth over a distance Δ_c. Note that this crest reversal distance is the same for the two winds, as the orientation of the elongating dune is such that the fluxes perpendicular to the crest are of equal magnitude and cancel each other (see section 1.5.2).

As shown by figure 4.7(b), the dune shape ratio lies between 0.5 and 0.65, values corresponding respectively to the triangular and parabolic shapes. Importantly, this value is reached for a minimal dune size $W_c \sim 15\ l_0$, which could originate from two different mechanisms. First, as the dune is thinner at the tip, each wind might have the time to develop the transverse instability and break the tip during a single blow duration. As a result, the tip would break at a width $W \propto \sqrt{Q_\perp T}$ controlled by the blow duration, following scalings detailed in Guignier *et al.* (2013). Second, the dune might break due to hydrodynamical reasons related to the minimal dune size (see section 1.3.2, chapter 2 and chapter 3). Then, the tip breaks at a width related to the cut-off wavelength of the instability characteristic of this wind regime. Since the minimum width in figure 4.7(b) appears independent of the wind reorientation period, this mechanism seems relevant in the interpretation of our simulations. However, this width also looks independent of the transport threshold, whereas the instability cut-off wavelength is a function of u_*/u_{th}. Then, further study is needed to confirm this hypothesis, with larger variations of the wind reorientation period and different transport ratio/divergence angles.

When the lower part is large compared to the reworked upper part, sections are well approximated by trapezoid of bases W and Δ_c and height H (see the dashed lines in

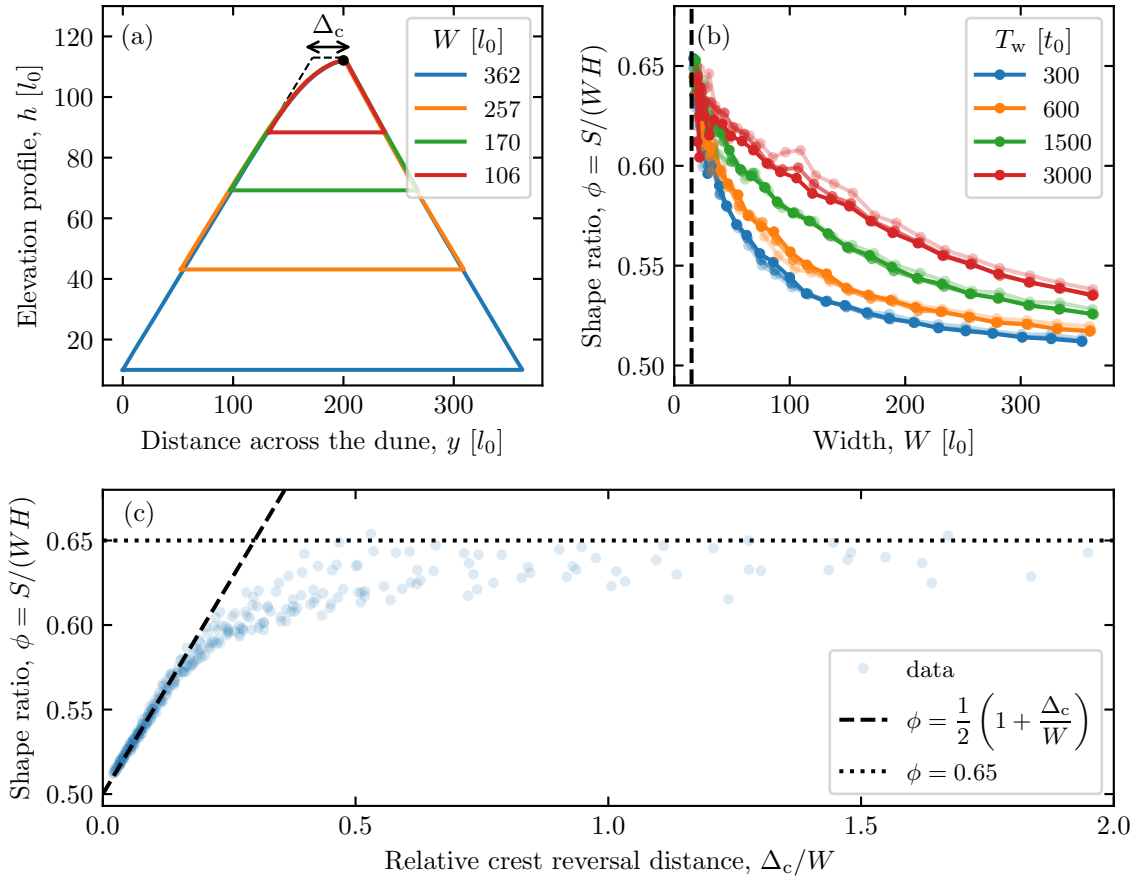

Figure 4.7 – Cross sections of a linear dune and associated fluxes. (a) Cross sections of an elongating linear dune for $T_w = 3000\ t_0$ and $\tau_1 = 0\ \tau_0$. They superimpose when matching the crests (black dot). (b) Dune shape ratio as a function of the dune width. Colors indicate different wind reorientation periods, and an increasing transparency indicate increasing values of the transport threshold ($\tau_1 \in \{0, 10, 20\}\ \tau_0$). (c) Dune shape ratio as a function of the rescaled crest reversal distance, for all different wind reorientation periods and transport thresholds present in (b).

figure 4.7(a)). The corresponding shape ratio $\phi = S/(WH)$ is then:

$$\phi = \frac{1}{2}\left(1 + \frac{\Delta_c}{W}\right). \tag{4.3}$$

As shown by figure 4.7(b), this is well verified in the limit of large dunes ($\Delta_c/W \to 0$), for various wind reorientation periods and transport thresholds.

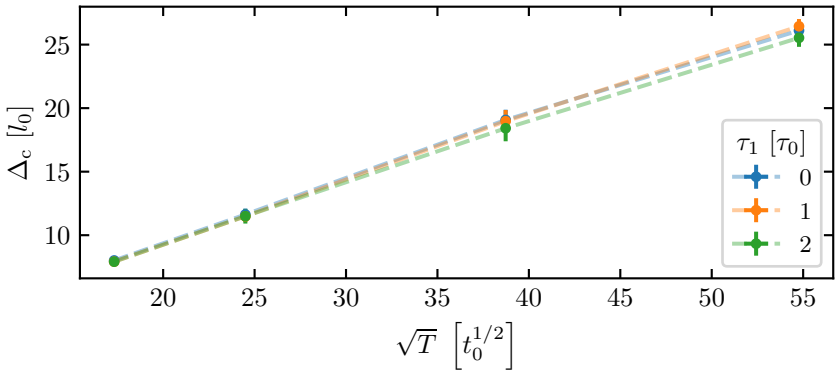

Figure 4.8 – Crest reversal distance as a function of the wind reorientation period.

Impact of the wind reorientation period

The reworked part of the dune is the same for all cross sections (figure 4.7(a)), but it depends on the wind regime. More specifically, figure 4.8 shows that most of its variation is due to the wind reorientation period, with little scattering due to the transport threshold τ_1.

The corresponding volume, proportional to $L_{eq}\Delta_c^2$, is also the sediment volume transported during half the wind reorientation period:

$$L_{eq}\Delta_c^2 \simeq L_{eq} Q_\perp \frac{T}{2}, \tag{4.4}$$

where $Q_\perp$ is a characteristic flux in the direction perpendicular to the crest. Leaving aside prefactors, it leads to:

$$\Delta_c \propto \sqrt{Q_\perp T}, \tag{4.5}$$

whose variation in $\sqrt{T}$ is in agreement with figure 4.8.

The appropriate characteristic flux to use in this scaling is harder to specify. At the crest, the flux in the perpendicular direction Q_y depends on the cross section, and increases roughly linearly with the dune aspect ratio, as discussed in section 1.4.1 (figure 4.9(a)). From this relationship, one can infer two different characteristic fluxes. The y-intercept corresponds to the flux on a flat sand bed ($H/W \to 0$ on figure 4.9(a)), and the slope to the additional flux induced by the presence of a topography. The first clearly depends on the transport threshold, while the second seems to be independent of it.

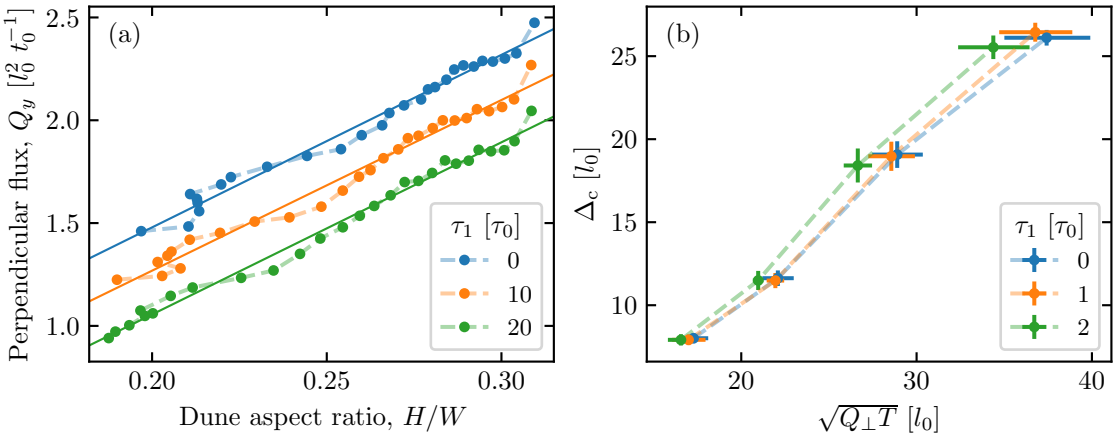

Figure 4.9 – (a) Flux at the crest in the direction perpendicular to the dune, averaged over time, as a function of the dune aspect ratio. Here, $T_w = 300\ t_0$. (b) Crest reversal distance as a function of the characteristic distance $\sqrt{Q_\perp T}$.

As most of the variation of the crest reversal distance Δ_c is due to the wind reorientation period, we look for a characteristic flux $Q_\perp$ relatively constant over T_w and τ_1, such that the additional flux induced by the presence of the topography is a good candidate. However, taking it into account in the scaling only increases the scattering of the points (figure 4.9(b) with respect to figure 4.8). This is probably due to the estimation of $Q_\perp$, whose uncertainty is larger than its variation with respect to τ_1 and T_w, but further investigation is needed.

4.2.3 Discussion

In this work, we show that isolated elongating linear dunes can reach an equilibrium state, controlled by the balance between the input flux and the losses. Importantly, we notice the presence of a threshold in terms of input flux under which the dune cannot elongate. As a result, above the threshold input discharge, the dune can elongate infinitely, until it interacts with other dunes or topographic obstacles.

The equilibrium length is an easy observable in satellite images, and could thus be used to investigate sediment budget in dune fields. However, before that, the input and lost discharge J_{in} and J_{ex}, as well as the output flux along the dune q_{out}, must be related to overall quantities of the studied site. For a dune elongating behind an obstacle of width W_{obs}, the input discharge is related to the the free flux of the area, and thus to the resultant sand flux Q_0 as $J_{in} \propto W_{obs} Q_0$. The sediment discharge lost at the dune tip then depends on the dynamic of the calving process. However, averaged over time, it can be related to the minimal dune width as $J_{in} \simeq W_c Q_\parallel$, where $Q_\parallel$ is the component of the resultant sand flux parallel to the crest. Finally, the outflux q_{out}, corresponding to the sediment that escape the slip faces, needs calibration in terms of their efficiency as sand traps, depending on the wind regime.

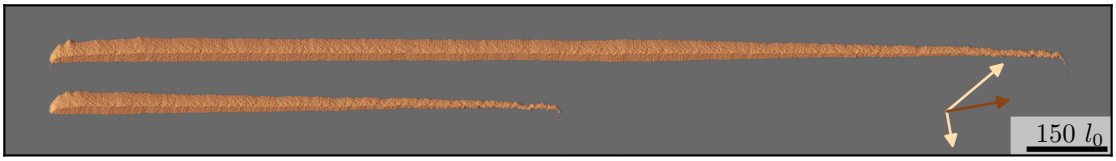

Figure 4.10 – Two interacting linear dunes at equilibrium. The two sediment sources at the dune heads have an equal input discharge of 3.2 $l_0^3\ t_0^{-1}$.

Narteau *et al.* (2009) have shown that the unitary length and time scales of the model, l_0 and t_0, are about 0.5 m and 8×10^{-4} yr for Earth-like conditions. The dune in figure 4.5(b), 1200 l_0 long for a maximum width of 60 l_0, would then correspond on Earth to a dune 600 m long with a maximum width of 30 m. Its input discharge, of 4.1 $l_0^3\ t_0^{-1}$, would be 640 $m^3\ yr^{-1}$. Note that the obstacle is usually much wider than the dune (see figure 4.5(a)). Such an input discharge could be reproduced by a 200 m wide obstacle and a free flux of 3.2 $m^2\ yr^{-1}$. This is much smaller than typical resultant sand fluxes, as expected for areas with non-erodible beds, where linear dunes elongate.

In natural situations, wind regimes are various, and often more complicated that the bidirectional one studied in this work; our results should thus be tested with respect to different divergence angles and transport ratios. Furthermore, natural linear dunes are rarely completely isolated, and often form clusters or fields. Besides collisions, they interact by exchanging fluxes, which modifies the balance described in (4.1). As shown by figure 4.10, when two dunes are side by side, the equilibrium length of one is longer, as it gains a sediment influx along its crest from the losses of the other one. Within a dune field, all losses along dunes are counterbalanced by gains from losses of nearby dunes, which could lead to unlimited elongation.

Chapter 5

Large scale analysis of the Namib Sand Sea

Sunrise over vegetated star dunes, Namibia - Paul van Schalkwyk

Contents

5.1 Introduction

Sand fluxes and dune properties are essential components of the evolution of arid areas (Pye & Tsoar 1990, Livingstone & Warren 1996, Thomas 2011, Lancaster 2013). However, setting up direct measurements of sediment transport and bed elevation with a global spatial coverage is difficult. This is why they are often derived from wind data (Fryberger & Dean 1979, Wasson & Nanninga 1986, Bullard *et al.* 1996, Blumberg & Greeley 1996, Lancaster *et al.* 2002, Wang *et al.* 2002, Pearce & Walker 2005, Livingstone *et al.* 2010, Jewell & Nicoll 2011, Lü *et al.* 2017, Gao *et al.* 2018).

Recent climate reanalyses based on global atmospheric models, such as ERA-40 or ERA-Interim (Uppala & et al. 2005, Dee *et al.* 2011), now allow large-scale studies of arid areas (Blumberg & Greeley 1996, Livingstone *et al.* 2010, Esteves *et al.* 2011, Ashkenazy *et al.* 2012, Courrech du Pont *et al.* 2014, Gao *et al.* 2018). However, their spatial resolution (~ 80 km) implies average quantities that do not resolve the smaller scales, ranging from the study of individual dunes to the border of mountains (Livingstone *et al.* 2010). Lately, the release of ERA5 provides up to 70 years of hourly wind properties at a much higher spatial resolution (~ 30 km), even almost 10 times higher for the specific ERA5-Land subset (~ 9 km) (Hersbach *et al.* 2020).

In this chapter, we show how to derive quantities of interest (resultant sand flux, dune orientation, etc.) from theoretical models on sand fluxes (Iversen & Rasmussen 1999, Durán *et al.* 2011) and dune growth (Courrech du Pont *et al.* 2014, Gadal *et al.* 2019) using the ERA5-Land dataset. We apply this data analysis method to the example of the Namib Sand Sea, where in situ field measurements are used to check the validity of this dataset, and to calibrate the derivation of the sand fluxes. We then compute the sediment and dune properties for the entire desert, and show that they match field observations.

Note that this chapter reports preliminary work from this collaboration with researchers at Oxford, Southampton and Loughborough Universities. Further developments are therefore under way, notably on the comparison between computed quantities and field observations, as well as on the implications of this work for the development of the Namib Sand Sea.

5.2 From wind data to sand fluxes

In this study, sand fluxes are derived from wind data that come from different sources: climate reanalyses and in situ measurements.

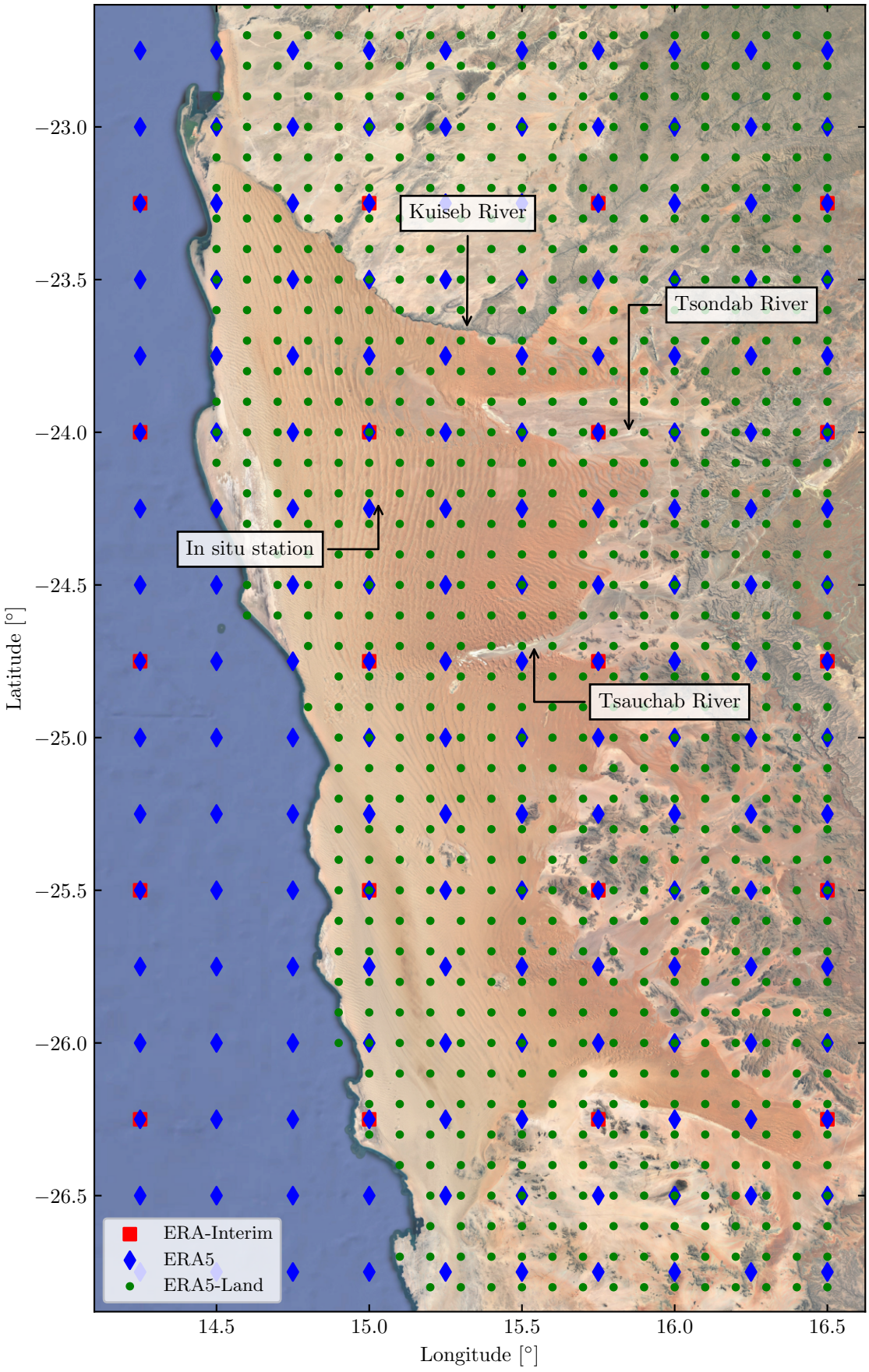

Figure 5.1 – The Namib Sand Sea, with the grids corresponding to different climate reanalyses. Satellite image: Google^{TM}, Maxar Technologies.

5.2.1 Datasets

Climate reanalyses

Climate reanalyses provide numerical estimates of various climate-related quantities (temperature, humidity, winds, etc.) at a global cover (typically the whole Earth). They are based on forecast models, which are forced at certain spatial or temporal points by observations using data assimilation systems. Improvements in models coupling different parts of the climate system, such as atmosphere, land surface, ocean, sea ice or carbon cycle, as well as the incorporation of new types of observations, such as satellite records, have led to the release of different generations of climate reanalyses since the 1980s.

In this work, we mention three successive generations of climate reanalyses produced by the European Centre for Medium-Range Weather Forecasts (ECMWF):

- **ERA-Interim** has been released to replace ERA-40 dataset (Uppala & et al. 2005). It covers the period from 1 January 1979 to 31 August 2019, with a temporal resolution of 6 hours, and a spatial resolution of 0.75°, i.e. ~ 80 km (Dee *et al.* 2011).
- **ERA5** has been released in 2018 to replace ERA-Interim, whose production has now stopped. It covers the period from 1 January 1950 to within 5 days of real time. Many improvements have been made over its predecessor. The main one relates to much higher temporal and spatial resolutions, of 1 hour and 0.25° (i.e. ~ 30 km), respectively, thanks to new data assimilation systems (Hersbach *et al.* 2020).
- **ERA5-Land** is a replay of the ERA5 reanalysis at a finer spatial resolution of 0.1°, i.e. ~ 9 km. There is no coupling to the data assimilation system, and observations influence the simulation indirectly only through the forcing by the ERA5 dataset. It however incorporates a new model for land/atmosphere interactions. Note that it will cover the period from 1950 to present, but has now only been released for the period 2001–2018.

The grids of the three datasets are represented in figure 5.1. Due to its much finer spatial resolution, we use in the following the ERA5-Land dataset.

In situ measurements

In situ measurements are provided by a station placed in the middle of the Namib Sand Sea (figure 5.1) from 20 June 2015 to 15 September 2018. Wind strength is measured by a cup anemometer at a height of 2.6 m, and direction by a wind vane at a height of 2 m, both every 10 min (figure 5.2). Transport intensity is measured by SENSIT, an instrument that uses a piezoelectric surface to count the number of particle impacts during the interval between two wind measurements (Stout & Zobeck 1996). The surface is cylindrical, with a diameter of 23.5 mm, and extends from the surface to a height of 12 mm, which is about

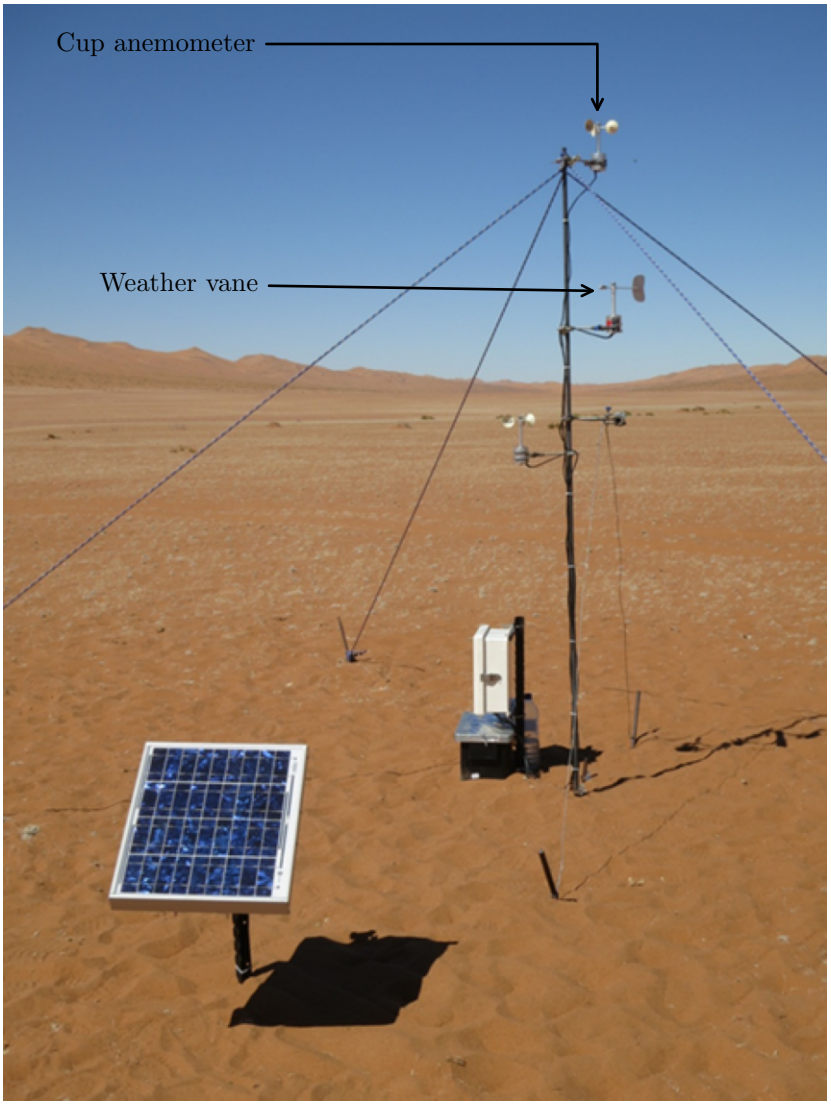

Figure 5.2 – Picture of the station providing the in situ measurements.

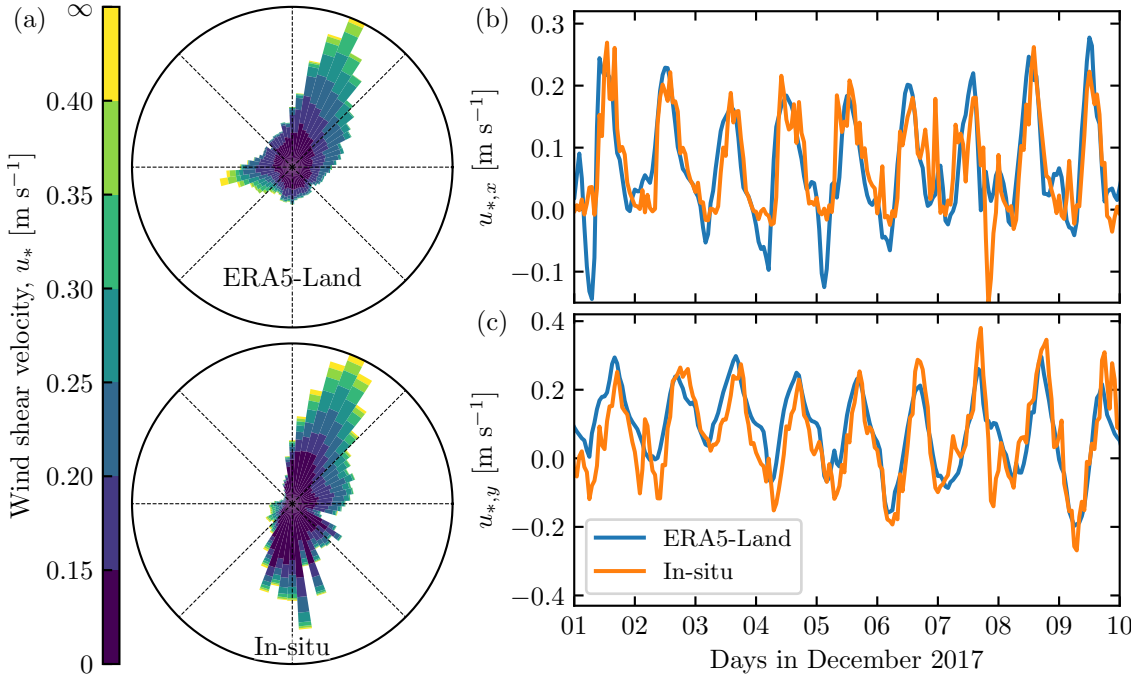

Figure 5.3 – Comparison between the ERA5-Land and in situ datasets. (a) Corresponding wind roses. (b) x-component and (c) y-component of the shear velocity during the dominant southerly wind as a function of time. Here, shear velocities are calculated with an aerodynamic roughness of $z_0 = 1$ mm.

the typical thickness of the saltation layer (Creyssels *et al.* 2009). Note that, because the station is in an interdune between two large (~ 50 m high) linear dunes, we should expect to see some surface wind funnelling (see figure 5.2).

5.2.2 Comparison of the two datasets

The two wind datasets are represented in figure 5.3. Both wind roses exhibit a similar dominant wind blowing towards the north-northwest in winter. Note the difference in terms of secondary summer winds. The easterly wind present in the ERA5-Land dataset is replaced in the in situ measurements by a small northerly wind. Note that the existence of this easterly wind is not an artefact of the reanalysis dataset, as it is present in the data from the Gobabeb meteorological station (Livingstone *et al.* 2010). This difference is then probably due to the giant dunes on either side of the station. Since they are approximately perpendicular to the easterly wind, the corresponding shadow zone is then large enough to encompass the station. This drastically reduces the wind velocity perceived in the interdune, but also probably induces some wind redirection.

As shown by figure 5.3(b) and 5.3(c), the correspondance between the two datasets of the x (northward) and y (eastward) components of the shear velocity is remarkable during the dominant wind, in winter. Note that the differences are stronger for the x-component, supporting that the giant dunes impact the wind by the station. Climate

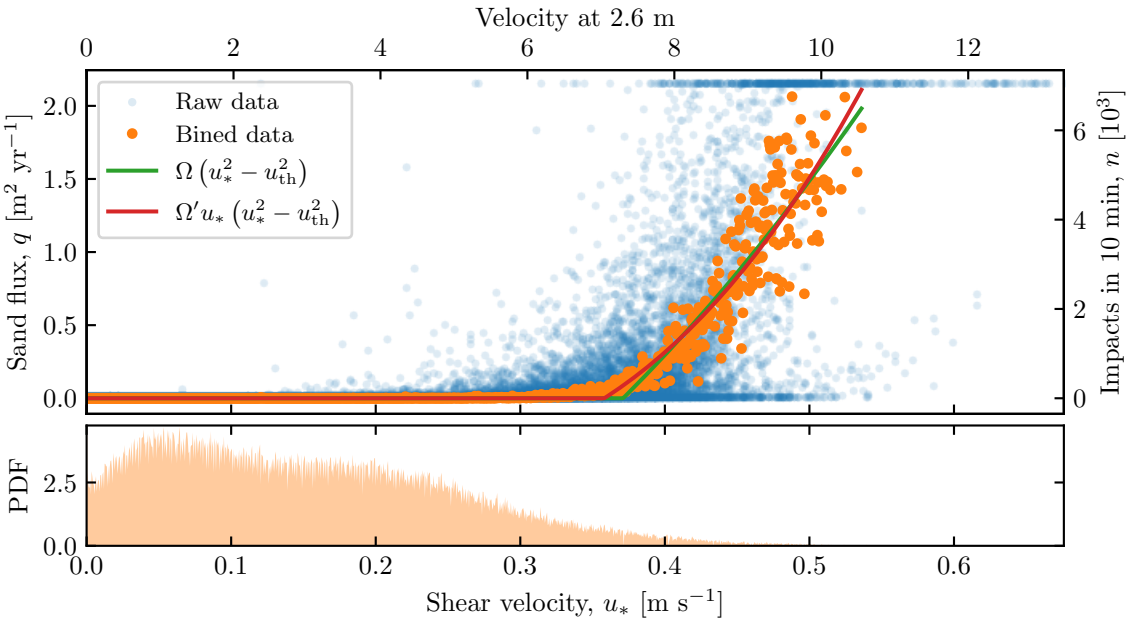

Figure 5.4 – Transport law from in situ measurements. The raw data are averaged into bins of 0.01 m s^{-1} in terms of velocity at 2.6 m. The corresponding distribution is shown in (b). The fits give $\Omega = 13.5$ s^{-1} and $u_{\rm th} = 0.37$ m s^{-1} (or equivalently 7.3 m s^{-1} at 2.6 m) for the quadratic law, and $\Omega' = 25.1$ s^{-1} and $u_{\rm th} = 0.36$ m s^{-1} (or equivalently 7.1 m s^{-1} at 2.6 m) for the Bagnold law.

reanalysis datasets may thus not be suited to the study of small scales patterns developing in the interdune. However, they are able to reproduce most of the wind seasonal variability, necessary to the study of sand flow paths and giant dune patterns at the sand sea scale.

5.2.3 Calibration of the transport law

Figure 5.4 shows the number of impacts detected by SENSIT as a function of the wind velocity for the whole period of measurements. It exhibits a clear threshold, above which the number of impacts increases with the wind velocity. Note that SENSIT saturates at 7000 counts. After averaging the data into bins, we can fit transport laws to the resulting points (we checked that the results are independent of the bin size). We obtain a threshold velocity of 7.1 ± 0.2 m s^{-1}, independently of the transport law (figure 5.4).

In order to compare with theoretical predictions of the threshold velocity and the sand flux, the data first need to be converted in terms of shear velocity and sand fluxes. The shear velocity is inferred from the law of the wall (1.4) using an aerodynamic roughness z_0 of 1 mm. This leads directly to a threshold shear velocity of $u_{\rm th} = 0.36 \pm 0.01$ m s^{-1}. It can also be calculated from (1.14), using the fluid and grain properties. The grain diameter is taken from the mode of distributions made from local samples, giving $d = 550$ μm (figure 5.5). Unfortunately, we do not have any measurements of the grain and fluid densities. As grains in the Namib Sand Sea are largely composed of quartz (Garzanti *et al.* 2012, Eckardt *et al.*

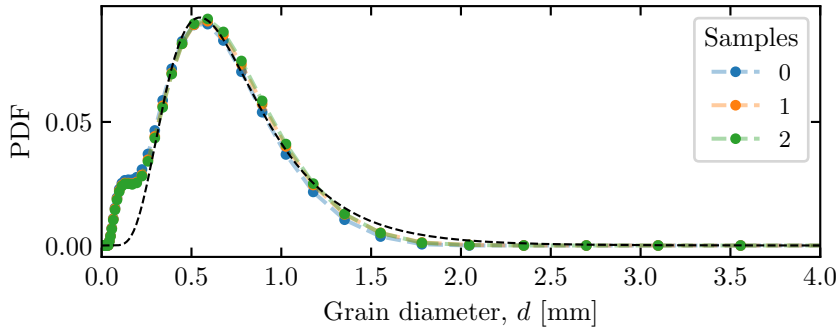

Figure 5.5 – Grain size distributions for three different samples taken near the station. The dotted black line is the fit of a log normal distribution, leading to a most probable value of $d = 550$ μm.

2013), we use a grain density of $\rho_s = 2.7$ kg m^{-3}. Combined with a typical value of the air density, $\rho_f = 1.2$ kg m^{-3}, it leads to $u_{th} = 0.35$ m s^{-1}, in agreement with our measurements.

The sand fluxes are derived from the number of impacts n using:

$$q = \frac{4}{3}\pi\left(\frac{d}{2}\right)^3 \frac{n}{\phi \Delta_t W_s}, \tag{5.1}$$

where $\Delta_t = 10$ min is the measurement duration and $W_s = 23.5$ mm the apparent width of SENSIT, i.e. the diameter of the cylindrical surface. The fit of the measured sand fluxes leads to a prefactor in front of the transport law (1.19) of $\Omega = 12 \pm 1$ s^{-1} (see figure 5.4). They are then about 35 times smaller than the fluxes calculated using the calibration (1.20) of this prefactor presented in section 1.2.3, which leads to $\Omega = 420$ s^{-1}. This is due to the duration of our measurements, that makes SENSIT saturate in terms of counts just above the transport threshold.

In conclusion, these in situ data allow the measurement of the threshold velocity, but also the validation of its theoretical expression, hence confirming the grain diameter and density. Unfortunately, the fitted transport law cannot be used due to the saturation of SENSIT.

However, the extracted threshold velocity corresponds to the grain properties of our in situ station, i.e. to the interdune between two giant linear dunes. While the sand there is dynamic and will transfer from dune to dune across the interdune, it is coarser than the sand found on the dune bodies and crests, ranging from 180 μm to 250 μm (Lancaster 1981, Livingstone 1987, Eckardt *et al.* 2013). In the following, all sand fluxes are thus derived from the calibrated theoretical expressions of the threshold velocity (1.14) and saturated sand flux (1.20) using a typical grain diameter 200 μm, more relevant to dune dynamics.

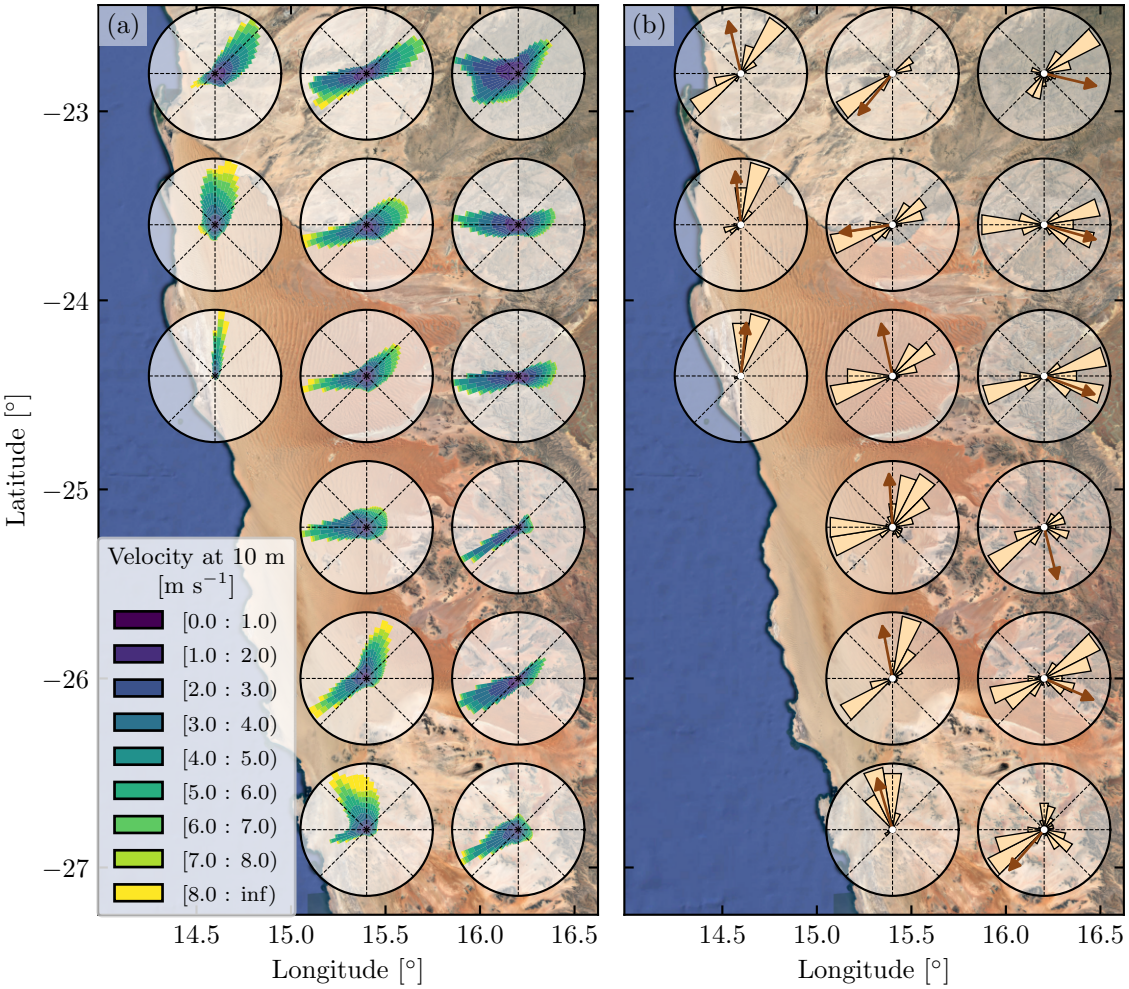

Figure 5.6 – Wind and sand fluxes across the Namib Sand Sea from the ERA5-Land dataset. (a) Some wind roses, spaced of 0.8°. (b) Corresponding angular distributions of the sand fluxes, calculated using a hydrodynamic roughness of 1 mm, and the sediment and fluid properties given in section 5.2.3. The resultant sand flux direction is given by the brown arrow. Flux intensities are detailed in figure 5.7.

5.3 Winds and sand fluxes across the Namib Sand Sea

Using the ERA5-Land dataset, we derive from the wind velocity at 10 m the sand fluxes corresponding to sediment grains analogous to those at the station. The method is the same as the one used in chapter 2, described in appendix A.2. It is based on the calculation of the shear velocity using the law of the wall (1.4), followed by the use of the transport law (1.19). From the time series of the sand fluxes, we define the resultant sand flux as the vectorial time average $\langle \boldsymbol{q}_{\text{sat}} \rangle$. Note that in the literature, its magnitude $\| \langle \boldsymbol{q}_{\text{sat}} \rangle \|$ is sometimes referred to as the *Resultant Drift Potential* (or RDP), and its direction the *Resultant Drift Direction* (or RDD). Likewise, we define the scalar time average $\langle \| \boldsymbol{q}_{\text{sat}} \| \rangle$, also referred to as *Drift potential* (or DP).

5.3.1 Wind regimes

Wind roses corresponding to this analysis are shown in figure 5.6(a), exhibiting various wind regimes across the Namib Sand Sea. From west to east, the wind regime changes from unimodal on the coast to multidirectional as one approaches the mountains. This variation is also associated with a decrease in wind strength. In the middle of the sand sea, the giant linear dunes are shaped by a well defined bidirectional wind regime (figure 5.3(a) and figure 5.6(a)).

5.3.2 Sand fluxes

The corresponding angular distributions of the sand fluxes are shown in figure 5.6(b). Note that not all of the resulting sand flows are directed northward, which is a notable difference with respect to the output of the ERA40 and ERA-Interim datasets (Livingstone *et al.* 2010). In particular, the flux distributions are in agreement with in situ measurements from Lancaster (1985) and the Gobabeb meteorological station (Livingstone 2003), both around the Kuiseb river bordering the northern edge of the Namib Sand Sea.

The magnitude of the resultant sand flux $\|\langle \boldsymbol{q}_{\text{sat}} \rangle\|$ is shown in figure 5.7(a) along flux lines running through the sand sea. The sand is transported from the coast and the south to the north, following the spatial evolution of the wind regimes. Note that $\|\langle \boldsymbol{q}_{\text{sat}} \rangle\|$ decreases along the sand flow paths, reflecting that the Namib Sand Sea is a zone of sediment deposition.

In terms of transport, wind multidirectionality is usually represented using the ratio between vectorial and scalar time average of the sand flux, $\|\langle \boldsymbol{q}_{\text{sat}} \rangle\| / \langle \|\boldsymbol{q}_{\text{sat}}\| \rangle$. As shown by figure 5.7(b), high values of this ratio indicate unidirectional wind regimes, typical of the coast. Low values correspond to wind regimes where transport directions cancel each others, nearby topographical obstacles.

5.4 Dune morphology

5.4.1 Dune shape

As discussed in chapter 1, wind directionality is, along with sediment availability, one of the two dominant factors controlling dune shape (see figure 1.3). Different pattern morphologies have thus been reported depending on the $\|\langle \boldsymbol{q}_{\text{sat}} \rangle\| / \langle \|\boldsymbol{q}_{\text{sat}}\| \rangle$-value (Livingstone & Warren 1996). Then, barchan and transverse dunes are found for $\|\langle \boldsymbol{q}_{\text{sat}} \rangle\| / \langle \|\boldsymbol{q}_{\text{sat}}\| \rangle \gtrsim 0.7$, star dunes for $\|\langle \boldsymbol{q}_{\text{sat}} \rangle\| / \langle \|\boldsymbol{q}_{\text{sat}}\| \rangle \lesssim 0.3$, and linear dunes in between (McKee 1979, Wasson & Hyde 1983, Lancaster 1994, Livingstone & Warren 1996).

Figure 5.8 shows different patterns in the Namib Sand Sea along an eastward transect around the 26^{th} parallel south. From west to east, the dune morphology shifts from

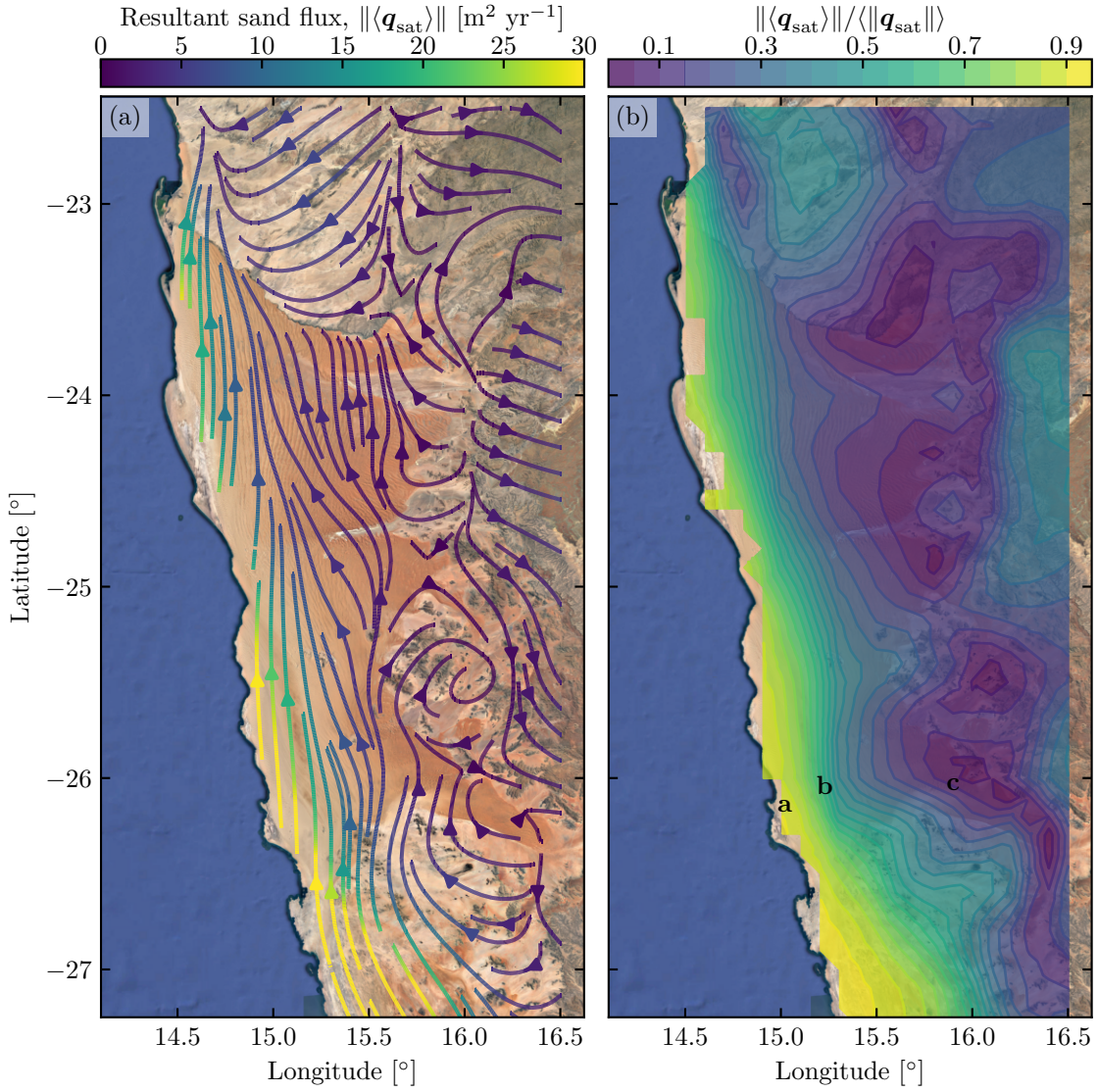

Figure 5.7 – (a) Flux lines following the resultant sand flux. (b) Ratio between the resultant sand flux (i.e. vectorial average) and the scalar average of the sand flux. Letters indicate the position of the three sites shown in figure 5.8.

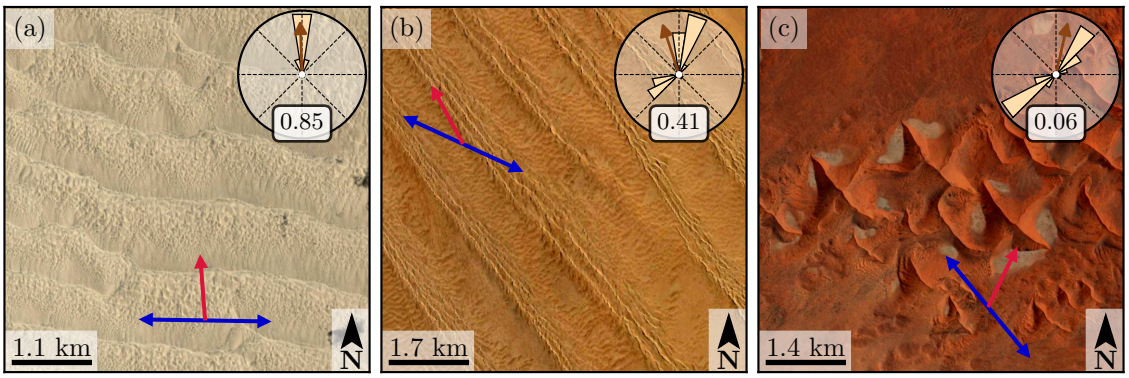

Figure 5.8 – Different dune morphologies along an eastward transect around the 26$^{\text{th}}$ parallel south. (a) Transverse dunes close to the coast. (b) Linear dunes in the middle of the sand sea. (c) Star dunes nearby the mountains. Sites are indicated in figure 5.7(b). The ratio $\|\langle \boldsymbol{q}_{\text{sat}} \rangle\| / \langle \|\boldsymbol{q}_{\text{sat}}\| \rangle$ is indicated just below the angular distributions of the sand flux. Predicted orientations are shown in red (elongation mechanism, equation (1.46)) and blue (bed instability, equation (1.45)).

transverse, to linear, and then star dunes as one approaches the mountains, in agreement with the decrease in $\|\langle \boldsymbol{q}_{\text{sat}} \rangle\| / \langle \|\boldsymbol{q}_{\text{sat}}\| \rangle$. Furthermore, the corresponding values of this ratio fall nicely into the categories given above. Note that barchan dunes can also be found along the coast where the sand availability is lower.

5.4.2 Dune orientation

Dune orientations can be predicted from the angular distributions of the sand fluxes using the theoretical models described in this manuscript. First, we use the model of Courrech du Pont *et al.* (2014) described in section 1.5.2, and compute the two dune orientations corresponding to the elongation mechanism (equation (1.46)) and the bed instability (equation (1.45)). The only parameter here is the flux-up ratio γ, that we take equal to 1.7, from calibrations using field results and laboratory experiments (Courrech du Pont *et al.* 2014).

Then, the orientation resulting from the bed instability is also computed using the extension of the linear stability analysis to multidirectional wind regimes presented in chapter 3 (see equation 3.61). The characteristic flux and the wind velocity ratio are then calculated at each time step from our wind data. However, this model has parameters for which we do not have measurements. The hydrodynamic coefficients are set to $\mathcal{A}_0 = 3.6$ and $\mathcal{B}_0 = 1.9$, values derived from the field analysis presented in chapter 2. The avalanche slope μ is taken to the usual value of $\tan(35°)$.

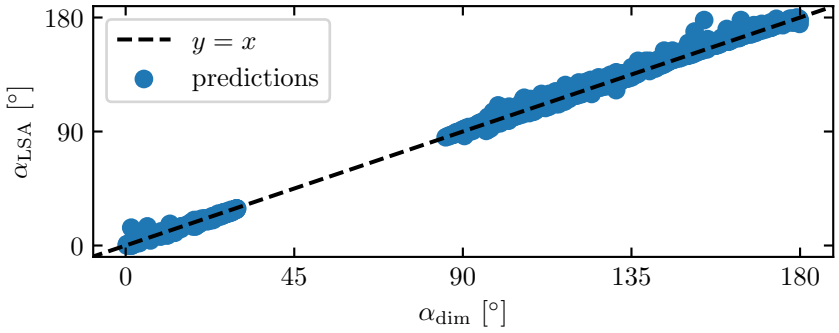

Figure 5.9 – Comparison between the dune orientations for the bed instability predicted by the model of Courrech du Pont *et al.* (2014), α_{dim}, and the linear stability analysis, α_{LSA}, for all points of the grid shown in figure 5.1. The standard deviation of the residuals is 3°.

Comparison between the two models

In chapter 3, we have shown that the two models predicts the same orientation. However, this correspondance was tested only in strictly bidirectional flow regimes, and found only for specific values of flux-up ratio γ and velocity ratio u_*/u_{th}. Furthermore, figure 3.6 shows that the linear stability analysis can predict a wide diversity of orientations depending on the velocity ratio.

Nevertheless, figure 5.9 shows that the orientations predicted by the two models are fairly the same, with an average difference of 3°. This is remarkable as the predictions of the linear stability analysis integrate various velocity ratios, depending on the time step as well as the spatial location. This suggests that wind variability, in terms of strength or direction, tends to smooth out effects related to the velocity ratio (slope effects and hydrodynamic recirculations), so that the growth rate remains mainly controlled by wind geometry, which corresponds to the model of Courrech du Pont *et al.* (2014).

Qualitative comparison with satellite images

The predicted orientations are shown on the northern half of the Namib Sand Sea on figure 5.10. Overall, they correspond qualitatively to those visible on the satellite image: on the coast, transverse dune orientation matches the prediction of the bed instability (blue lines), and in the middle of the sand sea, linear dune orientation agrees with the prediction of the elongation mechanism (red lines).

However, between the 23$^{\mathrm{th}}$ et 24$^{\mathrm{th}}$ parallel south, our predictions differ of about 15° from the observed linear dune orientation, that slightly tends to incline westward, following the Kuised river bed. Other discrepancies of this magnitude exist, and cannot be attributed to the choice of the γ value, which has little impact on the prediction of orientations (figure 5.10), especially from those corresponding to the bed instability. Note that they

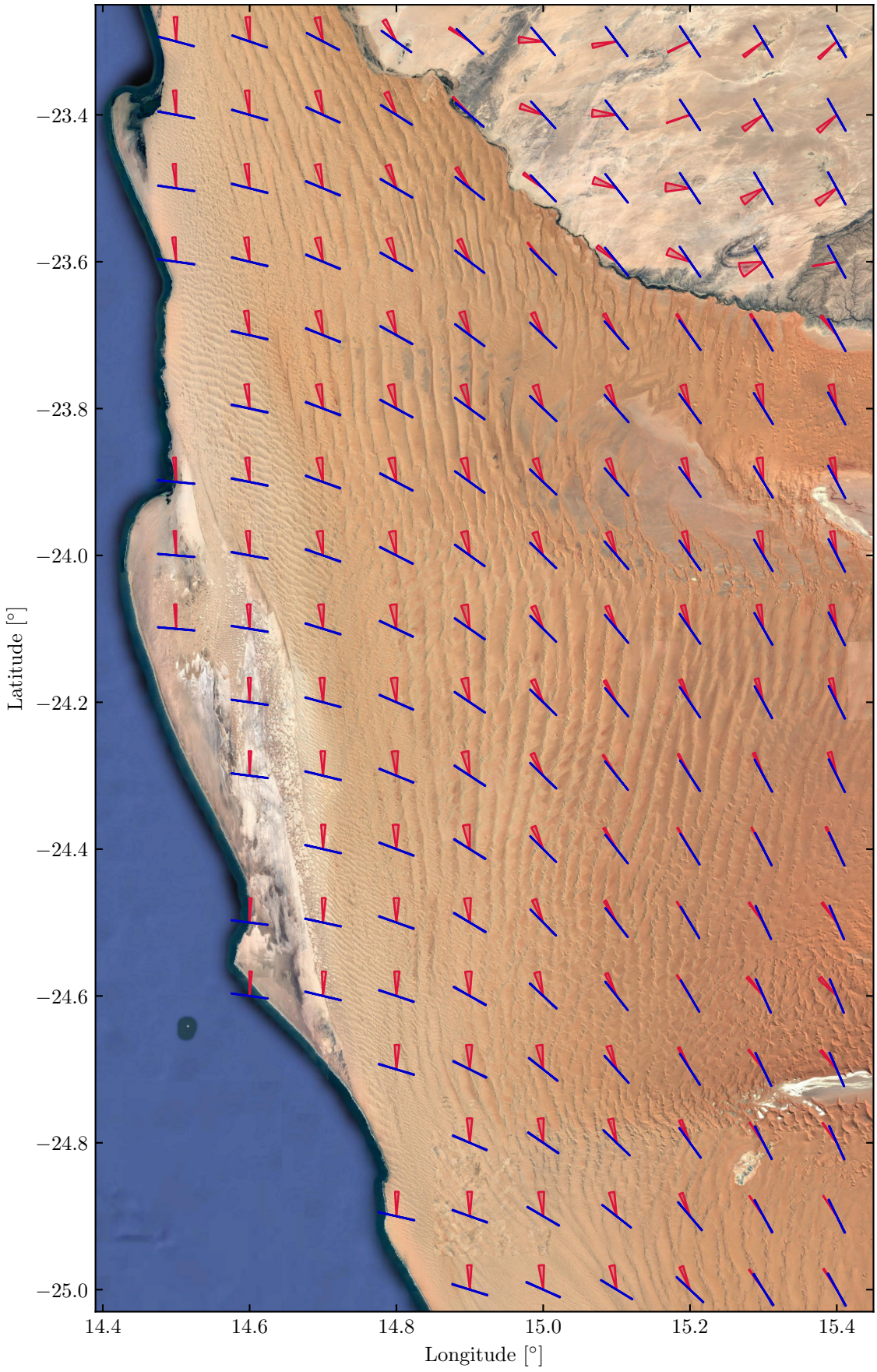

Figure 5.10 – Predicted orientations in the northern part of the Namib Sand Sea corresponding to the elongation mechanism (red) and the bed instability (blue). Wedges correspond to the whole range of solutions when γ is varied from 0 to ∞. For the bed instability, both models are used, and orientations superimpose (see also figure 5.9).

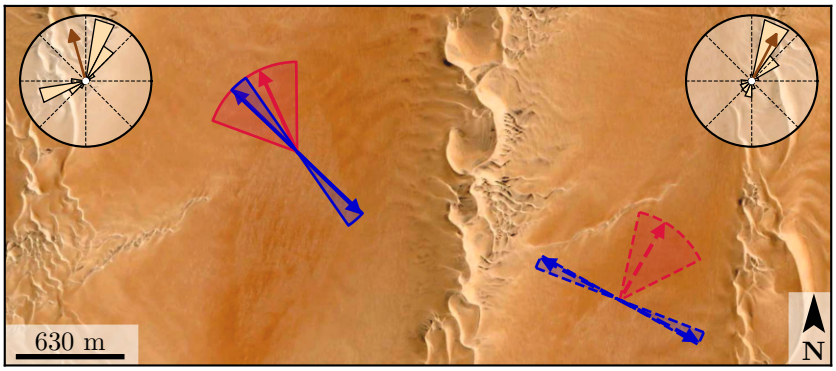

Figure 5.11 – Crossing dunes between giant linear dunes in the Namib Sand Sea (−24.14°, 15.01°). The roses show sand flux angular distributions. Arrows indicates the orientations predicted using the model of Courrech du Pont *et al.* (2014) for the elongation mechanism (red) and the bed instability (blue). Wedges indicate the areas covered by these arrows when the grain size is varied from 0 μm to 600 μm. The left rose and the plain arrows/wedges correspond to the ERA5-Land dataset, and the right rose and dashed arrows to the in situ measurements. Satellite images: Google$^{\text{TM}}$, Maxar Technologies.

often occur near obstacles related to water flows, such as the three main rivers indicated in figure 5.1. This may explain why this effect cannot be extracted from the wind data.

5.5 Discussion

In this chapter, we present preliminary results from a method for desert large-scale analysis, based on climate reanalysis datasets. After assessing the validity of the wind data from the ERA5-Land dataset, we derive sediment fluxes and dune orientations for the entire Namib Sand Sea. Our data show the local impact of topographic obstacles on sediment flow paths as well as the spatial evolution of the ratio $\|\langle \boldsymbol{q}_{\text{sat}} \rangle\| / \langle \|\boldsymbol{q}_{\text{sat}}\| \rangle$, reflecting the high spatial resolution of the wind data. As a result, the computed angular distributions of the sand fluxes agree with the literature, in contrast to what has been previously derived using the ERA-Interim and ERA-40 datasets (Livingstone *et al.* 2010). Furthermore, we checked using satellite images that dune orientations and shapes agree with our predictions.

As shown in figure 5.11, only the orientations of the giant dunes are reproduced by the ERA5-Land dataset. Smaller scale patterns, such as these crossing dunes elongating in between two linear dunes, are sensible to the modifications of the large-scale wind induced by the bordering giant dunes. Their orientation can then be predicted from our in situ measurements (red dashed arrow in 5.11). Although these different orientations may result from the evolution of wind regimes through different climatic periods (Bristow *et al.* 2007, Lim *et al.* 2016), we show here that they can be explained by modern winds.

The computed fluxes correspond to the chosen grain properties, which change along the dune profiles or across the desert (Lancaster 1981, Lancaster & Ollier 1983, Lancaster

1983, Watson 1986, Lancaster & Teller 1988, Fenwick 1991, Yamagata 2010, Livingstone *et al.* 2010). As a result, including a detailed spatial distribution of grain properties over the entire desert in this type of analysis would thus enhance the quality of the calculated sand fluxes, and thus of all related quantities (predicted dune orientations, erosion and deposition rates, dune growth rates). More generally, it could be improved by taking into account all parameters affecting sediment transport, such as vegetation, rainfall or moisture content (Livingstone & Warren 1996, Andreotti *et al.* 2012b).

This analysis is applicable to all active deserts on Earth, currently in progress for the Lut (Iran) and Taklamacan (China) deserts, but also to other planetary bodies where global coverage by wind data is available.

Chapter 6

Conclusion et perspectives

Dome dune corridor in the Rub'al-Khali, Yemen - George Steinmetz

Contents

Dunes emerge while selecting their own wavelength and orientation. In this manuscript, we investigated how both depend on the external natural conditions, as the wind regime or the sand availability, using a theoretical approach combined with numerical modeling, subaqueous experiments and field analyses.

6.1 Bed instability

We first investigated the destabilization of a loose sediment bed using a field study at White Sands, Mexico. Over there, the unimodal sand flux distribution allows the simplification of the problem to an idealized case where only transverse dunes form under a unidirectional wind. On the upwind margin, where incipient dunes emerge, we found that elevation profiles exhibit spatially exponentially amplifying trends, typical of a convective instability that simultaneously grows and propagates. Our measurements of the most unstable mode properties, i.e. wavelength, propagation velocity, growth length and local growth rate, also match the prediction of the linear stability analysis, assessing its validity in describing the process of dune emergence from a loose sediment bed.

We then extended this linear stability analysis to bidirectional wind regimes. We found that the emerging pattern integrates the two winds, instead of being a combination of two patterns produced by each of the two winds. Both incipient orientation, wavelength and growth rate then vary according to the wind regime. Predicted orientations are in agreement with previous studies under bidirectional flows (Rubin & Hunter 1987, Rubin & Ikeda 1990, Courrech du Pont *et al.* 2014), but can be modified depending on the distance to the transport threshold. In addition, we found that the variation of the wavelength and growth rate is dominated by a geometrical effect resulting in up to 30% decrease when the two wind directions are perpendicular. This is supported by subaqueous experiments and numerical simulations, in which we also found a clear discrepancy between reversing and non-reversing dunes. This might be the signature of enhanced non-linear effects for reversing dunes, and needs further investigation.

6.1.1 Coarsening and increase of the wavelength

In natural dune patterns, the observed wavelength is often much larger than the incipient one, as it has increased since emergence due to coarsening (see figure 6.1). As discussed in section 1.4.2 of chapter 1, understanding and quantifying these processes is still an open issue, despite their primary importance in the evolution of dune fields. More importantly, the increase of the wavelength, and the associated scalings, have never been investigated under natural, multidirectional, wind regimes.

In the experiments presented in chapter 3, coarsening processes are impacted by the wind regime (Figure 6.1). The larger the divergence angle, the faster the wavelength

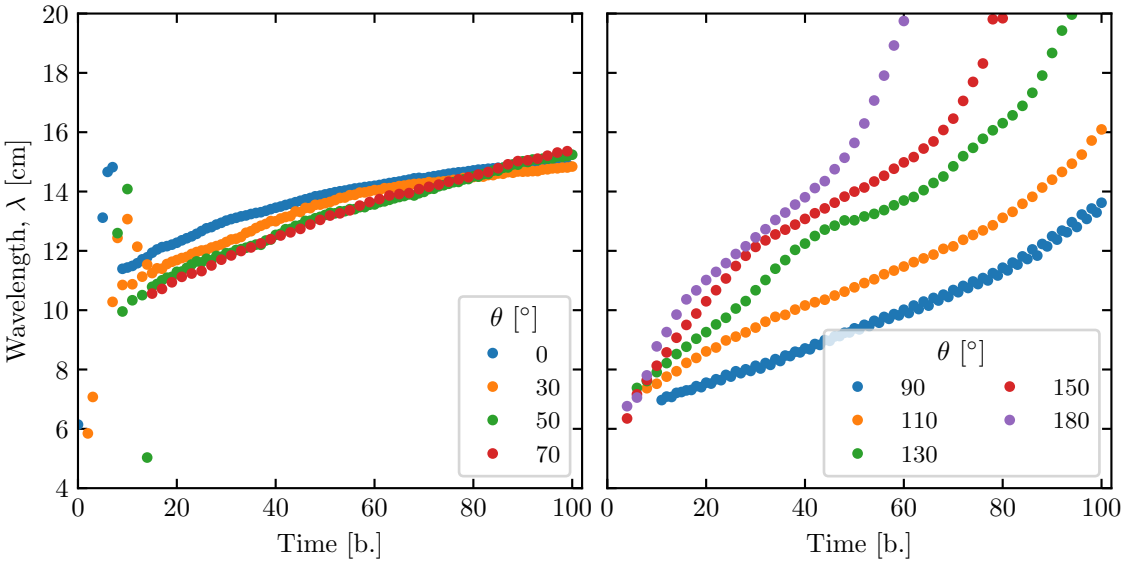

Figure 6.1 – Wavelength as a function of time for different angles θ between the two flow directions, in the experimental setup presented in chapter 3.

increases. However, coarsening for reversing dunes ($\theta < 90°$) is much faster than for non-reversing dunes ($\theta > 90°$). At first, this can be understood with the same argument detailed in section 3.4.4, pointing out enhanced non-linearities under reversing flows, as each wind blow encounters an avalanche slope. However, it is surprising that the fastest wavelength increase occurs for $\theta = 180°$, where the resultant transport is null, and thus where defect migration should be the smallest. These are new results that have never been reported in the literature to our knowledge, and further studies are required to understand and quantify it.

6.1.2 Elimination of defects

In many different physical situations, from convective rolls to liquid cristals, coarsening is deeply related to the diffusion and annihilation of defects present in the patterns (Rasenat *et al.* 1990, Bodenschatz *et al.* 1991, Pargellis *et al.* 1992, Pismen 1999, Desai & Kapral 2009, Hansen *et al.* 2009, Black *et al.* 2017). As a result, the study of defect dynamics in dune patterns is still an active research topic, driven by its potential in dating dune fields (Werner & Kocurek 1999, Huntley *et al.* 2008, Rachal & Dugas 2009, Bourke *et al.* 2009, Skarke & Trembanis 2011, Telfer *et al.* 2017, Scuderi 2019).

Recently, Day & Kocurek (2018) have shown that many different dune fields on Earth, Mars and Titan verify the same scaling law $I^* \propto \lambda^2$, where I^* is the defect density of the dune field, and λ its wavelength. This result, based on a dimensional analysis, strongly suggests that dune interactions remain the same during all stage of coarsening. Note that, in their study, two trends corresponding to two proportionality coefficients arise, which might depend on dune type (reversing vs non-reversing dunes), wind regime or sand

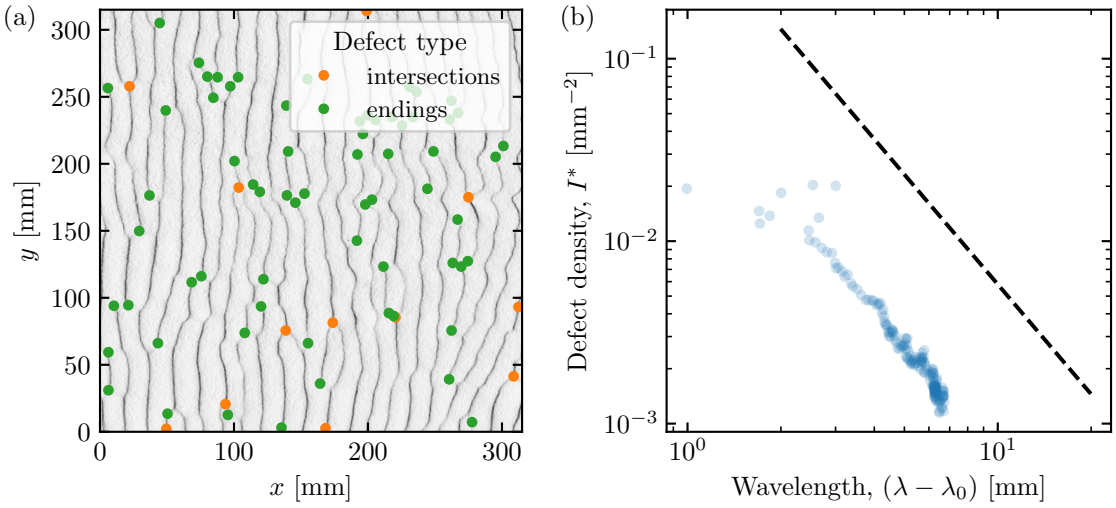

Figure 6.2 – (a) Automatic defect detection on a picture from the experiment presented in chapter 3, after 136 blows and for $\theta = 0°$. (b) Corresponding defect density as a function of the pattern wavelength for the 170 first blows. The dashed line represents $I^* \propto \lambda^{-2}$.

availability.

Using the same experimental setup as described in chapter 3, or analogous simulations in the ReSCAL dune model, we can track the defects through time (see figure 6.2(a)) and see that the same scaling law is recovered (figure 6.2(b)). By extending this analysis to different situations, we could assess the impact of wind regime or sand availability on defect dynamics and pattern coarsening.

6.2 Elongating dunes

In the second half of this thesis, we investigated the early stage of linear dune elongation. Fields of elongating dunes often exhibit a clear periodicity, characteristic of an instability. However, as elongation occurs over non-erodible beds from a sediment source, it cannot be described by the stability analysis of a sediment bed described in chapter 2 and 3. By means of numerical simulations, we study the elongation of incipient dunes from the border of an avalanche slope making the transition between a flat sand layer and a non-erodible bed. We found that all linear dunes elongate at the same constant velocity, independently of the initial imposed wavelength. In addition, their wavelength coincides at all times with the wavelength of the pattern developing on the sand layer. This suggests that their spatial arrangement is in fact a juxtaposition of individual structures controlled by spatial initial/boundary conditions, which can result themselves from another instability.

Elongating dunes thus need to be studied as individual objects. This is the work of Rozier *et al.* (2020), which I was able to participate in during my thesis. By means of numerical simulation, we studied the elongation of an isolated linear dune. We found that

it can reach an equilibrium state controlled by the balance between input sediment flux and losses. Importantly, this equilibrium is, unlike barchan dunes, stable. The corresponding dune shape is then mainly controlled by the wind reorientation period, relating to the length scale $\sqrt{QT}$.

6.2.1 Elongation under various wind regimes

Number of our results are in fact wind regime dependent. For example, changing the divergence angle or the transport ratio leads to different dune orientations with respect to the wind directions. The aspect ratio of the dune as seen by the winds is also different, which changes the efficiency of sand trapping by the avalanche slope and thus the losses along the dune.

As a result, our numerical simulations now need to be extended to a wider range of wind regimes before being reliably used to interpret field data. For example, on Titan, methane storms, which blow in addition to the usual bidirectional wind regime, appear to control the direction of linear dune elongation, showing the importance of studying trimodal wind regimes (Charnay *et al.* 2015). Another related issue adresses the impact of the wind variability in terms of orientation. Under a unidirectional wind regime, Gao *et al.* (2018) show that the standard deviation of the wind orientation controls the transition from barchan to dome dunes. Its impact under bidirectional (or multidirectional) wind regime on dune elongation remains to be studied, and could be at the origin of "complex linear dune" (Livingstone & Warren 1996, Wang *et al.* 2004), and further to a transition to train of dome or star dunes.

6.2.2 Breaking of a sand bar under multidirectional wind regimes

As shown in section 4.1.4, elongation also occurs from pre-existing dunes. In this case, the linear dune is not fixed, and the dune head is often shaped as an asymmetric barchan or a dome dune (Figure 4.4A). In one hand, the dune head migrates roughly in the direction of the resultant flux. On the other hand, the body does not migrate as the fluxes perpendicular to the crest cancel each other. The interplay between these two parts can lead to the destabilization of the entire structure. However, elongation is also able to reattach parts of the dune that would break (Reffet *et al.* 2010), leading to curved nail-shaped dunes (Figure 4.1B).

The dynamics of sand bar break-up under multidirectional regimes has not been studied much yet, and the ReSCAL dune model could be an appropriate tool to investigate it. Recently, this problem has been addressed using a simplified theoretical model for the crest line dynamics. Nakao-Kusune *et al.* (2020) show that, for reversing dunes, specific orientations exist for which all modes of the transverse instability are stable. Using their model, we could compute these stable orientations for different wind regimes and compare

them to the orientations predicted by Courrech du Pont *et al.* (2014). This would allow the study of other parameters influencing the orientation of elongating dunes, such as the upstream influx present in natural fields of elongating dunes.

Finally, the impact of the wind reorientation period on the stability of linear dunes remains to be investigated. When one of the two winds blows long enough/strong enough with respect to the dune width (typically $\sqrt{QT} \gg W$), it can also destabilize the dune before the other wind can re-stabilize the sand bar. Natural linear dunes are also referred to as "seif" because they often exhibit sinuous crest lines, which could result from the development of the transverse instability. These models could then be used to investigate the minimal linear dune width under which the crest line will destabilize and break in one blow duration.

6.3 Sand sea analysis

In the last chapter, we couple the theoretical framework on dune morphodynamics and sediment transport to wind data from climate reanalyses, and run a large scale analysis of the Namib Sand Sea. Thanks to the high resolution of our data, the computed sand fluxes encompass the influence of topographical obstacles, contrary to previous studies (Livingstone *et al.* 2010). The predicted dune shapes and orientations correspond to field observations from satellite images on different sites.

Unfortunately, we did not have time to check by hand the correspondance between predictions and observations across the whole sand sea. A complementary analysis would be to compute the dune properties from elevation data. For example, the NASA's Shuttle Radar Topography Mission provides data at a spatial resolution of 30 m over the entire Earth, on which the giant dunes of the Namib Sand Sea are clearly visible. Extracting the dunes widths, heights, orientations and shapes from these digital elevation model would allow a quantitative comparison with our predictions, but also add a significant contribution to the database created by our analysis.

Dune sizes (widths and heights) would also give access to dune growth, elongation and migration rates (see chapter 1). For example, following Lucas *et al.* (2015), the elongation rate of linear dunes scales with their width W as $e \propto (1+\gamma)Q/W$, with a proportionality coefficient around 10. For the linear dunes close to the Kuiseb river, bordering the northern edge of the Namib Sand Sea, we find $W \simeq 400$ m, with corresponding sediment fluxes around 10 $\mathrm{m}^2\ \mathrm{yr}^{-1}$ (see figure 5.7(a)). We infer elongation rates of $\simeq 1$ m yr^{-1}, in agreement with previous studies (Stone 2013, Bristow *et al.* 2007, Paillou *et al.* 2020). One can push the analysis further by pointing out that these dunes elongate over paleo-channels of the Kuiseb river (figure 6.3). As the width covered by these paleo-channels is around 8 km, we find that they are at least older than 8 kyrs, in agreement with Paillou *et al.* (2020).

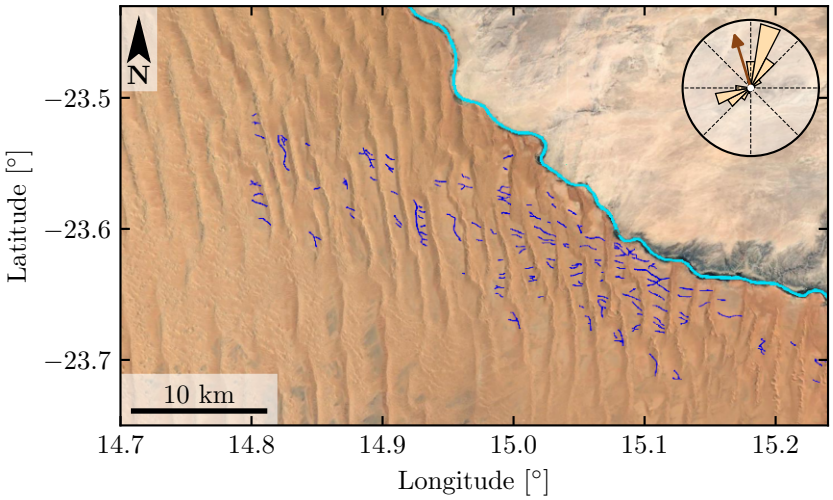

Figure 6.3 – The Kuiseb river, bordering the northern edge of the Namib Sand Sea. Light blue: current river bed. Dark blue: paleo-channels. The rose show the sand flux angular distribution over this area, and the brown arrow the direction of the resultant sand flux. Adapted from Paillou *et al.* (2020).

Desert-scale analyses such as this one then allows to discuss the evolution of dune fields, in addition to unravel their apparent complexity.

Appendices

Appendix A

Supplements to chapter 2

A.1 Measurements of the angle of repose

The avalanche slope μ of a granular material can be measured from the shape of a conical pile built with these grains. Its value depends on the grains' shape, and, because it enters the parameters of the linear stability analysis, we have measured it for the gypsum particles that compose the dunes at the the upwind margin of the White Sands. The experimental setup is presented in figure A.1. We fill a cylindrical tube with the grains and slowly pull it up. The grains flow out of the tube bottom, forming, in a quasi-static way, a conical pile. The slope of the pile evolves through a succession of avalanches. We take pictures after every incremental lift of the tube. We have so obtained data for 39 cones of different volumes. On these pictures, we detect the edges of the pile by simple image processing, and fit them by straight lines to measure the corresponding slope. The results are shown in figure A.1. The values are nicely independent of the pile height, as it should for homothetic cones, showing that finite size effects (the piles are small) can be neglected. These data allow us to obtain a mean value:

$$\mu = 0.79 \pm 0.05, \tag{A.1}$$

corresponding to an avalanche angle $\simeq 38°$. It is slightly larger than the usual value of $35°$, in agreement with the elongated and angular shape of the grains (see figure A.2). The dispersion of the data relates to the metastability of the avalanching process.

A.2 Wind data processing

The sand fluxes are derived from the wind data of the KHMN weather station at the Holloman air base (32°51′N, 106°06′W) corresponding to the topography measurements, between 2007 and 2010. The method of analysis used here is based on that described

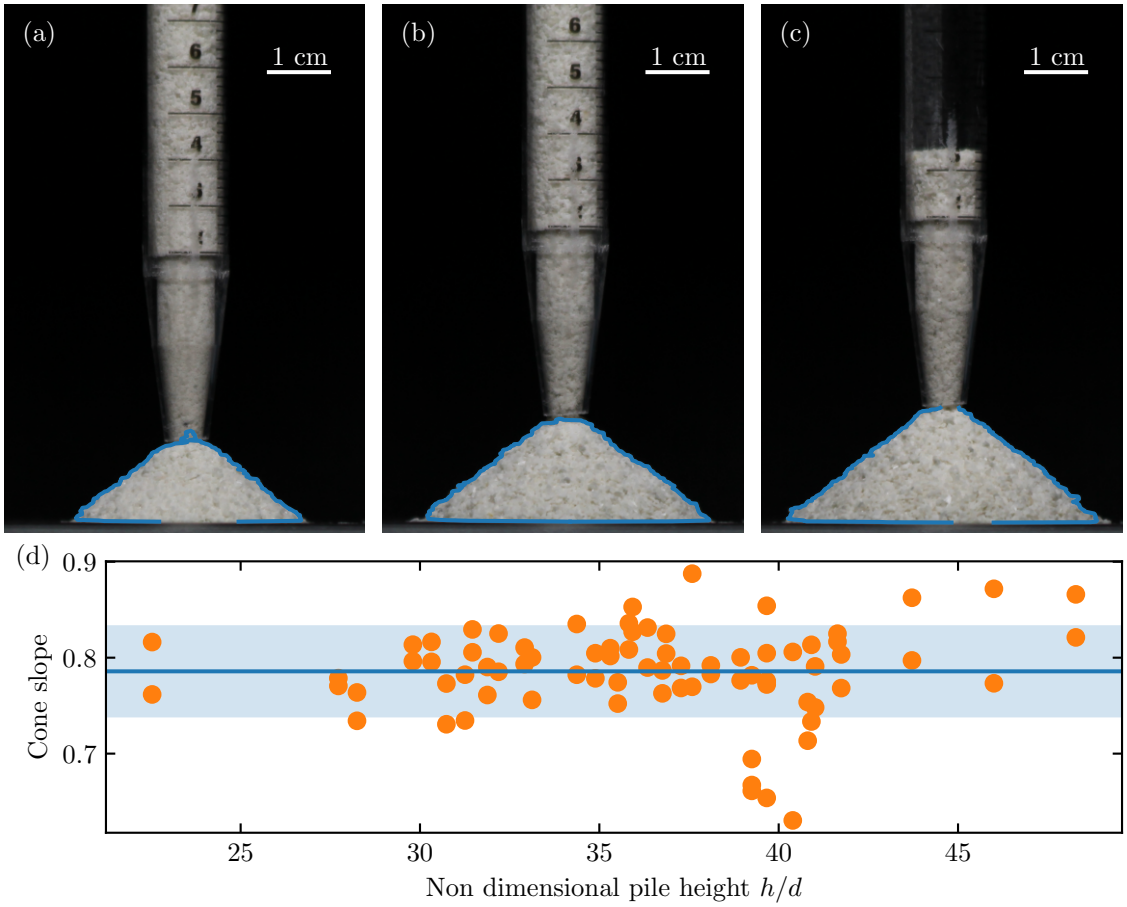

Figure A.1 – Measurement of the avalanche slope. (a-c) Evolution of the sand pile when the tube is pulled up. Contour detection is shown by the blue lines. (d) Measured slope as a function of the non dimensional pile height, where $d = 435$ μm is the d_{50} of the particular sample we have used. The blue line is the mean value, and the shaded area represents one standard deviation above and below it.

Figure A.2 – In situ image of representative gypsum grains on the upwind margin; their oblate shape and large size can be seen. The contrast and brightness of grains have been adjusted so their shapes are identifiable.

in the supplementary material of (Courrech du Pont *et al.* 2014). The data are hourly measurements of the wind velocity u_t and direction θ_t at 10 m height, with velocity and angle bins of 0.5 m/s and 10°, respectively. The sub-letter t indicates here the time of the corresponding data.

The sediment flux depends on the shear velocity u_*, characteristic to the logarithmic velocity vertical profile of the wind $u(z) = u_*/\kappa \ln(z/z_0)$ inside the turbulent boundary layer. $\kappa = 0.4$ is the von Kármán constant and z_0 is the aerodynamic roughness. At time t, this law of the wall is reciprocally used to estimate the shear velocity from the wind measurement as:

$$u_{*,t} = \kappa \frac{u_t}{\ln\left(\frac{z}{z_0}\right)}, \tag{A.2}$$

where z is set to the height at which the wind data have been recorded. Here we take $z_0 \simeq 1$ mm, associated with the thickness of the saltation layer.

Furthermore, the wind shear velocity exceeds a threshold u_{th} to maintain steady saltation. Its value is empirically given by

$$u_{\mathrm{th}} = 0.1\sqrt{\frac{\rho_{\mathrm{p}}}{\rho_{\mathrm{f}}} g d}, \tag{A.3}$$

where ρ_{p} and ρ_{f} are the grain and air density, d the grain diameter and g the gravitational acceleration Iversen & Rasmussen (1999). The saturated flux can then be computed at

each time step using the transport law Ungar & Haff (1987):

$$\boldsymbol{q}_{\mathrm{sat},t} = \begin{cases} \Omega\left(u_{*,t}^2 - u_{\mathrm{th}}^2\right)\boldsymbol{e}_{\theta_t} & \text{if} \quad u_{*,t} > u_{\mathrm{th}}, \\ 0 & \text{else}, \end{cases} \tag{A.4}$$

where $\boldsymbol{e}_{\theta_t} = (\cos\theta_t, \sin\theta_t)$ is a unit vector, and $\Omega = 25\,(\rho_{\mathrm{f}}/\rho_{\mathrm{p}})\sqrt{d/g}$ is a dimensional constant calibrated by measurements and numerical simulations (see review of (Durán *et al.* 2011)). From this time series, one can define the resultant sand flux. Likewise, we also compute the characteristic sand flux Q as:

$$\boldsymbol{Q}_t = \begin{cases} \Omega\, u_{*,t}^2 \boldsymbol{e}_{\theta_t} & \text{if} \quad u_{*,t} > u_{\mathrm{th}}, \\ 0 & \text{else}. \end{cases} \tag{A.5}$$

Finally, as the sand flux direction is mostly unimodal, dune growth and migration mainly result from the component of the fluxes aligned with the resultant sand flux direction β, perpendicular to the dune crests. The relevant characteristic sand flux for the study of the spatial development of the dune instability then become:

$$Q_t = \begin{cases} \Omega\, u_{*,t}^2 \cos\left(\theta_t - \beta\right) & \text{if} \quad u_{*,t} > u_{\mathrm{th}}, \\ 0 & \text{else}. \end{cases} \tag{A.6}$$

Note that Q_t can have positive or negative values depending on the orientation of the sand flux at time with respect to the resultant (average) sand flux direction. Quantification of the impact of the variations in wind direction can then be done by looking at the ratio between scalar and vector average of the characteristic sand flux. Using the wind data we obtain

$$\langle |Q_t| \rangle = 38 \pm 5 \ \mathrm{m}^2\ \mathrm{yr}^{-1}, \tag{A.7}$$

$$\langle Q_t \rangle = 23 \pm 3 \ \mathrm{m}^2\ \mathrm{yr}^{-1}, \tag{A.8}$$

resulting in

$$\frac{\langle Q_t \rangle}{\langle |Q_t| \rangle} \simeq 0.6. \tag{A.9}$$

Appendix B

Supplements to chapter 3

B.1 Inertial flow over an inclined sinusoidal topography

In this section, we describe the properties of an inertial flow over an inclined sinusoidal topography. We thus consider a three-dimensional inviscid stationary flow ($R_e \gg 1$) described by the following Euler equations,

$$\rho_f \left(\boldsymbol{v} \cdot \nabla\right) \boldsymbol{v} = -\nabla P + \rho_f \boldsymbol{g}, \tag{B.1}$$

$$\nabla \cdot \boldsymbol{v} = 0, \tag{B.2}$$

$$\boldsymbol{v}_{surface} \cdot \boldsymbol{n} = 0, \tag{B.3}$$

where $\boldsymbol{v} = (u, v, w)$ is the flow velocity, P the pressure, g the gravity, ρ_f the fluid density and $\boldsymbol{n}$ the unitary vector normal to the topography, flowing along $\boldsymbol{e}_x$ over a flat bed, such that this base state is described by $\boldsymbol{v}^0 = U\boldsymbol{e}_x$, $P^0(z) = P_0 - \rho_f g z$ and $h^0 = 0$. We introduce in the previous equilibrium state a small perturbation of the topography of amplitude ζ

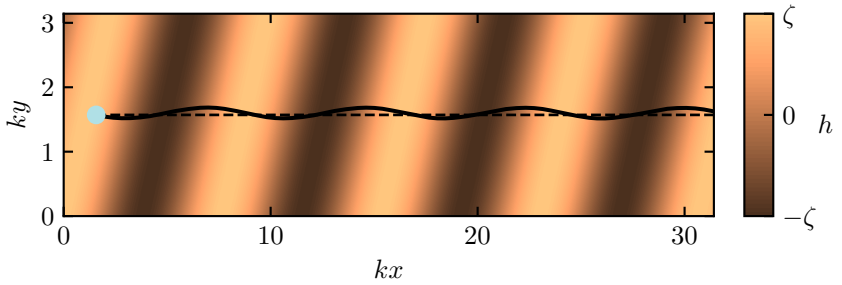

Figure B.1 – Stream line of an inertial flow over a sinusoidal inclined topography at the height of the bed, seen from above. Here, we take $k\zeta = 0.25$. The base line is represented in dashes.

such that $\eta = k\zeta \ll 1$, writing all quantities as:

$$X(x,y,t) = X^0 + \underbrace{X^1(x,y,t)}_{O(\eta)} + O\left(\eta^2\right), \tag{B.4}$$

The equations then becomes at the first linear order :

$$U\frac{\partial \boldsymbol{v}^1}{\partial x} = -\frac{1}{\rho_f}\nabla P^1, \tag{B.5}$$

$$\nabla \cdot \boldsymbol{v}^1 = 0, \tag{B.6}$$

$$U\frac{\partial h^1}{\partial x} = w^1_{z=0}. \tag{B.7}$$

Rescaling every velocity by U, and pressure by ρU^2, the previous equations now reads on their non-dimensional form as

$$\frac{\partial \boldsymbol{v}^1}{\partial x} = -\nabla P^1, \tag{B.8}$$

$$\nabla \cdot \boldsymbol{v}^1 = 0, \tag{B.9}$$

$$\frac{\partial h^1}{\partial x} = w^1_{z=0}. \tag{B.10}$$

Using a sinusoidal perturbation of the bed elevation as:

$$h = \zeta e^{ik(\cos\alpha x + \sin\alpha y - ct)}, \tag{B.11}$$

we look for solutions of the form:

$$X = X_0(z)e^{ik(\cos\alpha x + \sin\alpha y - ct)}, \tag{B.12}$$

the previous system now reads:

$$u_0 = -p_0, \tag{B.13}$$

$$v_0\cos\alpha = -p_0\sin\alpha, \tag{B.14}$$

$$w_0 ik\cos\alpha = -\frac{\partial p_0}{\partial z}, \tag{B.15}$$

$$ik\left(u_0\cos\alpha + v_0\sin\alpha\right) = -\frac{\partial w_0}{\partial z}, \tag{B.16}$$

$$w_{0,z=0} = ik\zeta\cos\alpha, \tag{B.17}$$

Solving leads to the non-dimensional expression of the Fourier transform of the quan-

tities

$$u_0 = k\zeta e^{-kz}\cos^2\alpha \tag{B.18}$$

$$v_0 = k\zeta e^{-kz}\cos\alpha\sin\alpha \tag{B.19}$$

$$w_0 = ik\zeta e^{-kz}\cos\alpha \tag{B.20}$$

$$\hat{p} = -k\zeta e^{-kz}\cos^2\alpha \tag{B.21}$$

As shown by figure B.1 in (x,y) plane, the corresponding streamline oscillates asymmetrically around the base line. As the flow also follows the topography in the (y, z) plane, the three dimensional structure of the streamline is an helix.

B.2 Measurement of the diffusion length in the ReSCAL dune model

Due to the transition for diffusion present in the ReSCAL dune model, erodible cells does not move only along the streamwise direction. At each time step, they have a probability to jump either at the left or the right instead of moving along the flow direction. In order to quantify this process, we run simulations where we put only one cell on the non-erodible bed, and follow its trajectory for different random seeds. As shown by figure B.2(a), the trajectories disperses as the cell travel downstream. We then measure the variance across the different trajectories of the particle cross-stream position for each streamwise position x. Figure B.2(b) shows that the cross-stream variance increases linearly with the streamwise distance, as expected for random walkers.

Following Seizilles *et al.* (2014), a diffusion length can be defined from this linear relationship:

$$\sigma y^2 = 2l_{\mathrm{d}}x. \tag{B.22}$$

Repeating this process for different values of the transition rate Λ_{d}, we find $l_d = 0.078\Lambda_{\mathrm{d}}$.

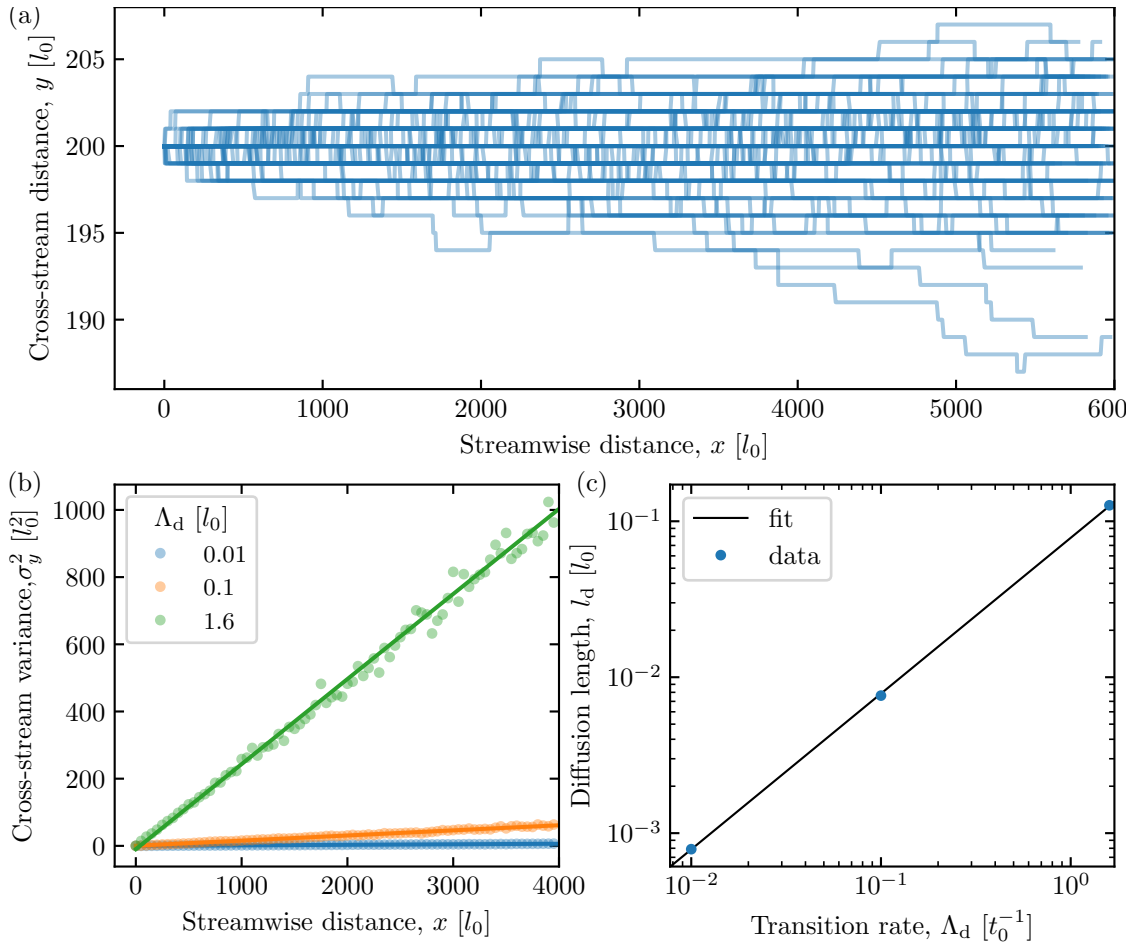

Figure B.2 – Measurement of the diffusion length in the ReSCAL model. (a) Different erodible cell trajectories over a flat non-erodible ground in the ReSCAL dune model for $\Lambda_d = 0.01\ t_0^{-1}$. (b) Variance of the cross stream cell position across the different trajectories as a function of the streamwise distance for different value of Λ_d. (c) Diffusion length as a function of Λ_d. The linear fit gives a slope of $0.078\ l_0 t_0$.

List of Figures

List of Tables

Bibliography

Abramian, A., Devauchelle, O., Seizilles, G., & Lajeunesse, E. 2019a. Boltzmann distribution of sediment transport. *Physical review letters*, **123**(1), 014501. 25

Abramian, A., Devauchelle, O., & Lajeunesse, E. 2019b. Streamwise streaks induced by bedload diffusion. *Journal of Fluid Mechanics*, **863**, 601–619. 114

Almeida, M. P., Parteli, E. J. R., Andrade, J. S., & Herrmann, H. J. 2008. Giant saltation on Mars. *Proceedings of the National Academy of Sciences*, **105**(17), 6222–6226. 28

Alvarez, C. A., & Franklin, E. M. 2019. Horns of subaqueous barchan dunes: A study at the grain scale. *Physical Review E*, **100**(4), 042904. 39

Anderson, R. S. 1987. A theoretical model for aeolian impact ripples. *Sedimentology*, **34**(5), 943–956. 16

Anderson, R. S., & Haff, P. K. 1988. Simulation of eolian saltation. *Science*, **241**(4867), 820–823. 117

Anderson, R. S., & Hallet, B. 1986. Sediment transport by wind: toward a general model. *Geological Society of America Bulletin*, **97**(5), 523–535. 117

Andreotti, B. 2004. A two-species model of aeolian sand transport. *J. Fluid Mech.*, **510**, 47–70. 19, 21, 25, 28, 30, 116

Andreotti, B., Claudin, P., & Douady, S. 2002a. Selection of dune shapes and velocities: Part 1: Dynamics of sand, wind and barchans. *Eur. Phys. J. B*, **28**(Aug.), 321–339. 18, 26, 29, 32, 39, 91, 117

Andreotti, B., Claudin, P., & Douady, S. 2002b. Selection of dune shapes and velocities: Part 2: A two-dimensional modelling. *The European Physical Journal B-Condensed Matter and Complex Systems*, **28**, 341–352. 17, 29, 30, 32, 36, 40, 60, 114

Andreotti, B., Claudin, P., & Pouliquen, O. 2006. Aeolian sand ripples: experimental study of fully developed states. *Physical review letters*, **96**(2), 028001. 16

Andreotti, B., Fourriere, A., Ould-Kaddour, F., Murray, B., & Claudin, P. 2009. Giant aeolian dune size determined by the average depth of the atmospheric boundary layer. *Nature*, **457**, 1120. 46, 134, 140

Andreotti, B., Claudin, P., & Pouliquen, O. 2010. Measurements of the aeolian sand transport saturation length. *Geomorphology*, **123**(3-4), 343–348. 29, 30, 38, 60, 61, 62, 74, 139

Andreotti, B., Claudin, P., Devauchelle, O., Durán, O., & Fourrière, A. 2012a. Bedforms in a turbulent stream: ripples, chevrons and antidunes. *J. Fluid Mech.*, **690**, 94–128. 32, 60, 85, 86, 88, 105, 114

Andreotti, B., Forterre, Y., & Pouliquen, O. 2012b. *Les milieux granulaires-entre fluide et solide: Entre fluide et solide*. EDP sciences. 11, 16, 19, 23, 24, 26, 27, 88, 112, 166

Ashkenazy, Y., Yizhaq, H., & Tsoar, H. 2012. Sand dune mobility under climate change in the Kalahari and Australian deserts. *Climatic Change*, **112**(3-4), 901–923. 152

Athanassiadou, M., & Castro, I. P. 2001. Neutral flow over a series of rough hills: a laboratory experiment. *Boundary-layer meteorology*, **101**(1), 1–30. 34

Baas, A. C. W. 2002. Chaos, fractals and self-organization in coastal geomorphology: simulating dune landscapes in vegetated environments. *Geomorphology*, **48**(1-3), 309–328. 117, 121

Baas, A. C. W., & Nield, J. M. 2007. Modelling vegetated dune landscapes. *Geophysical Research Letters*, **34**(6). 117

Baas, J. H. 1999. An empirical model for the development and the equilibrium morphology of current ripples in fine sand. *Sedimentology*, **46**, 123–138. 61

Bacik, K. A, Lovett, S., Colm-cille, P. C., & Vriend, N. M. 2020. Wake induced long range repulsion of aqueous dunes. *Physical Review Letters*, **124**(5), 054501. 79

Baddock, M.C., Livingstone, I., & Wiggs, G.F.S. 2007. The geomorphological significance of airflow patterns in transverse dune interdunes. *Geomorphology*, **87**, 322–336. 39, 41, 98

Baddock, M.C., Nield, J.M., & Wiggs, G.F.S. 2018. Early-stage aeolian protodunes: Bedform development and sand transport dynamics. *Earth Surface Processes and Landforms*, **43**, 339–346. 40, 61, 134

Bagnold, R.A. 1941. *The Physics of Wind Blown Sand and Desert Dunes: London*. 21, 25, 27, 29, 42, 103

Bagnold, R.A. 1956. The flow of cohesionless grains in fluids. *Phil. Trans. R. Soc. Lond. A*, **249**, 235–297. 87

Baitis, E., Kocurek, G., Smith, V., Mohrig, D., Ewing, R. C., & Peyret, A.-P. B. 2014. Definition and origin of the dune-field pattern at White Sands, New Mexico. *Aeolian Research*, **63**, 269–287. 62

Bishop, S. R., Momiji, H., Carretero-González, R., & Warren, A. 2002. Modelling desert dune fields based on discrete dynamics. *Discrete Dynamics in Nature and Society*, **7**(1), 7–17. 117

Black, C. T., Forrey, C., & Yager, K. G. 2017. Thickness-dependence of block copolymer coarsening kinetics. *Soft Matter*, **13**(18), 3275–3283. 171

Blumberg, D. G., & Greeley, R. 1996. A comparison of general circulation model predictions to sand drift and dune orientations. *Journal of Climate*, **9**(12), 3248–3259. 152

Bodenschatz, E., Weber, A., & Kramer, L. 1991. Interaction and dynamics of defects in convective roll patterns of anisotropic fluids. *Journal of statistical physics*, **64**(5-6), 1007–1015. 171

Bourke, M. C., Ewing, R. C., Finnegan, D., & McGowan, H. A. 2009. Sand dune movement in the Victoria Valley, Antarctica. *Geomorphology*, **109**(3-4), 148–160. 171

Bourke, M. C., Lancaster, N., Fenton, L. K., Parteli, E.J.R., Zimbelman, J.R., & Radebaugh, J. 2010. Extraterrestrial dunes: An introduction to the special issue on planetary dune systems. *Geomorphology*, **121**, 1–14. 54, 133

Bristow, C. S., Duller, G. A. T., & Lancaster, N. 2007. Age and dynamics of linear dunes in the Namib Desert. *Geology*, **35**(6), 555–558. 165, 174

Britter, R. E., Hunt, J. C. R., & Richards, K. J. 1981. Air flow over a two-dimensional hill: studies of velocity speed-up, roughness effects and turbulence. *Quarterly Journal of the Royal Meteorological Society*, **107**(451), 91–110. 34, 41

Buffington, J. M., & Montgomery, D. R. 1997. A systematic analysis of eight decades of incipient motion studies, with special reference to gravel-bedded rivers. *Water Resources Research*, **33**(8), 1993–2029. 23

Bullard, J. E., Thomas, D. S. G., Livingstone, I., & Wiggs, G. F. S. 1996. Wind energy variations in the southwestern Kalahari Desert and implications for linear dunefield activity. *Earth Surface Processes and Landforms*, **21**(3), 263–278. 152

Bullard, J.E., & Livingstone, I. 2002. Interactions between aeolian and fluvial systems in dryland environments. *Area*, **34**(1), 8–16. 140

Burr, D. M., Bridges, N. T., Marshall, J. R., Smith, J. K., White, B. R., & Emery, J. P. 2015. Higher-than-predicted saltation threshold wind speeds on Titan. *Nature*, **517**(7532), 60–63. 25

Cao, S., Wang, T., Ge, Y., & Tamura, Y. 2012. Numerical study on turbulent boundary layers over two-dimensional hills–effects of surface roughness and slope. *Journal of wind engineering and industrial aerodynamics*, **104**, 342–349. 34

Charnay, B.and Barth, E., Rafkin, S., Narteau, C., Lebonnois, S., Rodriguez, S., Courrech Du Pont, S., & Lucas, A. 2015. Methane storms as a driver of Titan's dune orientation. *Nature Geoscience*, **8**(5), 362–366. 173

Charru, F. 2006. Selection of the ripple length on a granular bed sheared by a liquid flow. *Physics of Fluids*, **18**, 121508. 29, 32

Charru, F. 2011. *Hydrodynamic instabilities*. Vol. 37. Cambridge University Press. 66

Charru, F., & Hinch, E. J. 2000. 'Phase diagram'of interfacial instabilities in a two-layer Couette flow and mechanism of the long-wave instability. *Journal of Fluid Mechanics*, **414**, 195–223. 32

Charru, F., Andreotti, B., & Claudin, P. 2013. Sand ripples and dunes. *Annual Review of Fluid Mechanics*, **45**, 469–493. 30, 35, 60, 74, 78, 91, 101, 105, 109, 134

Chopard, B., & Droz, M. 1998. *Cellular automata modeling of physical systems*. 118

Clark, A. H., Shattuck, M. D., Ouellette, N. T., & O'Hern, C. S. 2017. Role of grain dynamics in determining the onset of sediment transport. *Physical Review Fluids*, **2**(3), 034305. 117

Claudin, P., & Andreotti, B. 2006. A scaling law for aeolian dunes on Mars, Venus, Earth, and for subaqueous ripples. *Earth Planet. Sci. Lett.*, **252**, 30–44. 25, 26, 29, 32, 38, 60, 104

Claudin, P., Wiggs, G.F.S., & Andreotti, B. 2013. Field evidence for the upwind velocity shift at the crest of low dunes. *Boundary-layer Meteorol.*, **148**, 195–206. 32, 34, 35, 38, 41, 60, 61, 78, 86, 105

Coleman, S. E., & Melville, B. W. 1996. Initiation of bed forms on a flat sand bed. *Journal Hydraulic Engineering*, **122**, 301–310. 17, 61

Coleman, Stephen E, & Melville, Bruce W. 1994. Bed-form development. *Journal of hydraulic engineering*, **120**(5), 544–560. 17, 46

Colombini, M. 2004. Revisiting the linear theory of sand dune formation. *Journal of Fluid Mechanics*, **502**, 1–16. 32, 60

Colombini, M., & Stocchino, A. 2011. Ripple and dune formation in rivers. *Journal of Fluid Mechanics*, **673**, 121–131. 32

Cooper, W. S. 1958. *Coastal sand dunes of Oregon and Washington.* Vol. 72. Geological Society of America. 61

Courrech du Pont, S. 2015. Dune morphodynamics. *Comptes Rendus Physique*, **16**, 118–138. 16, 39, 40, 42, 47, 60, 97, 117, 139, 187

Courrech du Pont, S., Narteau, C., & Gao, X. 2014. Two modes for dune orientation. *Geology*, **42**, 743–746. 8, 12, 39, 42, 43, 46, 48, 49, 50, 51, 52, 54, 62, 83, 84, 93, 95, 96, 97, 101, 102, 107, 124, 127, 128, 133, 134, 136, 137, 139, 152, 162, 163, 165, 170, 174, 181, 188, 190

Creyssels, M., Dupont, P., Ould El Moctar, A., Valance, A., Cantat, I., Jenkins, J.T., Pasini, J.M., & Rasmussen, K.R. 2009. Saltating particles in a turbulent boundary layer: experiment and theory. *J. Fluid Mech.*, **625**, 47–74. 27, 28, 156

Csahók, Z., Misbah, C., Rioual, F., & Valance, A. 2000. Dynamics of aeolian sand ripples. *The European Physical Journal E*, **3**(1), 71–86. 16

Cutts, J.A., & Smith, R.S.U. 1973. Eolian deposits and dunes on Mars. *Journal of Geophysical Research*, **78**, 4139–4154. 133

Day, M., & Kocurek, G. 2018. Pattern similarity across planetary dune fields. *Geology*, **46**, 999–1002. 128, 141, 171

Dee, D.P., Uppala, S.M., Simmons, A.J., Berrisford, P., Poli, P., Kobayashi, S., Andrae, U., Balmaseda, M.A., Balsamo, G., Bauer, P., *et al.* . 2011. The ERA-Interim reanalysis: Configuration and performance of the data assimilation system. *Q. J. R. Meteorol. Soc.*, **137**, 553–597. 85, 152, 154

Delorme, P., Wiggs, G. F. S., Baddock, M. C., Claudin, P., Nield, J.M., & Valdez, A. 2020. Dune initiation in a bimodal wind regime. *Submitted to Journal of geophysical research.* 128

Desai, R. C., & Kapral, R. 2009. *Dynamics of Self-organized and Self-assembled Structures.* Cambridge University Press. 171

Devauchelle, O., Malverti, L., Lajeunesse, E., Lagrée, P.-Y., Josserand, C., & Nguyen Thu-Lam, K.-D. 2010. Stability of bedforms in laminar flows with free surface: from bars to ripples. *J. Fluid Mech.*, **642**, 329–348. 32, 60, 85

Dey, S. 2003. Threshold of sediment motion on combined transverse and longitudinal sloping beds. *J. Hydraul. Res.*, **41**, 405–415. 22, 26, 88

d'Humieres, D., Lallemand, P., & Frisch, U. 1986. Lattice gas models for 3D hydrodynamics. *EPL (Europhysics Letters)*, **2**(4), 291. 118

Diniega, S., Kreslavsky, M., Radebaugh, J., Silvestro, S., Telfer, M., & Tirsch, D. 2017. Our evolving understanding of aeolian bedforms, based on observation of dunes on different worlds. *Aeolian research*, **26**, 5–27. 133

Dong, Z., Wei, Z., Qian, G., Zhang, Z., Luo, W., & Hu, G. 2010. "Raked" linear dunes in the Kumtagh Desert, China. *Geomorphology*, **123**(1-2), 122–128. 54

Durán, O. 2007. *Vegetated dunes and barchan dune fields.* Ph.D. thesis, Institut für Computerphysik der Universit ät Stuttgart. 20

Durán, O., & Herrmann, H. J. 2006. Vegetation against dune mobility. *Physical review letters*, **97**(18), 188001. 11

Durán, O., & Moore, L. J. 2013. Vegetation controls on the maximum size of coastal dunes. *Proceedings of the National Academy of Sciences*, **110**(43), 17217–17222. 117

Durán, O., Schwämmle, V., Lind, P. G., & Herrmann, H. J. 2009. The dune size distribution and scaling relations of barchan dune fields. *Granular Matter*, **11**(1), 7–11. 44

Durán, O., Parteli, E. J. R., & Herrmann, H. J. 2010. A continuous model for sand dunes: Review, new developments and application to barchan dunes and barchan dune fields. *Earth Surface Processes and Landforms*, **35**(13), 1591–1600. 117

Durán, O., Claudin, P., & Andreotti, B. 2011. On aeolian transport: Grain-scale interactions, dynamical mechanisms and scaling laws. *Aeolian Research*, **3**, 243–270. 19, 22, 23, 24, 25, 26, 27, 28, 29, 30, 60, 115, 152, 182

Durán, O., Andreotti, B., & Claudin, P. 2012. Numerical simulation of turbulent sediment transport, from bed load to saltation. *Phys. Fluids*, **24**, 103306. 87, 117

Durán, O., Claudin, P., & Andreotti, B. 2014. Direct numerical simulations of aeolian sand ripples. *Proceedings of the National Academy of Sciences*, **111**(44), 15665–15668. 16, 117

Durán, O., Andreotti, B., Claudin, P., & Winter, C. 2019. A unified model of ripples and dunes in water and planetary environments. *Nature Geoscience*, **12**(5), 345–350. 32, 46, 60, 61, 104, 105, 116

Eastwood, E., Nield, J.M., Baas, A., & Kocurek, G. 2011. Modelling controls on aeolian dune-field pattern evolution. *Sedimentology*, **58**, 1391–1406. 117

Eckardt, F. D., Livingstone, I., Seely, M., & Von Holdt, J. 2013. The surface geology and geomorphology around Gobabeb, Namib Desert, Namibia. *Geografiska Annaler: Series A, Physical Geography*, **95**(4), 271–284. 157, 158

Elbelrhiti, H., Claudin, P., & Andreotti, B. 2005. Field evidence for surface-wave-induced instability of sand dunes. *Nature*, **437**, 720–723. 31, 32, 36, 38, 41, 43, 61, 74, 78, 79, 114

Elbelrhiti, H., Andreotti, B., & Claudin, P. 2008. Barchan dune corridors: field characterization and investigation of control parameters. *Journal of Geophysical Research*, **113**(F02S15). 40, 43, 44, 98, 103, 134

Endo, N., Taniguchi, K., & Katsuki, A. 2004. Observation of the whole process of interaction between barchans by flume experiments. *Geophysical Research Letters*, **31**(12). 44

Esteves, L. S., Williams, J. J., & Brown, J. M. 2011. Looking for evidence of climate change impacts in the eastern Irish Sea. *Natural Hazards and Earth System Sciences*, **11**(6), 1641–1656. 152

Ewing, R. C., Kocurek, G., & Lake, L. W. 2006. Pattern analysis of dune-field parameters. *Earth Surface Processes and Landforms: The Journal of the British Geomorphological Research Group*, **31**(9), 1176–1191. 12, 18

Ewing, R. C., McDonald, G. D., & Hayes, A. G. 2015. Multi-spatial analysis of aeolian dune-field patterns. *Geomorphology*, **240**, 44–53. 63, 78

Ewing, R.C., & Kocurek, G. 2010. Aeolian dune-field pattern boundary conditions. *Geomorphology*, **114**, 175–187. 46, 61, 134

Fenton, L. K., Michaels, T. I., & Beyer, R. A. 2014a. Inverse maximum gross bedform-normal transport 1: How to determine a dune-constructing wind regime using only imagery. *Icarus*, **230**, 5–14. 12, 53, 78

Fenton, L. K., Michaels, T. I., Chojnacki, M., & Beyer, R. A. 2014b. Inverse maximum gross bedform-normal transport 2: Application to a dune field in Ganges Chasma, Mars and comparison with HiRISE repeat imagery and MRAMS. *Icarus*, **230**, 47–63. 12, 53, 78

Fenwick, G. A. 1991. Grain size and easterly wind influences on dunes of the north central Namib desert. *Zeitschrift für Geomorphologie*, **35**(3), 283–292. 166

Fernandez-Cascales, L., Lucas, A., Rodriguez, S., Gao, X., Spiga, A., & Narteau, C. 2018. First quantification of relationship between dune orientation and sediment availability, Olympia Undae, Mars. *Earth and Planetary Science Letters*, **489**, 241–250. 12, 53, 78

Fernandez Luque, R., & Van Beek, R. 1976. Erosion and transport of bed-load sediment. *J. Hydraul. Res.*, **14**, 127–144. 22, 26, 88

Finnigan, J. J., Raupach, M. R., Bradley, E. F., & Aldis, G. K. 1990. A wind tunnel study of turbulent flow over a two-dimensional ridge. *Boundary-Layer Meteorology*, **50**(1-4), 277–317. 34

Forterre, Y., & Pouliquen, O. 2008. Flows of dense granular media. *Annu. Rev. Fluid Mech.*, **40**, 1–24. 19

Fourrière, A., Claudin, P., & Andreotti, B. 2010. Bedforms in a turbulent stream: formation of ripples by primary linear instability and of dunes by nonlinear pattern coarsening. *J. Fluid Mech.*, **649**, 287–328. 30, 32, 34, 35, 36, 38, 39, 46, 60, 61, 68, 78, 91, 104, 105, 109, 114

Franklin, E. M., & Charru, F. 2011. Subaqueous barchan dunes in turbulent shear flow. Part 1. Dune motion. *Journal of Fluid Mechanics*, **675**, 199. 39

Frederick, K.A., & Hanratty, T.J. 1988. Velocity measurements for a turbulent nonseparated flow over solid waves. *Exp. Fluids*, **6**, 477–486. 34, 105

Frisch, U., Hasslacher, B., & Pomeau, Y. 1986. Lattice-gas automata for the Navier-Stokes equation. *Physical review letters*, **56**(14), 1505. 118

Fryberger, S.G., & Dean, G. 1979. Dune forms and wind regime. *A study of global sand seas*, **1052**, 137–169. 61, 152

Gadal, C., Narteau, C., Courrech du Pont, S., Rozier, O., & Claudin, P. 2019. Incipient bedforms in a bidirectional wind regime. *Journal of Fluid Mechanics*, **862**, 490–516. 85, 138, 152

Gadal, Cyril, Narteau, Clément, Courrech du Pont, Sylvain, Rozier, Olivier, & Claudin, Philippe. 2020. Periodicity in fields of elongating dunes. *Geology*, **48**(4), 343–347. 132

Gallaire, F., & Brun, P. T. 2017. Fluid dynamic instabilities: theory and application to pattern forming in complex media. *Philosophical Transactions of the Royal Society A*, **375**, 20160155. 66

Gao, X., Zhang, D., Rozier, O., & Narteau, C. 2014. Transport capacity and saturation mechanism in a real-space cellular automaton dune model. *Advances in Geosciences*, **37**(37), 47–47. 120

Gao, X., Narteau, C., & Rozier, O. 2015a. Development and steady states of transverse dunes: A numerical analysis of dune pattern coarsening and giant dunes. *Journal of Geophysical Research: Earth Surface*, **120**, 2200–2219. 17, 45, 46, 79, 118, 119, 120, 134

Gao, X., Narteau, C., Rozier, O., & Courrech Du Pont, S. 2015b. Phase diagrams of dune shape and orientation depending on sand availability. *Scientific reports*, **5**, 14677. 42, 50, 53, 79, 97, 120, 124, 128, 132, 134

Gao, X., Narteau, C., & Rozier, O. 2016. Controls on and effects of armoring and vertical sorting in aeolian dune fields: a numerical simulation study. *Geophysical Research Letters*, **43**(6), 2614–2622. 117, 120

Gao, X., Gadal, C., Rozier, O., & Narteau, C. 2018. Morphodynamics of barchan and dome dunes under variable wind regimes. *Geology*, **46**, 743–746. 117, 120, 134, 152, 173

Gao, Xin. 2013. *Development, stability and orientation of dune fields*. Ph.D. thesis, Université Paris VII - Denis Diderot. 124

Garratt, J. R. 1994. The atmospheric boundary layer. *Earth-Science Reviews*, **37**(1-2), 89–134. 21

Garzanti, E., Andò, S., Vezzoli, G., Lustrino, M., Boni, M., & Vermeesch, P. 2012. Petrology of the Namib Sand Sea: long-distance transport and compositional variability in the wind-displaced Orange Delta. *Earth-Science Reviews*, **112**(3-4), 173–189. 157

Génois, M., Courrech Du Pont, S., Hersen, P., & Grégoire, G. 2013a. An agent-based model of dune interactions produces the emergence of patterns in deserts. *Geophysical Research Letters*, **40**, 3909–3914. 44, 134

Génois, M., Courrech Du Pont, S., Hersen, P., & Grégoire, G. 2013b. Spatial structuring and size selection as collective behaviours in an agent-based model for barchan fields. *The European Physical Journal B*, **86**(11), 447. 134

Giudice, A. L., & Preziosi, L. 2020. A fully Eulerian multiphase model of windblown sand coupled with morphodynamic evolution: Erosion, transport, deposition, and avalanching. *Applied Mathematical Modelling*, **79**, 68–84. 117

Groh, C., Wierschem, A., Aksel, N., Rehberg, I., & Kruelle, C. A. 2008. Barchan dunes in two dimensions: Experimental tests for minimal models. *Physical Review E*, **78**(2), 021304. 40

Guignier, L., Niiya, H., Nishimori, H., Lague, D., & Valance, A. 2013. Sand dunes as migrating strings. *Physical Review E*, **87**, 052206. 46, 48, 134, 144

Hansen, H., Redinger, A., Messlinger, S., Stoian, G., Krug, J., & Michely, T. 2009. Rapid coarsening of ion beam ripple patterns by defect annihilation. *Physical review letters*, **102**(14), 146103. 171

Hardisty, J., & Whitehouse, R.J.S. 1988. Evidence for a new sand transport process from experiments on Saharan dunes. *Nature*, **332**, 532–534. 22, 88

He, Y. C., Chan, P. W., & Li, Q. S. 2014. Field measurements of wind characteristics over hilly terrain within surface layer. *Wind and Structures*, **19**(5), 541–563. 34

Hersbach, H., Bell, B., Berrisford, P., Hirahara, S., Horányi, A., Muñoz-Sabater, J., Nicolas, J., Peubey, C., Radu, R., Schepers, D., *et al.* . 2020. The ERA5 global reanalysis. *Quarterly Journal of the Royal Meteorological Society*. 17, 45, 51, 53, 142, 152, 154

Hersen, P. 2004a. *Morphogenèse et Dynamique des Barchanes*. Ph.D. thesis, Université Paris IV. 41, 143

Hersen, P. 2004b. On the crescentic shape of barchan dunes. *The European Physical Journal B-Condensed Matter and Complex Systems*, **37**, 507–514. 18, 39, 116, 117, 134, 143, 187

Hersen, P., & Douady, S. 2005. Collision of barchan dunes as a mechanism of size regulation. *Geophysical Research Letter*, **32**. 39, 44, 79

Hersen, P., Douady, S., & Andreotti, B. 2002. Relevant length scale of barchan dunes. *Physical Review Letter*, **89**, 264301. 37, 39, 40, 101

Hersen, P., Andersen, K. H., Elbelrhiti, H., Andreotti, B., Claudin, P., & Douady, S. 2004. Corridors of barchan dunes: Stability and size selection. *Physical Review E*, **69**, 011304. 40, 41

Hesp, P. A., & Hastings, K. 1998. Width, height and slope relationships and aerodynamic maintenance of barchans. *Geomorphology*, **22**(2), 193–204. 40

Ho, T. D., Valance, A., Dupont, P., & Ould El Moctar, A. 2011. Scaling laws in aeolian sand transport. *Phys. Rev. Lett.*, **106**, 094501. 113

Howard, A. D. 1977. Effect of slope on the threshold of motion and its application to orientation of wind ripples. *Geological Society of America Bulletin*, **88**(6), 853–856. 116

Howard, A. D., Morton, J. B., Gad-El-Hak, M., & Pierce, D. B. 1978. Sand transport model of barchan dune equilibrium. *Sedimentology*, **25**(3), 307–338. 39

Hunt, J. C. R., & Snyder, W. H. 1980. Experiments on stably and neutrally stratified flow over a model three-dimensional hill. *Journal of Fluid Mechanics*, **96**(4), 671–704. 33

Hunt, J. C. R., Richards, K. J., & Brighton, P. W. M. 1988a. Stably stratified shear flow over low hills. *Quarterly Journal of the Royal Meteorological Society*, **114**(482), 859–886. 33

Hunt, J. C. R., Leibovich, S., & Richards, K. J. 1988b. Turbulent shear flows over low hills. *Quarterly Journal of the Royal Meteorological Society*, **114**, 1435–1470. 32, 33, 41, 60

Huntley, D. A., Coco, G., Bryan, K. R., & Murray, A. B. 2008. Influence of "defects" on sorted bedform dynamics. *Geophysical Research Letters*, **35**(2). 171

Iacono, C. L., Guillén, J., Guerrero, Q., Durán, R., Wardell, C., Hall, R. A., Aslam, T., Carter, G. D. O., Gales, J. A., & Huvenne, V. A. I. 2020. Bidirectional bedform fields at the head of a submarine canyon (NE Atlantic). *Earth and Planetary Science Letters*, **542**, 116321. 128

Iversen, J. D., & Rasmussen, K. 1994. The effect of surface slope on saltation threshold. *Sedimentology*, **41**(4), 721–728. 26

Iversen, J. D., Pollack, J. B., Greeley, R., & White, B. R. 1976. Saltation threshold on Mars: The effect of interparticle force, surface roughness, and low atmospheric density. *Icarus*, **29**(3), 381–393. 26

Iversen, J. D., Greeley, R., Marshall, J. R., & Pollack, J. B. 1987. Aeolian saltation threshold: the effect of density ratio. *Sedimentology*, **34**(4), 699–706. 25, 26

Iversen, J.D., & Rasmussen, K. 1999. The effect of wind speed and bed slope on sand transport. *Sedimentology*, **46**, 723–731. 28, 62, 88, 115, 152, 181

Jackson, P.S., & Hunt, J.C.R. 1975. Turbulent wind flow over a low hill. *Q. J. R. Meteorol. Soc.*, **101**, 929–955. 33, 41

Jerolmack, D. J., Reitz, M. D., & Martin, R. L. 2011. Sorting out abrasion in a gypsum dune field. *Journal of Geophysical Research*, **116**, F02003. 62

Jerolmack, D. J., Ewing, R. C., Falcini, F., Martin, R. L., Masteller, C., Phillips, C., Reitz, M. D., & Buynevich, I. 2012. Internal boundary layer model for the evolution of desert dune fields. *Nature Geoscience*, **5**(3), 206–209. 62

Jewell, P. W., & Nicoll, K. 2011. Wind regimes and aeolian transport in the Great Basin, USA. *Geomorphology*, **129**(1-2), 1–13. 152

Jia, P., Andreotti, B., & Claudin, P. 2017. Giant ripples on comet 67P/Churyumov–Gerasimenko sculpted by sunset thermal wind. *Proceedings of the National Academy of Sciences*, **114**, 2509–2514. 61, 133

Kamphuis, J. W. 1974. Determination of sand roughness for fixed beds. *Journal of Hydraulic Research*, **12**(2), 193–203. 21

Katsuki, A., Nishimori, H., Endo, N., & Taniguchi, K. 2005. Collision dynamics of two barchan dunes simulated using a simple model. *Journal of the Physical Society of Japan*, **74**(2), 538–541. 39, 79

Kennedy, J. F. 1963. The mechanics of dunes and antidunes in erodible-bed channels. *Journal of Fluid Mechanics*, **16**, 521–544. 32, 60

Khosronejad, A., & Sotiropoulos, F. 2017. On the genesis and evolution of barchan dunes: morphodynamics. *Journal of Fluid Mechanics*, **815**, 117–148. 39, 117

Kim, H. G., Patel, V. C., & Lee, C. M. 2000. Numerical simulation of wind flow over hilly terrain. *Journal of wind engineering and industrial aerodynamics*, **87**(1), 45–60. 34

Kochanski, K., Defazio, G.-C., Green, E., Barnes, R., Downie, C., Rubin, A., & Rountree, B. 2019. Rescal-snow: Simulating snow dunes with cellular automata. *Journal of Open Source Software*, **4**(42), 1699. 118

Kocurek, G., & Ewing, R. C. 2005. Aeolian dune field self-organization – implications for the formation of simple versus complex dune-field patterns. *Geomorphology*, **72**(1-4), 94–105. 18

Kocurek, G., Townsley, M., Yeh, E., Havholm, K. G., & Sweet, M. L. 1992. Dune and dune-field development on Padre Island, Texas, with implications for interdune deposition and water-table-controlled accumulation. *Journal of Sedimentary Research*, **62**(4), 622–635. 61

Kocurek, G., Carr, M., Ewing, R. C., Havholm, K. G., Nagar, Y. C., & Singhvi, A. K. 2007. White Sands dune field, New Mexico: age, dune dynamics and recent accumulations. *Sedimentary Geology*, **197**, 313–331. 77

Kocurek, G., Ewing, R. C., & Mohrig, D. 2010. How do bedform patterns arise ? New views on the role of bedform interactions within a set of boundary conditions. *Earth surface processes and landforms*, **35**(1), 51–63. 17

Kok, J. F., & Renno, N. O. 2009. A comprehensive numerical model of steady state saltation (COMSALT). *Journal of Geophysical Research: Atmospheres*, **114**(D17). 28

Kouakou, K.K., & Lagrée, P.-Y. 2005. Stability of an erodible bed in various shear flows. *The Eur. Phys. J. B*, **47**, 115–125. 32

Kroy, K., Sauermann, G., & Herrmann, H. J. 2002a. Minimal model for aeolian sand dunes. *Phys. Rev. E*, **66**, 031302. 32, 60, 117

Kroy, K., Sauermann, G., & Herrmann, H. J. 2002b. Minimal Model for Sand Dunes. *Phys. Rev. Lett.*, **88**, 054301. 32, 34, 60

Lagrée, P.-Y. 2003. A triple deck model of ripple formation and evolution. *Physics of Fluids*, **15**, 2355–2368. 32, 60

Lämmel, M., Rings, D., & Kroy, K. 2012. A two-species continuum model for aeolian sand transport. *New Journal of Physics*, **14**(9), 093037. 25

Lancaster, N. 1981. Grain size characteristics of Namib Desert linear dunes. *Sedimentology*, **28**(1), 115–122. 158, 165

Lancaster, N. 1982. Linear dunes. *Prog. Phys. Geogr.*, **6**, 475–504. 18, 50, 132

Lancaster, N. 1983. *Controls of dune morphology in the Namib sand sea.* Vol. 38. Elsevier. 165

Lancaster, N. 1985. Winds and sand movements in the Namib sand sea. *Earth Surface Processes and Landforms*, **10**(6), 607–619. 160

Lancaster, N. 1989. Star dunes. *Prog. Phys. Geogr.*, **13**, 67–91. 18

Lancaster, N. 1994. *Dune morphology and dynamics.* Springer. 160

Lancaster, N. 2013. *Geomorphology of desert dunes.* Routledge. 17, 152

Lancaster, N., & Ollier, C. D. 1983. Sources of sand for the Namib sand sea. *Zeitschrift für Geomorphologie*, **45**, 73–83. 165

Lancaster, N., & Teller, J. T. 1988. Interdune deposits of the Namib sand sea. *Sedimentary Geology*, **55**(1-2), 91–107. 166

Lancaster, N., Nickling, W. G., Neuman, C. K. M., & Wyatt, V. E. 1996. Sediment flux and airflow on the stoss slope of a barchan dune. *Geomorphology*, **7**, 55–62. 41

Lancaster, N., Kocurek, G., Singhvi, A., Pandey, V., Deynoux, M., Ghienne, J.-F., & Lô, K. 2002. Late Pleistocene and Holocene dune activity and wind regimes in the western Sahara Desert of Mauritania. *Geology*, **30**(11), 991–994. 152

Langlois, V., & Valance, A. 2007a. Formation and evolution of current ripples on a flat sand bed under turbulent water flow. *European Physical Journal E*, **22**, 201–208. 61

Langlois, Vincent, & Valance, Alexandre. 2007b. Initiation and evolution of current ripples on a flat sand bed under turbulent water flow. *The European Physical Journal E*, **22**(3), 201–208. 46

Lapôtre, M. G. A., & et al. 2016. Large wind ripples on Mars: a record of atmospheric evolution. *Science*, **353**, 55–58. 61

Lapôtre, M. G. A., Ewing, R. C., Weitz, C. M., Lewis, K. W., Lamb, M. P., Ehlmann, B. L., & Rubin, D. M. 2018. Morphologic diversity of Martian ripples: implications for large-ripple formation. *Geophysical Research Letters*, **45**, 10229–10239. 61

Lee, D. B., Ferdowsi, B., & Jerolmack, D. J. 2019. The imprint of vegetation on desert dune dynamics. *Geophysical Research Letters*, **46**(21), 12041–12048. 79

Lettau, H.H., & Lettau, K. 1978. Experimental and micrometeorological field studies of dune migration. *Pages 110–147 of: Exploring in the World's driest climate*. University of Wisconsin. 42

Lim, S., Chase, B. M., Chevalier, M., & Reimer, P. J. 2016. 50,000 years of vegetation and climate change in the southern Namib Desert, Pella, South Africa. *Palaeogeography, Palaeoclimatology, Palaeoecology*, **451**, 197–209. 165

Lima, I. A., Araújo, A. D., Parteli, E. J. R., Andrade, J. S., & Herrmann, H. J. 2017. Optimal array of sand fences. *Scientific reports*, **7**, 45148. 117

Liu, X., & Dong, Z. 2004. Experimental investigation of the concentration profile of a blowing sand cloud. *Geomorphology*, **60**(3-4), 371–381. 27

Livingstone, I. 1987. Grain-size variation on a 'complex'linear dune in the Namib Desert. *Geological Society, London, Special Publications*, **35**(1), 281–291. 158

Livingstone, I. 2003. A twenty-one-year record of surface change on a Namib linear dune. *Earth Surface Processes and Landforms: The Journal of the British Geomorphological Research Group*, **28**(9), 1025–1031. 160

Livingstone, I., & Warren, A. 1996. *Aeolian geomorphology: an introduction*. Addison Wesley Longman Ltd. 17, 18, 152, 160, 166, 173, 187

Livingstone, I., Bristow, C., Bryant, R. G., Bullard, J., White, K., Wiggs, G. F. S., Baas, A. C. W., Bateman, M. D., & Thomas, D. S. G. 2010. The Namib Sand Sea digital database of aeolian dunes and key forcing variables. *Aeolian Research*, **2**(2-3), 93–104. 152, 156, 160, 165, 166, 174

Loiseleux, T., Gondret, P., Rabaud, M., & Doppler, D. 2005. Onset of erosion and avalanche for an inclined granular bed sheared by a continuous laminar flow. *Phys. Fluids*, **17**, 103304. 88

Lorenz, R. D., & Zimbelman, J. R. 2014. *Dune worlds: How windblown sand shapes planetary landscapes*. Springer Science & Business Media. 133

Lorenz, R.D., Wall, S., Radebaugh, J., Boubin, G., Reffet, E., Janssen, M., Stofan, E., Lopes, R., Kirk, R., Elachi, C., *et al.* . 2006. The sand seas of Titan: Cassini RADAR observations of longitudinal dunes. *Science*, **312**, 724–727. 133

Lü, P., Dong, Z., Narteau, C., & Rozier, O. 2016. Morphodynamic mechanisms for the formation of asymmetric barchans: improvement of the Bagnold and Tsoar models. *Environmental earth sciences*, **75**(3), 259. 54, 120

Lü, P., Narteau, C., Dong, Z., Rozier, O., & Courrech du Pont, S. 2017. Unravelling raked linear dunes to explain the coexistence of bedforms in complex dunefields. *Nature Communications*, **8**, 14239. 54, 117, 120, 136, 139, 141, 152

Lü, P., Dong, Z., & Rozier, O. 2018. The combined effect of sediment availability and wind regime on the morphology of aeolian sand dunes. *Journal of Geophysical Research: Earth Surface*, **123**(11), 2878–2886. 53, 120

Lucas, A., Rodriguez, S., Narteau, C., Charnay, B., Courrech du Pont, S., Tokano, T., Garcia, A., Thiriet, M., Hayes, A.G., Lorenz, R.D., *et al.* . 2014. Growth mechanisms and dune orientation on Titan. *Geophysical Research Letter*, **41**(17), 6093–6100. 50, 133, 141

Lucas, A., Narteau, C., Rodriguez, S., Rozier, O., Callot, Y., Garcia, A., & Courrech du Pont, S. 2015. Sediment flux from the morphodynamics of elongating linear dunes. *Geology*, **43**, 1027–1030. 50, 134, 174

Lucas, A., Rodriguez, S., Lemonnier, F., Le Gall, A., MacKenzie, S., Ferrari, C., Paillou, P., & Narteau, C. 2019. Texture and Composition of Titan's Equatorial Sand Seas Inferred From Cassini SAR Data: Implications for Aeolian Transport and Dune Morphodynamics. *Journal of Geophysical Research: Planets*, **124**(11), 3140–3163. 128

Mainguet, M. 1984. A classification of dunes based on aeolian dynamics and the sand budget. *Pages 31–58 of: Deserts and arid lands*. Springer. 17, 18

Mainguet, M., & Callot, Y. 1978. L'Erg de Fachi-Bilma (Tchad-Niger). Contribution à la connaissance de la dynamique des ergs et des dunes des zones arides chaudes. 132

Mandea, M., Narteau, C., Panet, I., & Le Mouël, J.-L. 2015. Gravimetric and magnetic anomalies produced by dissolution-crystallization at the core-mantle boundary. *Journal of Geophysical Research: Solid Earth*, **120**(9), 5983–6000. 118

Martin, R. L., & Kok, J. F. 2017. Wind-invariant saltation heights imply linear scaling of aeolian saltation flux with shear stress. *Science advances*, **3**(6), e1602569. 25

Martin, R. L., & Kok, J. F. 2018. Distinct thresholds for the initiation and cessation of aeolian saltation from field measurements. *Journal of Geophysical Research: Earth Surface*, **123**(7), 1546–1565. 25

Mason, P. J., & King, J. C. 1985. Measurements and predictions of flow and turbulence over an isolated hill of moderate slope. *Quarterly journal of the royal meteorological society*, **111**(468), 617–640. 34

Mason, P. J., & Sykes, R. I. 1979. Flow over an isolated hill of moderate slope. *Quarterly Journal of the Royal Meteorological Society*, **105**(444), 383–395. 34, 41

Mazzuoli, M., Kidanemariam, A. G., & Uhlmann, M. 2019. Direct numerical simulations of ripples in an oscillatory flow. *Journal of Fluid Mechanics*, **863**, 572–600. 117

McKee, E. D. 1966. Structures of dunes at White Sands National Monument, New Mexico (and a comparison with structures of dunes from other selected areas) 1. *Sedimentology*, **7**(1), 3–69. 62

McKee, E.D. 1979. Introduction to a study of global sand seas. *Pages 1–19 of: A study of global sand seas*, vol. 1052. Professional Paper. 133, 160

Melo, H. P. M., Parteli, E. J. R., Andrade Jr, J. S., & Herrmann, H. J. 2012. Linear stability analysis of transverse dunes. *Physica A: Statistical Mechanics and its Applications*, **391**(20), 4606–4614. 48

Meyer-Peter, E., & Müller, R. 1948. Formulas for bed load transport. *Pages 39–64 of: Proceedings of the 2nd Meeting of the International Association for Hydraulic Structures Research*. Inter. Assoc. for Hydraul. Res., Delft, Netherlands. 87

Momiji, H., Carretero-González, R., Bishop, S. R., & Warren, A. 2000. Simulation of the effect of wind speedup in the formation of transverse dune fields. *Earth Surface Processes and Landforms: The Journal of the British Geomorphological Research Group*, **25**(8), 905–918. 117

Momiji, H., Nishimori, H., & Bishop, S. R. 2002. On the shape and migration speed of a proto-dune. *Earth Surface Processes and Landforms: The Journal of the British Geomorphological Research Group*, **27**(12), 1335–1338. 39

Nakao-Kusune, S., Sakaue, T., Nishimori, H., & Nakanishi, H. 2020. Stabilization of a straight longitudinal dune under bimodal wind with large directional variation. *Physical Review E*, **101**(1), 012903. 50, 173

Namikas, S. L. 2003. Field measurement and numerical modelling of aeolian mass flux distributions on a sandy beach. *Sedimentology*, **50**(2), 303–326. 27

Narteau, C., Le Mouël, J. L., Poirier, J. P., Sepúlveda, E., & Shnirman, M. 2001. On a small-scale roughness of the core-mantle boundary. *Earth and Planetary Science Letters*, **191**(1-2), 49–60. 118

Narteau, C., Zhang, D., Rozier, O., & Claudin, P. 2009. Setting the length and time scales of a cellular automaton dune model from the analysis of superimposed bed forms. *Journal of Geophysical Research: Earth Surface*, **114**, F03006. 12, 78, 109, 117, 118, 120, 121, 125, 136, 147

Neuman, C. K. M., Lancaster, N., & Nickling, W. G. 1997. Relations between dune morphology, air flow, and sediment flux on reversing dunes, Silver Peak, Nevada. *Sedimentology*, **44**(6), 1103–1111. 41

Nield, J. M., & Baas, A. C. W. 2008. Investigating parabolic and nebkha dune formation using a cellular automaton modelling approach. *Earth Surface Processes and Landforms*, **33**(5), 724–740. 117

Niiya, H.and Awazu, A., & Nishimori, H. 2010. Three-dimensional dune skeleton model as a coupled dynamical system of two-dimensional cross sections. *Journal of the Physical Society of Japan*, **79**, 063002. 48, 134

Nishimori, H., & Ouchi, N. 1993. Computational models for sand ripple and sand dune formation. *Int. J. Modern Physics B*, **7**, 2025–2034. 117

Nishimori, H., Yamasaki, M., & Andersen, K. H. 1998. A simple model for the various pattern dynamics of dunes. *International Journal of Modern Physics B*, **12**(03), 257–272. 117

Owen, P.R. 1964. Saltation of uniform grains in air. *J. Fluid Mech.*, **20**, 225–242. 27

Pähtz, T., & Durán, O. 2018. The cessation threshold of nonsuspended sediment transport across aeolian and fluvial environments. *Journal of Geophysical Research: Earth Surface*, **123**(8), 1638–1666. 25

Pähtz, T., Kok, J. F., Parteli, E. J. R., & Herrmann, H. J. 2013a. Flux Saturation Length of Sediment Transport. *Phys. Rev. Lett.*, **111**(Nov), 218002. 29, 30

Pähtz, T., Kok, J. F., Parteli, E. J. R., & Herrmann, H. J. 2013b. Flux saturation length of sediment transport. *Physical Review Letters*, **11**, 218002. 60

Pähtz, T., Omeradžić, A., Carneiro, M. V., Araújo, N. A. M., & Herrmann, H. J. 2015. Discrete element method simulations of the saturation of aeolian sand transport. *Geophysical Research Letters*, **42**(6), 2063–2070. 117

Pähtz, T., Clark, A. H., Valyrakis, M., & Durán, O. 2020. The physics of sediment transport initiation, cessation, and entrainment across aeolian and fluvial environments. *Reviews of Geophysics*, e2019RG000679. 25

Paillou, P., Lopez, S., Marais, E., & Scipal, K. 2020. Mapping Paleohydrology of the Ephemeral Kuiseb River, Namibia, from Radar Remote Sensing. *Water*, **12**(5), 1441. 174, 175

Pargellis, A. N., Finn, P., Goodby, J. W., Panizza, P., Yurke, B., & Cladis, P. E. 1992. Defect dynamics and coarsening dynamics in smectic-C films. *Physical Review A*, **46**(12), 7765. 171

Parteli, E.J., Durán, O., & Herrmann, H.J. 2007. Minimal size of a barchan dune. *Phys. Rev. E*, **75**, 011301. 37, 40, 117

Parteli, E.J., Durán, O., Tsoar, H., Schwämmle, V., & Herrmann, H.J. 2009. Dune formation under bimodal winds. *Proc. Nat. Ac. Sc.*, **106**, 22085–22089. 117

Parteli, E.J.R., Schwämmle, V., Herrmann, H.J., Monteiro, L.H.U., & Maia, L.P. 2006. Profile measurement and simulation of a transverse dune field in the Lençóis Maranhenses. *Geomorphology*, **81**, 29–42. 39, 98

Parteli, E.J.R., Andrade Jr, J.S., & Herrmann, H.J. 2011. Transverse instability of dunes. *Physical Review E*, **107**, 188001. 46, 48, 117, 134

Pearce, K. I., & Walker, I. J. 2005. Frequency and magnitude biases in the 'Fryberger' model, with implications for characterizing geomorphically effective winds. *Geomorphology*, **68**(1-2), 39–55. 152

Pedersen, A., Kocurek, G., Mohrig, D., & Smith, V. 2015. Dune deformation in a multidirectional wind regime: White Sands Dune Field, New Mexico. *Earth Surface Processes and Landforms*, **40**, 925–941. 62, 63

Phillips, J. D., Ewing, R. C., Bowling, R., Weymer, B. A., Barrineau, P., Nittrouer, J. A., & Everett, M. E. 2019. Low-angle eolian deposits formed by protodune migration, and insights into slipface development at White Sands dune field, New Mexico. *Aeolian Research*, **36**, 9–26. 61, 62, 64, 73, 77, 78, 187

Ping, L., Narteau, C., Dong, Z., Zhang, Z., & Courrech du Pont, S. 2014. Emergence of oblique dunes in a landscape-scale experiment. *Nature Geoscience*, **7**, 99–103. 39, 61

Pismen, L. M. 1999. *Vortices in nonlinear fields: From liquid crystals to superfluids, from non-equilibrium patterns to cosmic strings*. Vol. 100. Oxford University Press. 171

Poggi, D, Katul, GG, Albertson, JD, & Ridolfi, L. 2007. An experimental investigation of turbulent flows over a hilly surface. *Physics of Fluids*, **19**(3), 036601. 34

Prandtl, L. 1925. 7. Bericht über Untersuchungen zur ausgebildeten Turbulenz. *ZAMM-Journal of Applied Mathematics and Mechanics/Zeitschrift für Angewandte Mathematik und Mechanik*, **5**(2), 136–139. 21

Provoost, S., Jones, M. L. M., & Edmondson, S. E. 2011. Changes in landscape and vegetation of coastal dunes in northwest Europe: a review. *Journal of Coastal Conservation*, **15**(1), 207–226. 11

Pye, K., & Tsoar, H. 1990. *Aeolian sand and sand dunes*. London: Unwin Hyman. 16, 20, 32, 50, 152

Rachal, D. M., & Dugas, D. P. 2009. Historical dune pattern dynamics: White Sands dune field, New Mexico. *Physical Geography*, **30**(1), 64–78. 171

Rasenat, S., Steinberg, V., & Rehberg, I. 1990. Experimental studies of defect dynamics and interaction in electrohydrodynamic convection. *Physical Review A*, **42**(10), 5998. 171

Rasmussen, K. R., & Sørensen, M. 2008. Vertical variation of particle speed and flux density in aeolian saltation: Measurement and modeling. *Journal of geophysical research: earth surface*, **113**(F2). 27

Reffet, E., Courrech du Pont, S., Hersen, P., & Douady, S. 2010. Formation and stability of transverse and longitudinal sand dunes. *Geology*, **38**, 491–494. 12, 46, 48, 49, 50, 93, 101, 102, 107, 110, 132, 134, 173

Richards, K. J. 1980. The formation of ripples and dunes on an erodible bed. *Journal of Fluid Mechanics*, **99**, 597–618. 32, 60

Rotnicka, J. 2013. Aeolian vertical mass flux profiles above dry and moist sandy beach surfaces. *Geomorphology*, **187**, 27–37. 27

Rozier, O., & Narteau, C. 2014. A real-space cellular automaton laboratory. *Earth Surface Processes and Landforms*, **39**(1), 98–109. 118, 135

Rozier, O., Narteau, C., Gadal, C., Claudin, P., & Courrech du Pont, S. 2020. Elongation and stability of a linear dune. *Geophysical Research Letters*, **46**(24), 14521–14530. 132, 140, 172

Rubin, D.M., & Hunter, R.E. 1987. Bedform alignment in directionally varying flows. *Science*, **237**, 276–278. 48, 50, 52, 93, 127, 134, 136, 170

Rubin, D.M., & Ikeda, H. 1990. Flume experiments on the alignment of transverse, oblique, and longitudinal dunes in directionally varying flows. *Sedimentology*, **37**, 673–684. 48, 93, 101, 170

Runyon, K.D., Bridges, N.T., Ayoub, F., Newman, C.E., & Quade, J.J. 2017. An integrated model for dune morphology and sand fluxes on Mars. *Earth and Planetary Science Letters*, **457**, 204–212. 12, 53, 78

Sauermann, G., Kroy, K., & Herrmann, H. J. 2001. Continuum saltation model for sand dunes. *Phys. Rev. E*, **6403**, 031305. 17, 29, 60, 117

Sauermann, G., Andrade Jr, J. S., Maia, L. P., Costa, U. M. S., Araújo, A. D., & Herrmann, H. J. 2003. Wind velocity and sand transport on a barchan dune. *Geomorphology*, **54**(3-4), 245–255. 39, 42

Schlichting, H., Gersten, K., Krause, E., & Oertel, H. 1955. *Boundary-layer theory*. Vol. 7. Springer. 21

Schmeeckle, M. W. 2014. Numerical simulation of turbulence and sediment transport of medium sand. *Journal of Geophysical Research: Earth Surface*, **119**(6), 1240–1262. 117

Schwämmle, V., & Herrmann, H. J. 2005. A model of barchan dunes including lateral shear stress. *The European Physical Journal E*, **16**(1), 57–65. 39

Scuderi, Louis. 2019. The fingerprint of linear dunes. *Aeolian research*, **39**, 1–12. 171

Seizilles, G., Lajeunesse, E., Devauchelle, O., & Bak, M. 2014. Cross-stream diffusion in bedload transport. *Physics of Fluids*, **26**(1), 013302. 185

Sekine, M., & Parker, G. 1992. Bed-load transport on transverse slope. I. *J. Hydraul. Engng*, **118**, 513–535. 88

Selmani, H., Valance, A., Ould el Moctar, A., Dupont, P., & Zegadi, R. 2018. Aeolian sand transport in out-of-equilibrium regimes. *Geophysical Research Letters*, **45**, 1838–1844. 38, 61

Seppälä, M., & Lindé, K. 1978. Wind tunnel studies of ripple formation. *Geografiska Annaler: Series A, Physical Geography*, **60**(1-2), 29–42. 16

Sharma, V., Braud, L., & Lehning, M. 2019. Understanding snow bedform formation by adding sintering to a cellular automata model. *The Cryosphere*, **13**(12), 3239–3260. 118

Shields, A. 1936. Anwendung der Aehnlichkeitsmechanik und der Turbulenzforschung auf die Geschiebebewegung. *PhD Thesis Technical University Berlin*. 23

Shvidchenko, A. B., Pender, G., & Hoey, T. B. 2001. Critical shear stress for incipient motion of sand/gravel streambeds. *Water Resources Research*, **37**(8), 2273–2283. 23

Skarke, A., & Trembanis, A. C. 2011. Parameterization of bedform morphology and defect density with fingerprint analysis techniques. *Continental Shelf Research*, **31**(16), 1688–1700. 171

Smedman, A.-S., & Bergström, H. 1984. Flow characteristics above a very low and gently sloping hill. *Boundary-layer meteorology*, **29**(1), 21–37. 33

Sørensen, M. 1991. An analytic model of wind-blown sand transport. *Pages 67–81 of: Aeolian Grain Transport 1*. Springer. 42

Sørensen, M. 2004. On the rate of aeolian sand transport. *Geomorphology*, **59**(1-4), 53–62. 27

Stone, A. E. C. 2013. Age and dynamics of the Namib Sand Sea: A review of chronological evidence and possible landscape development models. *Journal of African Earth Sciences*, **82**, 70–87. 174

Stout, J. E., & Zobeck, T. M. 1996. Establishing the threshold condition for soil movement in wind-eroding fields. *Pages 65–72 of: Proceedings of International Conference on Air Pollution from Agricultural Operations*. Citeseer. 154

Stull, R. B. 1988. An Introduction to Boundary Layer Meteorology. *Kluwer Academic Publishers*. 21

Sun, R., & Xiao, H. 2016. CFD–DEM simulations of current-induced dune formation and morphological evolution. *Advances in water resources*, **92**, 228–239. 117

Swanson, T., Mohrig, D., & Kocurek, G. 2016. Aeolian dune sediment flux variability over an annual cycle of wind. *Sedimentology*, **63**, 1753–1764. 64

Sykes, R. I. 1980. An asymptotic theory of incompressible turbulent boundary layer flow over a small hump. *Journal of Fluid Mechanics*, **101**, 647–670. 32, 34, 60

Taniguchi, K., Endo, N., & Sekiguchi, H. 2012. The effect of periodic changes in wind direction on the deformation and morphology of isolated sand dunes based on flume experiments and field data from the Western Sahara. *Geomorphology*, **179**, 286–299. 101

Taylor, P. A., & Gent, P. R. 1974. A model of atmospheric boundary-layer flow above an isolated two-dimensional 'hill'; an example of flow above 'gentle topography'. *Boundary-Layer Meteorology*, **7**(3), 349–362. 33

Taylor, P. A., Mason, P. J., & Bradley, E. F. 1987. Boundary-layer flow over low hills. *Boundary-layer meteorology*, **39**(1-2), 107–132. 33

Telfer, M. W., Hesse, P. P., Perez-Fernandez, M., Bailey, R. M., Bajkan, S., & Lancaster, N. 2017. Morphodynamics, boundary conditions and pattern evolution within a vegetated linear dunefield. *Geomorphology*, **290**, 85–100. 171

Telfer, M.W., Parteli, E.J.R., Radebaugh, J., Beyer, R.A., Bertrand, T., Forget, F., Nimmo, F., Grundy, W.M., Moore, J.M., Stern, S. A., *et al.* . 2018. Dunes on Pluto. *Science*, **360**, 992–997. 133

Thomas, D. S. G. 2011. *Arid zone geomorphology: process, form and change in drylands*. John Wiley & Sons. 152

Tsoar, H. 1982. Internal structure and surface geometry of longitudinal (seif) dunes. *Journal of Sedimentary Research*, **52**(3), 823–831. 132

Tsoar, H. 1989. Linear dunes-forms and formation. *Progress in Physical Geography*, **13**(4), 507–528. 141

Tsoar, H. 2001. Types of aeolian sand dunes and their formation. *Pages 403–429 of: Geomorphological fluid mechanics*. Springer. 40

Ungar, J.E., & Haff, P.K. 1987. Steady state saltation in air. *Sedimentology*, **34**, 289–299. 26, 27, 28, 182

Uppala, S.M., & et al. 2005. The ERA-40 re-analysis. *Quarterly Journal of the Royal Meteorological Society*, **131**, 2961–3012. 85, 152, 154

Valance, A. 2011. Nonlinear sand bedform dynamics in a viscous flow. *Physical Review E*, **83**(3), 036304. 134

Valance, A., & Langlois, V. 2005. Ripple formation over a sand bed submitted to a laminar shear flow. *The European Physical Journal B-Condensed Matter and Complex Systems*, **43**(2), 283–294. 32

Vermeesch, P. 2011. Solitary wave behavior in sand dunes observed from space. *Geophysical Research Letters*, **38**(22). 44

Von Kármán, T. 1935. *Some aspects of the turbulence problem*. Guggenheim Aeronautical Laboratory. 21

Walker, I. J., & Nickling, W. G. 2003. Simulation and measurement of surface shear stress over isolated and closely spaced transverse dunes in a wind tunnel. *Earth Surface Processes and Landforms: The Journal of the British Geomorphological Research Group*, **28**(10), 1111–1124. 41

Walmsley, J. L., Salmon, J. R., & Taylor, P. A. 1982. On the application of a model of boundary-layer flow over low hills to real terrain. *Boundary-Layer Meteorology*, **23**(1), 17–46. 34

Wang, X., Dong, Z., Zhang, J., & Chen, G. 2002. Geomorphology of sand dunes in the Northeast Taklimakan Desert. *Geomorphology*, **42**(3-4), 183–195. 152

Wang, X., Dong, Z., Zhang, J., & Qu, J. 2004. Formation of the complex linear dunes in the central Taklimakan Sand Sea, China. *Earth Surface Processes and Landforms*, **29**(6), 677–686. 173

Ward, A.W., Doyle, K.B., Helm, P.J., Weisman, M.K., & Witbeck, N.E. 1985. Global map of eolian features on Mars. *Journal of Geophysical Research: Solid Earth*, **90**, 2038–2056. 133

Wasson, R. J., & Nanninga, P. M. 1986. Estimating wind transport of sand on vegetated surfaces. *Earth Surface Processes and Landforms*, **11**(5), 505–514. 152

Wasson, R.J., & Hyde, R. 1983. Factors determining desert dune type. *Nature*, **304**(5924), 337. 18, 134, 160

Watson, A. 1986. Grain-size variations on a longitudinal dune and a barchan dune. *Sedimentary geology*, **46**(1-2), 49–66. 166

Werner, B. T. 1990. A steady-state model of wind-blown sand transport. *The Journal of Geology*, **98**(1), 1–17. 28

Werner, B. T., & Kocurek, G. 1999. Bedform spacing from defect dynamics. *Geology*, **27**(8), 727–730. 171

Werner, B.T. 1995. Eolian dunes: computer simulations and attractor interpretation. *Geology*, **23**, 1107–1110. 117, 121

White, B. R. 1982. Two-phase measurements of saltating turbulent boundary layer flow. *International Journal of Multiphase Flow*, **8**(5), 459–473. 27

Wiggs, G. F. S. 2013. Dune morphology and dynamics. *Treatise on Geomorphology*, **11**, 201–218. 60

Wiggs, G. F. S., Livingstone, I., & Warren, A. 1996. The role of streamline curvature in sand dune dynamics: evidence from field and wind tunnel measurements. *Geomorphology*, **17**(1-3), 29–46. 41

Worman, S.L., Murray, A.B., Littlewood, R., Andreotti, B., & Claudin, P. 2013. Modeling emergent large-scale structures of barchan dune fields. *Geology*, **41**, 1059–1062. 44, 79, 134

Wu, X., Zou, X., Zheng, Z. C., & Zhang, C. 2011. Field measurement and scaled-down wind-tunnel model measurement of airflow field over a barchan dune. *Journal of arid environments*, **75**(5), 438–445. 41

Yalin, M. S. 1972. *Mechanics of sediment transport.* New York, U.S.A.: Pergamon Press Inc. 23

Yamagata, Kotaro. 2010. Recent grain-size coarsening of floodplain deposits and forest decline along the Kuiseb River, Namib Desert, Namibia. *African Study Monographs Supplementary Issue.* 166

Yang, B., Wang, Y., & Zhang, Y. 2009. The 3-D spread of saltation sand over a flat bed surface in aeolian sand transport. *Advanced Powder Technology*, **20**(4), 303–309. 112

Zeman, O., & Jensen, N. O. 1987. Modification of turbulence characteristics in flow over hills. *Quarterly Journal of the Royal Meteorological Society*, **113**(475), 55–80. 33

Zhang, D., Narteau, C., & Rozier, O. 2010. Morphodynamics of barchan and transverse dunes using a cellular automaton model. *J. Geophys. Res.*, **115**, F03041. 40, 46, 79, 120

Zhang, D., Narteau, C., Rozier, O., & Courrech du Pont, S. 2012. Morphology and dynamics of star dunes from numerical modelling. *Nature Geoscience*, **5**, 463–467. 18, 54, 117, 120, 134, 136

Zhang, D., Yang, X., Narteau, C., & Rozier, O. 2014. Mean sediment residence time in barchan dunes. *J. Geophys. Res. Earth Surf.*, **119**, 451–463. 120

Zhang, W., Kang, J.-H., & Lee, S.-J. 2007. Tracking of saltating sand trajectories over a flat surface embedded in an atmospheric boundary layer. *Geomorphology*, **86**(3-4), 320–331. 112, 120

Zheng, X.-J., Bo, T.-L., & Zhu, W. 2009. A scale-coupled method for simulation of the formation and evolution of aeolian dune field. *International Journal of Nonlinear Sciences and Numerical Simulation*, **10**(3), 387–396. 117

Zilker, D.P., Cook, G.W., & Hanratty, T.J. 1977. Influence of the amplitude of a solid wavy wall on a turbulent flow. Part 1. Non-separated flows. *J. Fluid Mech.*, **82**, 29–51. 34, 35, 105

Photo courtesy

- Chapter 1: Paul van Schalkwyk, *Sediment transport over a sand dune, Namibia*, http://paulvans.com/album/desert-coast.html?p=1
- Chapter 2: Ybratcher, *Balloon rally at the White Sands dune field, New Mexico, USA*, https://fr.m.wikipedia.org/wiki/Fichier:Balloon_Rally_White_Sands_NM.jpg
- Chapter 3: NASA's Earth Observatory, *Astronaut photograph of a dune pattern, Tenere Desert, Niger*, https://earthobservatory.nasa.gov/images/42070/sand-dunes-in-the-tenere-desert-niger
- Chapter 4: NASA/JPL-Caltech/Univ. of Arizona, *"Feathery Ridges", linear dunes on Mars*, https://mars.nasa.gov/resources/7138/feathery-ridges/
- Chapter 5: Paul van Schalkwyk, *Sunrise over vegetated star dunes, Namibia*, http://paulvans.com/album/desert-rain.html?p=1
- Chapter 6: George Steinmetz, *Dome dune corridor in the Rub'al-Khali, Yemen*, https://www.georgesteinmetz.com/collections/empty-quarter-collection/